One- and two-dimensional coordination assemblies incorporating 3,2′:6′,3″-terpyridine linkers

Inauguraldissertation

zur

Erlangung der Würde eines Doktors der Philosophie

vorgelegt der

Philosophisch-Naturwissenschaftlichen Fakultät

der Universität Basel

von

Dalila Rocco

Basel, 2023

Originaldokument gespeichert auf dem Dokumentenserver der Universität Basel

edoc.unibas.ch

Genehmigt von der Philosophisch-Naturwissenschaftlichen Fakultät

auf Antrag von

Prof. Dr. Edwin C. Constable

Prof. Dr. Christof Sparr

Prof. Dr. Mir Wais Hosseini

Basel, den 13. Dezember 2022

Prof. Dr. Marcel Mayor

Dekan der Philosophisch-Naturwissenschaftlichen Fakultät

Alla mia famiglia

Acknowledgments

First and foremost, I am deeply grateful to Prof. Dr. Catherine E. Housecroft and Prof. Dr. Edwin C. Constable for giving me the great opportunity to join their research group. Their trust, constant support and encouragement have been precious for my personal and professional development. I will always be proud to have worked with them during these years.

I would like to thank Prof. Dr. Christof Sparr for being my second supervisor and Prof. Dr. Mir Wais Hosseini, who kindly accepted the role of external expert. I appreciate the time they made for reading my thesis and for being part of my defense committee.

I thank Prof. Dr. Murielle F. Delley for kindly agreeing to be the chair of my final examination.

Many thanks to the whole staff of the Chemistry Department for their work. In particular, to Dr. Alessandro Prescimone for measuring my crystals, solving the structures and for teaching me all I know about crystallography and diffractometers. Thanks to the analytics team for all their measurements: Sylvie Mittelheisser, Michael Pfeffer and especially Jonas Zurflüh, for additionally instructing me about the ESI-MS instrument and for always being available to help. To Beatrice Erismann and Isa Worni for their administrative work, to Dr. Bernhard Jung and the IT team, to Prof. Dr. Daniel Häussinger and his group for NMR support, to Markus Hauri, Susanne Foley and the workshop team.

A big thanks goes to the whole Constable/Housecroft research group, to the current and former members I met during the past years. I am happy I had the chance to carry out my PhD in such an enjoyable and friendly working environment. In particular, *spasibo* Masha for making me feel understood during my expat journey, from the very first day. Thanks to Guglielmo for introducing me to new music, new people, and for the adventures we lived together outside the lab. Thanks to Giacomo for sharing some knowledge about coordination polymers when I was new to the topic. Many thanks to Marco and Sven for all their help with technology, to Samantha and Anamarija for their work and dedication under my supervision; it has been a pleasure working with all of you.

A special thanks goes also to the Meier/Palivan group for "adopting" me. I am so lucky to have been unofficially part of your group as well, to join many of your events and to share amazing free time and trips around Switzerland, Germany and France with many of you. *Mamnunam* Shabnam for your friendship throughout these four years. Many thanks to Ricco, Moritz, Maryame, Alessandro, Maria and all the others for counting me as one of you.

Additional thanks to Carlotta and Giacomo P. for their friendship, and to all the amazing people I have met during my time at the University of Basel.

Lastly, I express my gratitude to my old friends, my family and Werner for their love and constant support.

Abstract

In the field of material sciences, coordination polymers represent a topic of interest, due to their extended structures and the associated properties. To date, the formation of these networks is a fascinating but not fully understood phenomenon, and the evidence of structure-property relationships makes the control of this process an issue of major concern. Towards this end, systematic studies in which one parameter is varied at one time could offer a meaningful contribution to gain a better comprehension of the factors that influence the assembly of one kind of structure over the other possibilities. This is especially true when flexible building blocks are chosen. Although a substantial part of the effort in this area has been centered on the use of rigid ligands, there is scope for developing metal coordination assemblies with more flexible components. In particular, in this PhD thesis, homologous series of ditopic 3,2′:6′,3″-terpyridine ligands have been synthesized following the one-pot procedure by Wang and Hanan, fully characterized (as described in Chapter 2) and their coordination chemistry has been explored focusing on two metal salts. Copper(II) acetate (which typically forms dinuclear paddle-wheel motifs) directed the assembly of 1D-chains (Chapter 3), while cobalt(II) thiocyanate led to the formation of 2D-nets with a (4,4) topology (Chapter 4); only one exception for each category is reported. All the obtained coordination polymers have been characterized via single-crystal XRD, solid state FT-IR and powder X-ray diffraction (PXRD), the latter to confirm whether the crystal chosen for structural determination was representative of the bulk sample. A structural determination and description is reported for each of the coordination assemblies, including comparisons to underline similarities and differences between the networks, in terms of topology, packing interactions and lattice solvents. Thermogravimetric analysis coupled with mass spectrometry (TGA-MS) has been conducted on some of the obtained polymers, with the purpose of identifying and quantifying the solvent released from the lattice under mild condition, i.e. without the net losing its crystallinity. Further TGA-MS measurements have been carried out to check whether the process of solvent extraction is reversible and if the removed solvent could be replaced by other small molecules.

In Chapter 5, the notion of "expanded ligands" is introduced, referring to analogs of conventional ligands in which the donor sites are separated by metal-containing groups. With the aim of combining this concept of metalloligands with terpyridine-based building blocks, in the last part of the thesis asymmetric bis(terpyridines) have been prepared, containing the 2,2′:6′,2″-terpyridine bis(chelating) unit on one end and the divergent ditopic 3,2′:6′,3″- or 4,2′:6′,4″- terpyridine unit on the other. Homoleptic iron(II) complexes of the asymmetric bisterpyridine compounds have been synthesized; these are tetratopic metal-containing molecules, which represent a new type of expanded ligands, i.e. the expanded version of the purely organic bis(terpyridines), and are potential building blocks for the assembly of coordination polymers. All the intermediates and the final compounds have been fully characterized, and several crystallization experiments with different metal salts have been

carried out in attempts to obtain supramolecular architectures incorporating the newly-prepared expanded ligands.

Most of the work in this thesis has been published in the following articles and communications:

1. Rocco, D.; Housecroft, C.E.; Constable, E.C. Synthesis of Terpyridines: Simple Reactions - What Could Possibly Go Wrong? *Molecules* **2019**, *24*, 1799; doi: 10.3390/molecules24091799.
2. Rocco, D.; Prescimone, A.; Klein, Y.M.; Gawryluk, D.J.; Constable, E.C.; Housecroft, C.E. Competition in Coordination Assemblies: 1D-Coordination Polymer or 2D-Nets Based on $Co(NCS)_2$ and 4′-(4-methoxyphenyl)-3,2′:6′,3″-terpyridine. *Polymers* **2019**, *11*, 1224; doi: 10.3390/polym11071224.
3. Rocco, D.; Manfroni, G.; Prescimone, A.; Klein, Y.M.; Gawryluk, D.J.; Constable, E.C.; Housecroft, C.E. Single and Double-Stranded 1D-Coordination Polymers with 4′-(4-Alkyloxyphenyl)-3,2′:6′,3″-terpyridines and $\{Cu_2(\mu\text{-}OAc)_4\}$ or $\{Cu_4(\mu_3\text{-}OH)_2(\mu\text{-}OAc)_2(\mu_3\text{-}OAc)_2(AcO\text{-}\kappa O)_2\}$ Motifs. *Polymers* **2020**, *12*, 318; doi: 10.3390/polym12020318.
4. Rocco, D.; Prescimone, A.; Constable, E.C.; Housecroft, C.E. Directing 2D-Coordination Networks: Combined Effects of a Conformationally Flexible 3,2′:6′,3″-Terpyridine and Chain Length Variation in 4′-(4-n-Alkyloxyphenyl) Substituents. *Molecules* **2020**, *25*, 1663; doi: 10.3390/molecules25071663.
5. Rocco, D.; Prescimone, A.; Constable, E.C.; Housecroft, C.E. Switching the Conformation of 3,2′:6′,3″-tpy Domains in 4′-(4-n-Alkyloxyphenyl)-3,2′:6′,3″-Terpyridines. *Molecules* **2020**, *25*, 3162; doi: 10.3390/molecules25143162.
6. Rocco, D.; Prescimone, A.; Constable, E.C.; Housecroft, C.E. Straight Versus Branched Chain Substituents in 4′-(Butoxyphenyl)-3,2′:6′,3″-terpyridines: Effects on (4,4) Coordination Network Assemblies. *Polymers* **2020**, *12*, 1823; doi: 10.3390/polym12081823.
7. Rocco, D.; Novak, S.; Prescimone, A.; Constable, E.C.; Housecroft, C.E. Manipulating the Conformation of 3,2′:6′,3″-Terpyridine in $[Cu_2(\mu\text{-}OAc)_4(3,2'\text{:}6',3''\text{-tpy})]_n$ 1D-Polymers. *Chemistry* **2021**, *3*, 182-198; doi: 10.3390/chemistry3010015.
8. Rocco, D.; Novak, S.; Prescimone, A.; Constable, E.C.; Housecroft, C.E. Coordination networks assembled from $Co(NCS)_2$ and 4′-[4-(naphthalen-1-yl)phenyl]-3,2′:6′,3″-terpyridine: Role of lattice solvents. *Polyhedron* **2021**, *208*, 115445; doi: 10.1016/j.poly.2021.115445.
9. Rocco, D.; Prescimone, A.; Constable, E.C.; Housecroft, C.E. Adapting (4,4) Networks through Substituent Effects and Conformationally Flexible 3,2′:6′,3″-Terpyridines. *Molecules* **2021**, *26*, 6337; doi: 10.3390/molecules26216337.
10. Rocco D.; Prescimone, A.; Constable E.C.; Housecroft, C.E. *CSD Communication*, **2021**; doi: 10.5517/ccdc.csd.cc28wfby.
11. Rocco, D.; Prescimone, A.; Housecroft, C.E. *CSD Communication*, **2022**; doi: 10.5517/ccdc.csd.cc2cyymx.

In addition, the candidate has coauthored the following paper with her Master's candidate Anamarija Nikoletić:

1. Rocco, D.; Nikoletić, A.; Prescimone, A.; Constable, E.C.; Housecroft, C.E. To Be or Not to Be a (4,4) Net: Reactions of 4′-{4-(*N*,*N*-Diethylaminophenyl)}- and 4′-{4-(*N*,*N*-Diphenylaminophenyl)}-3,2′:6′,3″- and 4,2′:6′,4″-Terpyridines with Cobalt(II) Thiocyanate. *Crystals* **2022**, *12*, 1136; doi: 10.3390/cryst12081136.

Abbreviations

2,2′:6′,2″-tpy	2,2′:6′,2″-terpyridine
3,2′:6′,3″-tpy	3,2′:6′,3″-terpyridine
4,2′:6′,4″-tpy	4,2′:6′,4″-terpyridine
4,4′-bpy	4,4′-bipyridine
B_2pin_2	Bis(pinacolato)diboron
COSY	Homonuclear correlation spectroscopy
CSD	Cambridge Structural Database
CP	Coordination polymer
δ	Chemical shift
DMF	*N,N*-Dimethylformamide
EtOH	Ethanol
FT-IR	Fourier-transform infrared spectroscopy
ESI-MS	Electrospray ionization mass spectrometry
HMBC	Heteronuclear multiple bond correlation
HMQC	Heteronuclear multiple-quantum correlation
HR-MS	High-resolution electrospray ionization mass spectrometry
MALDI-TOF	Matrix-assisted laser desorption ionization-time of flight
MeCN	Acetonitrile
MeOH	Methanol
MHz	Megahertz
MOF	Metal organic framework
m/*z*	Mass to charge ratio
NMR	Nuclear magnetic resonance
NOESY	Nuclear Overhauser effect spectroscopy
[Pd(dppf)Cl_2]	[1,1′-Bis(diphenylphosphano)ferrocene]dichloridopalladium(II)
ppm	Parts per million
SBU	Secondary building unit
PXRD	Powder X-ray diffraction
RT	Room temperature
TGA	Thermogravimetric analysis
UV-Vis	Ultraviolet-visible
XRD	Single-crystal X-ray diffraction

Table of Contents

Chapter 1 Introduction

The discovery of innovative functional materials has played a critical role in the development of new technologies and is one of the major aims of research within the field of material sciences. In this context, coordination polymers[1-3] (CPs) and metal-organic frameworks[4-6] (MOFs) have emerged rapidly as materials with a particular potential. CPs and MOFs constitute an interdisciplinary field with its origins in inorganic and coordination chemistry that has expanded rapidly in the last decades and attracted also the interest of the chemical industry.[7, 8] The diversity in both the focus and the scientific base of those involved has led to a variety of terminological usages for this class of compounds. According to the IUPAC definition, a coordination polymer is "a coordination compound with repeating coordination entities extending in 1, 2, or 3 dimensions"; whereas a metal-organic framework is "a coordination network with organic ligands containing potential voids".[9] The term "coordination polymer" will be used throughout this thesis. The approach to this field is *via* coordination chemistry. As defined by the IUPAC, "a coordination compound is any compound that contains a coordination entity. A coordination entity is an ion or neutral molecule that is composed of a central atom, usually that of a metal, to which is attached a surrounding array of atoms or groups of atoms, each of which is called a ligand".[10] Thus, the combination of metal ions with multitopic organic ligands through coordination bonds can lead to the formation of one-, two- or three-dimensional (1D, 2D or 3D) structures, with a huge diversity of topologies and properties. Coordination bonds hold together the building blocks. However, weaker inter- and intramolecular interactions such as hydrogen bonds, van der Waals or π-π stacking interactions contribute significantly to the assembly of 1D, 2D or 3D supramolecular architectures.[11,12]

1.1 Self-assembly processes

A noteworthy feature of coordination polymers is the reversibility of the interactions involved in their assembly. Errors in the association of the building blocks can readily be corrected during the growth of the network. This property is in contrast to the bonds in purely organic polymers, which are covalent and mainly irreversible.[1] The reversible process of coordination bond formation between metal building blocks and organic ligands that eventually leads to the formation of ordered crystalline structures, is referred to as a self-assembly process.[13] Therefore, self-assembly of coordination polymers is a very powerful tool with which to generate multidimensional structures that would otherwise be very difficult and time consuming to obtain by conventional organic chemical processes involving sequential bond formation. The control of the self-assembly process can lead to the formation of multidimensional structures which possess designed features. The interdisciplinary field that bridges solid-state and supramolecular chemistry, with the aim to direct the multidimensional

assembly and packing, is known as crystal engineering.[14] It studies the design and synthesis of solid-state structures with tailored assembly of materials with desirable features.

1.2 Applications

Functional properties such as surface area and porosity of coordination networks mainly depend on the selection of the metal ions and organic ligands for the building blocks.[15] On the other hand, the structural topology is influenced by the synthetic conditions, for example temperature, pH-value, solvent and ratio of the reactants.[16] By varying the building blocks as well as the synthesis conditions, the coordination assemblies can easily be modified. The use of vectorially preorganized building blocks for the rational design of 2- and 3-dimensional metal coordination architectures is a well-developed field,[17, 18] and leads to the customized assembly of metal-organic frameworks (MOFs) with widespread applications.[19] These include gas storage[20] and separation,[21-26] batteries,[15] photocatalysis[27] and solar cells,[28] drug delivery,[29] and water purification.[30, 31] Furthermore, there is scope to generate homochiral coordination networks,[32-34] which are of great interest as they possess well-structured internal chiral cavities, enhancing the capabilities of MOFs and extending the range of available applications.[35,36] The latter have potential for use as agents for enantioselective separations[37-39] and, for example, stereospecific transformations,[24, 40, 41] sensing[42] and catalysis.[43] More than one synthetic strategy is available, but the use of enantio-pure organic building blocks is the most reliable approach to homochiral CPs.[44] However, in this thesis, only one ligand containing a stereogenic center was used (as a racemate), and the corresponding coordination polymer with cobalt(II) thiocyanate crystallized in the centrosymmetric $P2_1/n$ space group (see Section 4.3).

1.3 Topological description and nomenclature of networks

Crystals are periodic materials that can be described as supramolecular architectures. Unlike discrete molecules, they possess translational symmetry and can be considered as infinite molecular assemblies containing particular sets of interactions repeated through space.[45] The topological analysis allows one to simplify complicated structures to straightforward networks which facilitates their understanding and design. Furthermore, it is a powerful approach to compare chemically different networks revealing underlying close relationships.[46] A network can be considered as a repeating pattern composed of inter-linked nodes. The number of unique nodes and linkers is finite. The individual nodes are connected to three or more nodes via linkers, and one linker can only connect two nodes. If a node is solely connected to two further nodes, then it is no longer a node and is referred to as a linker, and if a linker connects more than two nodes it becomes a node.[1] The metal center and the organic ligand (Figure 1) can act either as node or as linker or both, depending on their connectivity in the final structure. The chemical nature of the component is not the decisive factor but rather the structural role it plays.[46]

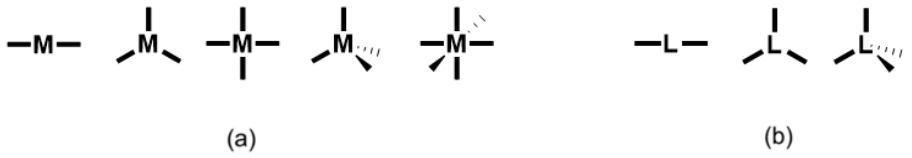

Figure 1. (**a**) Examples of metal centers with different numbers of free coordination sites; (**b**) selection of multidentate bridging ligands, represented in a general sense for a ligand **L**.

The description of networks only occurs in a topological and not in a geometric manner. Therefore, there is no topological difference between a square-planar and a tetrahedral 4-connecting node because they can be converted into each other by distortion and without breaking bonds.[1] Similarly, trigonal and T-shaped 3-connecting nodes are topologically identical although the former form a hexagonal network and the latter a brick-wall network.[46] Nevertheless, the geometry of the individual nodes might be important during the process of network design.

The nomenclature is furthermore important in order to uniquely and clearly identify a network. One possibility is to describe the shortest circuits that are present in the structures and the connectivity of the nodes in a numerical fashion. The shortest circuit refers to the number of nodes in the smallest cycle that can be formed and that includes two linkers originating from a particular node. The term "connectivity" in a coordination polymer refers to the connections formed between a metal center and the ligands that extend the coordination polymer itself. This means that the bonds with ligands that do not extend the assembly are not counted in this terminology; thus there is a distinction between coordination and connectivity. When neutral organic ligands (e.g. oligopyridines) with more than one donor atom are combined with $Co(NCS)_2$, the Co(II) center frequently shows a connectivity of four, while being hexacoordinated. It is also possible that solvent molecules, like MeOH or water, coordinate to the Co(II) center, thus reducing its connectivity. Some examples are reported below (Section 1.5.1) and one is discussed in the main part of this thesis. Networks where all the unique nodes have the same sized short circuits and the same connectivity are defined as "uniform", and can be described with a (n,p) notation. The first number (n) indicates the size of the shortest circuit, while the second number (p) refers to the connectivity of the respective node.[46] A (4,4) net therefore has the smallest circuit containing four nodes, each with a connectivity of 4 (Figure 2); this is the notation adopted in the present thesis for 2D coordination polymers.

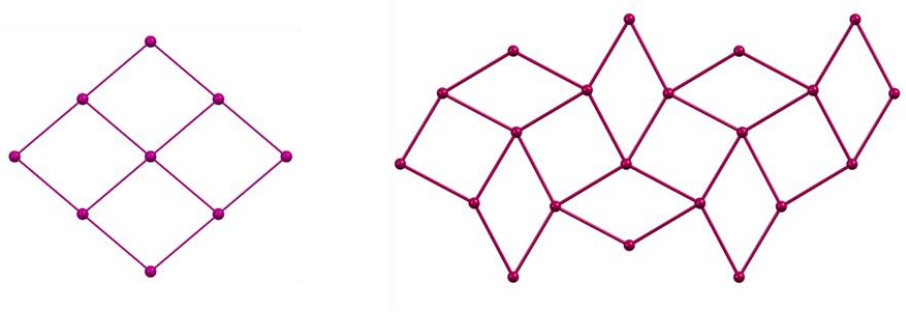

Figure 2. Examples of (4,4)-networks.

Coordination polymers where metal ions with a connectivity of two are bridged by two-donor ligands are identified as 1D. Structures where metal ions with multiple connectivity are combined with multitopic ligands can be defined either as 2D or 3D, depending on whether the metal ions are connected in two dimensions or in all three. In this thesis, the focus is on 1D and 2D structures.

1.4 Synthesis and characterization of coordination polymers

The formation of molecular networks remains an intriguing field. Knowing the theoretical connectivity of the chosen metal and the number and the disposition of the donor atoms of the organic ligand does not necessarily allow one to predict the nature of the resultant coordination network. The numerous non-covalent interactions and their poor directionality contribute to the non-predictability of the outcome. Furthermore, different networks can be formed under the exact same synthesis conditions; this phenomenon is known as polymorphism[12] and a few cases are described in this thesis. CPs are typically insoluble once they are assembled. Solvation might be achieved using strongly coordinating solvents, but the coordination of the solvent itself would change the structure of the coordination network, rendering it different from the original one.[1] The polymeric structures of the coordination networks are therefore characteristic of the solid state only. Consequently, in order to identify and describe the assemblies as well as the interactions within one network, the analytical method of choice is single-crystal X-ray diffraction (XRD). This crystallographic analysis allows detailed structural investigation of the coordination assembly. Eventually, precise structure-property correlations can be made.[1] The exponential increase in the synthesis and studies of coordination polymers in the recent years is certainly also due to the ability to perform routine single-crystal structural determinations. The low solubility of CPs makes it difficult to obtain single crystals suitable for XRD by using classical approaches like recrystallization. Crystals of X-ray quality must therefore be obtained directly from the synthetic reaction.[46, 47] This can be achieved through several methods. Hydro- or solvothermal conditions are frequently employed. High temperatures and high pressures allow the synthesis of polymeric coordination compounds characterized by high stability from reagents that are poorly soluble or poorly reactive under ambient conditions.[48] Microwave-assisted,

sonochemical, electrochemical or mechanochemical synthesis are among further known preparation methods.[49] Alternatively, crystals can be grown from a solution by slowly decreasing the solubility until oversaturation is reached and, therefore, crystals start to grow. There are several methods to decrease solubility such as slow evaporation of the solvent, slow cooling of a hot oversaturated solution, or diffusion of a non-solvent (so-called anti-solvent) into a solution containing both building blocks.[1] The solutions layering technique was chosen, by layering one solution (e.g. of the metal salt) over another solution (e.g. of the ligand); crystals grew during the slow diffusion of one solution into the other (Figure 3).

Figure 3. Crystals of a coordination polymer grown using the layering technique of solutions of a metal salt and a ligand. On top: pink methanol solution of $Co(NCS)_2$; at the bottom: chloroform solution of the chosen organic ligand; single crystals formed at the interface after the two solutions started diffusing one into the other.

Critical to all preparation methods is the slow formation of crystals, without any disturbance such as vibrations in order to obtain high quality crystals with the right size for the X-ray diffraction experiments.

1.5 Building blocks

Despite the difficulties encountered in the prediction of the resulting coordination polymer, the starting points remain the notional connectivity of the metal center, its geometry, and the number of the donor atoms in the organic ligand,[1] as well as the vectorial arrangement of the donor atoms and the flexibility of the ligand. First of all, the number of possible coordination bonds between the metal ion and the organic ligand influences the outcome and can promote the formation of structure with a specific dimensionality over the other possibilities.

The terms monotopic, ditopic, tritopic, tetratopic and multitopic describe the ability of an organic ligands to build a connection to one, two, three, four or multiple different metal

ions, respectively (Scheme 1). The directional assembly of coordination polymers and networks depends upon the compatibility of directing-nodes and linkers.[50]

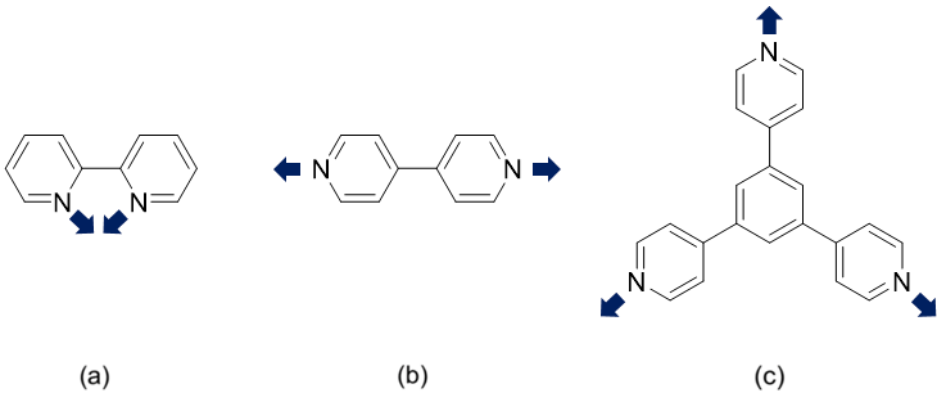

Scheme 1. Examples of (**a**) monotopic, (**b**) ditopic and (**c**) tritopic ligands.

1.5.1 Metal ions and secondary building units (SBUs)

The metal ions used in coordination polymers are usually transition metals (d-block) or lanthanoid metals (f-block). First-row elements like copper or cobalt as well as the d^{10} metals zinc(II), cadmium(II) or mercury(II) are common in CPs due to the predictability and/or flexibility of their coordination behavior, their kinetic lability as well as their stability and broad availability.[1, 51] Lanthanoid metals are also widespread building blocks in CPs due to their higher coordination numbers and physical properties including luminescence and magnetism.[52] The large variety of metals with different size, charge, oxidation state, hardness/softness and coordination behavior already presents a large number of possible building blocks for the coordination assemblies. The metal ion might be considered as an assembly template for the organic ligands.[12] This is particularly true in the case of the so-called secondary building units (SBUs), i.e. well-defined molecular units used to direct extended frameworks in a pre-determined and controlled fashion.[53] One of the simplest SBUs is the $M_2(\mu\text{-}O_2CR)_4$ paddle-wheel motif in which the axial sites of the dinuclear core provide linear directionality[53-56] (Scheme 2).

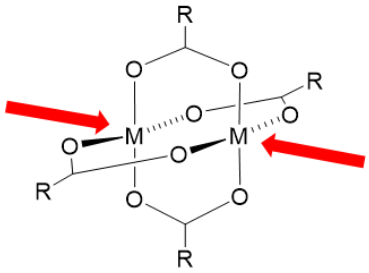

Scheme 2. Representation of an $\{M_2(\mu\text{-}O_2CR)_4\}$ paddle-wheel secondary building unit (SBU) with available coordination sites. There may or may not be a direct M–M bonding interaction depending upon the d^n configuration.

The manner in which the $M_2(\mu\text{-}O_2CR)_4$ units are connected in a coordination network depends upon the nature of the linkers, and also whether the R group in the bridging carboxylate is coordinatively innocent or not. In a simple case, where R is non-coordinating and the organic linker is a rigid rod, such as 4,4′-bipyridine (4,4′-bpy), a topologically and structurally linear 1D-chain is assembled, as for example in $[Mo_2(\mu\text{-}O_2C^tBu)_4(4,4'\text{-bpy})]_n$.[57] 3D Frameworks can be achieved by retaining a rigid linker, such as 4,4′-bpy, but introducing paddle-wheel units which incorporate multifunctional carboxylate ligands.[58] The use of organic dicarboxylates for connected paddle-wheel motifs in combination with rigid bidentate linkers is an established strategy for MOF design.[23, 59] Several examples of ditopic ligands combined with $\{M_2(\mu\text{-}O_2CR)_4\}$ (M = Cu, Zn; non-coordinating R) units have been reported, leading to 1D-coordination polymers with a linear topology.[60-64] Although paddle-wheel SBUs are typical, there is also the possibility of assembling lower or higher nuclearity motifs. To cite some examples, the reaction of $Zn(OAc)_2{\cdot}H_2O$ with **L1** (4′-(2′,3′,4′,5′,6′-pentafluorobiphenyl-4-yl)-4,2′:6′,4″-terpyridine) yielded crystals of the expected 1D-coordination polymer $[Zn_2(\mu\text{-}OAc)_4\mathbf{L1}]_n$ in addition to crystals of $[Zn_5(OAc)_{10}(\mathbf{L1})_4{\cdot}11H_2O]_n$ in the same crystallization tube.[62] The latter comprises quadruple-stranded polymer chains supported by $\{Zn_5(OAc)_{10}\}$ units. A similar example, involving copper(II) acetate instead of zinc(II) acetate, is presented in this thesis. Analogously, the formation of the expected 1D-coordination polymer $[Cu_2(\mu\text{-}OAc)_4(\mathbf{L2})]_n$ (**L2** being 4′-(4-methoxyphenyl)-3,2′:6′,3″-terpyridine) is reported together with the simultaneous formation of a double-stranded 1D-coordination polymer. More examples of multiple-stranded 1D-CPs have been observed from the reaction of cadmium(II) acetate or manganese(II) acetate with other ditopic ligands, again as a result of the assembly of non-paddle-wheel SBUs.[65-67] Limiting the search to polymers containing the copper(II) ion bonded to a pyridine ring incorporated in the ligand, there are several examples of different copper(II) acetate-based units in CPs, including several 1D-coordination polymers with the mononuclear $\{Cu(OAc)_2\}$ building block[68-78], as well as 2D-networks with the same mononuclear unit.[79, 80] Furthermore, some 1D-coordination polymers include alternating mononuclear $\{Cu(OAc)_2\}$ and dinuclear $\{Cu_2(\mu\text{-}OAc)_4\}$ paddle-wheel units along the chain,[81, 82] or alternating $\{Cu_2(\mu\text{-}OAc)_4\}$ paddle-wheel and dinuclear $\{Cu_2(OAc)_2(amp)_2\}^{2+}$ units, with amp = 2-(aminomethyl)pyridine), linked by bridging acetates.[83] Examples of copper-based CPs with higher nuclearity are also known, such as the 1D-CP with tetranuclear $\{Cu_4(OAc)_6(\mu_3\text{-}OH)_2\}$ units,[84] and even more complex frameworks[85] and MOFs[86] assembled from copper(II) acetate. Fujita and coworkers[87] reported a series of compounds containing diamond chain units composed of copper, hydroxide and acetate ions, and water molecules, prepared by the hydrolysis of copper acetate in aqueous solution containing organic sulfonates. An example of 1D chains containing a tetranuclear copper(II) acetate "paddle-wheel" complex formed from the dimerization of the copper(II) tetraacetate core has been published as well.[88] Despite these examples, copper(II) acetate tends to crystallize in the form of $\{Cu_2(\mu\text{-}OAc)_4\}$ paddle-wheel units, meaning that the reactions between $Cu(OAc)_2{\cdot}H_2O$ and ditopic ligands, as the ones used in this work, might typically be expected to lead to 1D-chains of general formula $[Cu_2(\mu\text{-}OAc)_4\mathbf{L}]_n$, as showed and discussed in the main part of this thesis.

Besides copper(II) acetate, the other metal salt extensively employed in this dissertation is cobalt(II) thiocyanate. While the former (with ditopic ligands) usually directs the assembly of 1D-coordination polymers, the latter is a potential 4-connecting node, i.e. the cobalt(II) center tends to assume an octahedral coordination with two sites occupied by thiocyanato ligands, often (but not exclusively) in *trans*-positions, thus yielding 2D-networks. Reactions of $Co(NCS)_2$ and ditopic ligands often produce 2-dimensional (4,4) nets,[63, 89-91] although the unexpected assembly of 3-dimensional architectures has been observed in a few cases.[92, 93] Sometimes, solvent molecules can coordinate to the cobalt(II) center, thus reducing its connectivity and leading to the assembly of 1D-chains. Usually this occurs with H_2O[94-96] or MeOH[90, 91, 97, 98] molecules, but there are examples with coordinated DMF[99] (dimethylformamide) or DMA[100] (dimethylacetamide) as well. 1D-chains can also be the result of the thiocyanate ligands assuming a N,S-bridging mode between metal centers.[101-107] Moreover, the structure with CSD refcode DACSAF presents a 1D looped chain.[108] This search is limited to Co(II) ions bonded to pyridine rings contained in the organic ligands and it is not exhaustive. Although a variety of situations may occur, 2D networks can be anticipated as the product of the reaction between cobalt(II) thiocyanate and ditopic ligands.

1.5.2 Organic ligands

The variety of available metal building blocks is complemented by the unlimited variety of the organic ligands which are employed to bridge the metal centers in the construction of CPs. This role usually requires multidentate ligands, namely with two or more donor atoms, which are referred to as ditopic, tritopic or tetratopic, according to their ability to coordinate to two, three or four different metal ions.[12] The multitude of organic components is the basis for the variety in structural topologies,[11] and the combination of organic and inorganic components opens the playground for the crystal engineering. The organic ligand can be designed in such a way as to meet the requirements for the desired network, tuning the physical properties and thus realizing various applications. Some of the relevant properties to consider are size, flexibility, solubility and the number of donor atoms.[1] For instance, the size of the ligand can be crucial for the resulting pore sizes, which in turn are decisive for the corresponding properties of the network.[109] Flexible ligands increase the number of different possible resulting networks, making the outcome more random, and complicating the prediction of the formed structure. Consequently, rigid ligands are more frequently used and are generally considered more attractive, as they provide a greater degree of control of the steric consequences, with well-defined, reliable coordination patterns. Nevertheless, the conflict between achieving a predetermined or a serendipitous assembly is an underlying problem for the coordination chemist or crystal engineer, and many well-intentioned attempts to prepare functional MOFs according to rational design have not been successful. The anticipated trends in the coordination of a ligand in a discrete molecular assembly do not necessarily transform to the expected infinite network.[110] Hence, although a key factor in controlling MOF assembly is the use of rigid organic linkers such as 4,4'-bipyridine,[17, 111] there is scope for developing

metal coordination assemblies with more flexible ligands, as a building block with less well-defined properties does not necessarily translate to less functional materials.[110] Constable and Housecroft have described similar self-assembly processes as examples of "fuzzy logic".[112] The studies reported in this thesis were carried out on conformationally flexible ditopic ligands, and illustrate how small changes in the substituent groups can be accommodated through the flexibility of the ligands themselves, without significantly affecting the topology of the network, as discussed below.

In the coordination bond formed between the metal center and the organic ligand, the latter acts as a Lewis base, and is typically either neutral or anionic. Covalently bonded elements, such as nitrogen, oxygen, sulfur, phosphorus, fluorine, chlorine, bromine or iodine, possessing free lone pairs can act as donor atoms in the corresponding ligand. However, the most common organic molecules adopted as Lewis bases in CPs contain either oxygen or nitrogen donors, in particular carboxylates or pyridines.[16] Polycarboxylates are multidentate anionic organic ligands with hard oxygen donors. Furthermore, carboxylates have variable coordinating, and therefore bridging, modes. Oligopyridines are practical building blocks for the assembly of one-dimensional chains or ladders, two-dimensional grids or three-dimensional networks. They are neutral Lewis bases (unless functionalized with additional charged groups) and can act as hydrogen-bond acceptors.[113] In this case, and in general employing neutral nitrogen ligands, additional charge balance is required and is achieved by the counterions from the original metal salt or other guests in the coordination network.[113] Schemes 3 and 4 show some examples of ligands with oxygen and nitrogen donor atoms commonly used in coordination polymers, although this illustrates only a small part of feasible organic ligands.[1, 12, 113, 114]

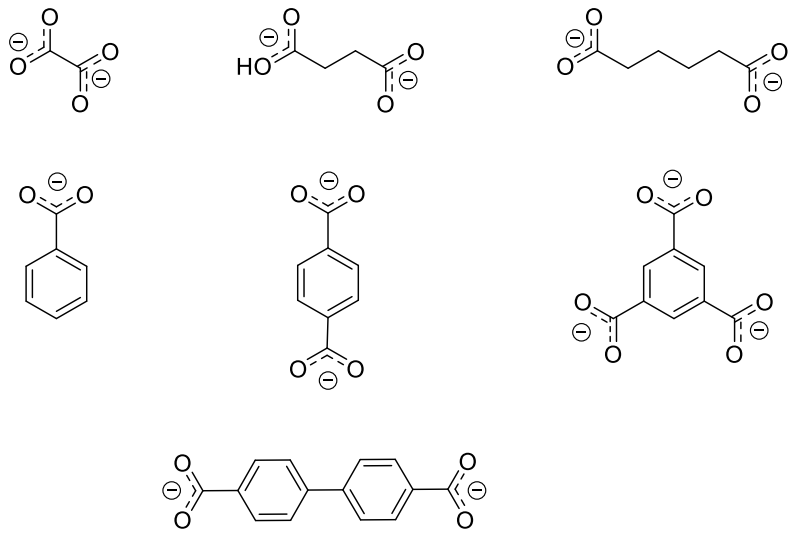

Scheme 3. Examples of some carboxylate-containing ligands commonly used as building blocks in coordination polymers; namely: oxalate, succinate, adipate, benzoate, terephthalate, benzene-1,3,5-tricarboxylate and [1,1'-biphenyl]-4,4'-dicarboxylate.

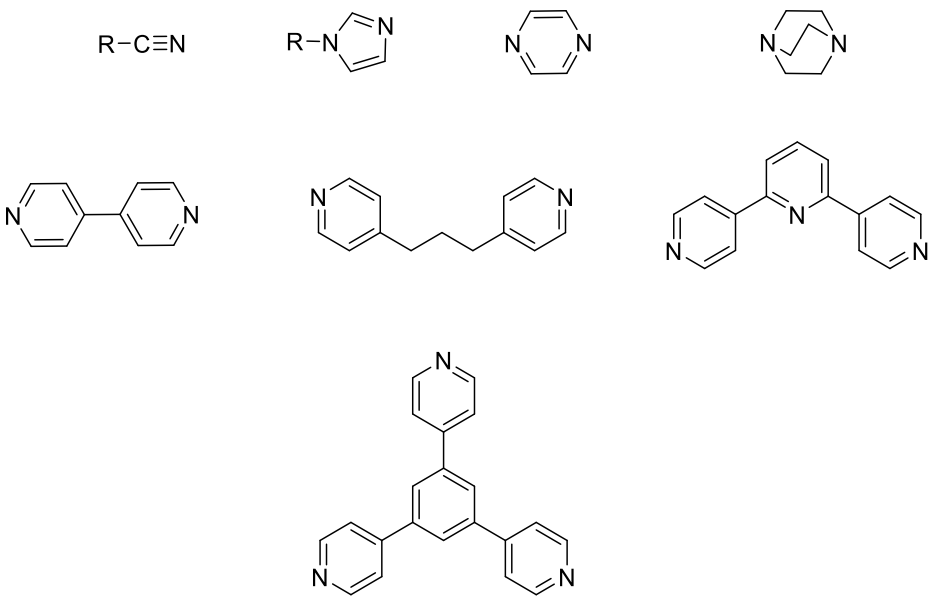

Scheme 4. Examples of prototypical ligands containing nitrogen donors used in the assembly of coordination polymers, namely: nitriles; imidazoles; pyrazine; 1,4-diazabicyclo[2.2.2]octane; 4,4′-bipyridine; 1,3-di(pyridin-4-yl)propane; 4,2′:6′,4″-terpyridine and 1,3,5-tri(pyridin-4-yl)benzene.

The ligands can be supplemented with functional groups, which provide further scope for inter- and intramolecular interactions. Another important factor to consider when choosing an organic ligand as building block in coordination assemblies is its solubility. This is due to the already mentioned fact that various synthetic methods involve in-situ self-assembly in solution. As a result, sufficient solubility of the organic ligand is a prerequisite for the success of these syntheses.[1] Of course, there is also the possibility of using more than one type of organic ligand or metal in the assembly of coordination polymers. These mixed building blocks, e.g. with different flexibility or connectivity, add additional functionality to the respective networks. This usually results in properties that cannot be achieved using solely one type of metal or ligand.[115]

1.6 Terpyridine ligands as building blocks in coordination polymers

The archetypal terpyridine (tpy) is 2,2′:6′,2″-tpy (Scheme 5a) which prefers a terdentate, bis-chelating mode of coordination to a metal ion.[116] A conformational change from *s-trans*,*s-trans* to *s-cis*,*s-cis* accompanies metal binding (compare Scheme 5a and 5b), and mononuclear complexes containing $\{M(tpy)_2\}$ (Scheme 5c) or $\{M(tpy)X_n\}$ domains are ubiquitous.[117-120] Examples of coordination compounds in which 2,2′:6′,2″-tpy ligands exhibit hypodentate modes are represented as well.[121] Thus, the introduction of a coordinatively non-innocent substituent is typically required to transform an $\{M(tpy)_2\}$ unit into a building block within an extended assembly,[122] namely to transform it into a divergent metal-binding domain. In fact,

there is a range of coordination polymers which feature substituted {M(tpy)$_2$} units as "expanded ligands", and this will be discussed in Chapter 5.

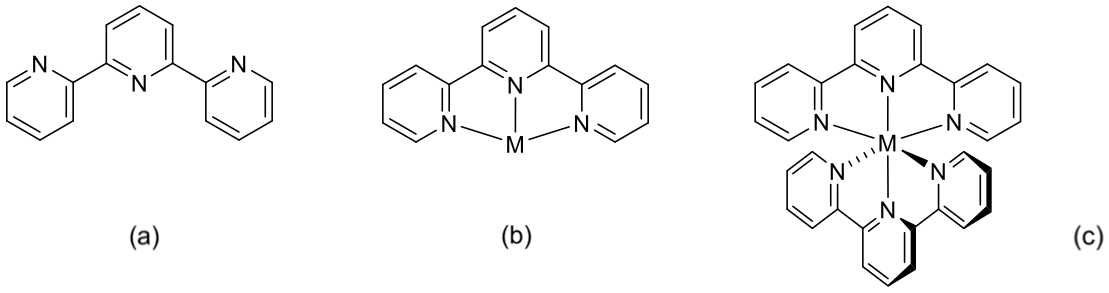

Scheme 5. (**a**) The archetypal terpyridine (2,2′:6′,2″-tpy) in *s-trans*,*s-trans* conformation; (**b**) chelating metal-binding mode of the 2,2′:6′,2″-tpy (monotopic ligand); (**c**) mononuclear complex containing the {M(tpy)$_2$} unit.

Certainly, 2,2′:6′,2′′-tpy is the most studied isomer of terpyridine, and its coordination chemistry and applications are exceptionally well developed. However, while retaining a tpy building block, the most efficient way to access 1D-, 2D- and 3D-coordination polymers is to turn to other isomers of terpyridine,[123] as another 47 of them can be drawn. Multitopic divergent tpy ligands are well suited as building blocks for supramolecular assemblies due to their nitrogen donor atoms,[124] and their use in CPs is further advantageous due to the large delocalized π-system over the pyridine rings, which enables beneficial π-π stacking interactions.[125] In terms of synthesis, some isomers are much more accessible than others. The first known synthesis for terpyridine derivatives is the one reported by Morgan and Burstall in 1932,[126] followed by other methods such as the one by Kröhnke *et al*. in 1976,[127] or the use of the Stille coupling,[128] for example. Nevertheless, the recently reported synthetic methods[129, 130] marked a significant improvement. Indeed, the functionalized terpyridines were easily obtained via a condensation sequence of aldol and Michael addition, involving the use of solid NaOH, followed by treatment with ammonium acetate or aqueous ammonia in a one-pot reaction, with high yield.[131]

Kröhnke methodology[132] and the one-pot approach of Wang and Hanan[130] (Scheme 6) represent straightforward routes to some of these compounds and permit immediate functionalization of the tpy unit, due to the introduction of an aryl group. Although a wide range of functionalities is tolerated, there are a few examples where cyclic products are favored, and this will be further discussed in the main part of this thesis.

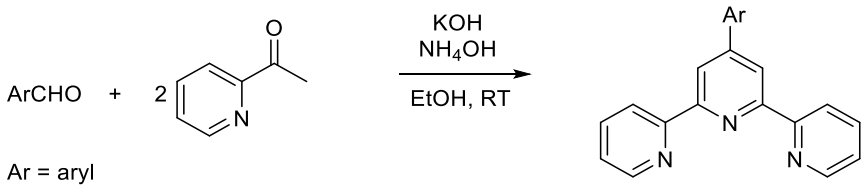

Scheme 6. Facile one-pot synthesis of 4′-aryl-2,2′:6′,2″-terpyridine.

Of all the possible isomers, the symmetrical (with respect to the equivalence of the outer pyridine rings) 4,2′:6′,4″- and 3,2′:6′,3″-tpy ligands (Scheme 7) are readily synthetically achievable using the cited strategies and have already attracted some interest. In contrast to 2,2′:6′,2″-tpy, 3,2′:6′,3″-tpy and 4,2′:6′,4″-tpy typically coordinate to two metal centres and are ditopic ligands, appropriate for the formation of coordination polymers and networks.[123, 133] Interestingly, these ligands only coordinate to metal ions through the outer pyridine rings. Searches of the Cambridge Structural Database (CSD, v. 2022.2.0) do not reveal any examples of metal complexes in which their central pyridine ring binds a metal ion. Functionalization in the 4′-position with coordinatively non-innocent substituents increases the connectivity of the building blocks, from ditopic linkers to 3- (or higher) connecting nodes.

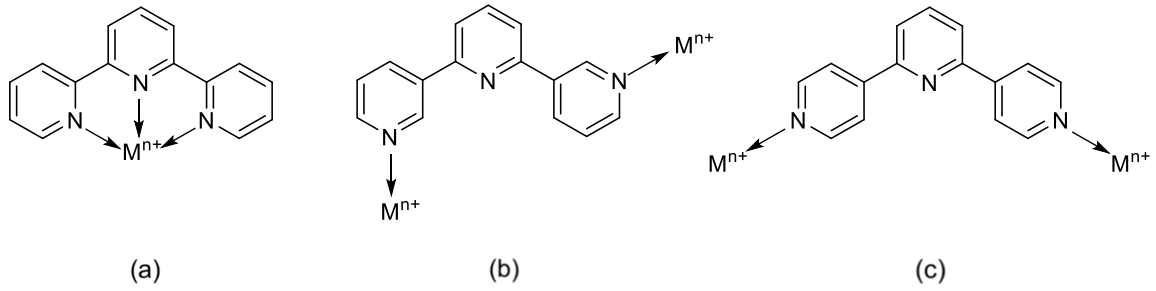

Scheme 7. (**a**) Monotopic chelating 2,2′:6′,2″-tpy unit; (**b**) ditopic 3,2′:6′,3″- and (**c**) ditopic 4,2′:6′,4″-tpy units.

The 3,2′:6′,3″-tpy and 4,2′:6′,4″-tpy metal-binding domains differ in their degrees of conformational flexibility.[134] Both ligands possess rotational freedom about the inter-annular C–C bonds. Whereas this rotation has no effect on the vectorial arrangement of the outer-ring nitrogen lone pairs in 4,2′:6′,4″-tpy, which constitutes a rigid V-shaped linker, it does cause conformational changes in 3,2′:6′,3″-tpy.[123, 125] Although the 3,2′:6′,3″-tpy unit can assume all the intermediate angle values, it is possible to identify three limiting planar conformations, shown in Scheme 8. The vectorial properties of the lone pairs of the outer N atoms in conformations **A** and **B** can be classified as divergent and, therefore favored when 3,2′:6′,3″-tpy ligands are incorporated as linkers in coordination polymers.[123] In contrast, conformation **C** is often observed in discrete molecular structures,[135-139] but it also appears in infinite assemblies.[125, 140, 141]

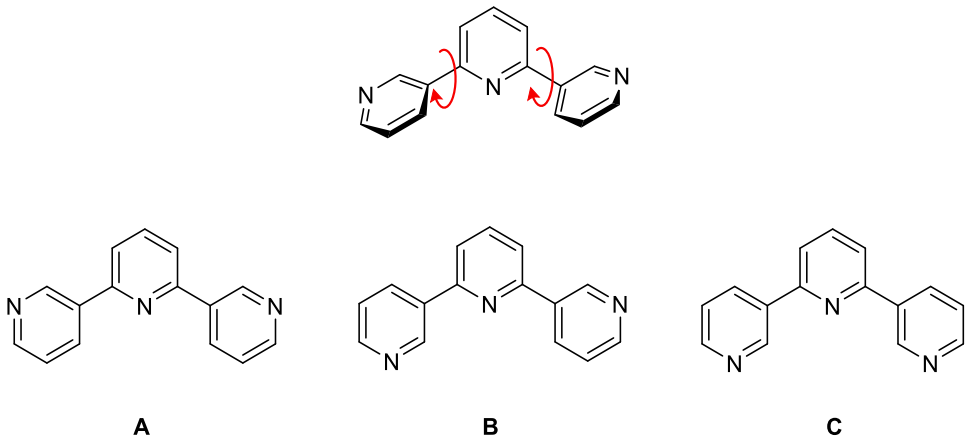

Scheme 8. Three limiting planar conformations derive from rotation about the inter-ring C–C bonds in 3,2′:6′,3″-tpy unit.

Even though these compounds are restricted to roles as linkers, unless functionalized with one or more additional donor groups, the conformational flexibility of 3,2′:6′,3″-tpy makes predictive network assembly more challenging. In light of this, it does not come as a surprise that the coordination chemistry of this tpy isomer has received less attention than that of the 4,2′:6′,4″-tpy, which became quite popular.[123] Coordination polymers featuring ditopic 3,2′:6′,3″-tpy linkers are relatively scarce, [90, 123, 133, 134, 142] although related ligands incorporating additional donors such as carboxylates and sulfonates have received some attention.[125, 141, 143] The conformational variation can be more complex than a switch between **A** and **B**, when 3,2′:6′,3″-tpy ligands are involved in networks formation. In fact, when the 3,2′:6′,3″-tpy unit exhibits conformation **B**, the labels *in* and *out* can be used to describe the orientation of the lone pair of each coordinating N atom with respect to the central N atom of the tpy unit. In this regard, three situations are possible (Scheme 9).

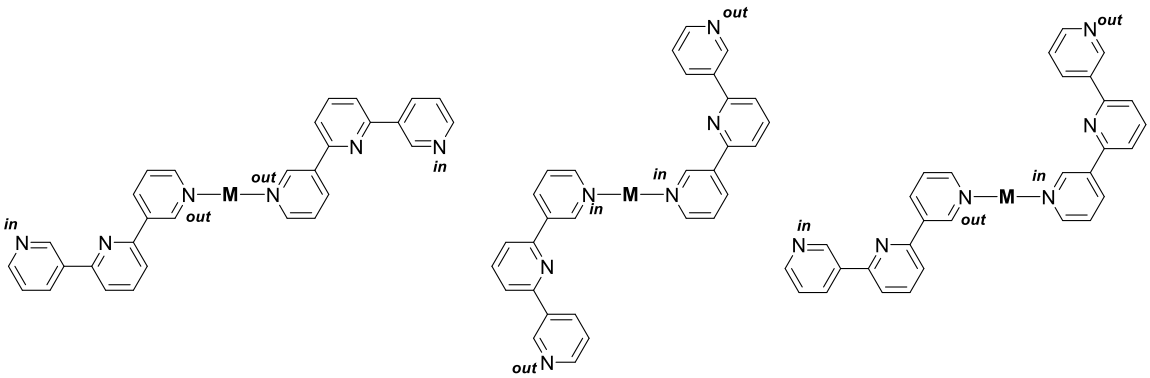

Scheme 9. Three coordination modes are possible for a *trans*-arrangement of ligands at a metal center, when the 3,2′:6′,3″-tpy unit adopts conformation **B**.

When the metal ion lies on an inversion center, only the *out*/*out* and *in*/*in* modes in Scheme 9 are permitted. This aspect will be further discussed in the main part of this thesis. This remark confirms that upon moving away from rigid-rod linkers assembly algorithms become less predictable[144, 145] and that the more flexible the building blocks, the more coincidental are the resulting coordination polymer structures. In this context, systematic studies in which only one parameter is varied at one time gain greater importance and provide the most valuable insight into design strategies to direct coordination architectures. However, such investigations are relatively scarce in the literature,[60, 146] and analysis of data from different research groups is often complicated by use of different solvents and crystallization methods. The fact that two or more metalloassemblies (e.g., metallocycles, metallopolymers) may be close in energy is the underlying principle for the development of libraries of architectures, but only a few examples have been reported.[147-151]

1.7 State of the art

The construction of materials with specific properties is one of the aims of crystal engineering. Due to the occurrence of structure-property relationship, the key point in CPs and MOFs research is to control the self-assembly process. In order to achieve that, a better understanding of the parameters governing crystal growth is of fundamental interest. The Constable/Housecroft group has long focused its research on various isomers of terpyridine and their studies have significantly contributed to the understanding of tpy-containing coordination polymers. Previous works showed that not only the nature of the substituents, but also the length of the alkyl chain in 4′-(4-alkyloxyphenyl)-4,2′:6′,4″-terpyridines can influence the packing and the topology of coordination networks generated upon reaction with metal salts.[60] Although rigid organic ligands have been preferred to units with less well-defined properties, there is scope for research on the latter, and systematic investigations assume an even more important role.

1.8 Aim of the thesis

The focus of the present work is a systematic investigation of the effect of substituents incorporated in organic ligands on the assembly of coordination networks. The building blocks of choice contain the less studied 3,2′:6′,3″-terpyridine unit. As seen, functionalization of the tpy moiety in the 4′-position is easily achieved using the one-pot method of Wang and Hanan.[130] This strategy has been adopted to synthesize homologous series of compounds which differ only in the length or in the branching of the alkyloxy chains, or in the nature of substituent groups. It does not come as a surprise that their presence and nature, also when coordinatively innocent, can both have a remarkable impact on the outcome in coordination polymer assembly. However, it remains a challenge to understand and define a clear algorithm that governs how these groups influence the result. The coordination chemistry of the

synthesized 3,2':6',3''-tpy compounds was investigated with a variety of metal salts, under crystal growth conditions. The two most promising inorganic building blocks in these regards were chosen, namely copper(II) acetate and cobalt(II) thiocyanate, and systematic investigations in which only one parameter is varied at one time were carried out, with the aim of providing a valuable insight.

Concerning the ligands synthesis, no efforts were made to optimize the reaction conditions to enhance the achieved yields. Moreover, no yields of the crystallization experiments are reported in this thesis, due to two main reasons. First of all, most of the prepared coordination polymers showed a low stability towards the loss of solvent, once taken out of the reaction tube (i.e. out of the reaction solvents). Secondly, these reactions have not been optimized in terms of time (see Section 6.4). As soon as visible single crystals grew, they were submitted for XRD measurements, however, it was possible to observe that the amount of product increased over time. As the main goal of the present work has been the characterization of the coordination species that formed, there has been no focus on optimizing nor determining yields.

References

1. S. R. Batten, S. M. Neville and D. R. Turner, *Coordination Polymers - Design, Analysis and Application*, RSC Publishing, Victoria, Australia, **2008**.
2. B. F. Abrahams, B. F. Hoskins and R. Robson, *J. Am. Chem. Soc.*, **1991**, 113, 3606-3607.
3. S. R. Batten and R. Robson, *Angew. Chem. Int. Ed.*, **1998**, 37, 1460-1494.
4. J. R. Long and O. M. Yaghi, *Chem. Soc. Rev.*, **2009**, 38, 1213-1214.
5. J. L. C. Rowsell and O. M. Yaghi, *Microporous Mesoporous Mater.*, **2004**, 73, 3-14.
6. H.-C. Zhou, J. R. Long and O. M. Yaghi, *Chem. Rev.*, **2012**, 112, 673-674.
7. A. U. Czaja, N. Trukhan and U. Müller, *Chem. Soc. Rev.*, **2009**, 38, 1284-1293.
8. M. Jacoby, *Chem. Eng. News*, **2008**, 86, 13-16.
9. S. R. Batten, N. R. Champness, X.-M. Chen, J. Garcia-Martinez, S. Kitagawa, L. Öhrström, M. O'Keeffe, M. P. Suh and J. Reedijk, *Pure Appl. Chem.*, **2013**, 85, 1715-1724.
10. IUPAC, *Nomenclature of Inorganic Chemistry, IUPAC Recommendations 2005 (the "Red Book")*, RSC Publishing, Cambridge, UK, **2005**.
11. B. Moulton and M. J. Zaworotko, *Chem. Rev.*, **2001**, 101, 1629-1658.
12. C. Janiak, *Dalton Trans.*, **2003**, 2781-2804.
13. G. R. Desiraju, *The Crystal as a Supramolecular Entity*, Wiley, **1996**.
14. D. Braga, G. R. Desiraju, J. S. Miller, A. G. Orpen and S. L. Price, *CrystEngComm*, **2002**, 4, 500-509.
15. B. B. Peterson, E. M. Andrews, F. Hung and J. C. Flake, *J. Power Sources*, **2021**, 492, 229658.
16. B. Som, M. D. Smith and L. S. Shimizu, *Polyhedron*, **2021**, 201, 115170.
17. O. M. Yaghi, M. O'Keeffe, N. W. Ockwig, H. K. Chae, M. Eddaoudi and J. Kim, *Nature*, **2003**, 423, 705-714.
18. D. J. Tranchemontagne, J. L. Mendoza-Cortés, M. O'Keeffe and O. M. Yaghi, *Chem. Soc. Rev.*, **2009**, 38, 1257-1283.
19. A. K. Nangia and G. R. Desiraju, *Angew. Chem. Int. Ed.*, **2019**, 58, 4100-4107.
20. S. Pioquinto-García, N. Tiempos-Flores, A. A. Rico-Barragan and N. E. Dávila-Guzmán, *Mater. Today: Proc.*, **2021**, 46, 3127-3130.
21. X. Zhao, Y. Wang, D.-S. Li, X. Bu and P. Feng, *Adv. Mater.*, **2018**, 30, 1705189.
22. J.-R. Li, J. Sculley and H.-C. Zhou, *Chem. Rev.*, **2012**, 112, 869-932.
23. B. Chen, S. Xiang and G. Qian, *Acc. Chem. Res.*, **2010**, 43, 1115-1124.
24. Z.-Y. Gu, C.-X. Yang, N. Chang and X.-P. Yan, *Acc. Chem. Res.*, **2012**, 45, 734-745.
25. H. Li, K. Wang, Y. Sun, C. T. Lollar, J. Li and H.-C. Zhou, *Mater. Today*, **2018**, 21, 108-121.
26. Z. R. Herm, E. D. Bloch and J. R. Long, *Chem. Mater.*, **2014**, 26, 323-338.
27. X. Zhang, X. Meng, J. Wang, Z. Ji, P. Lu, X. Wang and F. Chen, *Inorg. Chim. Acta*, **2021**, 523, 120416.
28. M. Seifpanah Sowmehesaraee, M. Ranjbar, M. Abedi and S. A. Mozaffari, *Sol. Energy*, **2021**, 214, 138-148.
29. A. Ringaci, A. V. Yaremenko, K. G. Shevchenko, S. D. Zvereva and M. P. Nikitin, *Chem. Eng. J.*, **2021**, 418, 129386.
30. J. Wen, Y. Fang and G. Zeng, *Chemosphere*, **2018**, 201, 627-643.
31. X. Li, B. Wang, Y. Cao, S. Zhao, H. Wang, X. Feng, J. Zhou and X. Ma, *ACS Sustainable Chem. Eng.*, **2019**, 7, 4548-4563.
32. P. Larpent, A. Jouaiti, N. Kyritsakas and M. W. Hosseini, *Dalton Trans.*, **2014**, 43, 2000-2006.
33. P. Larpent, A. Jouaiti, N. Kyritsakas and M. W. Hosseini, *Dalton Trans.*, **2014**, 43, 166-172.
34. P. Larpent, A. Jouaiti, N. Kyritsakas and M. W. Hosseini, *CrystEngComm*, **2019**, 21, 2534-2540.
35. H. M. Tay, N. Kyratzis, S. Thoonen, S. A. Boer, D. R. Turner and C. Hua, *Coord. Chem. Rev.*, **2021**, 435, 213763.
36. Y. Cui, B. Li, H. He, W. Zhou, B. Chen and G. Qian, *Acc. Chem. Res.*, **2016**, 49, 483-493.
37. B. Van de Voorde, B. Bueken, J. Denayer and D. De Vos, *Chem. Soc. Rev.*, **2014**, 43, 5766-5788.

38. J. Zhang and Z. Chen, *J. Chromatogr. A*, **2017**, 1530, 1-18.
39. T. Duerinck and J. F. M. Denayer, *Chem. Eng. Sci.*, **2015**, 124, 179-187.
40. D. Asnaghi, R. Corso, P. Larpent, I. Bassanetti, A. Jouaiti, N. Kyritsakas, A. Comotti, P. Sozzani and M. W. Hosseini, *Chem. Commun.*, **2017**, 53, 5740-5743.
41. Y. Liu, W. Xuan and Y. Cui, *Adv. Mater.*, **2010**, 22, 4112-4135.
42. M. M. Wanderley, C. Wang, C.-D. Wu and W. Lin, *J. Am. Chem. Soc.*, **2012**, 134, 9050-9053.
43. S. Bhattacharjee, M. I. Khan, X. Li, Q.-L. Zhu and X.-T. Wu, *Catalysts*, **2018**, 8, 120.
44. P. Larpent, A. Jouaiti, N. Kyritsakas and M. W. Hosseini, *Chem. Commun.*, **2013**, 49, 4468-4470.
45. M. W. Hosseini, *CrystEngComm*, **2004**, 6, 318-322.
46. S. R. Batten, *Comprehensive Coordination Chemistry III*, Elsevier, 3rd edn., **2021**.
47. J. D. Evans, B. Garai, H. Reinsch, W. Li, S. Dissegna, V. Bon, I. Senkovska, R. A. Fischer, S. Kaskel, C. Janiak, N. Stock and D. Volkmer, *Coord. Chem. Rev.*, **2019**, 380, 378-418.
48. X.-M. Chen and M.-L. Tong, *Acc. Chem. Res.*, **2007**, 40, 162-170.
49. Y.-R. Lee, J. Kim and W.-S. Ahn, *Korean J. Chem. Eng.*, **2013**, 30, 1667-1680.
50. R. Chakrabarty, P. S. Mukherjee and P. J. Stang, *Chem. Rev.*, **2011**, 111, 6810-6918.
51. V. Subramaniyam, P. V. Ravi and M. Pichumani, *J. Mol. Struct.*, **2022**, 1251, 131931.
52. H.-J. Chen, L.-Q. Chen, L.-R. Lin, L.-S. Long and L.-S. Zheng, *Inorg. Chem.*, **2021**, 60, 6986-6990.
53. M. J. Kalmutzki, N. Hanikel and O. M. Yaghi, *Sci. Adv.*, **2018**, 4.
54. T.-R. Lin, C.-H. Lee, Y.-C. Lan, S. Mendiratta, L.-L. Lai, J.-Y. Wu, K.-M. Chi and K.-L. Lu, *Polymers*, **2018**, 10, 1398.
55. S. Vagin, A. K. Ott and B. Rieger, *Chem. Ing. Tech.*, **2007**, 79, 767-780.
56. M. Köberl, M. Cokoja, W. A. Herrmann and F. E. Kühn, *Dalton Trans.*, **2011**, 40, 6834-6859.
57. H. Makoto, M. Masahiro, N. Ryoji, M. Hiroki and K. Kuninobu, *Bull. Chem. Soc. Jpn.*, **1994**, 67, 3125-3127.
58. Q. Yao, J. Sun, K. Li, J. Su, M. V. Peskov and X. Zou, *Dalton Trans.*, **2012**, 41, 3953-3955.
59. B. Li, H.-M. Wen, Y. Cui, W. Zhou, G. Qian and B. Chen, *Adv. Mater.*, **2016**, 28, 8819-8860.
60. Y. M. Klein, E. C. Constable, C. E. Housecroft, J. A. Zampese and A. Crochet, *CrystEngComm*, **2014**, 16, 9915-9929.
61. G. Zhang, Y.-X. Jia, W. Chen, W.-F. Lo, N. Brathwaite, J. A. Golen and A. L. Rheingold, *RSC Adv.*, **2015**, 5, 15870-15879.
62. E. C. Constable, C. E. Housecroft, S. Vujovic, J. A. Zampese, A. Crochet and S. R. Batten, *CrystEngComm*, **2013**, 15, 10068-10078.
63. E. C. Constable, C. E. Housecroft, P. Kopecky, M. Neuburger, J. A. Zampese and G. Zhang, *CrystEngComm*, **2012**, 14, 446-452.
64. V. N. Dorofeeva, A. M. Mishura, A. S. Lytvynenko, N. V. Grabovaya, M. A. Kiskin, S. V. Kolotilov, I. L. Eremenko and V. M. Novotortsev, *Theor. Exp. Chem.*, **2016**, 52, 111-118.
65. A. Castiñeiras, S. Balboa, E. Bermejo, R. Carballo, B. Covelo, J. Borras and J. A. Real, *Z. Anorg. Allg. Chem.*, **2002**, 628, 1116-1123.
66. S.-B. Zhou, C.-C. Du, X.-f. Wang, Y.-Z. Han, J.-L. Dong and D.-Z. Wang, *J. Chem. Crystallogr.*, **2017**, 47, 215-225.
67. E. C. Constable, G. Zhang, E. Coronado, C. E. Housecroft and M. Neuburger, *CrystEngComm*, **2010**, 12, 2139-2145.
68. F. Marchetti, N. Masciocchi, A. F. Albisetti, C. Pettinari and R. Pettinari, *Inorg. Chim. Acta*, **2011**, 373, 32-39.
69. M. Garai and K. Biradha, *Cryst. Growth Des.*, **2017**, 17, 925-932.
70. C.-J. Wang, H.-R. Ma, Y.-Y. Wang, P. Liu, L.-J. Zhou, Q.-Z. Shi and S.-M. Peng, *Cryst. Growth Des.*, **2007**, 7, 1811-1817.
71. L. Mei, T. H. Ming, L. Q. Rong, S. Jie, Y. S. Zhong and L. X. Liang, *J. Chem. Sci.*, **2009**, 121, 435-440.
72. R. Carballo, B. Covelo, M. S. El Fallah, J. Ribas and E. M. Vázquez-López, *Cryst. Growth Des.*, **2007**, 7, 1069-1077.

73. M. Barquín, M. J. González Garmendia, S. Pacheco, E. Pinilla, S. Quintela, J. M. Seco and M. R. Torres, *Inorg. Chim. Acta*, **2004**, 357, 3230-3236.
74. Y.-Y. Tang, C.-X. Ding, S.-W. Ng and Y.-S. Xie, *RSC Adv.*, **2013**, 3, 18134-18141.
75. L. Rajput, M. Sarkar and K. Biradha, *J. Chem. Sci.*, **2010**, 122, 707-720.
76. J.-F. Sun, G.-G. Hou and X.-P. Dai, *Acta Crystallogr., Sect. E: Struct. Rep. Online*, **2012**, 68, m91.
77. M. Desciak, J. Zubieta, R. S. Rarig Jr and R. L. LaDuca, *Acta Crystallogr., Sect. E: Struct. Rep. Online*, **2007**, 63, m435.
78. J. W. Uebler, B. S. Stone and R. L. LaDuca, *Z. Anorg. Allg. Chem.*, **2013**, 639, 1740-1745.
79. P. Díaz, J. Benet-Buchholz, R. Vilar and A. J. P. White, *Inorg. Chem.*, **2006**, 45, 1617-1626.
80. G. Zhang, E. Yashima and W.-D. Woggon, *Adv. Synth. Catal.*, **2009**, 351, 1255-1262.
81. P. Wang, Y.-B. Dong, J.-P. Ma, R.-Q. Huang and M. D. Smith, *Inorg. Chem. Commun.*, **2005**, 8, 596-599.
82. M. J. McIldowie, M. Mocerino, M. I. Ogden and B. W. Skelton, *Tetrahedron*, **2007**, 63, 10817-10825.
83. C. A. Crawford, E. F. Day, W. E. Streib, J. C. Huffman and G. Christou, *Polyhedron*, **1994**, 13, 2933-2942.
84. H. Ryo and M. Masahiro, *Bull. Chem. Soc. Jpn.*, **2005**, 78, 827-834.
85. F. L. Geyer, F. Rominger, M. Vogtland and U. H. F. Bunz, *Cryst. Growth Des.*, **2015**, 15, 3539-3544.
86. P. E. Ryan, C. Lescop, D. Laliberté, T. Hamilton, T. Maris and J. D. Wuest, *Inorg. Chem.*, **2009**, 48, 2793-2807.
87. W. Fujita, A. Tokumitu, Y. Fujii and H. Kikuchi, *CrystEngComm*, **2016**, 18, 8614-8621.
88. M. Iqbal, R. J. and P. Quayle, *Acta Cryst.*, **2015**, E71.
89. Y. M. Klein, A. Prescimone, E. C. Constable and C. E. Housecroft, *Polyhedron*, **2016**, 103, 58-65.
90. E. C. Constable, C. E. Housecroft, M. Neuburger, S. Vujovic, J. A. Zampese and G. Zhang, *CrystEngComm*, **2012**, 14, 3554-3563.
91. Y. M. Klein, A. Prescimone, E. C. Constable and C. E. Housecroft, *Materials*, **2017**, 10, 728.
92. Z. Yin, S. Zhang, S. Zheng, J. A. Golen, A. L. Rheingold and G. Zhang, *Polyhedron*, **2015**, 101, 139-145.
93. Y. M. Klein, A. Prescimone, M. B. Pitak, S. J.Coles, E. C. Constable and C. E. Housecroft, *CrystEngComm*, **2016**, 18, 4704-4707.
94. D. P. Martin, W. R. Knapp, R. M. Supkowski and R. L. LaDuca, *Inorg. Chim. Acta*, **2009**, 362, 1559-1564.
95. M. B. Duriska, S. M. Neville and S. R. Batten, *Chem. Commun.* , **2009**, 5579-5581.
96. J. Lu, T. Paliwala, S. C. Lim, C. Yu, T. Niu and A. J. Jacobson, *Inorg. Chem.*, **1997**, 36, 923-929.
97. S. Suckert, I. Jess and C. Näther, *Z. Anorg. Allg. Chem.*, **2017**, 643, 721-728.
98. H. Xu, Y. Song and H. Hou, *Inorg. Chim. Acta*, **2004**, 357, 3541-3548.
99. D. M. Shin, I. S. Lee and Y. K. Chung, *Cryst. Growth Des.*, **2006**, 6, 1059-1061.
100. B. Tian, G.-H. Ning, Q. Gao, L.-M. Tan, W. Tang, Z. Chen, C. Su and K. P. Loh, *ACS Appl. Mater. Interfaces*, **2016**, 8, 31067-31075.
101. S. Wöhlert, T. Fic, Z. Tomkowicz, S. G. Ebbinghaus, M. Rams, W. Haase and C. Näther, *Inorg. Chem.*, **2013**, 52, 12947-12957.
102. M. Rams, Z. Tomkowicz, M. Böhme, W. Plass, S. Suckert, J. Werner, I. Jess and C. Näther, *Phys. Chem. Chem. Phys.*, **2017**, 19, 3232-3243.
103. Y. Prananto, A. Urbatsch, B. Moubaraki, K. Murray, D. Turner, G. Deacon and S. Batten, *Aust. J. Chem.*, **2017**, 70, 516-528.
104. M. Böhme, A. Jochim, M. Rams, T. Lohmiller, S. Suckert, A. Schnegg, W. Plass and C. Näther, *Inorg. Chem.*, **2020**, 59, 5325-5338.
105. S. Wöhlert, J. Boeckmann, M. Wriedt and C. Näther, *Angew. Chem. Int. Ed.*, **2011**, 50, 6920-6923.

106. A. Jochim, M. Rams, M. Böhme, M. Ceglarska, W. Plass and C. Näther, *Dalton Trans.*, **2020**, 49, 15310-15322.
107. J. Werner, M. Rams, Z. Tomkowicz and C. Näther, *Dalton Trans.*, **2014**, 43, 17333-17342.
108. M. Das, S. Khullar and M. Sarkar, *Eur. J. Inorg. Chem.*, **2020**, 2020, 3174-3186.
109. J. L. C. Rowsell, A. R. Millward, K. S. Park and O. M. Yaghi, *J. Am. Chem. Soc.*, **2004**, 126, 5666-5667.
110. G. K. H. Shimizu, *J. Solid State Chem.*, **2005**, 178, 2519-2526.
111. Y. Liu and M. O'Keeffe, *Isr. J. Chem.*, **2018**, 58, 962-970.
112. V. Chaurin, E. C. Constable and C. E. Housecroft, *New J. Chem.*, **2006**, 30, 1740-1744.
113. C. Janiak and J. K. Vieth, *New J. Chem.*, **2010**, 34, 2366-2388.
114. H. S. Huh and S. W. Lee, *Bull. Korean Chem. Soc.*, **2006**, 27, 1839-1843.
115. X. Yin, A. Alsuwaidi and X. Zhang, *Microporous Mesoporous Mater.*, **2022**, 330, 111633.
116. D. Toledo, A. Vega, N. Pizarro, R. Baggio, O. Peña, T. Roisnel, J.-Y. Pivan and Y. Moreno, *J. Solid State Chem.*, **2017**, 253, 78-88.
117. E. C. Constable, in *Adv. Inorg. Chem.*, ed. H. J. Emeléus, Academic Press, **1986**, vol. 30, pp. 69-121.
118. E. C. Constable, *Chem. Soc. Rev.*, **2007**, 36, 246-253.
119. C. Wei, Y. He, X. Shi and Z. Song, *Coord. Chem. Rev.*, **2019**, 385, 1-19.
120. E. C. Constable, *Angew. Chem. Int. Ed.*, **2007**, 46, 2748-2749.
121. E. C. Constable and C. E. Housecroft, *Coord. Chem. Rev.*, **2017**, 350, 84-104.
122. C. E. Housecroft and E. C. Constable, *CHIMIA*, **2019**, 73, 462.
123. C. E. Housecroft and E. C. Constable, *Chem. Commun.*, **2020**, 56, 10786-10794.
124. H. Li and F. Wang, *Inorg. Chim. Acta*, **2020**, 502, 119351.
125. T.-T. Wang, J.-L. Zhang, H.-M. Hu, Y. Cheng, L.-L. Xue, X. Wang and B.-Z. Wang, *Polyhedron*, **2018**, 151, 43-50.
126. G. T. Morgan and F. H. Burstall, *J. Chem. Soc.*, **1932**, 20-30.
127. F. Kröhnke, *Synthesis*, **1976**, 1976, 1-24.
128. M. Heller and U. S. Schubert, *J. Org. Chem.*, **2002**, 67, 8269-8272.
129. G. W. V. Cave and C. L. Raston, *Chem. Commun.*, **2000**, 2199-2200.
130. J. H. Wang, G. S., *Synlett*, **2005**, 8, 1251-1254.
131. A. Jouaiti, *Synth. Commun.*, **2021**, 51, 1547-1555.
132. F. Kröhnke, *Angew. Chem., Int. Ed. Engl.*, **1963**, 2, 225-238.
133. C. E. Housecroft and E. C. Constable, *Molecules*, **2021**, 26, 3110.
134. C. E. Housecroft, *CrystEngComm*, **2015**, 17, 7461-7468.
135. Y. M. Klein, A. Lanzilotto, A. Prescimone, K. W. Krämer, S. Decurtins, S.-X. Liu, E. C. Constable and C. E. Housecroft, *Polyhedron*, **2017**, 129, 71-76.
136. J. Granifo, M. Vargas, M. T. Garland, A. Ibáñez, R. Gaviño and R. Baggio, *Inorg. Chem. Commun.*, **2008**, 11, 1388-1391.
137. J. Granifo, R. Gaviño, E. Freire and R. Baggio, *J. Mol. Struct.*, **2011**, 1006, 684-691.
138. M. Zhao, J. Tan, J. Su, J. Zhang, S. Zhang, J. Wu and Y. Tian, *Dyes Pigm.*, **2016**, 130, 216-225.
139. L. M. Henling and R. E. Marsh, *Acta Crystallogr., Sect. C: Struct. Chem.*, **2014**, 70, 834-836.
140. Y. Cheng, M.-L. Yang, H.-M. Hu, B. Xu, X. Wang and G. Xue, *J. Solid State Chem.*, **2016**, 239, 121-130.
141. L. Zhang, C.-J. Li, J.-E. He, Y.-Y. Chen, S.-R. Zheng, J. Fan and W.-G. Zhang, *J. Solid State Chem.*, **2016**, 233, 444-454.
142. S. M. Elahi, M. Raizada, P. K. Sahu and S. Konar, *Chem. - Eur. J.*, **2021**, 27, 5858-5870.
143. P. Yang, M.-S. Wang, J.-J. Shen, M.-X. Li, Z.-X. Wang, M. Shao and X. He, *Dalton Trans.*, **2014**, 43, 1460-1470.
144. E. C. Constable and C. E. Housecroft, in *Reference Module in Chemistry, Molecular Sciences and Chemical Engineering*, Elsevier, **2016**.
145. E. C. Constable and C. E. Housecroft, in *Comprehensive Inorganic Chemistry II (Second Edition)*, eds. J. Reedijk and K. Poeppelmeier, Elsevier, Amsterdam, **2013**, pp. 1-29.

146. D.-L. Long, A. J. Blake, N. R. Champness, C. Wilson and M. Schröder, *Chem. - Eur. J.*, **2002**, 8, 2026-2033.
147. X. Lu, X. Li, J.-L. Wang, C. N. Moorefield, C. Wesdemiotis and G. R. Newkome, *Chem. Commun.*, **2012**, 48, 9873-9875.
148. M. Schmittel, *Chem. Commun.*, **2015**, 51, 14956-14968.
149. F. Tuna, J. Hamblin, A. Jackson, G. Clarkson, N. W. Alcock and M. J. Hannon, *Dalton Trans.*, **2003**, 2141-2148.
150. E. C. Constable, C. E. Housecroft, T. Kulke, G. Baum and D. Fenske, *Chem. Commun.* , **1999**, 195-196.
151. P. T. Corbett, J. Leclaire, L. Vial, K. R. West, J.-L. Wietor, J. K. M. Sanders and S. Otto, *Chem. Rev.*, **2006**, 106, 3652-3711.

Chapter 2 Ligand synthesis and characterization

2.1 Ligand design

In order to gain a better understanding of the effects of the substituents in terms of both chain length and type, a series of ten 4′-(4-*n*-alkyloxyphenyl)-3,2′:6′,3″-terpyridines was synthesized (compounds **1**–**10**), followed by the series of the isomeric 4′-(4-butoxyphenyl)-3,2′:6′,3″-terpyridines (**11**–**13**) and two more 4′-(4-*iso*-alkyloxyphenyl)-3,2′:6′,3″-terpyridines (**14**, **15**), shown in Scheme 10. Among these compounds, only **6** has been previously reported.[1]

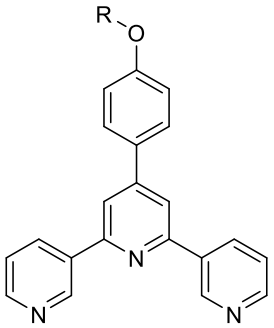

1 R = Me
2 R = Et
3 R = ^{n}Pr
4 R = ^{n}Bu
5 R = ^{n}Pent
6 R = ^{n}Hex
7 R = ^{n}Hept
8 R = ^{n}Oct
9 R = ^{n}Non
10 R = ^{n}Dec

11 R = *rac*-^{sec}Bu
12 R = ^{iso}Bu
13 R = ^{tert}Bu

14 R = ^{iso}Pr
15 R = ^{iso}Pent

Scheme 10. 4′-(4-*n*-Alkyloxyphenyl)-3,2′:6′,3″-terpyridines (compounds **1**–**15**) presented in this thesis.

The synthesis, the characterization and when possible, the coordination chemistry of the presented compounds with different metal salts are described in detail in the following chapters. The focus was then shifted towards extended aromatic systems, in which π-stacking interactions would be dominant. Therefore, a series of 4′-(4′-substituted-[1,1′-biphenyl-4-yl)-3,2′:6′,3″-terpyridines (**16**–**20**) and 4′-(4′-napththalen-1-yl)phenyl)-3,2′:6′,3″-terpyridine (**21**) were prepared (Scheme 11), characterized and their reactions with metal salts were investigated, including - in some cases - a study of the effect of the crystallization solvents in the assembly of the coordination networks.

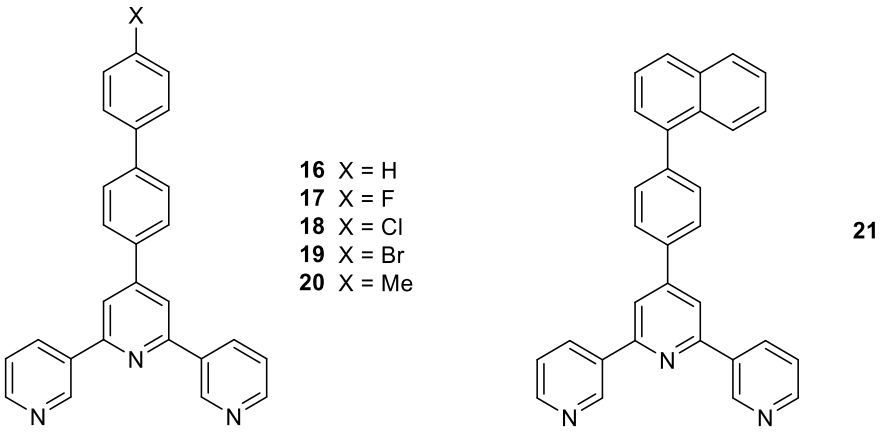

Scheme 11. Extended π-systems presented in this thesis: 4′-(4′-substituted-[1,1′-biphenyl-4-yl)-3,2′:6′,3″-terpyridines (**16**–**20**) and 4′-(4′-napththalen-1-yl)phenyl)-3,2′:6′,3″-terpyridine **21**.

2.2 Synthesis and characterization of 3,2′:6′,3″-terpyridine derivatives

The chosen synthetic approach was the standard one-pot method by Wang and Hanan[2] (Scheme 12), involving the reaction of two equivalents of 3-acetylpyridine with the appropriate 4-substituted benzaldehyde in a basic solution, followed by the addition of aqueous ammonia to give 3,2′:6′,3″-terpyridines in a range of 10–50% yields after purification (see Section 6.2). The facile one-pot procedure and the broad commercial availability of aromatic aldehydes made screening of a variety of ligands straightforward. 4-Alkyloxybenzaldehydes were dissolved in EtOH, followed by 3-acetylpyridine, crushed KOH and the slow addition of aqueous NH_3. The precipitation of a white solid was readily observed and the mixture was left stirring overnight at room temperature. Most of the presented terpyridines were isolated through filtration, washed with EtOH and H_2O, and purified through recrystallization from EtOH, resulting in a satisfactory purity level. No efforts were made to optimize the reaction conditions to enhance the achieved yields.

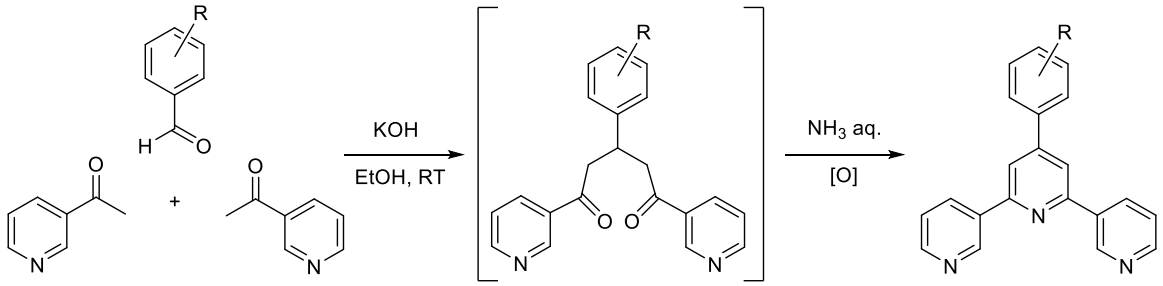

Scheme 12. Wang and Hanan's one-pot synthesis,[2] represented by a substituted benzaldehyde and 3-acetylpyridine (2 eq.). The reaction was complete within one day, while stirring at room temperature.

Thus, the functionalized tpy ligands were easily obtained *via* a condensation sequence of aldol addition and Michael addition. First, the enolate of 3-acetylpyridine is formed by treatment with KOH. The enolate undergoes aldol condensation yielding the α,β-unsaturated ketone. This reacts with a second enolate of 3-acetylpyridine and forms the soluble diketone intermediate (Scheme 12), which is normally not isolated. Addition of aqueous ammonia leads to a ring closing reaction and the formation of the inner pyridine ring. The product of the Wang and Hanan reaction is generally poorly soluble in ethanol/water mixtures and precipitates out of solution. A wide range of aromatic aldehydes are tolerated. However, in the cases of ligands **3** and **12**, the described procedure led to another kind of product, instead of the desired terpyridines (see Section 2.3). In order to obtain **3** and **12**, the standard one-pot synthesis was carried out as a first step to prepare 4-(3,2′:6′,3″-terpyridin-4′-yl)phenol, starting from 4-hydroxybenzaldehyde. The appropriate alkyl group was then introduced by nucleophilic substitution, reacting the substituted phenol with the corresponding alkyl bromide in DMF, at 70–80 °C, in the presence of anhydrous potassium carbonate as a base (Scheme 13).

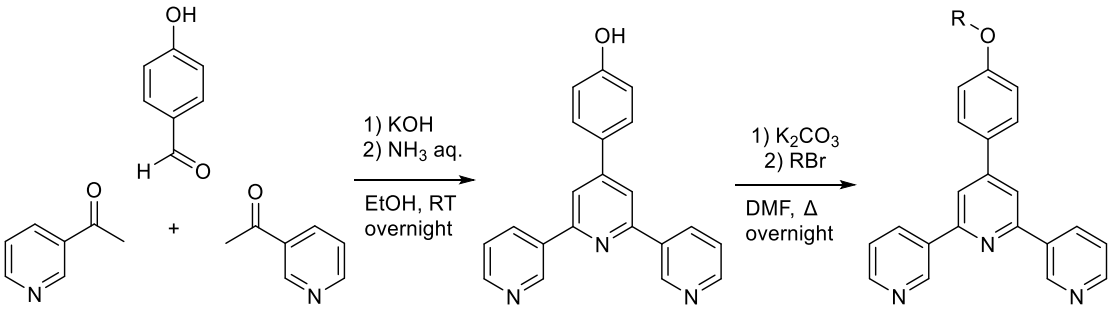

Scheme 13. Synthetic route to compounds **3**, **12**. Both the reactions were complete within one day.

A chromatographic column on silica was necessary to purify the products, as discussed in the next section and detailed in the Experimental Part. Scheme 14 shows a comprehensive view of the 4′-substituted 3,2′:6′,3″-tpy compounds presented in this thesis, including the atom labelling used for NMR spectroscopic assignments of the aromatic region.

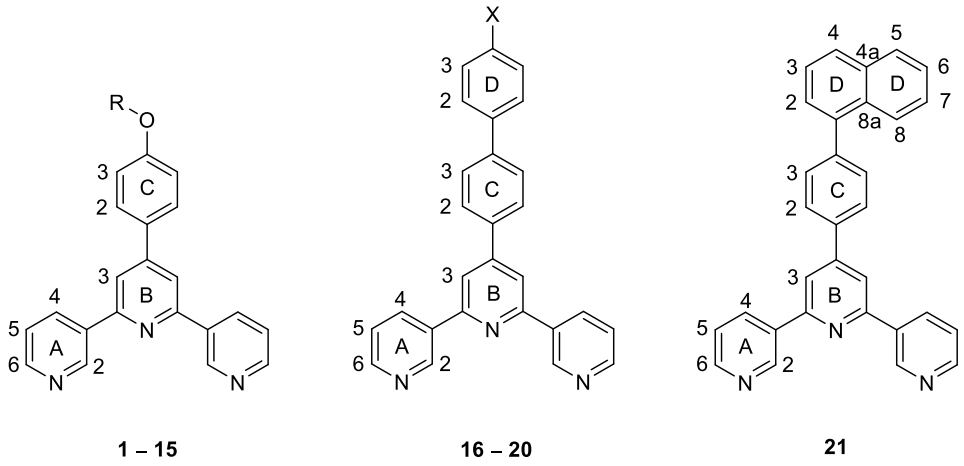

Scheme 14. Structures of ligands **1**–**21**, with atom labelling used for NMR spectroscopic assignments of the aromatic regions. The alkyl chain CH_2 groups are labelled a, b, c, ... starting with "a" for the group bond to the O-atom.

Compounds **1**–**21** were fully characterized by ^{1}H and $^{13}C\{^{1}H\}$ NMR spectroscopies, electrospray mass spectrometry (ESI-MS), elemental analysis or high-resolution mass spectrometry (HR-MS), melting point, and UV-Vis and FT-IR spectroscopies. The ^{1}H and $^{13}C\{^{1}H\}$ NMR spectra were readily assigned using COSY, NOESY, HMQC and HMBC 2D-methods. The introduction of different substituents has no significant influence on the spectroscopic signature of the 4'-phenyl-3,2':6',3''-tpy unit, as distinctly shown by the overlay of the ^{1}H NMR spectra of ligands **1**, **3**, **5**, **7** and **9** in Figure 4, and even more clearly in Figure 5, representing the expansion of the aromatic region.

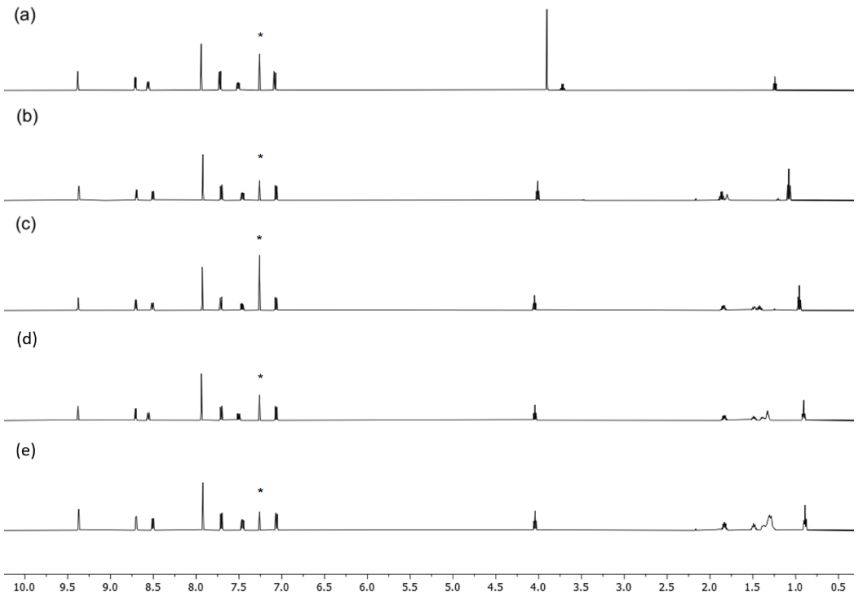

Figure 4. ^{1}H NMR spectra for compounds (**a**) **1**, (**b**) **3**, (**c**) **5**, (**d**) **7** and (**e**) **9** (500 MHz, $CDCl_3$, 298 K). * = residual $CHCl_3$.

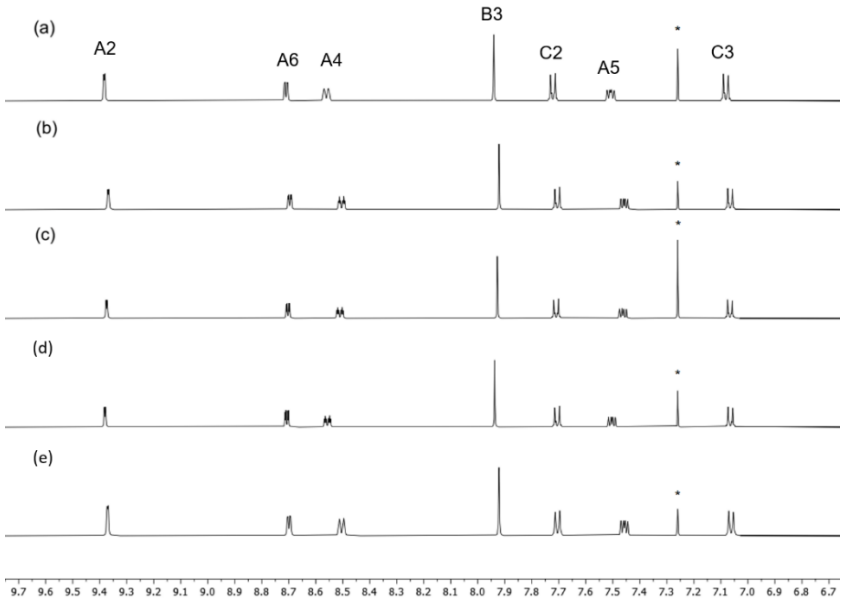

Figure 5. Aromatic region of the ^{1}H NMR spectra for compounds (**a**) **1**, (**b**) **3**, (**c**) **5**, (**d**) **7** and (**e**) **9** (500 MHz, $CDCl_3$, 298 K). * = residual $CHCl_3$.

The spectra are consistent with a time-averaged C2-symmetric ligand and protons H^{C2} and H^{C3} were distinguished by the NOESY crosspeak between H^{B3} and H^{C2} (Figure 6). The observation of NOESY crosspeaks between H^{B3} and H^{A2} and between H^{B3} and H^{A4} was useful for the assignment; protons H^{A2} and H^{A4} were distinguished by the multiplicity of the signals.

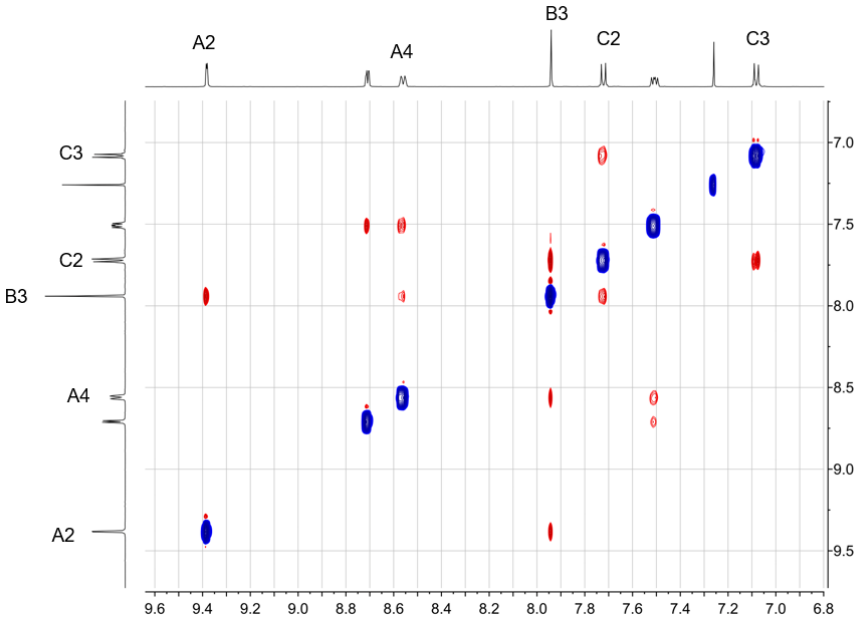

Figure 6. NOESY spectrum of **1** (500 MHz ^{1}H NMR, $CDCl_3$, 298 K).

The corresponding $^{13}C\{^1H\}$ NMR spectra are shown in Figure 7. The remaining ^1H NMR spectra are reported in the appendix, as well as the HMQC and HMBC spectra of all prepared organic compounds (Figures S1-S75).

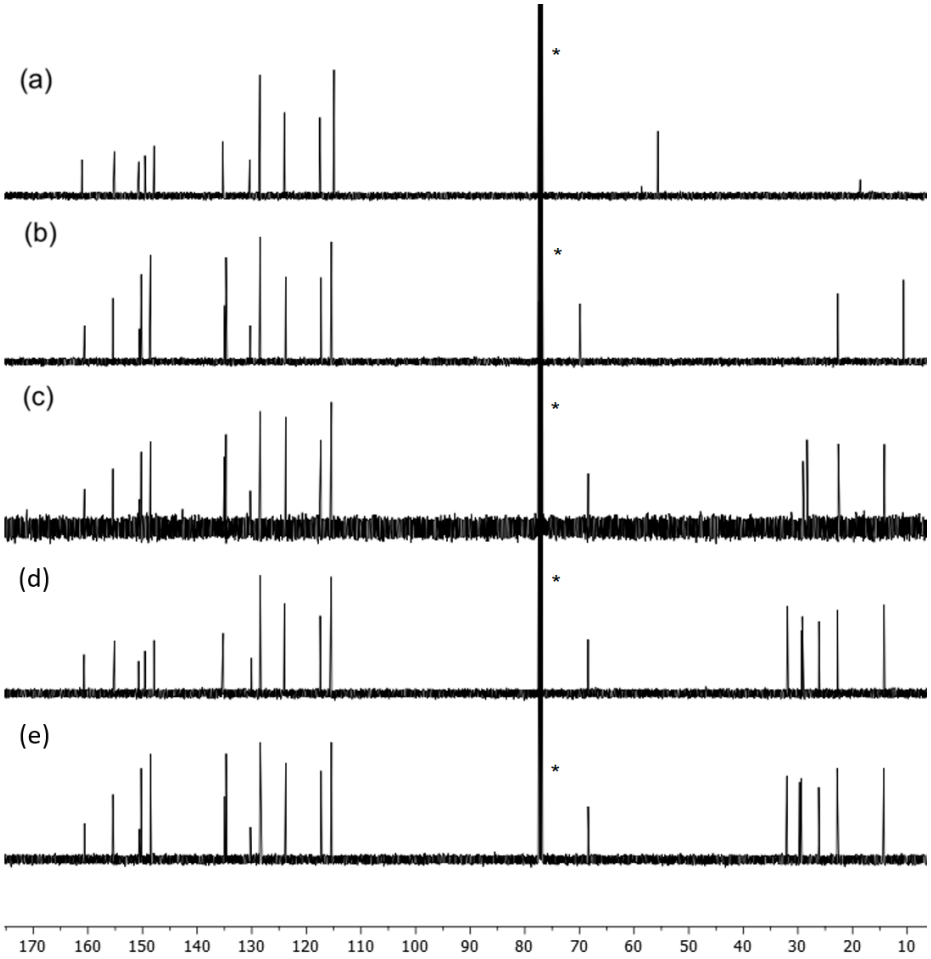

Figure 7. $^{13}C\{^1H\}$ NMR spectra for compounds (**a**) **1**, (**b**) **3**, (**c**) **5**, (**d**) **7** and (**e**) **9** (126 MHz, $CDCl_3$, 298 K). * = $CDCl_3$.

Figure 8 displays a comparison of the ^1H NMR spectra of ligands **16**–**20**, containing the extended aromatic systems. The signals arising from the protons in rings A, B, and C (see Scheme 14 for ring labels) are unaffected by the change in the substituent in ring D. Assignments of the signals for H^{D2} and H^{D3} were confirmed from the NOESY cross peaks between H^{C3} and H^{D2}, protons H^{C2} and H^{C3} being first distinguished using the NOESY H^{B3}/H^{C2} crosspeaks. The change from X = H in **16** (Scheme 14) to the halogen substituents in **17**, **18**, and **19** and Me group in **20** has the most significant effect on H^{D3}, consistent with expectations.[3]

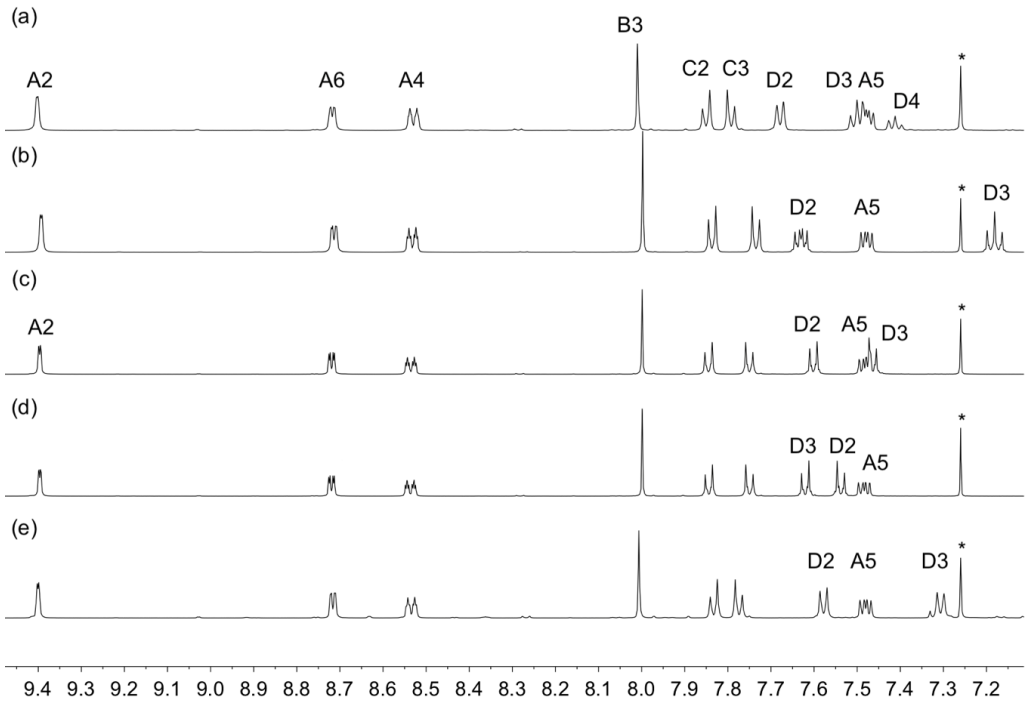

Figure 8. ^{1}H NMR spectra (aromatic region) for compounds (**a**) **16**, (**b**) **17**, (**c**) **18**, (**d**) **19** and (**e**) **20** (500 MHz, $CDCl_3$, 298 K). * = residual $CHCl_3$.

The electrospray (ESI-MS) mass spectra were recorded on acetonitrile solutions of the compounds, with the addition of a few drops of formic acid; in each case they show a base peak arising from the $[M+H]^+$ ion, with characteristic isotope patterns observed for compounds **18** and **19** (chloro- and bromo-derivative, respectively).

The solution absorption spectra of ligands **1**–**15**, bearing alkyloxy chains, exhibit intense absorptions in the UV region arising from spin-allowed $\pi^*\leftarrow$n and $\pi^*\leftarrow\pi$ transitions. Figure 9 shows the superimpositions of the fifteen recorded spectra, divided into three groups for the sake of clarity.

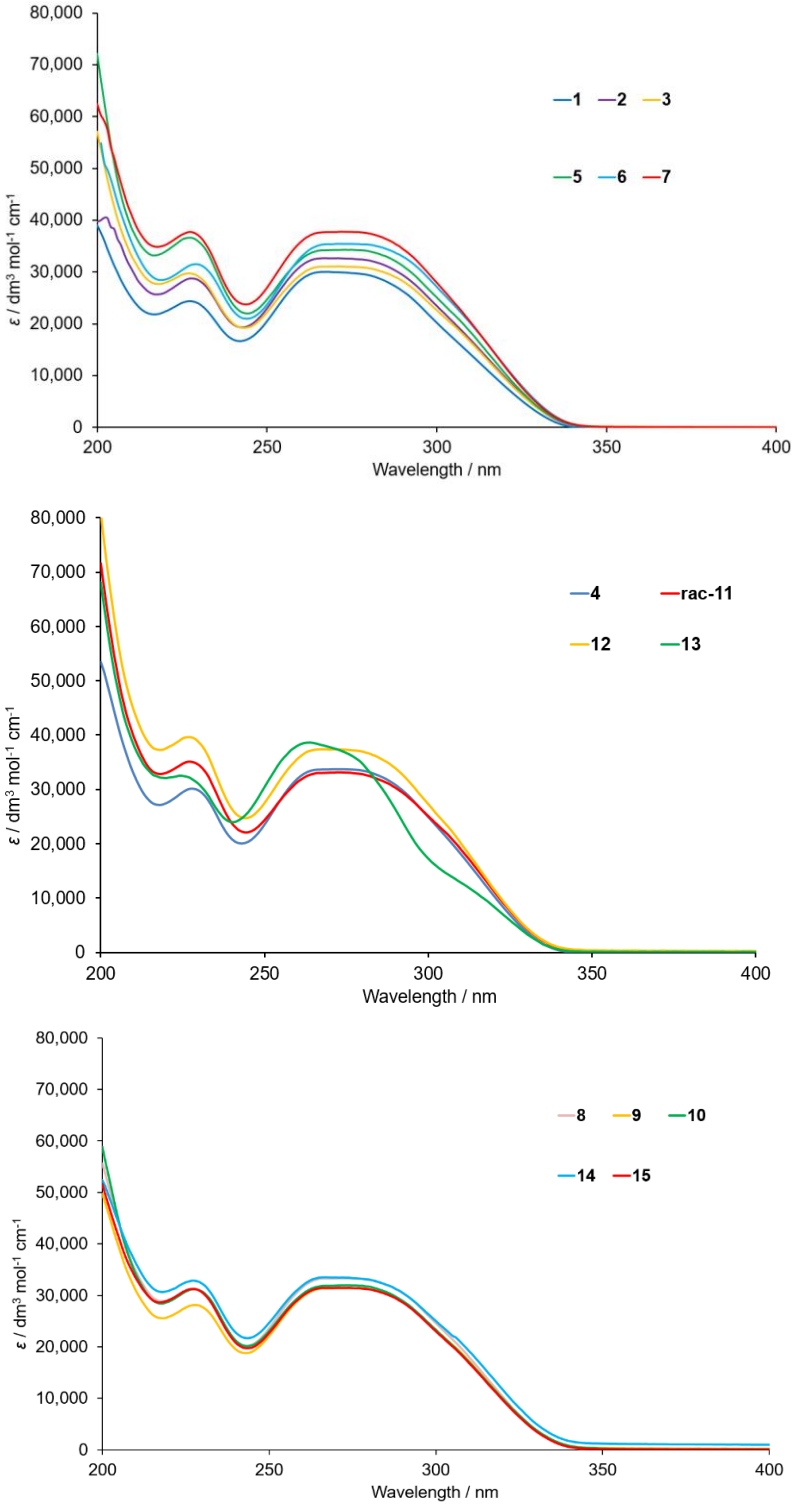

Figure 9. Solution absorption spectra (MeCN, 2.0-3.3 × 10^{-5} mol dm^{-3}) of compounds **1**–**15**.

The absorption spectra of compounds **16**–**21** are superimposed in Figure 10. Each spectrum is dominated by a broad and intense band arising principally from π*←π transitions. For the three halogen-substituted compounds, the value of λ_{max} shifts from 284 nm (F) to 288 nm (Cl) to 292 nm (Br). As expected, the solid-state IR spectra of the ligands are very similar.

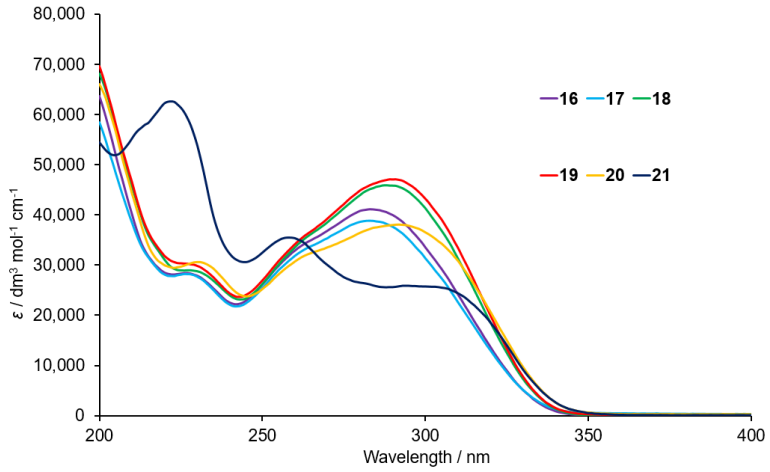

Figure 10. Solution absorption spectra (MeCN, 2.0 × 10^{-5} mol dm^{-3}) of compounds **16**–**21**.

2.3 3:2 Ketone-aldehyde condensation products

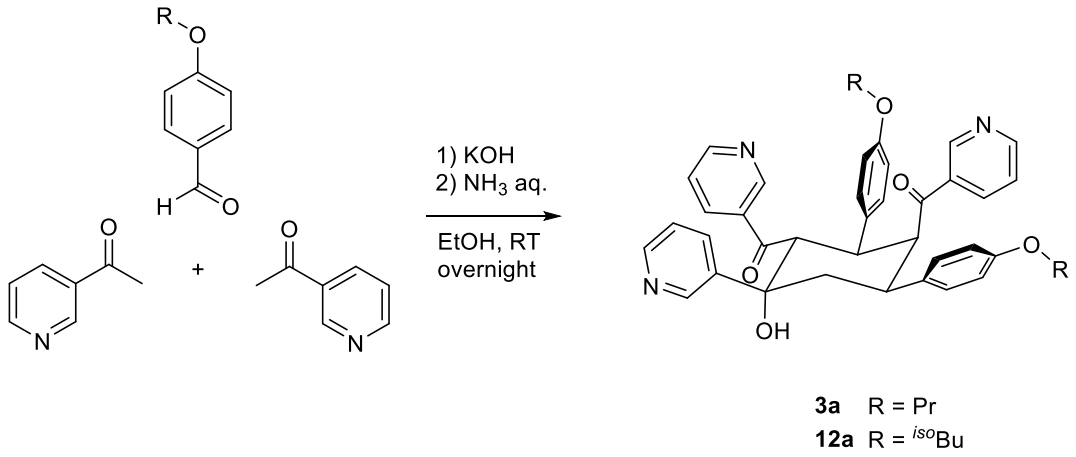

Scheme 15. The unexpected 3:2 condensation product obtained during attempts to prepare ligands **3** and **12**.

4-Propoxybenzaldehyde and 4-(2-methylpropoxy)benzaldehyde were reacted with 3-acetylpyridine in the presence of KOH in ethanol, followed by addition of aqueous NH_3, under identical conditions to those for the successful preparation of the analogous compounds. However, in these two cases, the precipitation of a white product began before ammonia was added. Despite that, the standard work up was performed and the solids were isolated, recrystallized from EtOH and fully characterized. These products exhibited NMR (see below), FT-IR (Figure 11 for compound **3a**) and absorption spectra with different profiles from those reported for the terpyridine ligands (Figure 12 shows a comparison with **3** and **12**). In particular, the IR spectra of the products exhibited a sharp absorption at 3495 cm^{-1} (**3a**) or at 3505 cm^{-1} (**12a**) attributable to an OH group. The ESI mass spectra of the product showed a base peak at *m*/*z* 656.31 or at 684.28 (**3a** and **12a**, respectively) suggesting the formation of the

cyclohexanol derivatives shown in Scheme 15. This class of product has been observed in a number of previous syntheses targeting various 2,2′:6′,2″-terpyridines.[4]

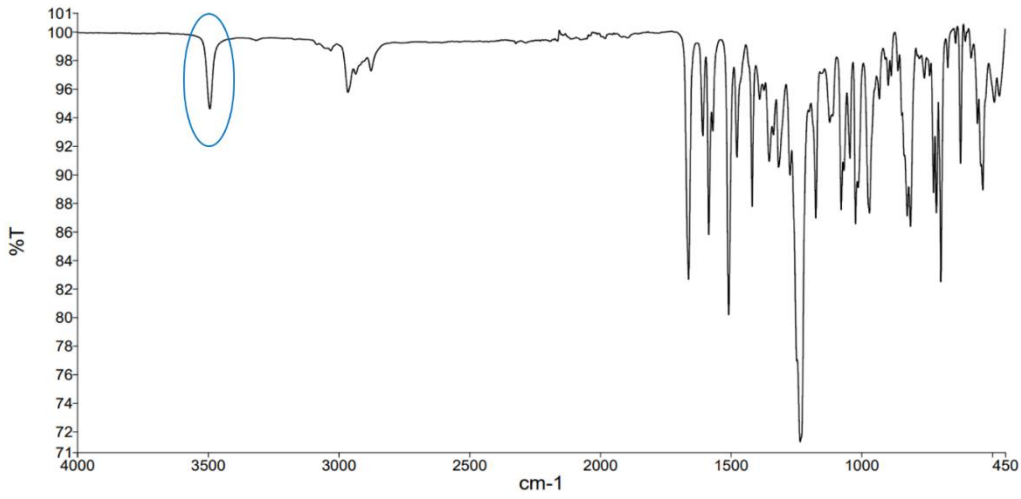

Figure 11. FT-IR spectrum of **3a**. The blue oval points out the sharp absorption at 3495 cm^{-1}, attributable to an OH group.

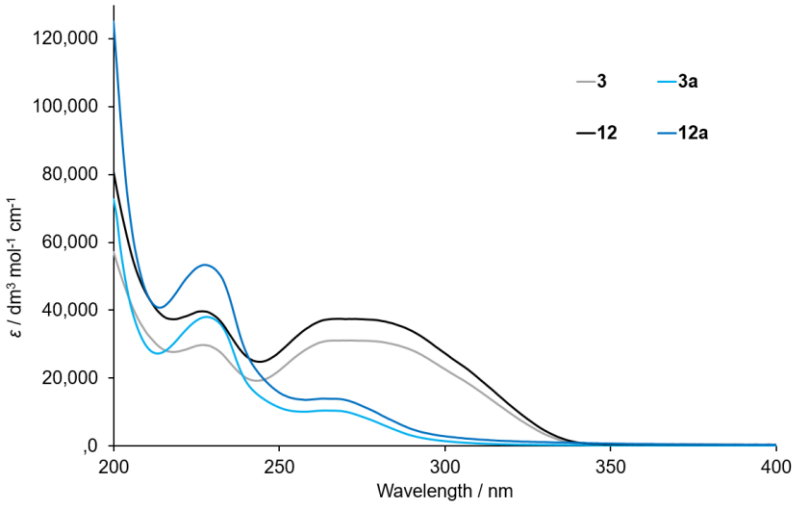

Figure 12. Comparison of the solution absorption spectra of compounds **3**, **3a**, **12** and **12a** (MeCN, 2.0-3.3 x 10^{-5} mol dm^{-3}).

The solution ^{1}H NMR spectrum of **3a** is displayed in Figure 13a and is consistent with the presence of three pyridine environments (rings A, B and C) and two 4-propyloxyphenyl environments (rings D and E); Figure 13b shows the structure of **3a** with atom labelling for NMR spectroscopic assignments. The ^{1}H NMR spectrum of the analogous compound **12a** comprises a similar set of signals (Figure S35). The spectra were assigned using COSY, NOESY,

HMQC and HMBC methods with critical NOESY crosspeaks being between H^{OH}/H^{C2}, $H^{D3}/H^{a'}$, H^{E3}/H^{a}, H^{D2}/H^{5}, H^{D2}/H^{6ax}, H^{E2}/H^{3} and H^{E2}/H^{2}. The spectroscopic characterization confirms the formation of **3a** and **12a**, although it offers no indication as to why these products precipitated from solution only in the case of the propoxy and the isobutyloxy substituents.

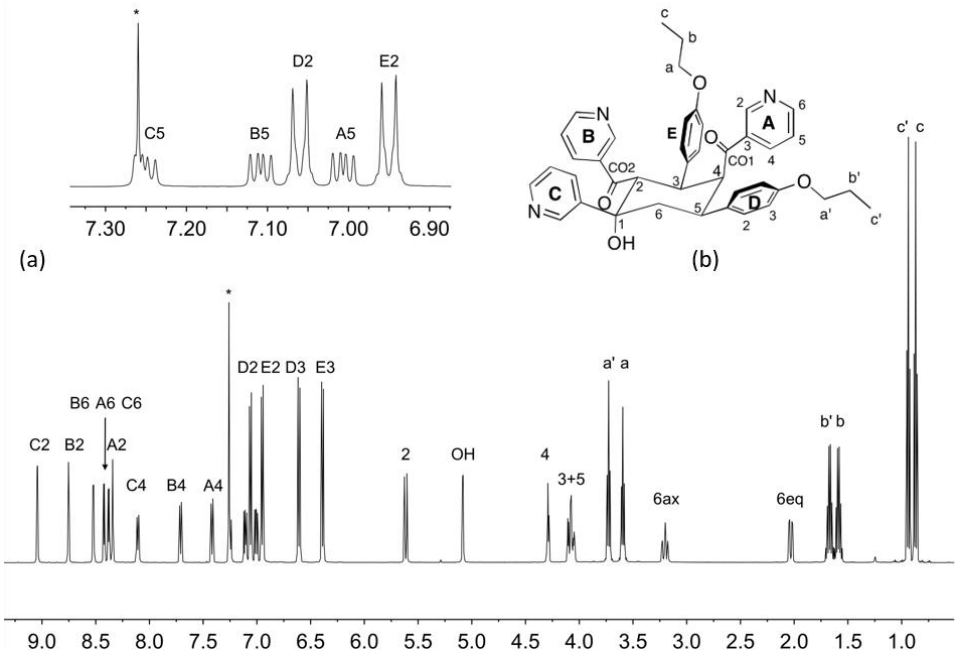

Figure 13. (**a**) ^{1}H NMR spectrum (500 MHz, $CDCl_3$, 298 K) of compound **3a**. * = residual $CHCl_3$. (**b**) Structure of **3a** with atom labelling.

The reaction in these two cases seemed to involve only the aldehyde, KOH and 3-acetylpyridine, so it was repeated in the absence of ammonia (Scheme 16) starting from three different benzaldehydes.

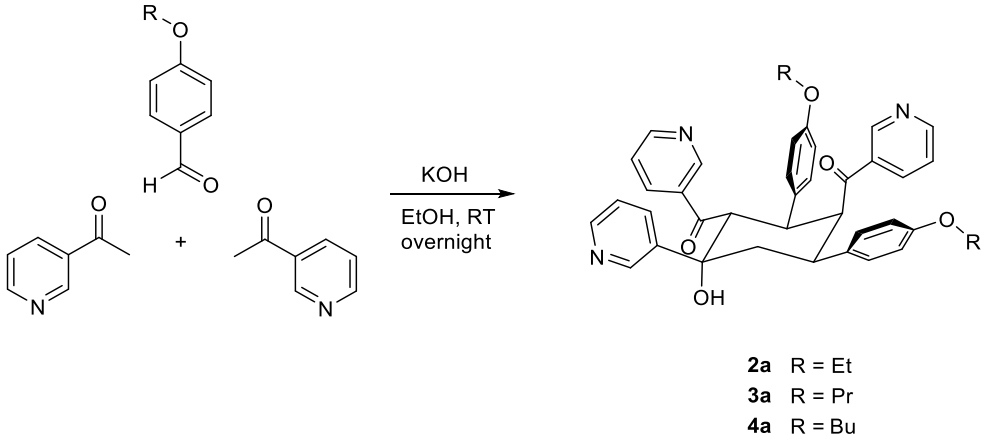

Scheme 16. Synthetic procedure to substituted cyclohexanol derivatives **2a**, **3a** and **4a**. The same conditions as for the synthesis of terpyridines were used, except for the absence of ammonia.

First, 4-propoxybenzaldehyde was reacted with 3-acetylpyridine at a 1:2 molar ratio in ethanol with KOH but without the addition of NH_3. This led to the formation of **3a** (confirmed by NMR spectroscopy) in 42.0% yield. The analogous reactions of 4-ethoxybenzaldehyde or 4-butyloxybenzaldehyde with 3-acetylpyridine in the presence of KOH in ethanol, without NH_3 were also performed (Scheme 16). In both cases, white precipitates formed within 5 minutes and the ESI-MS spectra of the products were consistent with their being **2a** and **4a**, the analogues of **3a**. Therefore, this was proved to be a facile method to prepare the 3:2 ketone-aldehyde condensation products, equally successful when starting from benzaldehydes that yield terpyridines when reacted in the presence of ammonia. Base peaks at m/z = 628.29 and 684.35 were assigned to $[\mathbf{2a}+H]^+$ and $[\mathbf{4a}+H]^+$, respectively. The ^{1}H NMR spectra of **2a**, **3a** and **4a** are shown in Figure 14.

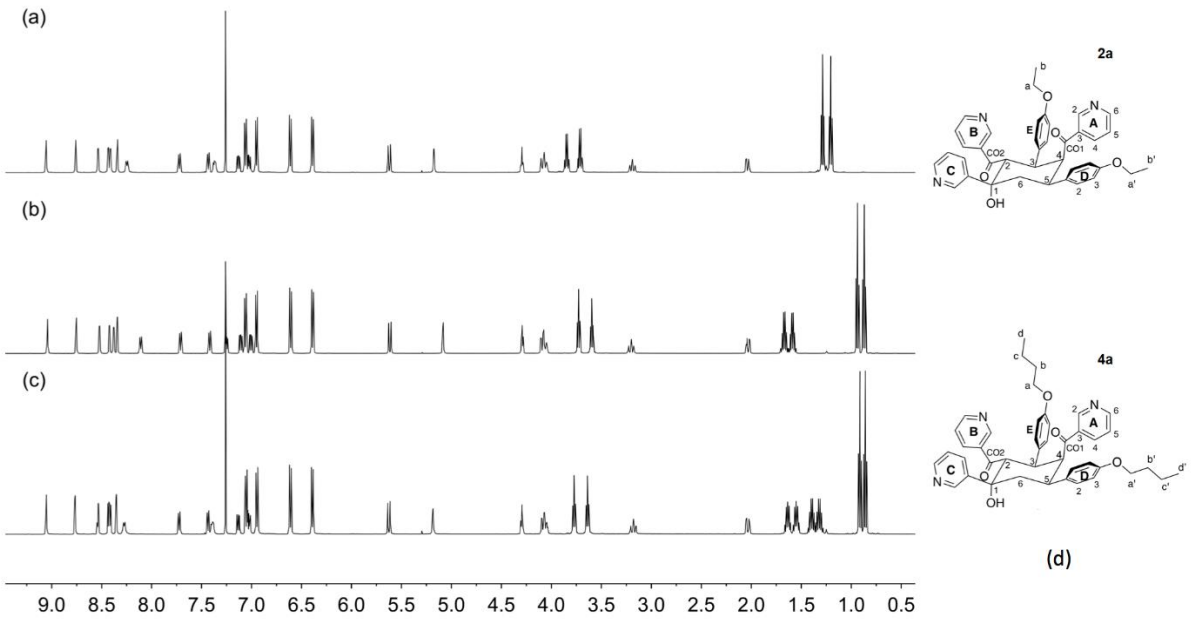

Figure 14. A comparison of the ^{1}H NMR (500 MHz, $CDCl_3$, 298 K) spectra of the cyclic products (**a**) **2a**, (**b**) **3a** and (**c**) **4a**. The singlet at δ 7.26 ppm in each spectrum is residual $CHCl_3$. (**d**) The structures of **2a** and **4a** with atom labelling for NMR spectroscopic assignments.

2.4 Two-step synthesis of ligands **3** and **12**

Ligands **3** and **12** were synthesized in two steps, according to Scheme 17. First, the one-pot reaction starting from 4-hydroxybenzaldehyde was performed, resulting in the ethanol/water soluble 4-(3,2′:6′,3″-terpyridin-4′-yl)phenol. This was isolated upon removal of excess ammonia, addition of water, extraction of impurities with dichloromethane and pH adjustment (up to ca. pH = 8) by addition of aqueous HCl (ca. 4%). Around this value of pH, the product precipitated from the mixture as a yellow solid, which was filtered, washed with water and dried; the ^{1}H NMR spectrum was in agreement with that previously reported for 4-(3,2′:6′,3″-terpyridin-4′-yl)phenol.[5] Subsequently, it was treated with the corresponding 1-

bromoalkane (1-bromopropane for **3** or 1-bromo-2-methylpropane for **12**) in *N,N*-dimethylformamide in the presence of potassium carbonate, at 70–80 °C (see experimental section) overnight.

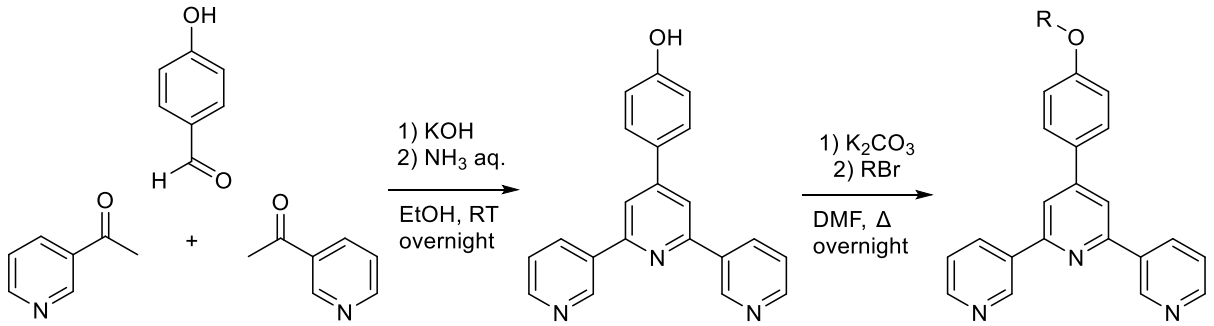

Scheme 17. Synthetic route to compounds **3**, **12**. Both the reactions were complete within one day.

Compounds **3** and **12** were isolated, purified through column chromatography on silica and fully characterized (see details in the Sections 6.2.1.4 and 6.2.1.15), showing similar characteristics to the analogous compounds previously described.

2.5 Ligand structures[6]

Single-crystal structures were obtained for ligands **6**–**9**. Single crystals of ligand **6** were obtained by storing an EtOH solution of the compound at 2–5 °C for one day; X-ray quality crystals of **7** were immediately obtained upon recrystallization from EtOH. Suitable crystals of **8** and **9** were obtained upon recrystallization from EtOH and storing the solutions at 2–5 °C for some days. Compounds **6**, **7** and **8** crystallize in the monclinic space groups $P2_1/n$ (**6**) and $P2_1/c$ (**7** and **8**), while **9** crystallizes in the triclinic space group $P\bar{1}$. The asymmetric unit in each structure contains two independent, but structurally similar, molecules. Figures 15 and 16 depict one independent molecule of each compound. Bond lengths and angles are unexceptional. It is worth noting that the $C_{phenylene}$–O bond is shorter than the $C_{methylene}$–O bond (see captions to Figures 15 and 16), consistent with π-conjugation extending from the arene ring to the O atom; the C–O–C bond angles lie in the range 118.18(13)° to 120.10(14)° (captions to Figures 15 and 16) and these values are consistent with sp^2 hybridization at the O atom. The angles between the least squares planes through adjacent pairs of aromatic rings are compiled in Table 1. While the range of values is quite large, there is a general trend for the phenylene/pyridine twist angles to be larger than the pyridine/pyridine twist angles, an observation that is associated with π-stacking interactions between 3,2′:6′,2″-tpy units (see below). The *n*-alkyloxy chain adopts an extended conformation in all the molecules, and this is associated with the packing interactions discussed later.

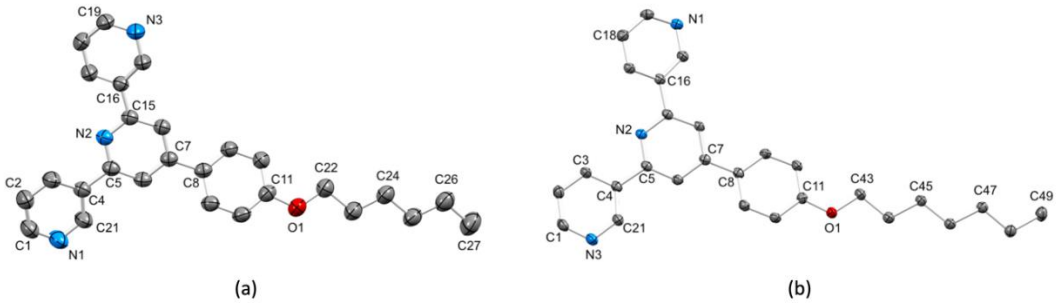

Figure 15. ORTEP representations of one of the two independent molecules of (**a**) **6** and (**b**) **7** (ellipsoids are plotted at a 40% probability level, and H atoms are omitted for clarity). For **6**: C11–O1 = 1.3612(19) Å, C22–O1 = 1.406(2) Å, C11–O1–C22 = 120.10(14)° and for the second independent molecule, the corresponding values are 1.3607(17) Å, 1.4254(18) Å, and 119.30(12)°. For **7**: C11–O1 = 1.3574(19) Å, C43–O1 = 1.4345(18) Å, C11–O1–C43 = 118.51(12)° and for the second independent molecule, the corresponding values are 1.3564(18) Å, 1.4341(18) Å, and 118.15(12)°.

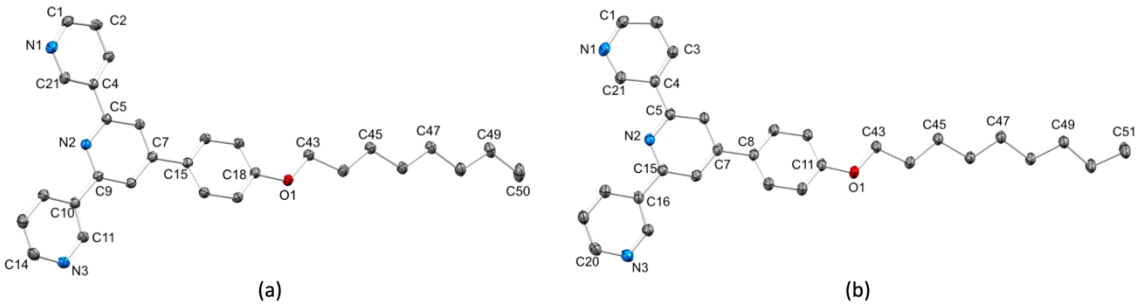

Figure 16. ORTEP representations of one of the two independent molecules of (**a**) **8** and (**b**) **9** (ellipsoids are plotted at a 40% probability level, and H atoms are omitted for clarity). For **8**: C18–O1 = 1.3633(13) Å, C43–O1 = 1.4349(13) Å, C18–O1–C43 = 119.23(8)° and for the second independent molecule, the corresponding values are 1.3630(13) Å, 1.4334(13) Å, and 119.49(8)°. For **9**: C11–O1 = 1.364(3) Å, C43–O1 = 1.437(3) Å, C11–O1–C43 = 118.3(2)° and for the second independent molecule, the corresponding values are 1.365(3) Å, 1.437(3) Å, and 118.22(19)°.

Table 1. Angles between the least squares planes of pairs of aromatic rings in compounds **6–9**; there are two crystallographic independent molecules of each compound. Conformations **A** and **B** are defined in Scheme 18.

Compound	Conformation	py - py /°	py - py /°	py - phenylene /°
6 molecule 1	**A**	13.0	14.3	19.0
6 molecule 2	**A**	16.0	14.2	24.4
7 molecule 1	**A**	18.2	9.0	15.5
7 molecule 2	**A**	7.8	14.6	23.1
8 molecule 1	**B**	16.8	5.7	20.6
8 molecule 2	**B**	19.3	4.1	27.8
9 molecule 1	**B**	5.9	7.2	20.2
9 molecule 2	**B**	3.1	7.1	27.1

The conformation of the 3,2′:6′,2″-tpy unit changes from **A** (Scheme 18) in compounds **6** and **7**, to **B** (Scheme 18) in **8** and **9**. A detailed look at the molecular packing gives an insight into the reasons for this conformational switch. There is no solvent in the crystal lattice in any of the structures, allowing a meaningful comparison of the crystal packing.

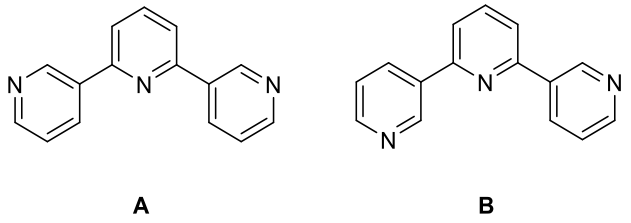

Scheme 18. The two limiting planar conformations adopted by the 3,2′:6′,2″-tpy unit in the solid state structures of ligands **6**–**9**.

In the solid state structure of **6**, pairs of crystallographically independent molecules interact through C–H...N weak hydrogen bonds (Figure 17a) within the unit cell, with C...N separations of 3.753(2), 3.412(2) and 3.449(2) Å; H...N distances are in the range 2.55–2.83 Å, the H atom being in calculated positions. This motif extends into a ribbon-assembly through bifurcated hydrogen bonds[7] with atoms N3 and N6 acting as bifurcated acceptors with C...N distances of 3.412(2) and 3.753(2) Å for N3, and 3.622(2) and 3.720(2) Å for N6. The N...H interactions are defined by the sum of the Bondi[8] N and H van der Waals radii in the program Mercury[9] with a default value of 1.20 Å for H; a value of 1.10 Å may be more realistic for organic structures.[10] The hydrogen-bonding pattern observed in Figure 17a reflects the fact that both of the independent 3,2′:6′,2″-tpy units exhibit conformation **A**. Figure 17b illustrates centrosymmetric pairing of *n*-hexyloxy chains of adjacent ribbons. The assembly propagates into a non-planar sheet lying approximately in the *ac*-plane, and Figure 17b illustrates that the hydrogen-bonded 2D-network sheet contains voids. Each square-shaped cavity is bordered on two sides by *n*-hexyloxy chains. The voids are occupied by adjacent sheets being woven together (Figures 18a and 18b), although in a simpler manner than in established biaxial weavings.[11] The interwoven sheets are closely associated through offset face-to-face π-stacking of centrosymmetric pairs of the central pyridine rings of the 3,2′:6′,3″-tpy units. For the crystallographically independent molecules of **6**, the π-stacking interactions exhibit inter-plane distances of 3.56 Å and 3.48 Å, and centroid...centroid distances of 3.96 Å and 3.58 Å, respectively. The head-to-tail arrangement of the offset-stacked pyridine rings is optimal in terms of the charge distribution in the pyridine rings.[12]

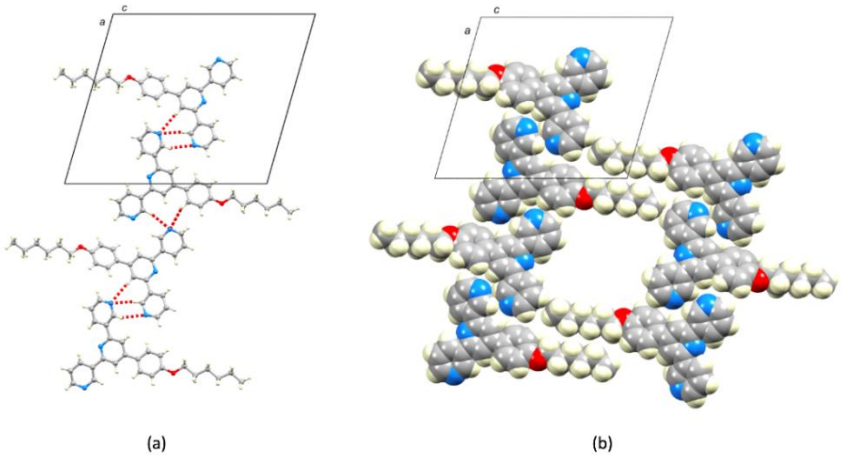

Figure 17. Molecules of **6** pack into 2D-sheets involving C–H...N weak hydrogen bonds and van der Waals interactions between *n*-hexyloxy chains. The unit cell is viewed down the *b*-axis. (**a**) C–H...N hydrogen bonds and (**b**) a space-filling representation of part of one supramolecular sheet showing one void between pairs of *n*-hexyloxy chains.

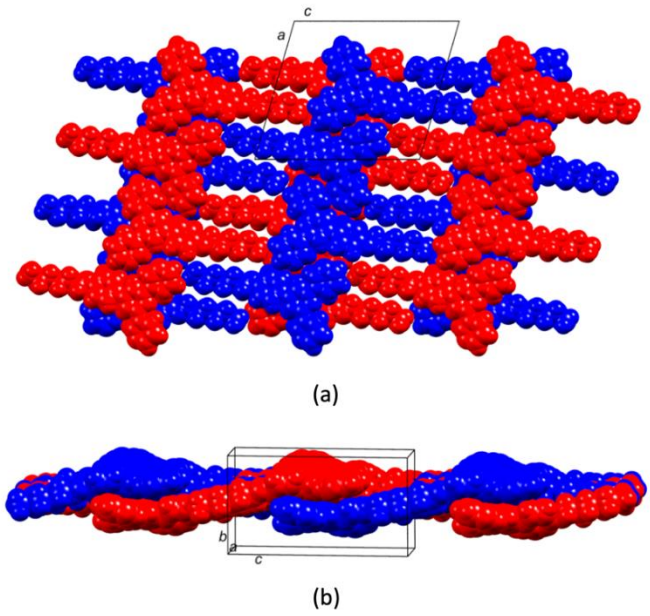

Figure 18. Part of two interwoven supramolecular sheets showing how the voids in one sheet (see Figure 17b) are occupied by *n*-hexyloxy chains from the next sheet. (**a**) Viewed down the *b*-axis, and (**b**) viewed approximately down the *a*-axis.

As shown in Figure 19a, molecules of **7** pack into ribbons with a similar C–H...N weak hydrogen bonding pattern as observed in the solid-state structure of **6**, and the same interwoven supramolecular network assembles (Figure 19b). The interwoven network is supported by offset, face-to-face π-stacking of pairs of crystallographically independent molecules of **7** (inter-plane angle = 7.0°, and centroid...centroid distance = 3.58 Å). The similarity between the packing in **6** and **7** negates the need for further discussion of the packing in **7**.

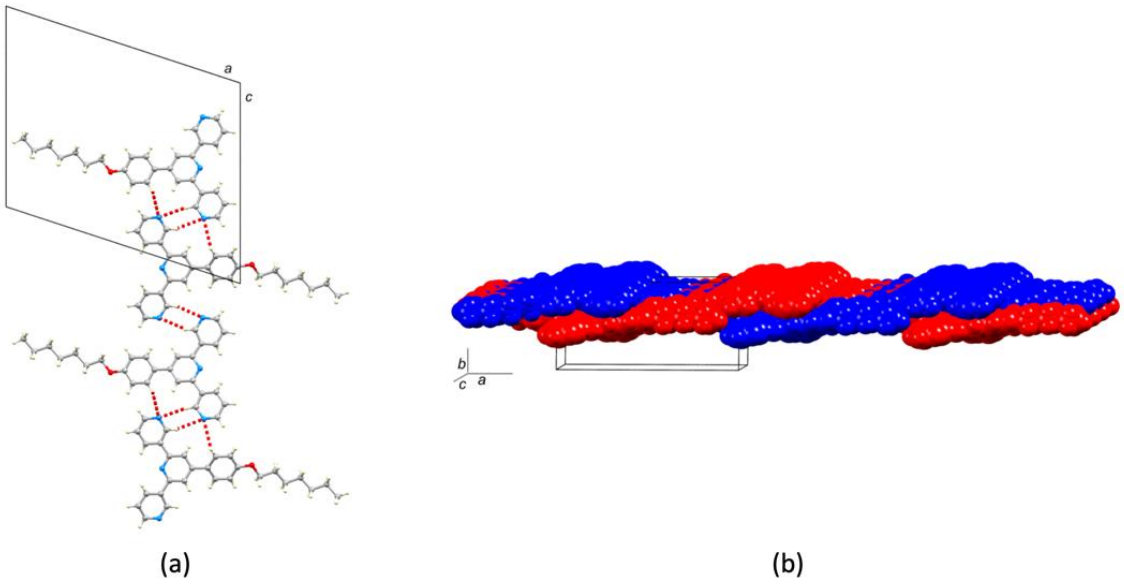

Figure 19. Packing of molecules of **7**. (**a**) Weak C–H...N hydrogen bonds within the supramolecular 2D-sheets. (**b**) Interwoven sheets.

The packing of the molecules in the lattice undergoes a major change on going from the *n*-hexyloxy and *n*-heptyloxy substituents in **6** and **7** to the longer chains in compounds **8** and **9**, and associated with this is a change in conformation of the 3,2′:6′,3″-tpy units from **A** to **B** (Scheme 18). In compound **8**, the two crystallographically independent molecules engage in an offset face-to-face π-stacking of the pyridine (py) rings containing N2 and N5 (Figure 20a). The angle between the ring-planes is 14.4° and the centroid...centroid distance is 3.88 Å. This paired motif is a principal packing unit in the lattice. Molecules of **8** pack into 2D-layers with inter-layer py...py π-stacking (Figure 20b,c) being augmented by C–$H_{methylene}$... π interactions.[13] The increase in the length of the *n*-alkyloxy chain leads to a greater role for van der Waals interactions compared to the packing in crystalline **6** and **7**, and this is more important within a 2D-layer (Figures 21) than between layers. Figure 21 also shows extensive C–H...N and C–H...O weak hydrogen bonding contacts within each 2D-layer, and optimization of these interactions clearly depends upon the conformation of the 3,2′:6′,3″-tpy domain.

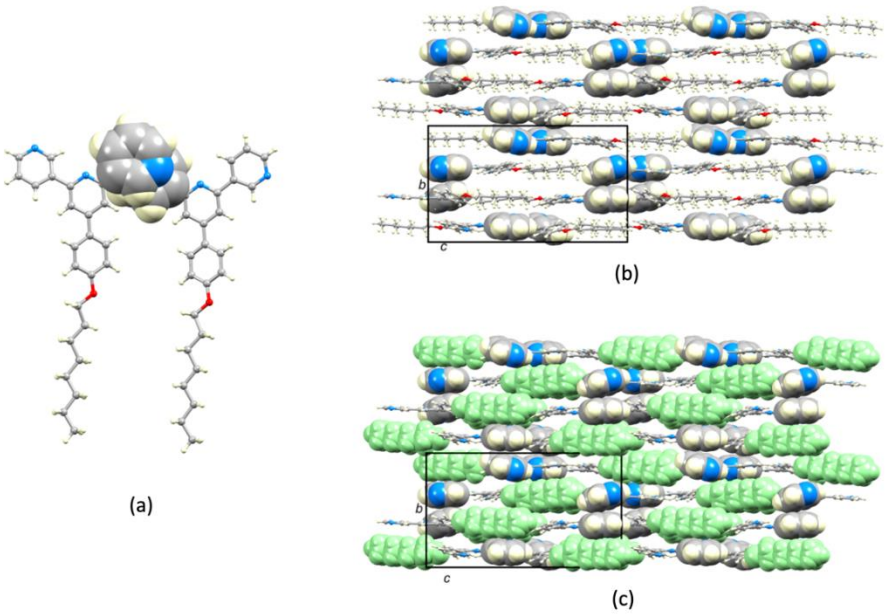

Figure 20. (**a**) Face-to-face π-stacking between pyridine rings (space-filling representation) of crystallographically independent molecules of **8**; (**b**) molecules of **8** pack into 2D-layers with the *n*-octyloxy chains in extended conformations; (**c**) the same view of the packing as in (**b**) with the *n*-octyloxy groups in space-filling representation (green).

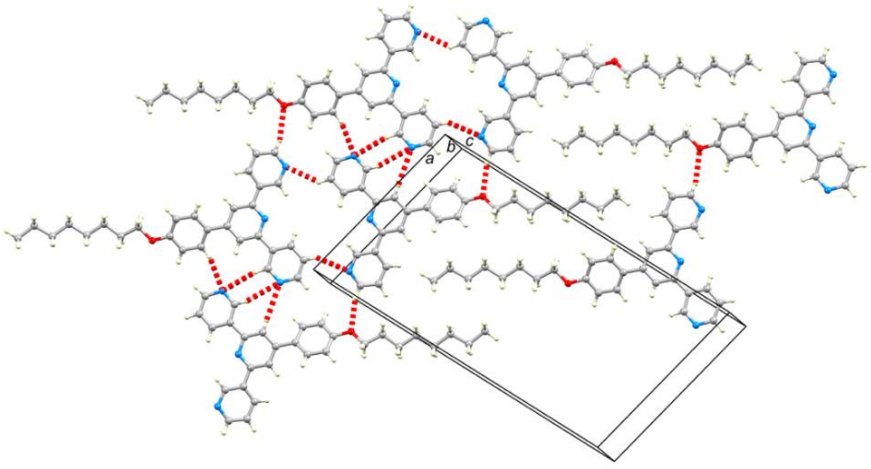

Figure 21. Within each layer of molecules of **8**, van der Waals interactions between *n*-alkyloxy chains, and C–H…N and C–H…O weak hydrogen bonds (red hashed lines) are important packing interactions.

Despite the change in space group on going from **8** ($P2_1/c$) to **9** ($P\bar{1}$), there are many similar features in the lattices of the two compounds, indicating that the longer *n*-octyloxy and *n*-nonyloxy chains impart similar influences on the crystal packing. Firstly, the two crystallographically independent molecules of **9** engage in face-to-face π-stacking. In contrast to the motif observed in **8** (Figure 20a), that in **9** involves stacking of the rings containing N1/N5 and those with N2/N4 (Figure 22a). The angles between the planes of the pairs of pyridine rings with N1/N5 and N2/N4 are 8.0° and 1.4°, respectively, and each of the two

centroid...centroid distances is 3.82 Å. The fact that each of the two independent 3,2′:6′,2″-tpy domains adopts conformation **B** leads to a favorable arrangement of the stacked pairs of rings in terms of the charge distribution within the heterocycles.[12] As in compound **8**, molecules of **9** are organized in 2D-sheets in which van der Waals interactions between extended *n*-alkyloxy chains play a dominant role (Figures 22b). Figure 23 shows that the packing involves a combination of C–H...N and C–H...O weak hydrogen bonds and van der Waals interactions between *n*-nonyloxy chains.

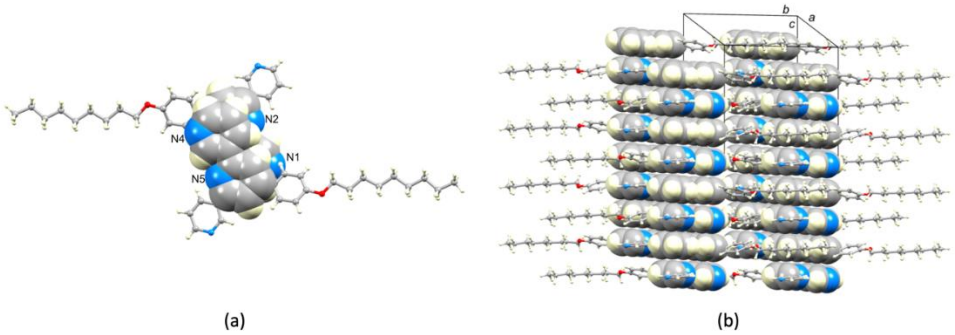

Figure 22. (**a**) Offset face-to-face π-stacking of two crystallographically independent molecules of **9**. (**b**) Packing of molecules of **9** into 2D-layers with the π-stacking shown in (**a**) highlighted in space-filling representation.

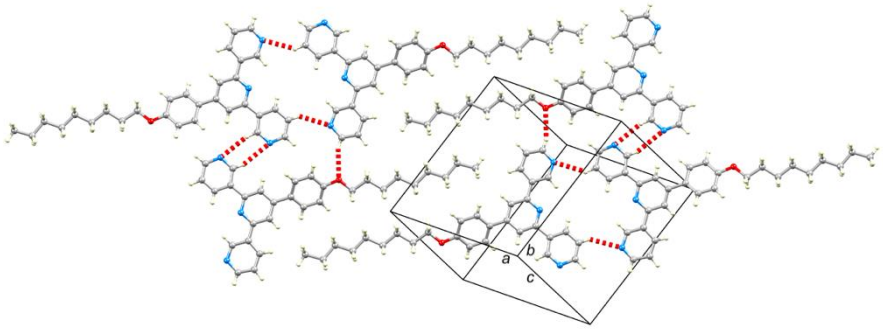

Figure 23. Packing of molecules of **9** within one 2D-sheet involves a combination of C–H...N and C–H...O weak hydrogen bonds and van der Waals interactions between *n*-nonyloxy chains.

2.6 Reactions of 3,2′:6′,3″-terpyridine ligands with metal salts

The synthesized ligands were allowed to react with a variety of metal salts under crystal growth conditions. Several salts were considered for this purpose and initially investigated. It was soon apparent that copper(II) acetate and cobalt(II) thiocyanate gave successful crystal growth in the range of chosen conditions, and became the main focus of this work (see the following Chapters). Although all the presented compounds were reacted with $Cu(OAc)_2 \cdot H_2O$ and $Co(NCS)_2$, only the reactions and the exact conditions that led to a crystallization and a

successful crystal structure are described, even though each experiment was carried out in a variety of concentrations and combinations of solvents. Among all the options, the elected methodology to grow single crystals was the layering technique. All single-crystal growth experiments were carried out using identical crystallization tubes (i.d. = 13.6 mm, volume = 24 mL), and by layering a solution of the chosen metal salt in methanol or acetonitrile over a chloroform, dichloromethane or toluene solution of the ligand. The test tube was then sealed with a septum and left to stand at room temperature until visible crystals had formed. If no crystals were visible after two weeks, the septum was pierced with a needle to allow slow evaporation and optimum crystal growth. Single crystals grew within one day and six months; although crystal growth was not complete within this period, crystals were removed for X-ray diffraction purposes and the yield of the material was not determined, due to its sensitivity towards loss of solvent in many cases. After a single crystal was selected for X-ray diffraction, the remaining crystals were filtered, washed with the crystallization solvents and their powder X-ray diffraction patterns (PXRD) and solid-state FT-IR spectra were recorded. In a few cases, thermogravimetric analysis coupled with mass spectrometry (TGA-MS) was additionally performed to identify and quantify the solvents released from the lattice of the coordination polymers during the heating phase (see below). PXRD was measured on each sample to confirm whether the chosen crystal was representative of the bulk material, and a Rietveld refinement of the diffraction patterns was performed with the software FULLPROF SUITE,[14, 15] using the structural model from the single-crystal refinement. In the few experiments where a correspondence was not found between predicted and experimental powder patterns, the crystallization setup was repeated and cell checks were carried out on a number of different crystals of the multiple batches to confirm whether other species had formed as single crystals, and to check for possible polymorphism. Eventually, a full X-ray measurement was performed when a new unit cell was determined. In particular, the search for other reaction products was necessary in the reactions of ligand **1** with copper(II) acetate (see Section 3.1) and with cobalt(II) thiocyanate (see Section 4.1). When more than one coordination polymer was identified as a product, a preparative scale reaction was also performed. These reactions were carried out in a round-bottomed flask, by adding the solid metal salt to a methanol solution of the ligand, while stirring. The formation of a suspension was immediately observed, and the product was either collected by filtration or centrifugation, then dried under vacuum up to constant weight. Elemental analysis and/or PXRD were measured in order to confirm the correspondence between the latter compound and one of the species identified *via* single-crystal XRD. A cell check was also performed when single crystals from different crystallization solvents, different concentrations or different M/L molar ratio grew, for a particular combination of ligand and metal salt.

2.7 Conclusions

The synthesis and the characterization of twenty-one 3,2′:6′,3″-terpyridine ligands, which include series of homologous compounds only differing by the length, the branching type or the nature of the substituent groups are reported. Functionalization of the tpy unit in the 4′-position was easily achieved using the one-pot method of Wang and Hanan.[2] This synthetic approach was successful for the majority of the compounds; however, for **3** and **12**, cyclohexanol derivatives were obtained. In these two cases, the 4-(3,2′:6′,3″-terpyridin-4′-yl)phenol route was adopted.

Compounds **1**–**21** were fully characterized by NMR, IR and absorption spectroscopies, mass spectrometry, melting point and elemental analysis or high-resolution mass spectrometry. Furthermore, four crystal structures were obtained and were described in detail, for **6**–**9**; similarities and differences in the 3,2′:6′,3″-tpy unit conformation and in the packing interactions were highlighted.

References

1. L. Li, Y. Z. Zhang, C. Yang, E. Liu, J. A. Golen and G. Zhang, *Polyhedron*, **2016**, 105, 115-122.
2. J. H. Wang, G. S., *Synlett*, **2005**, 8, 1251-1254.
3. S. B. Bienz, L.; Fox, T.; Meier, H. , *Spektroskopische Methoden in der Organischen Chemie*, Thieme, Stuttgart, Germany, 9th edn., **2016**.
4. D. Rocco, C. E. Housecroft and E. C. Constable, *Molecules*, **2019**, 24, 1799.
5. G. W. V. Cave and C. L. Raston, *J. Chem. Soc., Perkin Trans. 1*, **2001**, 3258-3264.
6. D. Rocco, A. Prescimone, E. C. Constable and C. E. Housecroft, *Molecules*, **2020**, 25, 3162.
7. G. Desiraju and T. Steiner, *The Weak Hydrogen Bond*, Oxford University Press, Oxford, England, **2001**.
8. A. Bondi, *J. Phys. Chem.*, **1964**, 68, 441-451.
9. C. F. Macrae, I. Sovago, S. J. Cottrell, P. T. A. Galek, P. McCabe, E. Pidcock, M. Platings, G. P. Shields, J. S. Stevens, M. Towler and P. A. Wood, *J. Appl. Crystallogr.*, **2020**, 53, 226-235.
10. R. S. Rowland and R. Taylor, *J. Phys. Chem.*, **1996**, 100, 7384-7391.
11. Y. Liu, M. O'Keeffe, M. M. J. Treacy and O. M. Yaghi, *Chem. Soc. Rev.*, **2018**, 47, 4642-4664.
12. C. Janiak, *J. Chem. Soc., Dalton Trans.*, **2000**, 3885-3896.
13. M. Nishio, *CrystEngComm*, **2004**, 6, 130-158.
14. J. Rodríguez-Carvajal, *Phys. B*, **1993**, 192, 55-69.
15. T. Roisnel and J. Rodríguez-Carvajal, In Proceedings of the Seventh European Powder Diffraction Conference (EPDIC 7), Barcelona, Spain, **2000**, 118-123.

Chapter 3 Coordination polymers with copper(II) acetate

Copper(II) acetate is one of the metal salts chosen for the investigation of the coordination chemistry of the 3,2′:6′,3″-tpy ligands described in Chapter 2. In the solid state it arranges in $\{Cu_2(\mu\text{-}OAc)_4\}$ paddle-wheel units, in which the axial sites of the dinuclear core provide linear directionality (Scheme 19). This feature promotes the formation of single-stranded 1D-coordination polymers as a result of the reactions between $Cu(OAc)_2{\cdot}H_2O$ and ditopic ligands.

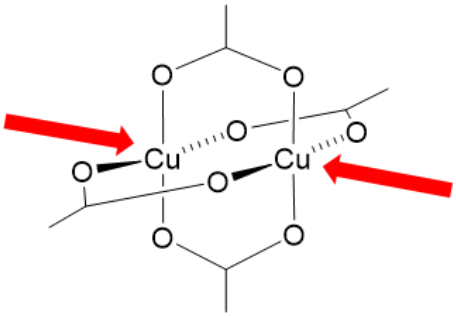

Scheme 19. Representation of the $\{Cu_2(\mu\text{-}O_2CCH_3)_4\}$ paddle-wheel secondary building unit (SBU) with red arrows pointing at the available coordination sites.

Although the paddle-wheel unit represents one of the simplest secondary building units (SBUs), crystallization conditions can affect the outcome of the reactions, and this moiety is not always retained. A number of examples of different motifs with lower or higher nuclearity have been reported in Chapter 1, exemplifying the variety of possible results. However, when the $\{Cu_2(\mu\text{-}OAc)_4\}$ SBU is maintained, the manner in which these units are connected in the coordination network depends upon the nature of the linkers. Hence, an investigation was carried out using flexible 3,2′:6′,3″-tpy ligands. In particular, the exploration of how the structures of the coordination assemblies were influenced by changes in the length of the alkyloxy tails in 4′-(4-*n*-alkyloxyphenyl)-3,2′:6′,3″-tpy ligands or by varying the nature of the substituent group in 4′-(4′-substituted-[1,1′-biphenyl-4-yl)-3,2′:6′,3″-tpy ligands is presented.

3.1 Reactions of **1** with $Cu(OAc)_2 \cdot H_2O$[1]

A first reaction (experiment 1) was carried out between **1** (Scheme 20a) and $Cu(OAc)_2 \cdot H_2O$ under crystal growth conditions by layering a chloroform solution of **1** on a methanol solution of the copper salt; the tube was sealed with a septum and left standing at room temperature. After two months, blue block crystals grew. The single crystal that was analyzed by XRD proved to be the 1D-polymer $[Cu_2(\mu\text{-}OAc)_4(\mathbf{1})]_n$, containing the anticipated dinuclear paddle-wheel units. However, the Rietveld analysis of the PXRD pattern (Figure 24b, see below) measured on the remaining crystals in the same tube showed that $[Cu_2(\mu\text{-}OAc)_4(\mathbf{1})]_n$ was not the main product of the reaction and that the selection of that single crystal had been fortuitous. The same crystallization experiment was carried out in parallel by Giacomo Manfroni, another PhD candidate in the same research group, and in this case (experiment 2), the solvent was allowed to evaporate more quickly, and a precipitate was formed. After filtration, the precipitate was redissolved in MeOH, and the solution was left to stand at room temperature. After several months, X-ray quality blue crystals were collected, and structural determination showed the formation of the double-stranded coordination polymer $[Cu_4(\mu_3\text{-}OH)_2(\mu\text{-}OAc)_2(\mu_3\text{-}OAc)_2(AcO\text{-}\kappa O)_2(\mathbf{1})_2]_n \cdot 2n$MeOH. The remainder of the crystals from experiment 2 were collected and analyzed by PXRD (Figure 24a). This time the analysis confirmed that the bulk materials from the crystal growth experiment carried out over several months (experiment 2) corresponded to $[Cu_4(\mu_3\text{-}OH)_2(\mu\text{-}OAc)_2(\mu_3\text{-}OAc)_2(AcO\text{-}\kappa O)_2(\mathbf{1})_2]_n \cdot 2n$MeOH; the same double-stranded polymer was proved to be the dominant product in experiment 1 as well (see Figure 24b).

A preparative scale reaction of $Cu(OAc)_2 \cdot H_2O$ and **1** (2:1 molar ratio) was carried out in MeOH and a pale-blue solid immediately formed. This was filtered, dried and analyzed. Elemental analysis showed to be in agreement with a stoichiometry of $Cu(OAc)_2(\mathbf{1})$, and PXRD (Figure 24c) was consistent with the material being $[Cu_2(\mu\text{-}OAc)_4(\mathbf{1})]_n$. These results indicate that, on a preparative scale, ligand **1** reacts with $Cu(OAc)_2 \cdot H_2O$ to immediately yield the linear 1D-coordination polymer $[Cu_2(\mu\text{-}OAc)_4(\mathbf{1})]_n$. However, when the reaction is carried out under conditions of crystal growth by layering over a period of months, the incorporation of hydroxido ligands and formation of $\{Cu_4(\mu_3\text{-}OH)_2(OAc)_6\}$-clusters becomes dominant, as confirmed by the powder patterns of both experiments 1 and 2. Scheme 20b summarizes the series of reactions carried out between **1** and $Cu(OAc)_2 \cdot H_2O$, with the different conditions and outcomes.

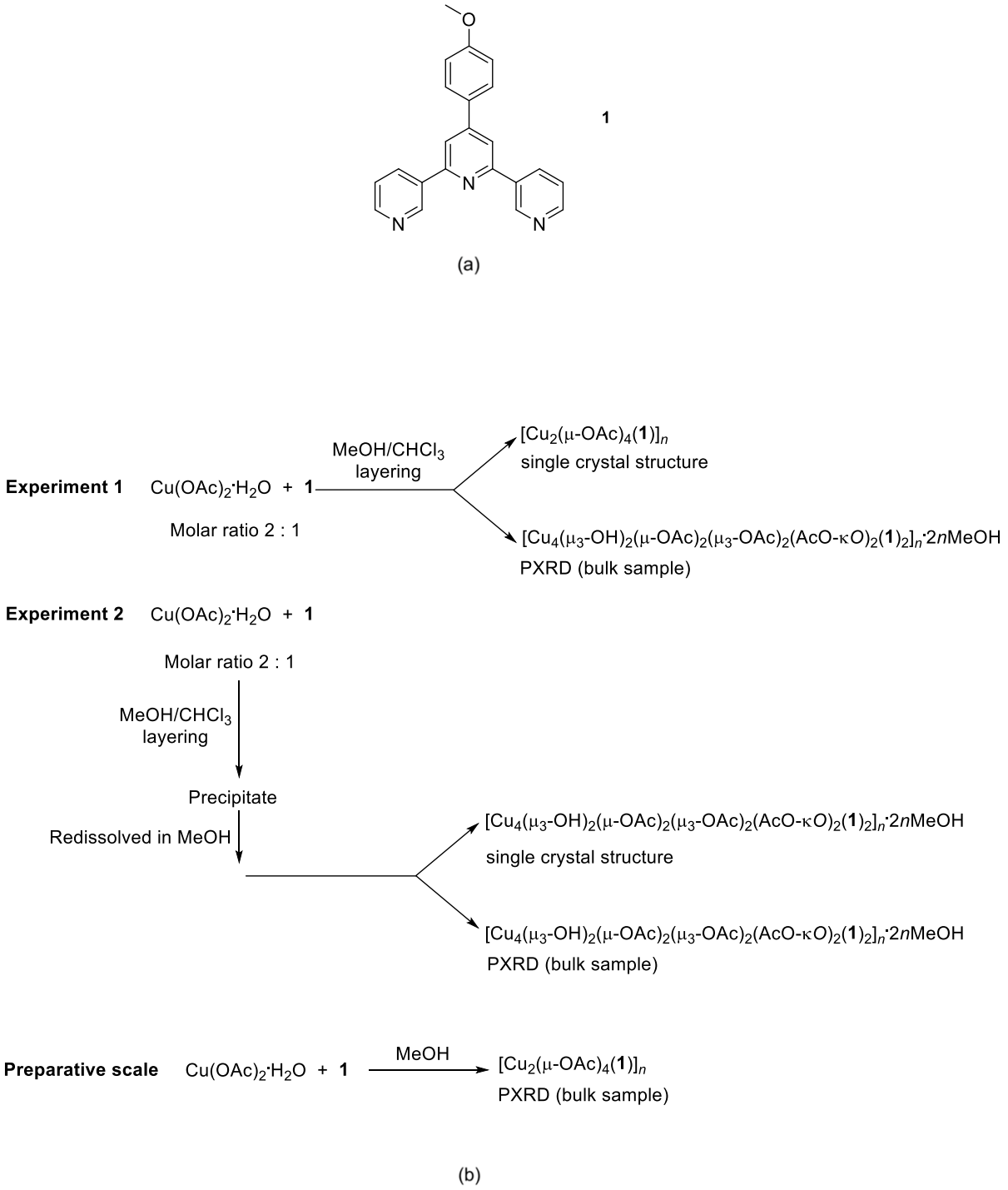

Scheme 20. (**a**) Structure of ligand **1**. (**b**) Summary of the reactions of ligand **1** with $Cu(OAc)_2 \cdot H_2O$. Crystal growths by layering (experiments 1 and 2) and the preparative scale reactions were carried out in air at ambient temperature.

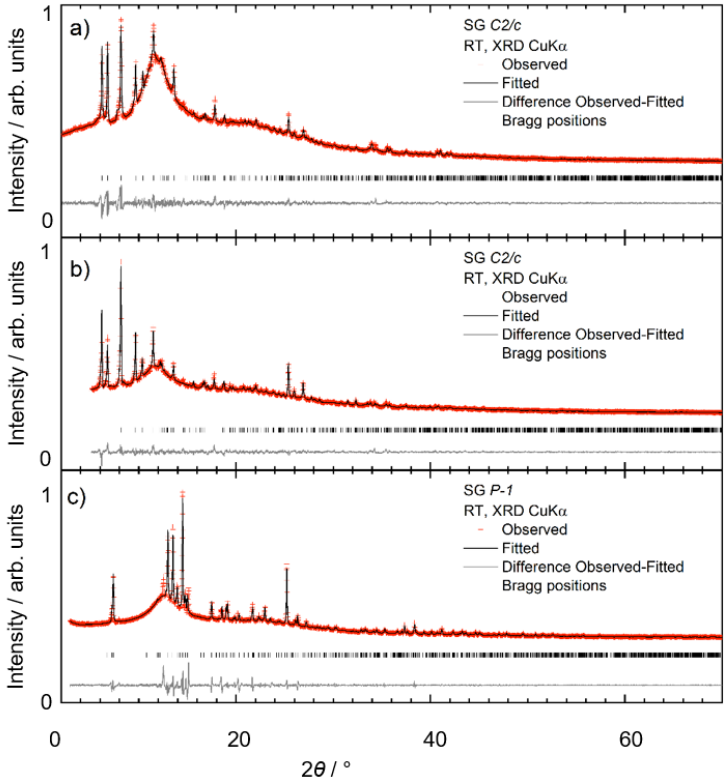

Figure 24. Laboratory X-ray diffraction (Cu$K\alpha_1$ radiation) pattern (red crosses) of (**a**) the bulk crystalline material from experiment 2 with fitting to the predicted pattern from the single-crystal determination of $[Cu_4(\mu_3\text{-}OH)_2(\mu\text{-}OAc)_2(\mu_3\text{-}OAc)_2(AcO\text{-}\kappa O)_2(\mathbf{1})_2]_n{\cdot}2n$MeOH; (**b**) the bulk crystalline material from experiment 1 with fitting to the predicted pattern from the single-crystal determination of $[Cu_4(\mu_3\text{-}OH)_2(\mu\text{-}OAc)_2(\mu_3\text{-}OAc)_2(AcO\text{-}\kappa O)_2(\mathbf{1})_2]_n{\cdot}2n$MeOH; (**c**) the crystalline material from the preparative scale synthesis with fitting to the predicted pattern from the single-crystal determination of $[Cu_2(\mu\text{-}OAc)_4(\mathbf{1})]_n$ at room temperature. The black line corresponds to the best fit from the profile-matching refinement. Lower vertical marks denote the Bragg peak positions. The bottom line in each plot represents the difference between experimental and calculated points.

After PXRD, solid-state FT-IR spectra were measured on the bulk materials from experiments 1 and 2 and from the preparative scale reaction of **1** with $Cu(OAc)_2{\cdot}H_2O$ (full spectra are shown in the supplementary material of the corresponding publication). These were consistent with the conclusions drawn from the PXRD. Figure 25a shows an expansion of the region below 1760 cm^{-1} in the IR spectra of the bulk samples from experiments 1 and 2, confirming that the materials are the same, i.e. $[Cu_4(\mu_3\text{-}OH)_2(\mu\text{-}OAc)_2(\mu_3\text{-}OAc)_2(AcO\text{-}\kappa O)_2(\mathbf{1})_2]_n{\cdot}2n$MeOH. The absorption observed at 3420 cm^{-1} is likely to arise from the O–H stretch of the hydroxido ligands.[2, 3] A comparison of the IR spectra of the bulk sample from experiment 1 with that of the product from the preparative scale reaction is shown in Figure 25b . The absorption at 916 cm^{-1} present in the spectrum of $[Cu_4(\mu_3\text{-}OH)_2(\mu\text{-}OAc)_2(\mu_3\text{-}OAc)_2(AcO\text{-}\kappa O)_2(\mathbf{1})_2]_n{\cdot}2n$MeOH (Figure 25a and black line in Figure 25b) is tentatively assigned to a vibrational mode of the μ_3-OH group.[4]

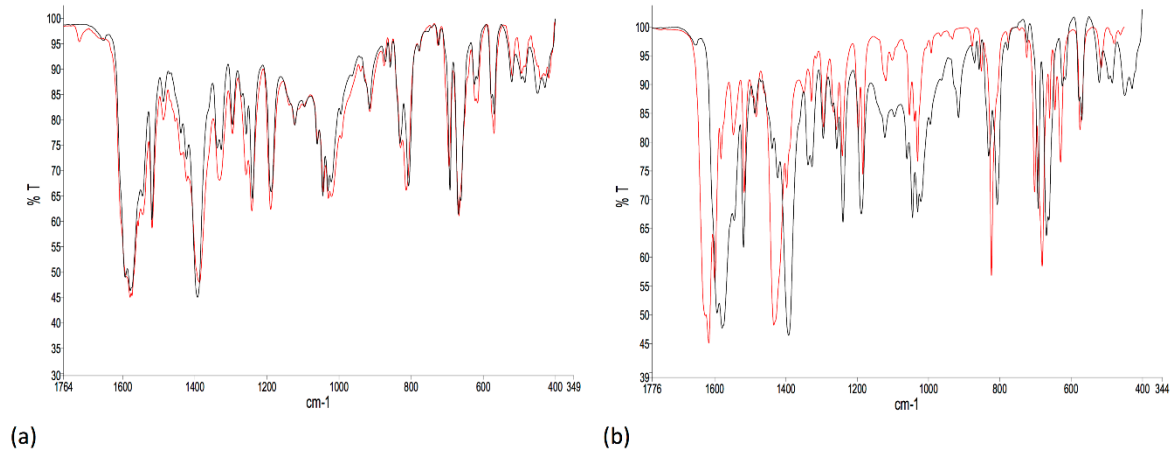

Figure 25. Normalized FT-IR spectra (solid-state) of the bulk materials from (**a**) experiment 1 (black line) and experiment 2 (red line), and (**b**) experiment 1 (black line, $[Cu_4(\mu_3\text{-}OH)_2(\mu\text{-}OAc)_2(\mu_3\text{-}OAc)_2(AcO\text{-}\kappa O)_2(\mathbf{1})_2]_n{\cdot}2n$MeOH) and the preparative scale reaction (red line, $[Cu_2(\mu\text{-}OAc)_4(\mathbf{1})]_n$).

As shown in Scheme 20b, reactions between ligand **1** and copper(II) acetate led to two distinct coordination polymers; the description of $[Cu_2(\mu\text{-}OAc)_4(\mathbf{1})]_n$ is detailed below, while the second one can be found in the corresponding publication.[1] $[Cu_2(\mu\text{-}OAc)_4(\mathbf{1})]_n$ crystallizes in the triclinic space group *P*–1, and an ORTEP-style diagram of the asymmetric unit is depicted in Figure 26; Cu–N and Cu–O bond lengths are given in Table 2.

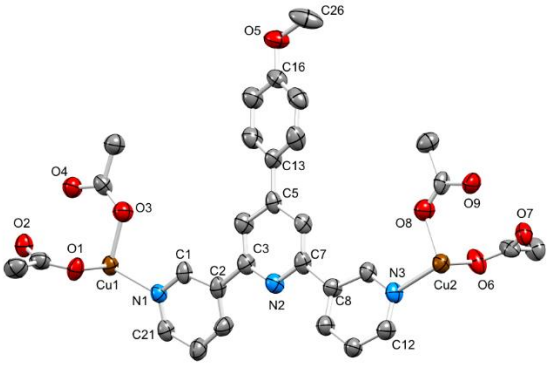

Figure 26. ORTEP-style representation of the asymmetric unit in $[Cu_2(\mu\text{-}OAc)_4(\mathbf{1})]_n$ with ellipsoids plotted at 40% probability level and H atoms omitted.

Table 2. Selected bond lengths in $[Cu_2(\mu\text{-}OAc)_4(\mathbf{1})]_n$.

Cu–O / Å	**Cu–N / Å**
1.964(8), 1.977(8), 1.987(9), 1.987(9)	2.150(9)
1.943(8), 1.984(9), 1.953(9), 1.965(9)	2.156(8)

Ligand **1** adopts conformation **A** (Scheme 21) and $\{Cu_2(\mu\text{-}OAc)_4\}$ paddle-wheel units connect the ligands together; thus $[Cu_2(\mu\text{-}OAc)_4(\mathbf{1})]_n$ results in a zigzag 1D chain (Figure 27).

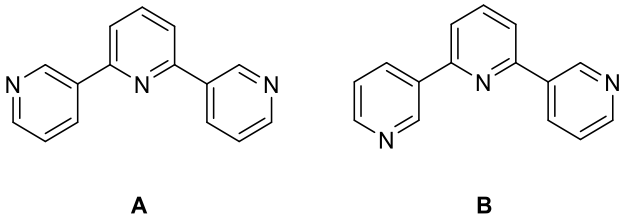

Scheme 21. The limiting planar conformations adopted by the 3,2′:6′,2″-tpy unit in the coordination polymers assembled with copper(II) acetate.

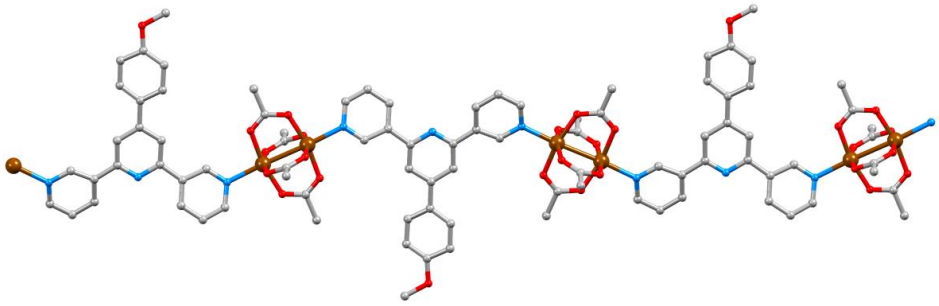

Figure 27. Part of one chain in $[Cu_2(\mu\text{-}OAc)_4(\mathbf{1})]_n$.

The central pyridine ring is non-coordinating. The 3,2′:6′,3″-unit is close to planar with angles between the least squares mean planes of the pyridine rings containing N1/N2 and N2/N3 being 11.1 and 17.5°, respectively. The phenyl ring is twisted only 19.5° out of the plane of the central pyridine ring. The near-planarity is a consequence of the head-to-tail stacking of the 4′-(4-methoxyphenyl)pyridine units in adjacent chains (Figure 28a). The stacked phenyl rings are offset, and although the inter-plane separation of 4.15 Å and centroid…centroid separation of 4.65 Å are larger than is ideal for face-to-face π-stacking,[5] the interaction is augmented by $CH_{MeO}\ldots\pi_{pyridine}$ contacts (CH…centroid = 2.91 Å). Along a 1D polymer chain, ligands **1** lie on alternate sides of the chain and extension of the stacking interactions depicted in Figure 28a leads to the formation of 2D sheets (Figure 28b). Figure 28c illustrates that two of the four acetato ligands of each $\{Cu_2(\mu\text{-}OAc)_4\}$ unit are accommodated in cavities in an adjacent sheet. An important detail with respect to the structures discussed in later sections is that the methoxy group is accommodated within the pocket of a 3,2′:6′,3″-tpy domain in the adjacent chain (Figure 28d). The closest $H_{MeO}\ldots H_{tpy}$ distances are 2.3 and 2.8 Å. The overall efficiency of the packing in $[Cu_2(\mu\text{-}OAc)_4(\mathbf{1})]_n$ is demonstrated by the lack of any solvent of crystallization.

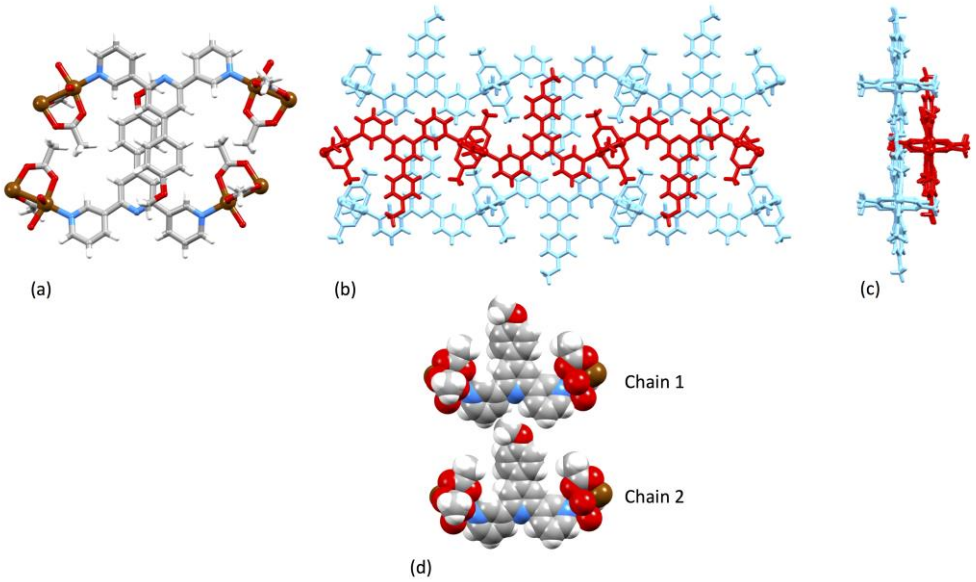

Figure 28. Packing in $[Cu_2(\mu\text{-}OAc)_4(\mathbf{1})]_n$. (**a**) Head-to-tail stacking of 4′-(4-methoxyphenyl)pyridine units in adjacent chains; (**b**) extended stacking interactions lead to the formation of 2D sheets – the red and blue chains lie in adjacent sheets; (**c**) an orthogonal view of the diagram (**b**) showing the accommodation of acetato ligands in cavities in the adjacent sheet; (**d**) accommodation of a methoxy group in one chain in the pocket of a 3,2′:6′,3″-tpy domain in an adjacent chain.

Changes to the crystallization and work-up conditions resulted in the growth of blue crystals of $[Cu_4(\mu_3\text{-}OH)_2(\mu\text{-}OAc)_2(\mu_3\text{-}OAc)_2(AcO\text{-}\kappa O)_2(\mathbf{1})_2]_n{\cdot}2n$MeOH. This 1D coordination polymer crystallizes in the monoclinic space group *C*2/*c* and consists of ligands **1** (in conformation **B** in Scheme 21) linked by tetranuclear copper clusters. The asymmetric unit contains one independent ligand **1** and half of a copper cluster; the second half is generated by inversion. Consequently, the polymer is double-stranded, as shown in Figure 29a. The cluster (Figure 29b) comprises a planar array of four Cu atoms.

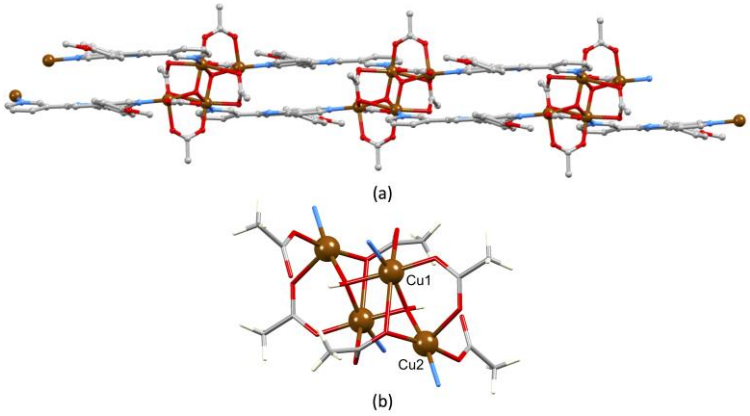

Figure 29. (**a**) Part of one double-stranded chain (solvent omitted); (**b**) the cluster unit in $[Cu_4(\mu_3\text{-}OH)_2(\mu\text{-}OAc)_2(\mu_3\text{-}OAc)_2(AcO\text{-}\kappa O)_2(\mathbf{1})_2]_n{\cdot}2n$MeOH. Crystals that allowed this structural determination were obtained by Giacomo Manfroni. Experimental and crystallographic details can be found in the corresponding publication.[1]

3.2 Reactions of **4**, **5** and **7** with $Cu(OAc)_2{\cdot}H_2O$[1]

Methanol solutions of $Cu(OAc)_2{\cdot}H_2O$ layered over chloroform solutions of **4**, **5** or **7** (Scheme 22) with a 2:1 molar ratio of metal : ligand yielded blue crystals. After selection of single crystals for structure determination, the remaining crystals were analyzed by powder diffraction. PXRD refinements confirmed that the bulk material was representative, in each case, of the analyzed single crystal (Figures 30a–30c).

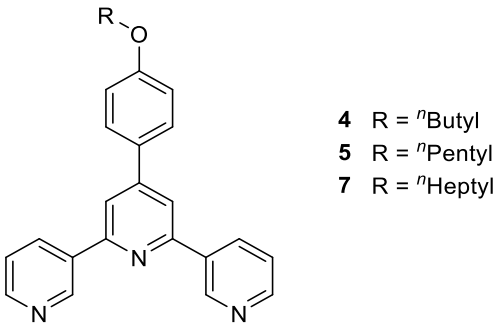

Scheme 22. The structures of ligands **4**, **5** and **7**.

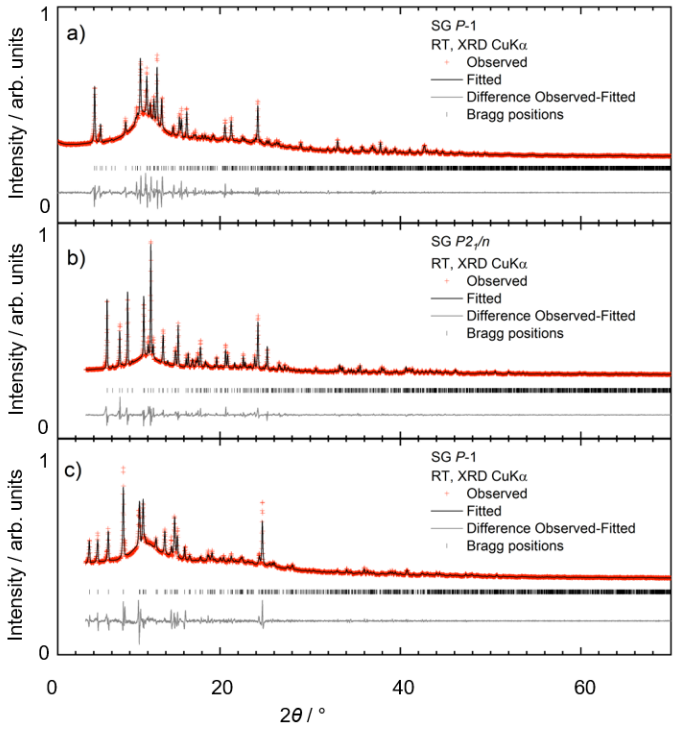

Figure 30. Laboratory X-ray diffraction ($CuK\alpha_1$ radiation) pattern (red crosses) of (**a**) $[Cu_4(\mu\text{-}OAc)_8(\mathbf{4})_2]_n{\cdot}1.25n$MeOH, (**b**) $[Cu_2(\mu\text{-}OAc)_4(\mathbf{5})]_n$ and (**c**) $[Cu_2(\mu\text{-}OAc)_4(\mathbf{7})]_n{\cdot}0.2n$$CHCl_3$ at room temperature. The black line corresponds to the best fit from the profile-matching refinement. Lower vertical marks denote the Bragg peak positions. The bottom line in each plot represents the difference between experimental and calculated points.

The compounds $[Cu_4(\mu\text{-}OAc)_8(\mathbf{4})_2]_n \cdot 1.25n MeOH$ and $[Cu_2(\mu\text{-}OAc)_4(\mathbf{7})]_n \cdot 0.2n CHCl_3$ crystallize in the triclinic space group *P*–1, while $[Cu_2(\mu\text{-}OAc)_4(\mathbf{5})]_n$ crystallizes in the monoclinic space group $P2_1/n$. All three compounds are 1D coordination polymers with the 4′-substituted 3,2′:6′,3″-tpy ligands linking $\{Cu_2(\mu\text{-}OAc)_4\}$ paddle-wheel units. The ORTEP-style diagrams of the asymmetric units of the structures are shown in Figures 31–33.

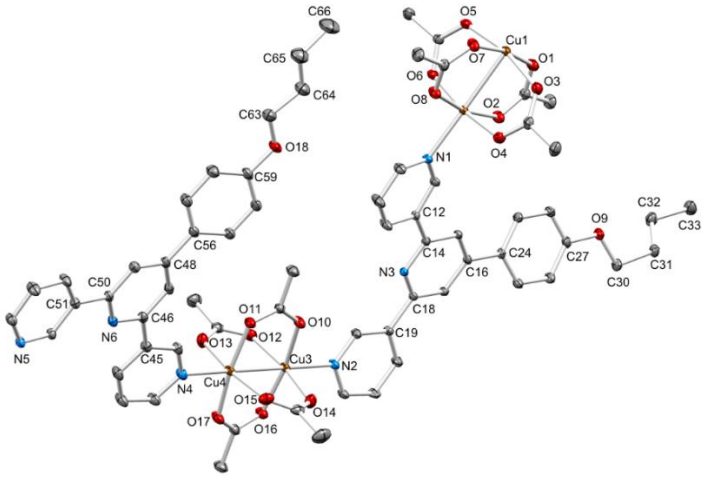

Figure 31. ORTEP-style representation of the asymmetric unit in $[Cu_4(\mu\text{-}OAc)_8(\mathbf{4})_2]_n \cdot 1.25n MeOH$ with ellipsoids plotted at 40% probability level and H atoms and solvent molecules omitted.

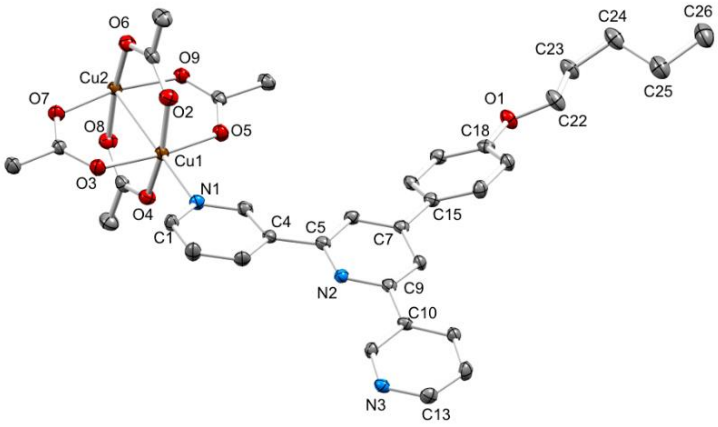

Figure 32. ORTEP-style representation of the asymmetric unit in $[Cu_2(\mu\text{-}OAc)_4(\mathbf{5})]_n$ with ellipsoids plotted at 40% probability level and H atoms omitted.

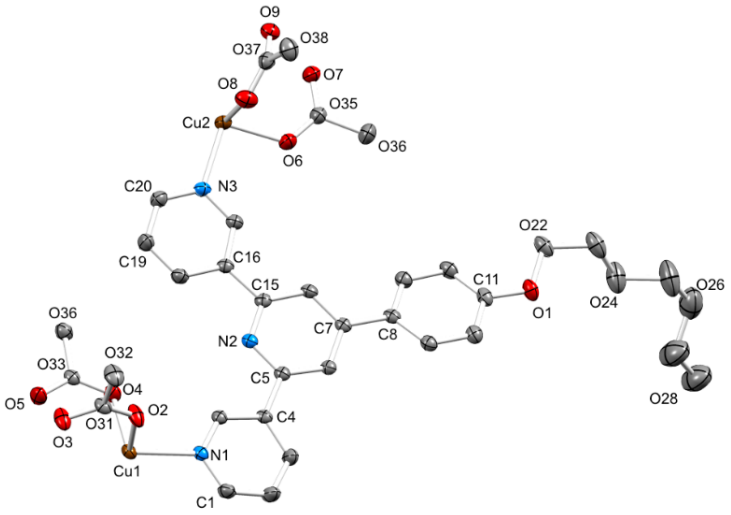

Figure 33. ORTEP-style representation of the asymmetric unit in $[Cu_2(\mu\text{-}OAc)_4(\mathbf{7})]_n \cdot 0.2n CHCl_3$ with ellipsoids plotted at 40% probability level and H atoms and solvent molecules omitted.

In $[Cu_4(\mu\text{-}OAc)_8(\mathbf{4})_2]_n \cdot 1.25n MeOH$, there are two independent ligands and two independent $\{Cu_2(\mu\text{-}OAc)_4\}$ units. In the latter, the Cu–O bond lengths lie in the range 1.9544(15)– 1.9971(15) Å (Table 3, see below), and the geometries of the paddle-wheel units are similar. The crystallographically independent ligands **4** differ in the conformations of the *n*-butyl chains, only one being fully extended. Cu–O and Cu–N bond lengths for all three structures are given in Table 3 and are unexceptional. The alkyloxy chains in $[Cu_2(\mu\text{-}OAc)_4(\mathbf{7})]_n \cdot 0.2n CHCl_3$ and $[Cu_2(\mu\text{-}OAc)_4(\mathbf{5})]_n$ are in partly extended conformations. The 1D coordination polymer chains in $[Cu_4(\mu\text{-}OAc)_8(\mathbf{4})_2]_n \cdot 1.25n MeOH$, $[Cu_2(\mu\text{-}OAc)_4(\mathbf{7})]_n \cdot 0.2n CHCl_3$ and $[Cu_2(\mu\text{-}OAc)_4(\mathbf{5})]_n$ are displayed in Figures 34, 35 and 36, respectively.

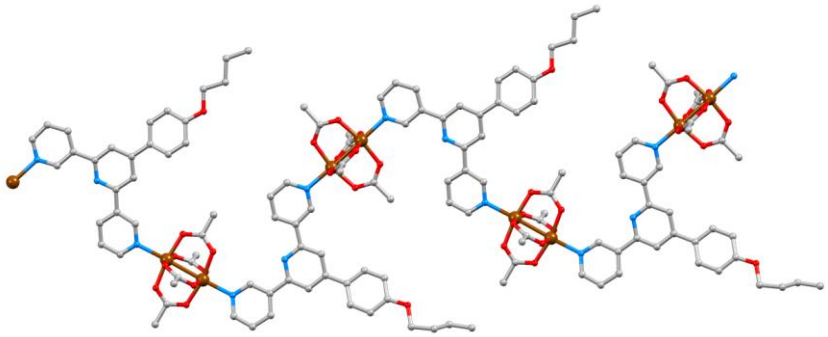

Figure 34. Part of one chain in $[Cu_4(\mu\text{-}OAc)_8(\mathbf{4})_2]_n \cdot 1.25n MeOH$; H atoms and solvent molecules are omitted for clarity.

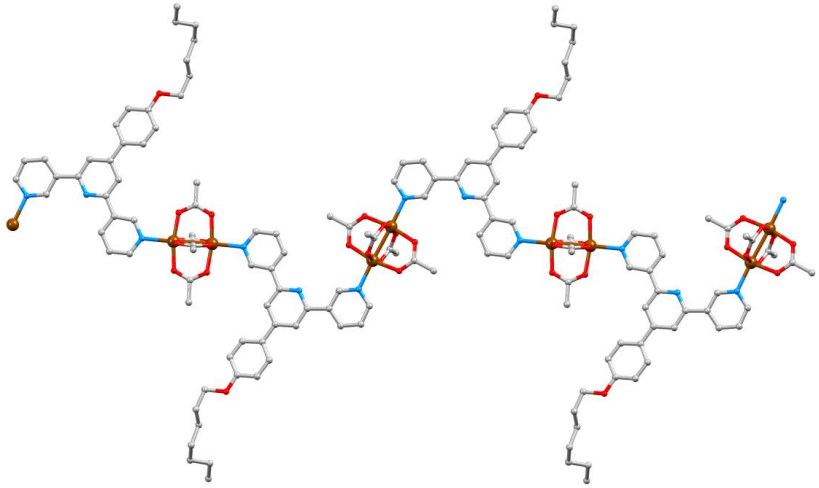

Figure 35. Part of one chain in $[Cu_2(\mu\text{-}OAc)_4(\mathbf{7})]_n \cdot 0.2n CHCl_3$. The *n*-heptyl chain is disordered and only the major occupancy site is shown; H atoms and solvent molecules are omitted for clarity.

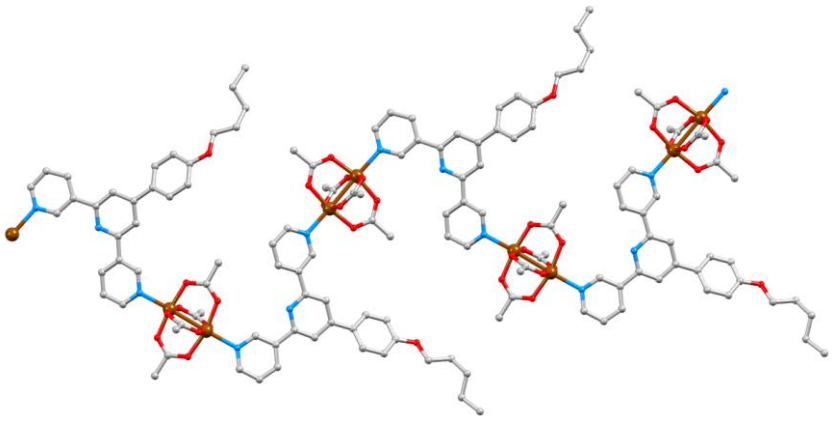

Figure 36. Part of one chain in $[Cu_2(\mu\text{-}OAc)_4(\mathbf{5})]_n$; H atoms are omitted.

Table 3. Selected bond lengths in the $\{Cu_2(\mu\text{-}OAc)_4\}$-containing coordination polymers.

Coordination polymer	Cu–O / Å	Cu–N / Å
$[Cu_4(\mu\text{-}OAc)_8(\mathbf{4})_2]_n \cdot 1.25n MeOH$	1.9659(16), 1.9764(16), 1.9728(15), 1.9777(16), 1.9786(15), 1.9803(15), 1.9753(15), 1.9544(15), 1.9805(16), 1.9671(15), 1.9971(15), 1.9580(15), 1.9745(16), 1.9808(15), 1.9716(16), 1.9839(15)	2.1672(18), 2.1717(17), 2.1875(17), 2.1709(17)
$[Cu_2(\mu\text{-}OAc)_4(\mathbf{5})]_n$	1.964(4), 1.992(4), 1.959(4), 1.988(4), 1.951(4), 1.950(4), 1.992(4), 1.997(4)	2.205(4), 2.161(4)
$[Cu_2(\mu\text{-}OAc)_4(\mathbf{7})]_n \cdot 0.2n CHCl_3$	1.963(2), 1.967(2), 1.976(2), 1.976(2), 1.976(2), 1.974(2), 1.982(2), 1.972(2)	2.163(3), 2.149(3)

In each, the 3,2′:6′,3″-tpy domain exhibits conformation **B** (Scheme 21) in contrast to conformation **A** observed in $[Cu_2(\mu\text{-}OAc)_4(\mathbf{1})]_n$. However, a comparison of Figures 34–36 reveals a further distinction between the coordination modes. When the ligand assumes conformation **B**, the labels *in* and *out* can be used to describe the orientation of each N lone pair with respect to the central pyridine ring of the 3,2′:6′,3″-tpy unit (Scheme 23).

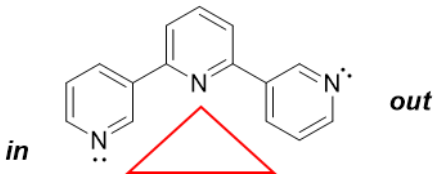

Scheme 23. With the 3,2′:6′,3″-tpy unit in conformation **B** (defined in Scheme 21), the outer nitrogen lone pairs point in or out with respect to the cavity (red triangle) defined by the central pyridine ring.

Considering the axial coordination sites of the paddle-wheel units, it is possible to identify *in/out/in/out…* or *out/out/in/in….* sequences along a 1D-chain, as exemplified in Scheme 24, depending on the way the 3,2′:6′,3″-tpy units are arranged one after the other along the chain.

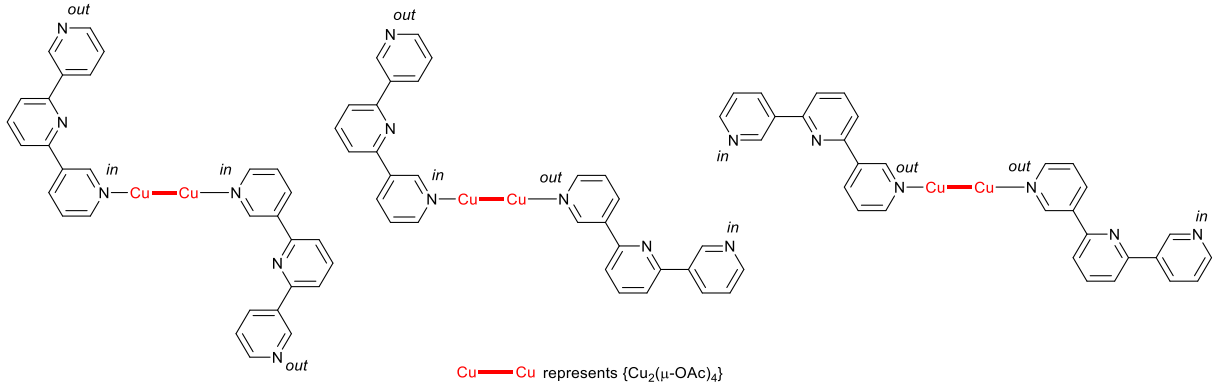

Scheme 24. In conformation **B**, there are three possible arrangements of the 3,2′:6′,3″-tpy units in the axial sites of the $\{Cu_2(\mu\text{-}OAc)_4\}$ motif if the two ligands are coplanar.

Hence, in Figure 34 (working left to right across the diagram), a coordination pattern along the chain as *out/in* for each $\{Cu_2(\mu\text{-}OAc)_4\}$ unit in $[Cu_4(\mu\text{-}OAc)_8(\mathbf{4})_2]_n{\cdot}1.25n$MeOH can be observed. Similarly, in Figure 35, the coordination sequence is *out/in* for each $\{Cu_2(\mu\text{-}OAc)_4\}$ unit in $[Cu_2(\mu\text{-}OAc)_4(\mathbf{5})]_n$. However, in Figure 36, the chain in $[Cu_2(\mu\text{-}OAc)_4(\mathbf{7})]_n{\cdot}0.2n$CHCl$_3$ has the sequence *out/out* for one $\{Cu_2(\mu\text{-}OAc)_4\}$ unit followed by *in/in* for the next, and so on. The structure of the missing member of this series $[Cu_2(\mu\text{-}OAc)_4(\mathbf{6})]_n{\cdot}0.5n$MeOH where **6** = 4′-(4-*n*-hexyloxyphenyl)-3,2′:6′,3″-tpy, has been reported by Zhang and coworkers.[6] As illustrated in Figure 37, the polymer chain possesses the same *in/in/out/out*... arrangement as in the *n*-

heptyloxy analogue $[Cu_2(\mu\text{-}OAc)_4(\mathbf{7})]_n{\cdot}0.2n CHCl_3$. The packing discussion that follows helps to rationalize the dependence of the coordination mode on the length of the alkyloxy tail.

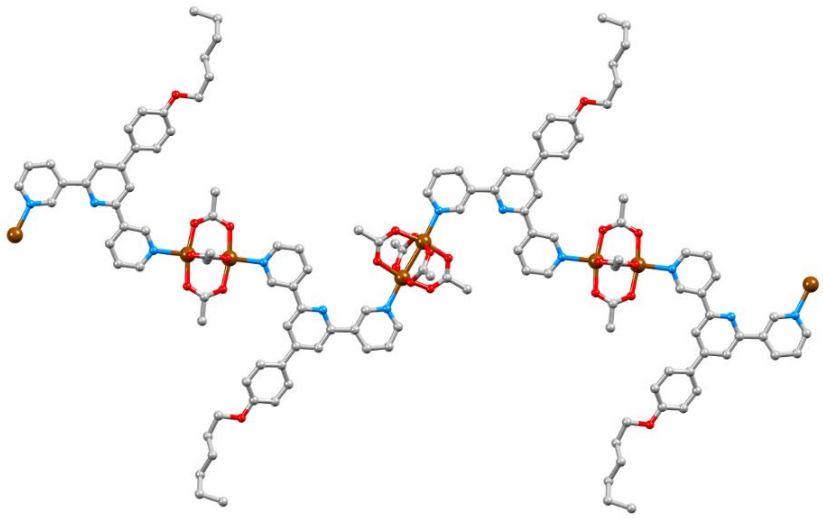

Figure 37. Part of one chain in $[Cu_2(\mu\text{-}OAc)_4(\mathbf{6})]_n{\cdot}0.5$MeOH, drawn using data retrieved from the CSD, refcode SADBIL.[6]

In each of the three structures, the 1D coordination polymer chains pack side-by-side to form 2D sheets. Figure 38 compares the packing of two adjacent chains (each runs left to right in the figure as defined by the blue arrows) in $[Cu_4(\mu\text{-}OAc)_8(\mathbf{4})_2]_n{\cdot}1.25n$MeOH (Figure 38a), $[Cu_2(\mu\text{-}OAc)_4(\mathbf{5})]_n$ (Figure 38b) and $[Cu_2(\mu\text{-}OAc)_4(\mathbf{7})]_n{\cdot}0.2n CHCl_3$ (Figure 38c). At first glance, Figures 38a and 38b indicate similar packing, but closer inspection reveals a translational shift of chain 2 with respect to chain 1 on going from Figure 38a to 38b. While the *n*-butoxy chains are aligned to optimize van der Waals packing interactions (Figures 38a), pairs of *n*-pentyloxy chains are offset and a potential interaction is partially interrupted by an acetato methyl group (Figure 38b). The space-filling representation in Figure 38b shows a centrosymmetric embrace between *n*-pentyloxy and methyl units. With an increase in the length of the alkyloxy tail to *n*-heptyloxy, the packing of polymer chains in a 2D sheet undergoes a significant change (Figure 38c) with van der Waals interactions between partly extended *n*-heptyloxy tails being the dominant in-sheet interactions. The cavity visible in Figure 38c is occupied, not by solvent molecules, but by ligands **7** from the next sheet.

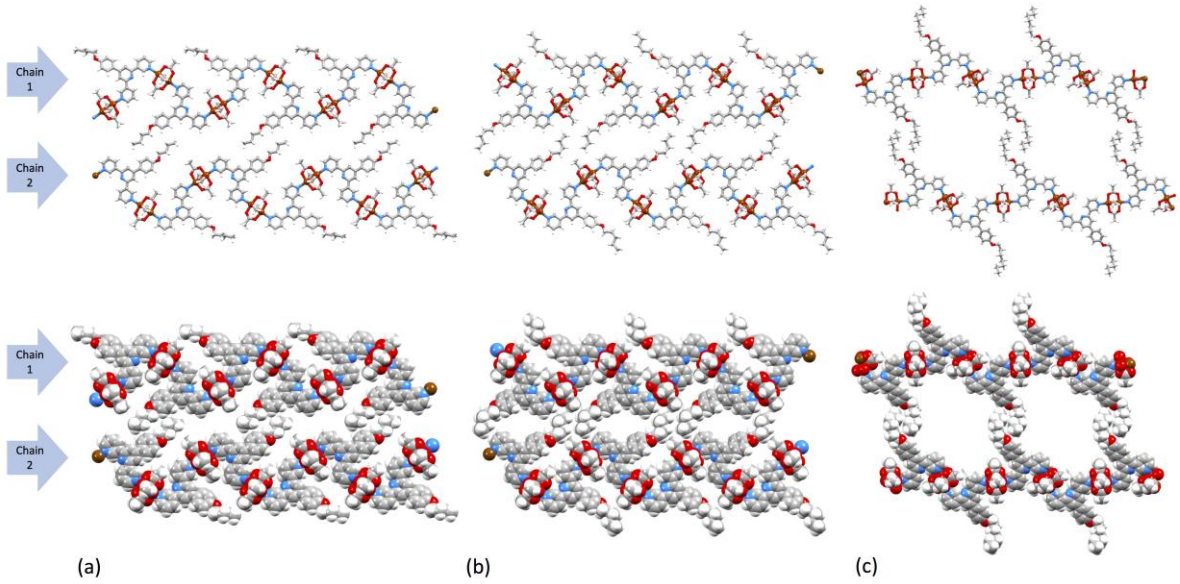

Figure 38. Packing of two adjacent chains (each runs left to right) shown in ball-and-stick and space-filling representations in (**a**) $[Cu_4(\mu\text{-}OAc)_8(\mathbf{4})_2]_n \cdot 1.25n$MeOH, (**b**) $[Cu_2(\mu\text{-}OAc)_4(\mathbf{5})]_n$, and (**c**) $[Cu_2(\mu\text{-}OAc)_4(\mathbf{7})]_n \cdot 0.2n$$CHCl_3$. Solvent molecules in (**a**) and (**c**) are omitted. In (**c**), the *n*-heptyl chain is disordered, and only the major occupancy site is shown.

The differences in inter-sheet packing in $[Cu_4(\mu\text{-}OAc)_8(\mathbf{4})_2]_n \cdot 1.25n$MeOH, $[Cu_2(\mu\text{-}OAc)_4(\mathbf{5})]_n$ and $[Cu_2(\mu\text{-}OAc)_4(\mathbf{7})]_n \cdot 0.2n$$CHCl_3$ are illustrated in Figure 39. In $[Cu_4(\mu\text{-}OAc)_8(\mathbf{4})_2]_n \cdot 1.25n$MeOH, each sheet comprising side-by-side packed 1D-polymer chains is essentially planar, and pairs of adjacent sheets interact through face-to-face π-stacking between centrosymmetric pairs of central pyridine rings of ligands **4** (inter-plane separation = 3.30 Å, centroid…centroid distance = 3.53 Å) (Figure 39a). The packing is similar in $[Cu_2(\mu\text{-}OAc)_4(\mathbf{5})]_n$ (Figure 39b) with an inter-plane separation between the π-stacked pyridine rings of 3.63 Å and a centroid…centroid separation of 4.33 Å. However, Figure 39b shows that the sheets in $[Cu_2(\mu\text{-}OAc)_4(\mathbf{5})]_n$ are ruffled in contrast to the planar sheets in $[Cu_4(\mu\text{-}OAc)_8(\mathbf{4})_2]_n \cdot 1.25n$MeOH. The packing undergoes a more significant change on going to $[Cu_2(\mu\text{-}OAc)_4(\mathbf{7})]_n \cdot 0.2n$$CHCl_3$ (Figure 39c). Face-to-face interactions involve phenyl…pyridine…pyridine π-stacking.

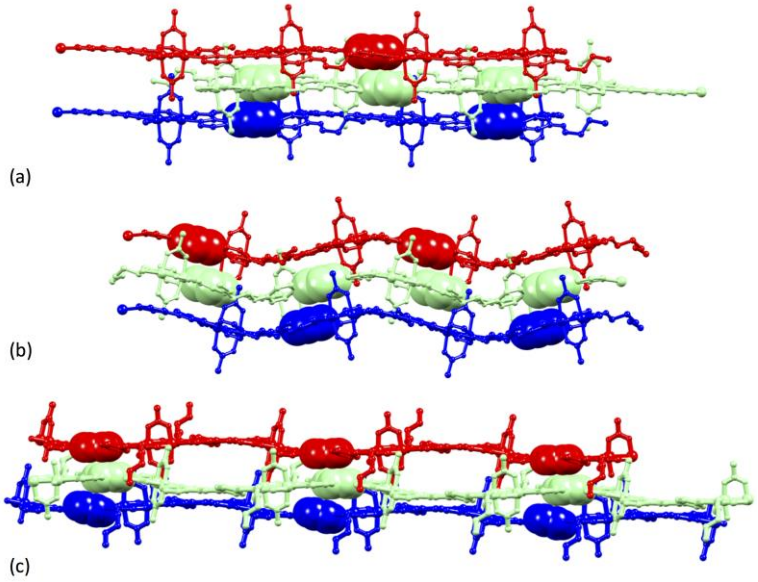

Figure 39. Packing of three adjacent 2D sheets (each comprising 1D polymer chains) in (**a**) $[Cu_4(\mu\text{-}OAc)_8(\mathbf{4})_2]_n \cdot 1.25n$MeOH, (**b**) $[Cu_2(\mu\text{-}OAc)_4(\mathbf{5})]_n$ and (**c**) $[Cu_2(\mu\text{-}OAc)_4(\mathbf{7})]_n \cdot 0.2n$$CHCl_3$. Solvent molecules and H atoms are omitted.

3.3 Reactions of **16**–**20** with $Cu(OAc)_2 \cdot H_2O$[7]

Parts of the work described in this section were carried out in collaboration with Master's candidate Samantha Novak.

Ligands **16**–**20** (Scheme 25), bearing biphenyl groups, were reacted with copper(II) acetate under the crystal growth conditions described in section 2.6 and in the experimental part. The obtained crystals were analyzed via single-crystal XRD, PXRD and FT-IR. These reactions yielded five 1D coordination polymers containing the ubiquitous $\{Cu_2(OAc)_4\}$ paddle-wheel motif, corresponding to the general formulation of $[Cu_2(\mu\text{-}OAc)_4\mathbf{L}]_n$, with **L** = **16**–**20**.

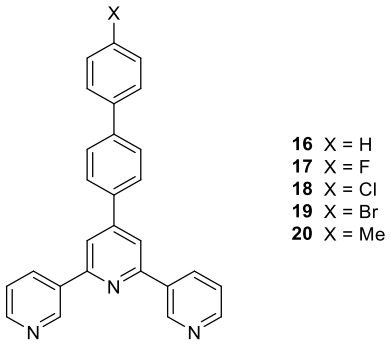

Scheme 25. The structures of ligands **16**–**20**.

Powder X-ray diffraction patterns confirm that the single-crystal structure is representative of the bulk sample in each case (see below). The polymers $[Cu_2(\mu\text{-}OAc)_4(\mathbf{16})]_n$ and $[Cu_2(\mu\text{-}OAc)_4(\mathbf{17})]_n$ crystallize in the monoclinic space group *C*2/*c* with similar cell dimensions (see Sections 6.5.2.5 and 6.5.2.6) and are isostructural (X = H in **16** and X = F in **17**). In contrast, $[Cu_2(\mu\text{-}OAc)_4(\mathbf{18})]_n$, $[Cu_2(\mu\text{-}OAc)_4(\mathbf{19})]_n$ and $[Cu_2(\mu\text{-}OAc)_4(\mathbf{20})]_n{\cdot}n$MeOH crystallize in the triclinic space group *P*–1, again with similar cell dimensions for the series of compounds (X = Cl in **18**, Br in **19** and Me in **20**). Only the coordination compound containing ligand **20** contains lattice solvent. ORTEP-type diagrams of the repeating units in each coordination polymer are displayed in Figures 40 and 41, and selected bond lengths are given in Table 4.

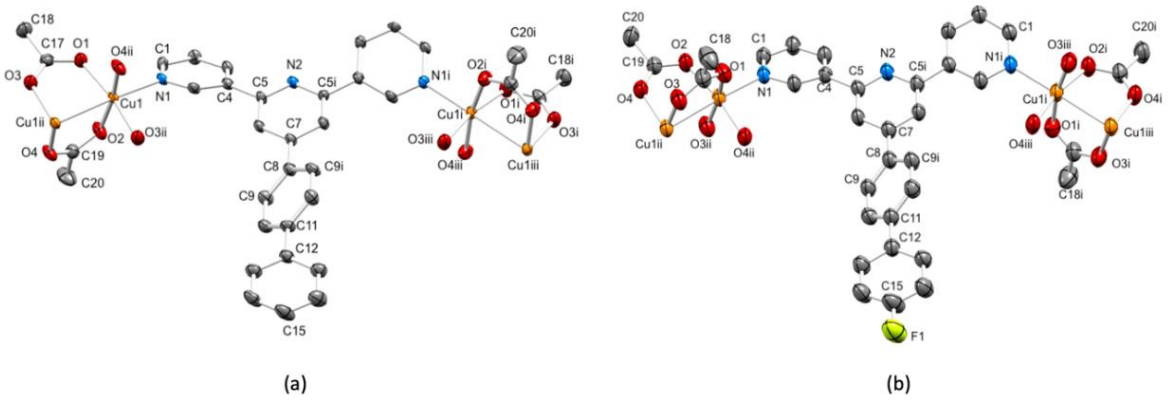

Figure 40. The repeat units (with symmetry-generated atoms) in (**a**) $[Cu_2(\mu\text{-}OAc)_4(\mathbf{16})]_n$ (ellipsoids plotted at 50% probability level; symmetry codes: i = 1–*x*, *y*, $^3/_2$–*z*; ii = $^3/_2$–*x*, $^1/_2$–*y*, 1–*z*; iii = –$^1/_2$+*x*, $^1/_2$–*y*, $^1/_2$+*z*) and (**b**) $[Cu_2(\mu\text{-}OAc)_4(\mathbf{17})]_n$ (ellipsoids plotted at 40% probability level; symmetry codes: i = 1–*x*, *y*, $^1/_2$–*z*; ii = $^1/_2$–*x*, $^3/_2$–*y*, 1–*z*; iii = $^1/_2$+*x*, $^3/_2$–*y*, –$^1/_2$+*z*). H atoms are omitted for clarity.

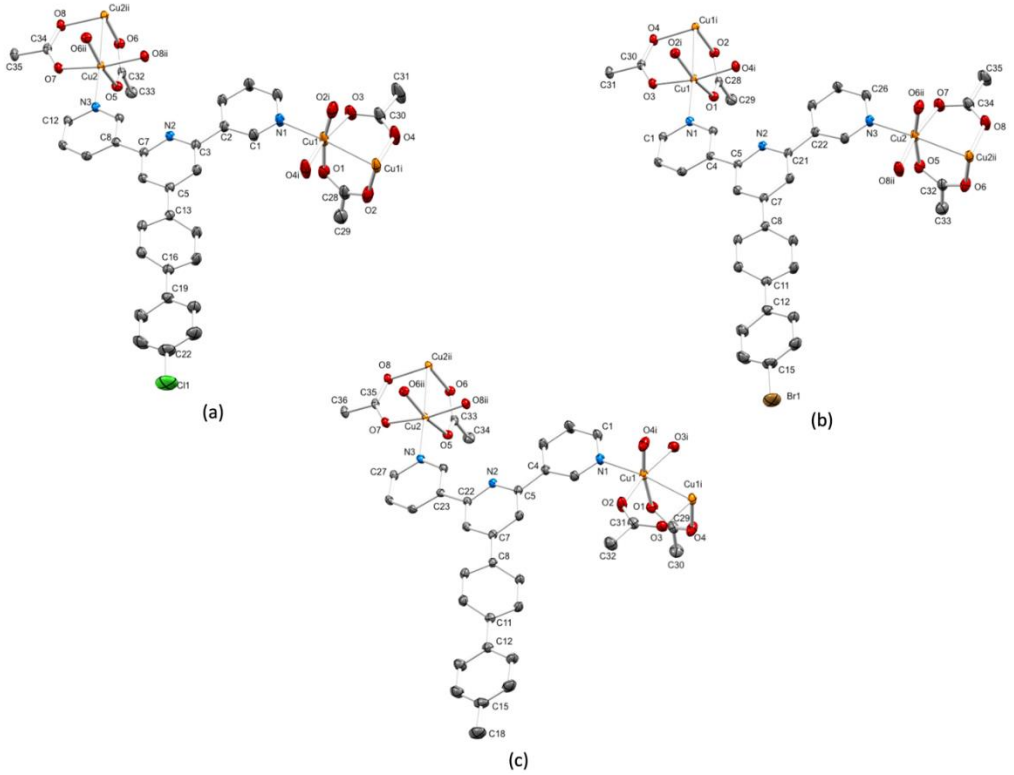

Figure 41. The repeat units (with symmetry-generated atoms) in (**a**) $[Cu_2(\mu\text{-}OAc)_4(\mathbf{18})]_n$ (symmetry codes: i = 1–*x*, 2–*y*, 2–*z*; ii = 2–*x*, 2–*y*, 1–*z*), (**b**) $[Cu_2(\mu\text{-}OAc)_4(\mathbf{19})]_n$ (symmetry codes: i = 2–*x*, 2–*y*, 1–*z*; ii = 1–*x*, 2–*y*, 2–*z*), and (**c**) $[Cu_2(\mu\text{-}OAc)_4(\mathbf{20})]_n{\cdot}n$MeOH (solvent molecule omitted; symmetry codes: i = 1–*x*, 2–*y*, 2–*z*; ii = 2–*x*, 2–*y*, 1–*z*), All ellipsoids are plotted at 40% probability level, and H atoms are omitted for clarity.

Table 4. Selected bond lengths in the copper(II) coordination polymers.

Compound	Cu–O / Å	Cu–N / Å	Cu···Cu / Å
$[Cu_2(\mu\text{-}OAc)_4(\mathbf{16})]_n$	1.954(4), 1.975(4), 1.990(4), 1.961(4)	2.157(4)	2.6051(13)
$[Cu_2(\mu\text{-}OAc)_4(\mathbf{17})]_n$	1.953(5), 1.994(5), 1.979(5), 1.959(5)	2.168(5)	2.6149(17)
$[Cu_2(\mu\text{-}OAc)_4(\mathbf{18})]_n$	1.9760(18), 1.9894(18), 1.9759(18), 1.9789(18), 1.979(3), 1.970(2), 1.966(3), 1.971(3)	2.167(2), 2.151(2)	2.6292(8), 2.6319(7)
$[Cu_2(\mu\text{-}OAc)_4(\mathbf{19})]_n$	1.973(2), 1.983(2), 1.976(2), 1.979(2), 1.981(3), 1.971(2), 1.972(3), 1.974(3)	2.153(2), 2.158(3),	2.6352(8), 2.6235(9)
$[Cu_2(\mu\text{-}OAc)_4(\mathbf{20})]_n{\cdot}n$MeOH	1.9885(15), 1.9787(15), 1.9773(15), 1.9756(15), 1.9887(18), 1.9700(18), 1.9809(19), 1.9644(19)	2.1510(18), 2.1813(19)	2.6551(6), 2.6331(6)

The bond parameters for the {$Cu_2(\mu\text{-}OAc)_4$} units are unexceptional, and the Cu–N bond distances are typical with the exception of Cu1–N1 in [$Cu_2(\mu\text{-}OAc)_4$(**20**)]$_n$·nMeOH. This bond is somewhat elongated (2.1813(19) Å), and this appears to be associated with the presence of a MeOH molecule which is hydrogen-bonded to one acetato bridge (Figure 42) and resides in a pocket close to one Cu–N bond.

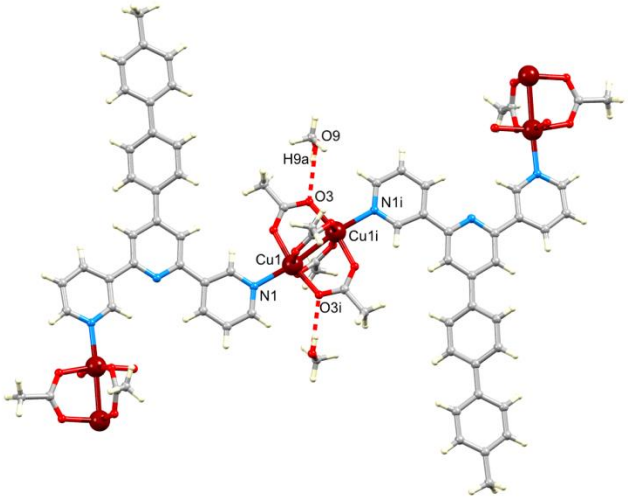

Figure 42. Hydrogen-bonded MeOH molecule in [$Cu_2(\mu\text{-}OAc)_4$(**20**)]$_n$·nMeOH, which resides in a pocket close to the Cu1–N1 bond. Symmetry code: i = 1–x, 2–y, 2–z.

Before describing the crystalline structures in detail, it is immediately apparent that the five coordination polymers fall into two structural classes, which differ in the conformation of the 3,2′:6′,3″-tpy unit. In the two polymers containing ligands **16** (X = H) and **17** (X = F), the 3,2′:6′,3″-tpy unit adopts conformation **A** (Scheme 21); in the remaining three copper complexes (bearing ligands **18**, **19** and **20**) it adopts conformation **B**. This switch in the conformation of the 3,2′:6′,3″-tpy metal-binding domain can be attributed to the increased steric demands of the Cl, Br or Me substituents, compared to H and F substituents. Of course, this change implies a concomitant change in dominant packing interactions, discussed below. This part of the study underlines how the 3,2′:6′,3″-tpy domain can adapt to different steric demands of substituents through its conformational flexibility.

The angles between the planes of pairs of adjacent aromatic rings are compiled in Table 5, and the data reveal that the 3,2′:6′,3″-tpy unit is closer to being planar in [$Cu_2(\mu\text{-}OAc)_4$(**18**)]$_n$, [$Cu_2(\mu\text{-}OAc)_4$(**19**)]$_n$ and [$Cu_2(\mu\text{-}OAc)_4$(**20**)]$_n$·nMeOH than in [$Cu_2(\mu\text{-}OAc)_4$(**16**)]$_n$ and [$Cu_2(\mu\text{-}OAc)_4$(**17**)]$_n$. In addition, the angles between the planes of adjacent rings in the central three-arene ring unit are greater in coordinated ligands **16** and **17** than in **18**–**20**. An inspection of the dominant packing interactions provides an insight into these differences.

Table 5. Angles between ring-planes in the copper(II) coordination polymers.

Coordination polymer	py - py /°	py - phenylene /°	phenylene – phenyl /°
$[Cu_2(\mu\text{-}OAc)_4(\mathbf{16})]_n$	25.1	38.3	41.7
$[Cu_2(\mu\text{-}OAc)_4(\mathbf{17})]_n$	21.1	39.8	38.5
$[Cu_2(\mu\text{-}OAc)_4(\mathbf{18})]_n$	8.0, 4.5	24.0	27.2
$[Cu_2(\mu\text{-}OAc)_4(\mathbf{19})]_n$	8.1, 4.0	22.9	26.5
$[Cu_2(\mu\text{-}OAc)_4(\mathbf{20})]_n \cdot n$MeOH	6.5, 4.0	27.8	28.1

In $[Cu_2(\mu\text{-}OAc)_4(\mathbf{16})]_n$ and $[Cu_2(\mu\text{-}OAc)_4(\mathbf{17})]_n$, ligand conformation **A** leads to a zigzag profile for each 1D-polymer chains and adjacent chains are arranged with the biphenyl unit directed into the V-shaped cavity of a neighbouring 3,2′:6′,2″-tpy unit (Figure 43). This leads to the assembly of 2D-sheets. Interestingly, the arrangement shown in Figure 43 results in short repulsive H…H contacts in $[Cu_2(\mu\text{-}OAc)_4(\mathbf{16})]_n$, while these are replaced by attractive H…F contacts in $[Cu_2(\mu\text{-}OAc)_4(\mathbf{17})]_n$. This observation suggests that these contacts are not important in supporting the assembly, and this is reminiscent of the isostructural nature of $[Cu_2(\mu\text{-}OAc)_4(\mathbf{L})]_n$ and $[Cu_2(\mu\text{-}OAc)_4(\mathbf{L1})]_n$ in which **L** is 4′-([1,1′-biphenyl]-4-yl)-4,2′:6′,4″-terpyridine and **L1** is 4′-(2′,3′,4′,5′,6′-pentafluoro[1,1′-biphenyl]-4-yl)-4,2′:6′,4″-terpyridine.[8] The X…C separations for the X…H–C contacts in the bifurcated interactions in Figure 43 are 3.11 Å for X = H and 3.16 Å for X = F. The dominant packing forces in $[Cu_2(\mu\text{-}OAc)_4(\mathbf{16})]_n$ and $[Cu_2(\mu\text{-}OAc)_4(\mathbf{17})]_n$ are the head-to-tail π-stacking between pairs of [1,1′-biphenyl]pyridine units displayed in Figure 44. Each pair of arene rings adopts an offset arrangement optimal for a π-π interaction.[5] For the pyridine…phenyl interaction in $[Cu_2(\mu\text{-}OAc)_4(\mathbf{16})]_n$, the centroid…centroid distance is 3.97 Å, and the angle between the ring planes is 3.4°; the corresponding parameters in $[Cu_2(\mu\text{-}OAc)_4(\mathbf{17})]_n$ are 3.97 Å and 1.4°. For the centrosymmetric pair of phenylene rings, the distances between the ring planes and between their centroids are 3.75 and 3.97 Å, respectively, in $[Cu_2(\mu\text{-}OAc)_4(\mathbf{16})]_n$, and 3.71 and 3.96 Å in $[Cu_2(\mu\text{-}OAc)_4(\mathbf{17})]_n$. The cavities in each sheet visible in Figure 44 are occupied by $\{Cu_2(\mu\text{-}OAc)_4\}$ carboxylate groups from an adjacent layer which protrude above and below each sheet.

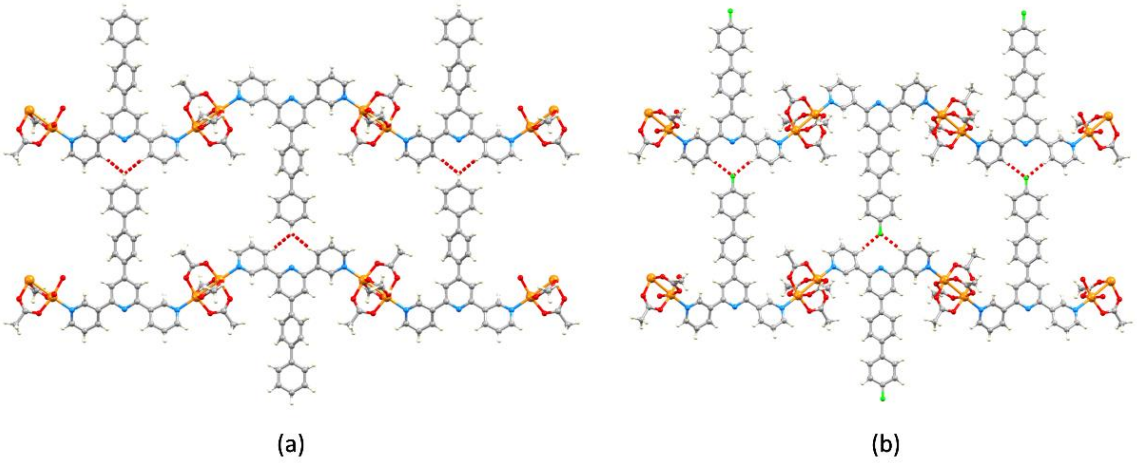

Figure 43. Packing of two adjacent polymer chains in (**a**) $[Cu_2(\mu\text{-}OAc)_4(\mathbf{16})]_n$ and (**b**) $[Cu_2(\mu\text{-}OAc)_4(\mathbf{17})]$ within one 2D-sheet (see text). The hashed red lines highlight short H...H contacts in $[Cu_2(\mu\text{-}OAc)_4(\mathbf{16})]_n$ and complementary short H...F contacts in $[Cu_2(\mu\text{-}OAc)_4(\mathbf{17})]_n$.

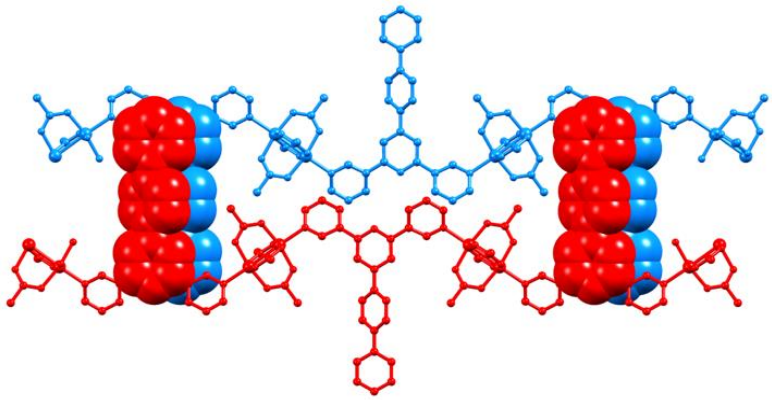

Figure 44. Head-to-tail π-stacking between pairs of [1,1′-biphenyl]pyridine units in adjacent sheets in $[Cu_2(\mu\text{-}OAc)_4(\mathbf{16})]_n$. The same motif is present in $[Cu_2(\mu\text{-}OAc)_4(\mathbf{17})]_n$. H atoms are omitted for clarity.

In each of $[Cu_2(\mu\text{-}OAc)_4(\mathbf{18})]_n$, $[Cu_2(\mu\text{-}OAc)_4(\mathbf{19})]_n$ and $[Cu_2(\mu\text{-}OAc)_4(\mathbf{20})]_n n$MeOH, the 3,2′:6′,3″-tpy adopts conformation **B** (Scheme 21), and the coordination arrangement at the paddle-wheel units (defined in Scheme 24) is *in/in/out/out*. Figure 45a illustrates part of one coordination polymer chain in $[Cu_2(\mu\text{-}OAc)_4(\mathbf{18})]_n$, and this structure is replicated in $[Cu_2(\mu\text{-}OAc)_4(\mathbf{19})]_n$ and $[Cu_2(\mu\text{-}OAc)_4(\mathbf{20})]_n \cdot n$MeOH, as are the packing motifs described below. Figure 45b illustrates the interdigitation of 1D-polymer chains to produce 2D-sheets. The profile of the chain in Figure 45a contrasts with the zigzag nature of the polymers in Figure 44, and packing interactions are necessarily different. The near planarity of the 3,2′:6′,3″-tpy unit (Table 5) reflects the involvement of this domain in crystal packing. Centrosymmetric pairs of pyridine rings containing N3 (N3 and N3^{iii}, symmetry code iii = 1–*x*, 1–*y*, 1–*z*) stack with an interplane distance of 3.34 Å and inter-centroid separation of 3.68 Å.

The pyridine ring with N1 engages in a face-to-face contact with the phenyl ring containing C22^{iv} (symmetry code iv = 1+*x*, 1+*y*, *z*) with a centroid...centroid distance of 3.94 Å and an angle between the ring planes of 11.1°. In addition, the pyridine ring containing N1 also sits over a biphenyl unit, thereby extending the stack of arene rings. The projection shown in Figure 45c illustrates how the layers comprise domains of π-stacked arene rings and columns of {$Cu_2(\mu\text{-}OAc)_4$} paddle-wheel units.

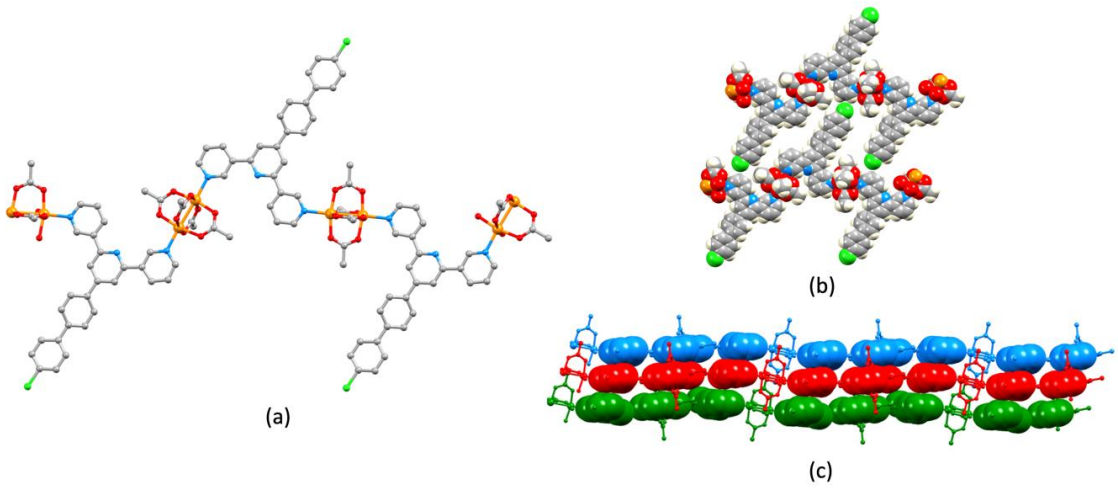

Figure 45. (**a**) Part of one polymer chain in $[Cu_2(\mu\text{-}OAc)_4(\mathbf{18})]_n$; (**b**) interdigitation of chains generates a 2D-sheet; (**c**) stacking of three adjacent sheets involves both pyridine and biphenyl rings.

To ensure that the single-crystal structures were representative of the bulk materials, powder X-ray diffraction patterns were determined for crystals remaining in the crystallization tubes after single crystals had been selected. As anticipated, the refinements (Figure 46) confirmed that the bulk materials of all the compounds were representative of the analyzed single crystals. Each peak in the experimental plots has a corresponding peak in the fitted spectra, and the differences in the intensities can be rationalized in terms of differences in the preferred orientations. Only $[Cu_2(\mu\text{-}OAc)_4(\mathbf{17})]_n$ shows minor impurities (ca. 10%). A comparison of Figure 46b with PXRD patterns for the precursors **17** and $Cu(OAc)_2{\cdot}H_2O$ did not reveal matching peaks; hence, the bulk sample contains a minor component which is probably a second coordination complex.

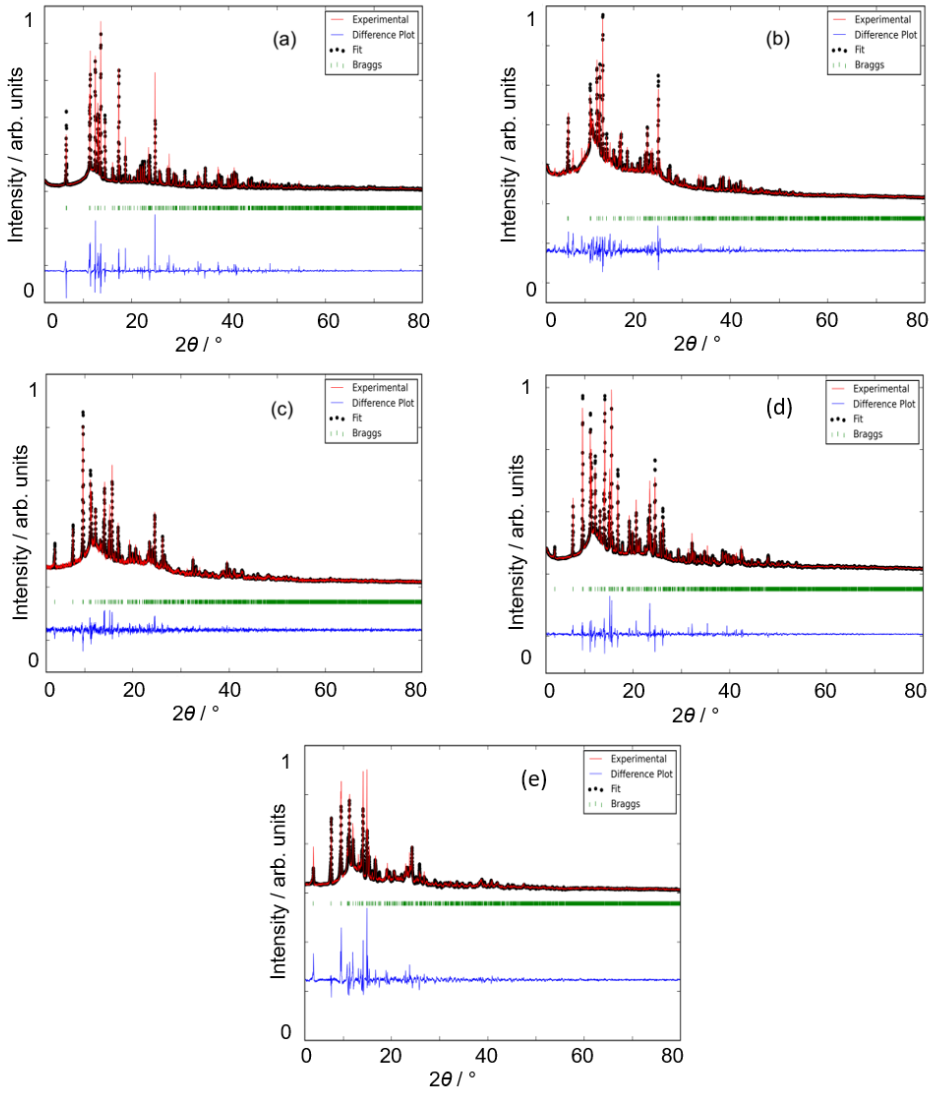

Figure 46. Powder X-ray diffraction (Cu*Kα* radiation) pattern (red lines) of the bulk crystalline material of (**a**) [Cu$_2$(μ-OAc)$_4$(**16**)]$_n$, (**b**) [Cu$_2$(μ-OAc)$_4$(**17**)]$_n$ (showing minor impurities, ca. 10%), (**c**) [Cu$_2$(μ-OAc)$_4$(**18**)]$_n$, (**d**) [Cu$_2$(μ-OAc)$_4$(**19**)]$_n$ and (**e**) [Cu$_2$(μ-OAc)$_4$(**20**)]$_n$·*n*MeOH with fitting to the predicted pattern from the single-crystal determination. The black dots correspond to the best fits from the Rietveld refinements. Green vertical marks show the Bragg peak positions. The blue line in each plot shows the difference between experimental and calculated points.

3.4 Conclusions

The coordination chemistry of nine 3,2′:6′,3″-terpyridine ligands with copper(II) acetate has been explored, yielding ten 1D-coordination polymers. In the case of ligand **1**, bearing the methoxy substituent, both the formation of [Cu$_2$(μ-OAc)$_4$(**1**)]$_n$ and [Cu$_4$(μ$_3$-OH)$_2$(μ-OAc)$_2$(μ$_3$-OAc)$_2$(AcO-κ*O*)$_2$(**1**)$_2$]$_n$·2*n*MeOH was observed. The former is a single-stranded 1D-polymer containing the {Cu$_2$(μ-OAc)$_4$} paddle-wheel motif, and the latter is assembled from centrosymmetric tetranuclear clusters linking pairs of ligands **1,** thus resulting in a double-stranded 1D-polymer. The preparative scale reaction of **1** with Cu(OAc)$_2$·H$_2$O immediately yielded [Cu$_2$(μ-OAc)$_4$(**1**)]$_n$. However, crystal-growth experiments carried out by layering over

a period of several months yielded predominantly the double-stranded 1D-coordination polymer. The systematic investigation of the effect of the chain length on the assembly of coordination networks was carried out involving ligands **4**, **5** and **7**, in addition to **1**. All the resulting compounds consist of single-stranded 1D-coordination polymers containing paddle-wheel units, and in each case, only the outer pyridine rings of the terpyridines coordinate to copper(II). However, the conformation of the 3,2′:6′,3″-tpy unit responds to changes in the length of the alkyloxy tails, and thus the dominant interactions in the packing in the crystal lattice change. In $[Cu_2(\mu\text{-}OAc)_4(\mathbf{1})]_n$, the 3,2′:6′,3″-tpy unit in **1** adopts conformation **A** (Scheme 21), resulting in zigzag 1D chains, while in the polymers containing ligands **4**, **5** and **7**, the 3,2′:6′,3″-tpy unit assumes conformation **B**, and van der Waals packing forces between alkyloxy chains become important, complementing the π-stacking interactions between phenyl… pyridine and pyridine…pyridine rings.

The second series of homologous ligands investigated consists of compounds **16**–**20**, bearing 1,1′-biphenyl groups with the 4′-substituents H, F, Cl, Br or Me. In this study, the steric demands of the substituents proved to be the key factor in causing a switch in the conformation of the 3,2′:6′,3″-tpy unit. Single-crystal structures of five 1D-coordination polymers with L = **16**–**20** and general formulation of $[Cu_2(\mu\text{-}OAc)_4\mathbf{L}]_n$ were determined. Compounds with X = H and X = F are isostructural zigzag polymers, where chains engage in π-stacking interactions between [1,1′-biphenyl]pyridine units and 1D-chains nest into one another to give 2D-sheets. The increased steric hindrance of the Cl, Br, or Me substituent induces a switch in the conformation of the 3,2′:6′,3″-tpy metal-binding domain from **A** to **B** and a concomitant change in dominant packing interactions to py–py and py–biphenyl face-to-face π-stacking. Both studies underline how the 3,2′:6′,3″-tpy domain can adapt to ligand modifications through its conformational flexibility while retaining the same connectivity.

References

1. D. Rocco, G. Manfroni, A. Prescimone, Y. M. Klein, D. J. Gawryluk, E. C. Constable and C. E. Housecroft, *Polymers*, **2020**, 12, 318.
2. A. Alsalme, M. Ghazzali, R. A. Khan, K. Al-Farhan and J. Reedijk, *Polyhedron*, **2014**, 75, 64-67.
3. S. Bette, R. K. Kremer, G. Eggert, C. C. Tang and R. E. Dinnebier, *Dalton Trans.*, **2017**, 46, 14847-14858.
4. J. R. Ferraro and W. R. Walker, *Inorg. Chem.*, **1965**, 4, 1382-1386.
5. C. Janiak, *J. Chem. Soc., Dalton Trans.*, **2000**, 3885-3896.
6. L. Li, Y. Z. Zhang, C. Yang, E. Liu, J. A. Golen and G. Zhang, *Polyhedron*, **2016**, 105, 115-122.
7. D. Rocco, S. Novak, A. Prescimone, E. C. Constable and C. E. Housecroft, *Chemistry*, **2021**, 3, 182-198.
8. E. C. Constable, C. E. Housecroft, S. Vujovic, J. A. Zampese, A. Crochet and S. R. Batten, *CrystEngComm*, **2013**, 15, 10068-10078.

Chapter 4 Coordination polymers with cobalt(II) thiocyanate

The second metal salt extensively employed in this work is cobalt(II) thiocyanate. While copper(II) acetate leads to a linear directionality, cobalt(II) tends to act as a potential 4-connecting node. It usually adopts octahedral coordination with two sites occupied by thiocyanato ligands, typically in *trans*-positions to one another, thus yielding 2D-assemblies with a topology of (4,4) nets when combined with ditopic ligands. However, as mentioned in the introduction (Chapter 1), the unexpected assembly of 3D architectures has been observed in a few cases, as well as the formation of 1D-chains, mainly due to solvent molecules reducing the connectivity of the cobalt(II) center or to the thiocyanate ligands assuming a N,S-bridging mode between metal ions. When (4,4) nets are formed, differences in the packing, in the interactions and in other parameters can be identified, even when the topology is the same. Most of the ligands presented in Chapter 2 were successfully crystallized in combination with cobalt(II) thiocyanate, thus allowing a systematic investigation in which one parameter is varied at one time, highlighting the versatility within 2D (4,4) networks.

4.1 Reactions of **1** with $Co(NCS)_2$[1]

A series of four crystallization experiments was carried out between **1** (Scheme 26) and $Co(NCS)_2$. In each test tube, a MeOH solution of the cobalt(II) salt was layered over a $CHCl_3$ solution of the tpy ligand. In experiments 1 and 2, identical conditions were chosen, and a molar ratio of $Co(NCS)_2$: **1** of 1:1; in experiments 3 and 4, molar ratios of $Co(NCS)_2$: **1** of 2:1 and 1:2 were used, respectively. Experiments 1, 3 and 4 were initially set up to monitor whether the different metal-to-ligand molar ratios would impact the outcome of the crystallization reaction. Experiment 1 yielded block-like single crystals of the one-dimensional polymer $[Co(\mathbf{1})(NCS)_2(MeOH)_2]_n$, where two molecules of methanol coordinate on the cobalt center. Although this result is not unprecedented,[2, 3] it is not the most predictable one. Cell dimension checks were carried out on a number of crystals from the same batch, and then PXRD was measured (Figure 48a); they all showed consistent results, as did the cell checks on crystals that grew in experiments 3 and 4, and the PXRD measured on the bulk sample from experiment 3 (Figure 48c), also consistent with the formation of the 1D polymer. Insufficient material was obtained from experiment 4, and a powder pattern could not be taken. In experiment 2 however, three different crystal types were found in different zones in the test tube. Blocks of $[Co(\mathbf{1})(NCS)_2(MeOH)_2]_n$ grew on the walls of the tube. Pink block-like crystals of $[Co(\mathbf{1})_2(NCS)_2]_n{\cdot}2.2n CHCl_3$ formed at the bottom of the tube and it is relevant that initially, the $CHCl_3$ solution of the ligand comprised the lower layer in the crystallization tube. Higher up on the walls of the tube, pink plates of $[Co(\mathbf{1})_2(NCS)_2]_n{\cdot}3n MeOH$ were obtained, consistent with growth in a zone where the concentration of methanol exceeds that of chloroform. As described below, $[Co(\mathbf{1})_2(NCS)_2]_n{\cdot}2.2n CHCl_3$ and $[Co(\mathbf{1})_2(NCS)_2]_n{\cdot}3n MeOH$ are

pseudopolymorphs, differing only in the inclusion of different amounts of different lattice solvent. However, the Rietveld refinement of the diffraction pattern (Figure 48b) confirmed that the bulk sample from experiment 2 was $[Co(\mathbf{1})(NCS)_2(MeOH)_2]_n$ once again, and only very small amounts of other species are observed, which could not be assigned to $[Co(\mathbf{1})_2(NCS)_2]_n{\cdot}3n$MeOH or $[Co(\mathbf{1})_2(NCS)_2]_n{\cdot}2.2n$CHCl$_3$.

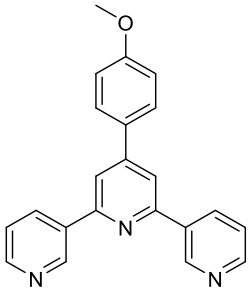

1

Scheme 26. Structure of ligand **1**.

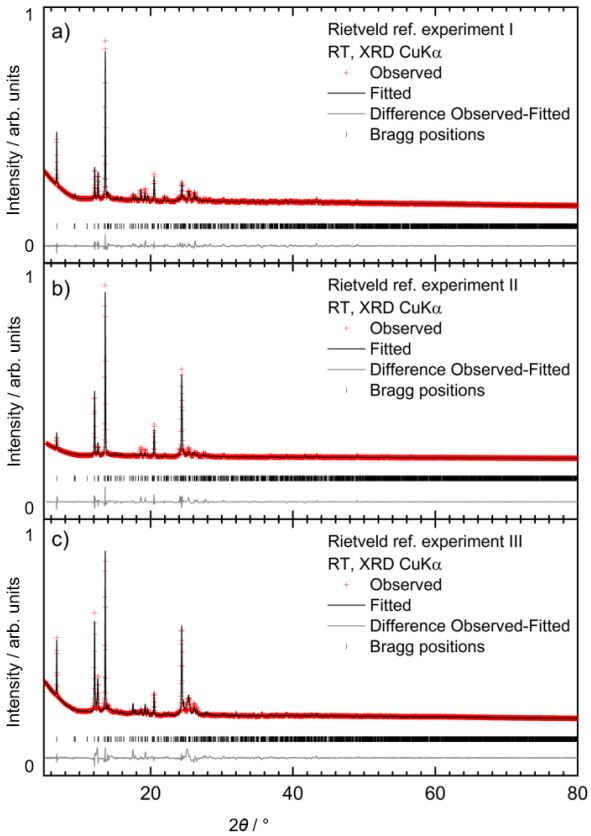

Figure 48. Laboratory X-ray diffraction (Cu$K\alpha_1$ radiation) pattern (red crosses) for (**a**) experiment 1, (**b**) experiment 2, and (**c**) experiment 3 at room temperature. The black line corresponds to the best fit from the Rietveld refinement analysis. Lower vertical marks denote the Bragg peak positions. The bottom grey line represents the difference between experimental and calculated points.

An additional reaction was carried out between **1** and $Co(NCS)_2$ on a preparative scale, with 1:1 metal-to-ligand molar ratio. Solid $Co(NCS)_2$ was added to a colorless solution of **1** in MeOH (see experimental section 6.4.3.1); immediate precipitation of a pale pink solid was observed, and the mixture was left stirring at room temperature for 15 h. The product was separated by centrifugation, followed by decantation of the supernatant liquid. The solid was washed with MeOH and with $CHCl_3$ to remove unreacted reagents and was then dried under vacuum. Although the product showed low crystallinity, peaks at low values of 2θ (in particular that at $2\theta = 6.82°$) in the PXRD pattern were consistent with $[Co(\mathbf{1})(NCS)_2(MeOH)_2]_n$. Summarizing, three coordination polymers were identified from the reactions of **1** with $Co(NCS)_2$: the main product, being the one-dimensional $[Co(\mathbf{1})(NCS)_2(MeOH)_2]_n$, and the two pseudopolymorphic two-dimensional $[Co(\mathbf{1})_2(NCS)_2]_n{\cdot}3n$MeOH and $[Co(\mathbf{1})_2(NCS)_2]_n{\cdot}2.2n$$CHCl_3$. It is noteworthy that experiment 2 yielded crystals of each type of polymer only after a longer crystallization time, compared to experiments 1, 3 and 4. This investigation highlights the interplay between thermodynamic and kinetic products from crystallization processes, and illustrates once again that the full understanding of the assembly algorithms of metallo-coordination polymers involving terpyridine ligands has not been reached.[4]

The structures are now described, starting with the main product $[Co(\mathbf{1})(NCS)_2(MeOH)_2]_n$, which crystallizes in the orthorhombic space group *Pbca*. The structure is closely related to that of $[Co\mathbf{L3}(NCS)_2(MeOH)_2]_n$ in which ligand **L3** is 4′-(*N*,*N*-dimethylaminophenyl)-3,2′:6′,3″-terpyridine (CSD refcode ZAWLUG, space group *Pbca*, a = 14.3014(8), b = 14.3112(7), c = 26.2091(12) Å).[3] The cobalt(II) centre in $[Co(\mathbf{1})(NCS)_2(MeOH)_2]_n$ is six-coordinate with *trans*-arrangements of pairs of ligands (Figure 49 shows an ORTEP-style representation). Ligand **1** coordinates through the outer pyridine rings to two different cobalt atoms, and the repeating unit propagates into a 1D-coordination polymer chain. Important bond distances and angles are given in the caption of Figure 49 and are unexceptional. The outer pyridine rings of ligand **1** are oriented so as to provide a building block similar to conformation **A** in Scheme 27. Rotation about the C–C inter-ring bonds would allow ligand **1** to assume an infinite number of rotational conformations. The 3,2′:6′,3″-tpy unit is twisted with angles of 35.2 and 21.2° between the least squares planes of the rings containing N1/N2 and N2/N3, respectively. In contrast, the central 4′-phenylpyridine unit deviates less from planarity with an angle of only 12.4° between the ring planes. This is associated with packing interactions between the chains (see below).

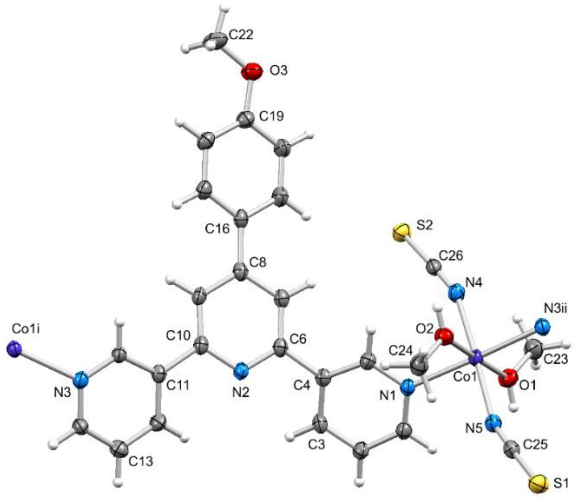

Figure 49. The repeating unit in the 1D chain of $[Co(\mathbf{1})(NCS)_2(MeOH)_2]_n$ with symmetry-generated atoms; ellipsoids are plotted at a 40% probability level. Symmetry codes: i = $^1/_2-x$, $1-y$, $-^1/_2+z$; ii = $^1/_2-x$, $1-y$, $^1/_2+z$. Selected bond distances and angles: Co1–O2 = 2.109(4), Co1–O1 = 2.084(4), Co1–N1 2.184(4), Co1–N5 = 2.073(4), Co1–N4 2.084(4), Co1–N3^{ii} = 2.196(4), O3–C19 = 1.362(6), O3–C22 = 1.422(7), O2–C24 1.439(7), O1–C23 = 1.417(7) Å; N5–Co1–N4 = 178.00(16), N1–Co1–N3^{ii} = 176.33(17), O1–Co1–O2 = 179.14(14), C24–O2–Co1 = 128.9(3), C23–O1–Co1 = 127.7(3), C19–O3–C22 = 117.7(4)°.

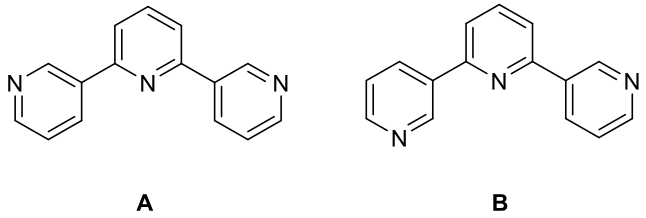

Scheme 27. The limiting planar conformations adopted by the 3,2′:6′,2″-tpy unit in the coordination polymers assembled with cobalt(II) thiocyanate.

The 1D-chains in $[Co(\mathbf{1})(NCS)_2(MeOH)_2]_n$ approximately follow the crystallographic *c*-axis. Figure 50 shows a view down the *b*-axis: adjacent chains associate through head-to-tail stacking of 4-methoxyphenylpyridine units. Although the inter-plane angle between stacked rings is 12.4°, the centroid$_{pyridine}$…plane$_{phenyl}$ and centroid…centroid distances are 3.25 and 3.64 Å, respectively, making these efficient interactions.[5] As Figure 50 shows, every other ligand in a given chain is oriented to opposite sides of the chain, and face-to-face π-stacking occurs between alternate pairs of ligands in adjacent chains, as depicted for the blue/green and yellow/purple coloured stacked units in Figure 51. The alternate stacking of the purple-coloured chain in Figure 51 with red- and orange-coloured chains leads to extended π-stacking, which interlocks the chains through the lattice.

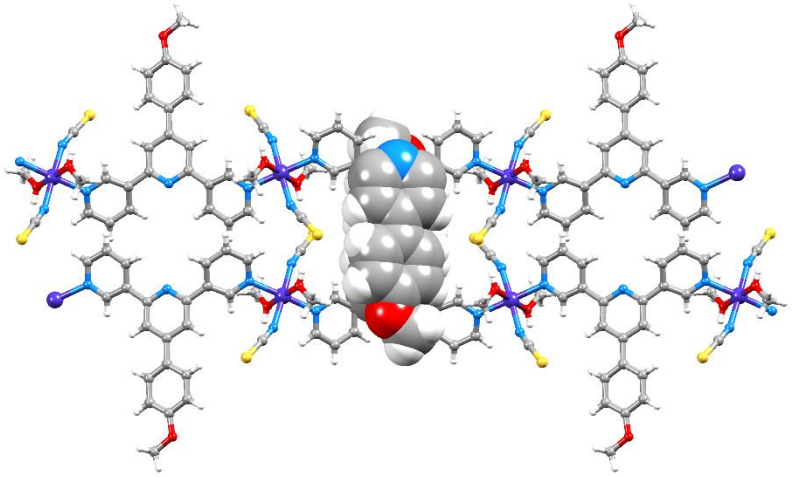

Figure 50. Packing of chains in $[Co(\mathbf{1})(NCS)_2(MeOH)_2]_n$. View down the *b*-axis showing head-to-tail π-stacking between 4-methoxyphenylpyridine units of pairs of ligands **1**.

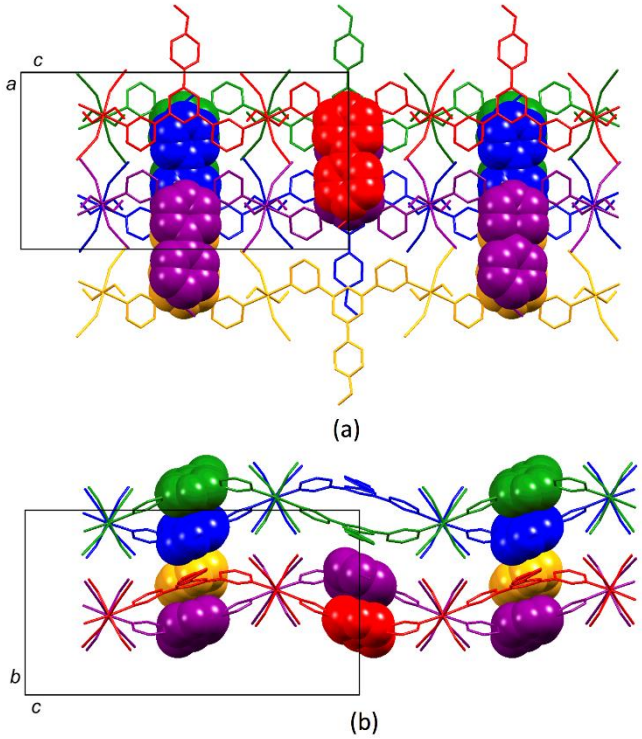

Figure 51. Packing of chains in $[Co(\mathbf{1})(NCS)_2(MeOH)_2]_n$. π-Stacking between 4-methoxyphenylpyridine units in four adjacent chains (each depicted in a different colour) is shown, (**a**) with the same part of the lattice viewed down the *b*-axis and (**b**) the *a*-axis.

$[Co(\mathbf{1})_2(NCS)_2]_n{\cdot}3n$MeOH and $[Co(\mathbf{1})_2(NCS)_2]_n{\cdot}2.2n$$CHCl_3$ crystallize in the monoclinic space groups $P2_1/n$ and $P2_1/c$, respectively and are pseudopolymorphs. Only the structure of $[Co(\mathbf{1})_2(NCS)_2]_n{\cdot}3n$MeOH is described in detail since the networks in the two structures are essentially the same. Figure 52 shows an overlay of the repeating units (with symmetry-generated atoms) in the two structures and the angles between the ring-planes given in the caption confirm the similarity of the structures. The six-coordinated cobalt atom lies on an inversion center.

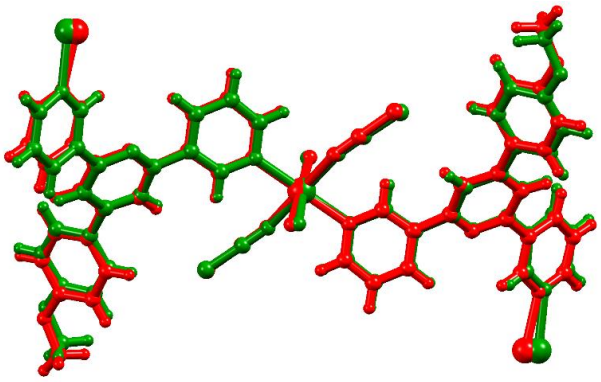

Figure 52. Overlay of the repeating units (with symmetry-generated atoms) in $[Co(\mathbf{1})_2(NCS)_2]_n \cdot 3n$MeOH (shown in red) and $[Co(\mathbf{1})_2(NCS)_2]_n \cdot 2.2n$CHCl$_3$ (in green). The solvent molecules are omitted. The angles between the planes of connected pyridine rings are 32.9 and 32.0° in $[Co(\mathbf{1})_2(NCS)_2]_n \cdot 3n$MeOH and 33.8 and 38.2° in $[Co(\mathbf{1})_2(NCS)_2]_n \cdot 2.2n$CHCl$_3$; the angle between the rings in the 4-methoxyphenylpyridine unit is 50.8° in $[Co(\mathbf{1})_2(NCS)_2]_n \cdot 3n$MeOH and 50.5° in $[Co(\mathbf{1})_2(NCS)_2]_n \cdot 2.2n$CHCl$_3$.

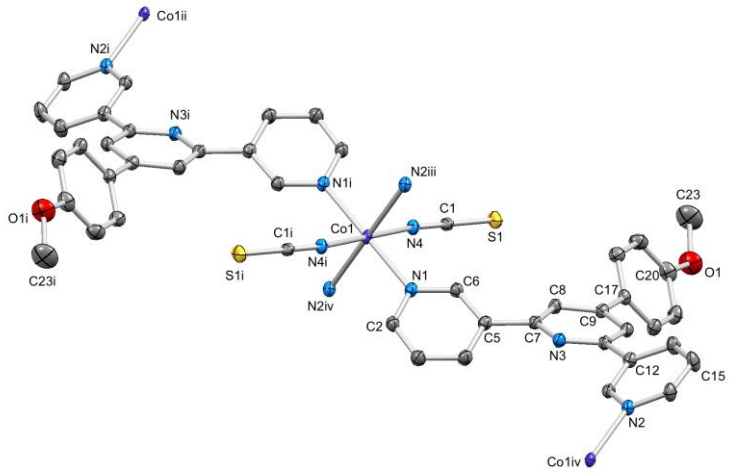

Figure 53. The repeating unit in the 2D network in $[Co(\mathbf{1})_2(NCS)_2]_n \cdot 3n$MeOH with symmetry-generated atoms; ellipsoids are plotted at a 40% probability level, and H atoms are omitted for clarity. Symmetry codes: i = $1-x$, $1-y$, $-z$; ii = $^1/_2-x$, $^1/_2+y$, $-^1/_2-z$; iii = $-^1/_2+x$, $^1/_2-y$, $-^1/_2+z$; iv = $^3/_2-x$, $^1/_2+y$, $^1/_2-z$. Selected bond distances: Co1–N4 2.0884(16), Co1–N2^{iii} = 2.2096(16), Co1–N1 = 2.1714(16), O1–C20 = 1.366(3), O1–C23 = 1.425(4) Å; C20–O1–C23 = 117.3(2)°, by symmetry, N1–Co1–N1^i = N2^{iii}–Co1–N2^{iv} = N4–Co1–N4^i =180.0°.

The repeating unit in $[Co(\mathbf{1})_2(NCS)_2]_n \cdot 3n$MeOH (with symmetry-generated atoms) is displayed in ORTEP-style in Figure 53, and the figure caption gives important bond parameters. All bond distances are as expected. The coordination mode of **1** mimics that in $[Co(\mathbf{1})(NCS)_2(MeOH)_2]_n$. Atom Co1 acts as a 4-connecting node and $[Co(\mathbf{1})_2(NCS)_2]_n \cdot 3n$MeOH is a (4,4) net with the organic ligands acting as linkers (Figure 54). In contrast to the conformation **A** adopted by **1** in $[Co(\mathbf{1})(NCS)_2(MeOH)_2]_n$, ligand **1** in $[Co(\mathbf{1})_2(NCS)_2]_n \cdot 3n$MeOH adopts a conformation similar to mode **B** in Scheme 27. The twist angles between the pyridine rings with N1/N3 and N3/N2 are 32.9 and 32.0°, and that between the rings in the 4-methoxyphenylpyridine unit is 50.8°.

The latter is significantly greater than the corresponding angle in $[Co(\mathbf{1})(NCS)_2(MeOH)_2]_n$ (12.4°) and reflects the fact that in the 2D-net, ligand **1** does not engage in π-stacking interactions. As Figure 55 shows, the 4-methoxyphenyl units protrude from the upper and lower sides of each (4,4) net and are accommodated in pockets in an adjacent sheet. The closest C–H…π contact between sheets is 3.55 Å (CH_{Me}…$centroid_{pyridine}$) which is rather long to be significant.[6]

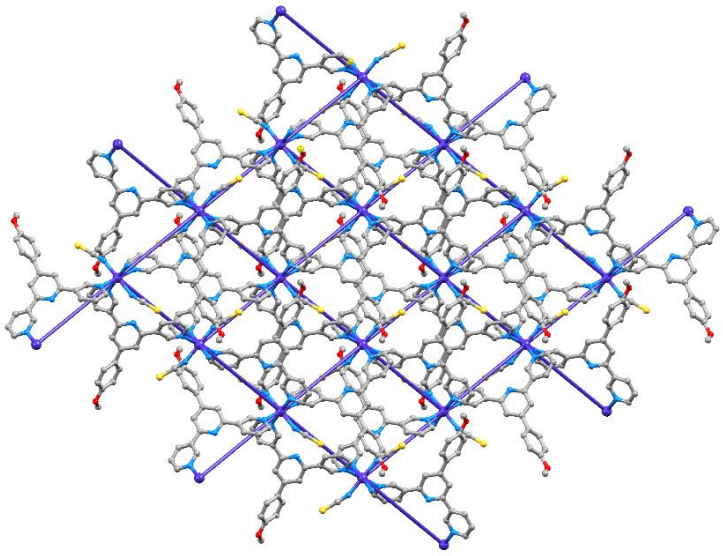

Figure 54. Part of one 2D network of $[Co(\mathbf{1})_2(NCS)_2]_n{\cdot}3n$MeOH showing the 4-connecting Co nodes in the (4,4) net.

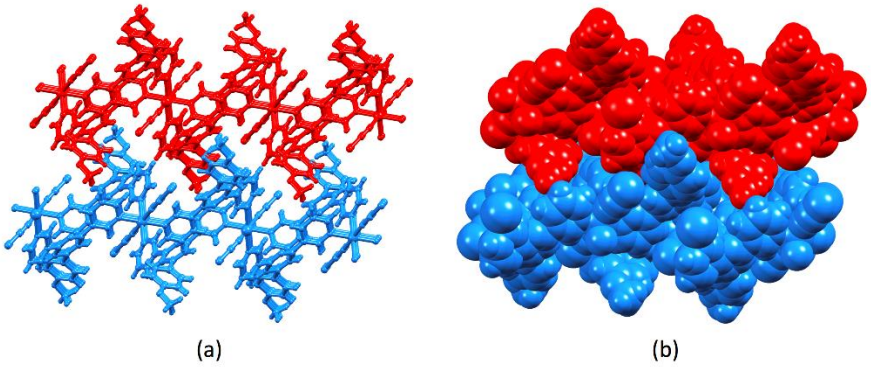

Figure 55. Parts of two adjacent 2D sheets in $[Co(\mathbf{1})_2(NCS)_2]_n{\cdot}3n$MeOH: (**a**) ball-and-stick and (**b**) space-filling representations.

In $[Co(\mathbf{1})_2(NCS)_2]_n{\cdot}3n$MeOH, SQUEEZE had to be applied to the solvent region, whereas in $[Co(\mathbf{1})_2(NCS)_2]_n{\cdot}2.2n$$CHCl_3$ the solvent was modelled as one $CHCl_3$ molecule disordered around an inversion center and one $CHCl_3$ disordered over two orientations. The $CHCl_3$ molecules occupy sites both within and between the 2D sheets, and presumably, MeOH molecules in $[Co(\mathbf{1})_2(NCS)_2]_n{\cdot}3n$MeOH occupy analogous sites.

4.2 Reactions of **2**–**6** with $Co(NCS)_2$[7]

Methanol solutions of cobalt(II) thiocyanate were layered over chloroform solutions of ligands **2**–**6** (Scheme 28) under the same room temperature conditions. For each ligand, the reactions were carried out in duplicates, using different metal : ligand molar ratios. However, only the conditions that led to crystal structures are reported and discussed here. Where multiple experiments with the same ligand originated X-ray quality crystals, cell checks were carried out on single crystals from the different batches. Irrespective of the initial ratios, the crystalline products were coordination networks in which the Co : ligand ratio was 1 : 2.

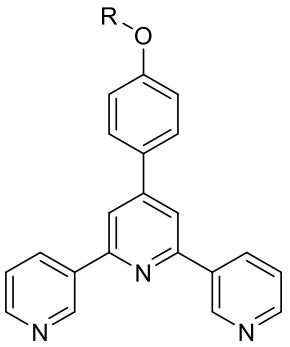

2 R = Ethyl
3 R = ^{n}Propyl
4 R = ^{n}Butyl
5 R = ^{n}Pentyl
6 R = ^{n}Hexyl

Scheme 28. The structures of ligands **2**–**6**.

Thus, the structures of five 2D-coordination networks have been determined with the formulae of $[Co(\mathbf{2})_2(NCS)_2]_n{\cdot}0.6n CHCl_3$, $[Co(\mathbf{3})_2(NCS)_2]_n{\cdot}4n CHCl_3{\cdot}0.25n H_2O$, $[Co(\mathbf{4})_2(NCS)_2]_n{\cdot}4n CHCl_3$, $[Co_2(\mathbf{5})_4(NCS)_4]_n$ and $[Co(\mathbf{6})_2(NCS)_2]_n$. After selection of single crystals for X-ray diffraction, the bulk materials were analyzed by solid-state IR spectroscopy and PXRD, according to the general procedure. The fingerprint regions of the IR spectra of single crystals or microcrystalline samples are all similar, consistent with analogous coordination behaviours of ligand **2**–**6** in the coordination assemblies; Figure 56 depicts the IR spectrum of $[Co(\mathbf{2})_2(NCS)_2]_n{\cdot}0.6n CHCl_3$, which is representative of the whole series, while the remaining spectra can be found in the Supporting Information of the corresponding publication.

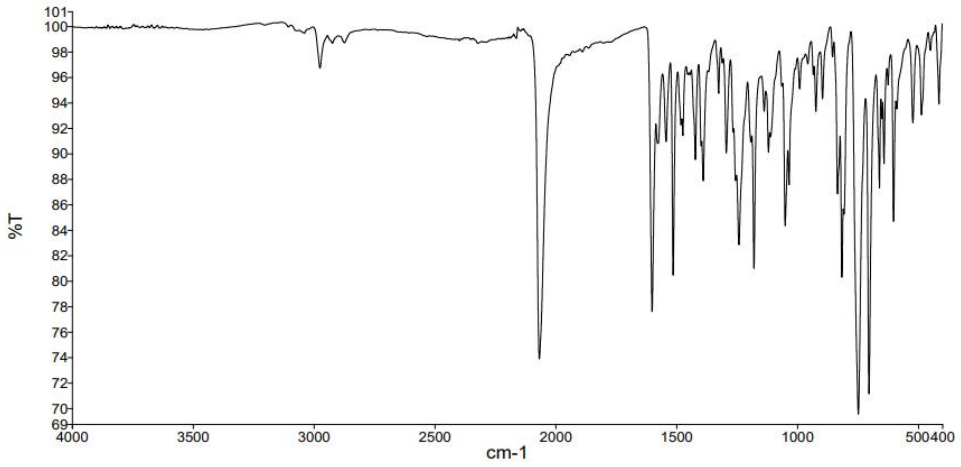

Figure 56. Solid-state IR spectrum of single crystals of $[Co(\mathbf{2})_2(NCS)_2]_n \cdot 0.6n CHCl_3$.

Each spectrum exhibits bands in the region between 2820 and 3100 cm^{-1} characteristic of the aromatic C–H stretches of the ligands. A strong absorption band in each IR spectrum at 2068 cm^{-1} (compounds with **2** and **3**), 2062 cm^{-1} (with **4**), 2074 cm^{-1} (with **5**), and 2072 cm^{-1} (with **6**) arises from the coordinated thiocyanate ligands.

Powder patterns were fitted to those predicted from the single-crystal structures (Figure 57), and the obtained data confirmed that selected crystals were representative of the bulk samples for each of the coordination networks discussed below.

$[Co(\mathbf{2})_2(NCS)_2]_n \cdot 0.6n CHCl_3$, $[Co(\mathbf{3})_2(NCS)_2]_n \cdot 4n CHCl_3 \cdot 0.25n H_2O$ and $[Co(\mathbf{4})_2(NCS)_2]_n \cdot 4n CHCl_3$ crystallize in the tetragonal space groups $P4/ncc$ or $P\text{–}42_1c$ (see Sections 6.5.3.4 – 6.5.3.6), while $[Co_2(\mathbf{5})_4(NCS)_4]_n$ and $[Co(\mathbf{6})_2(NCS)_2]_n$ crystallize in the monoclinic space groups $P2_1/n$ and $P2_1/c$, respectively. ORTEP diagrams of the asymmetric units with symmetry-generated atoms are displayed in Figures 58–62.

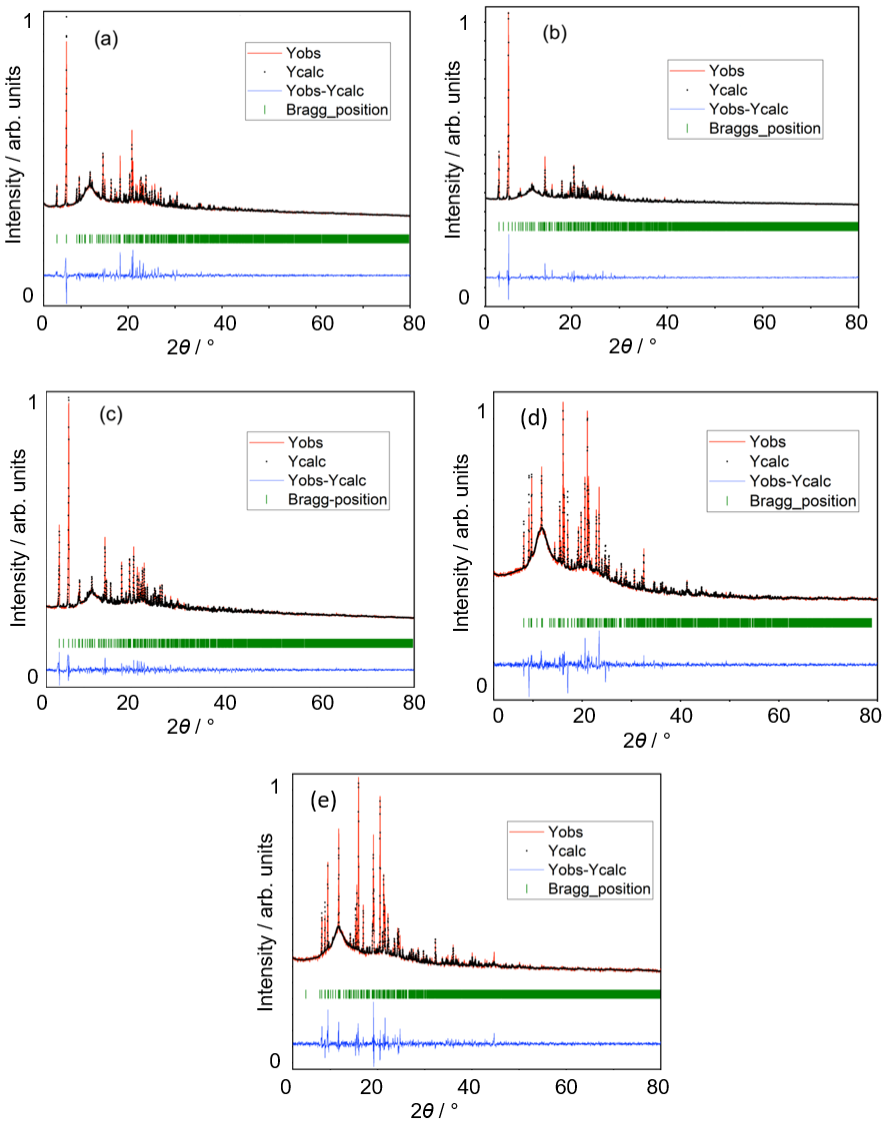

Figure 57. Laboratory powder X-ray diffraction (Cu$K\alpha$ radiation, 298 K) pattern (red trace) of each bulk crystalline material from which single crystals of (**a**) [Co(**2**)$_2$(NCS)$_2$]$_n$·0.6nCHCl$_3$, (**b**) [Co(**3**)$_2$(NCS)$_2$]$_n$·4nCHCl$_3$·0.25nH$_2$O, (**c**) [Co(**4**)$_2$(NCS)$_2$]$_n$·4nCHCl$_3$, (**d**) [Co$_2$(**5**)$_4$(NCS)$_4$]$_n$, and (**e**) [Co(**6**)$_2$(NCS)$_2$]$_n$ were selected. Each experimental powder pattern was fitted to the predicted pattern from the single-crystal determination. The black dots correspond to the best fit from the profile-matching refinement. Vertical green marks denote the Bragg peak positions. The blue line in each plot represents the difference between experimental and calculated points.

Each compound possesses a (4,4) net with Co centres as 4-connecting nodes. For the assemblies containing **2**, **3** and **4**, the (4,4) net comprises two geometrically different rhombi, and the nets pack in an ABAB... manner with cone-like arrangements of *n*-alkyloxyphenyl groups being accommodated in a similar unit in an adjacent net. An increase in the *n*-alkyloxy chain length has two consequences: there is a change in the conformation of the 3,2′:6′,3″-tpy metal-binding domain, and the (4,4) net comprises identical rhombi. Similarities and differences between the assemblies with ligands **2**–**6** and the previously reported [Co(**1**)$_2$(NCS)$_2$]$_n$·3nMeOH and [Co(**1**)$_2$(NCS)$_2$]$_n$·2.2nCHCl$_3$ are discussed below. The results demonstrate the effects of

combining a variable chain length in the 4′-(4-*n*-alkyloxyphenyl) substituents and a conformationally flexible 3,2′:6′,3″-tpy metal-binding domain. For this reason, the five structures are discussed together, with the focus on differences that correlate to the lengthening of the *n*-alkyloxy chain. In all the compounds, each cobalt atom is in an octahedral environment with a *trans*-arrangement of thiocyanato ligands and is bonded to one pyridine ring of four different 3,2′:6′,3″-tpy units. This is a familiar motif that persists through many of the structures described in this chapter. In each of $[Co(\mathbf{3})_2(NCS)_2]_n{\cdot}4n CHCl_3{\cdot}0.25nH_2O$, $[Co(\mathbf{4})_2(NCS)_2]_n{\cdot}4n CHCl_3$, and $[Co(\mathbf{6})_2(NCS)_2]_n$ there are two independent ligands. Bond parameters for the coordination spheres of the cobalt atoms are compared in Table 6 and are unexceptional. In keeping with expectations, the central pyridine ring of each ligand is non-coordinated.

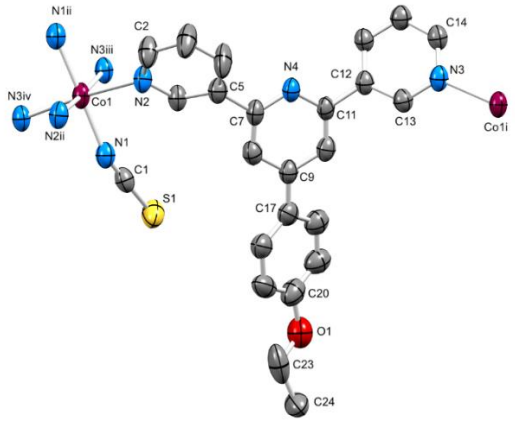

Figure 58. ORTEP representation of the asymmetric unit in $[Co(\mathbf{2})_2(NCS)_2]_n{\cdot}0.6nCHCl_3$ with symmetry-generated atoms. Ellipsoids are plotted at a 40% probability level, and H atoms are omitted. Symmetry codes: i = $^1/_2{-}y$, x, z; ii = $1{-}y$, $1{-}x$, $^3/_2{-}z$; iii = y, $^1/_2{-}x$, z; iv = $^1/_2{+}x$, $1{-}y$, $^3/_2{-}z$.

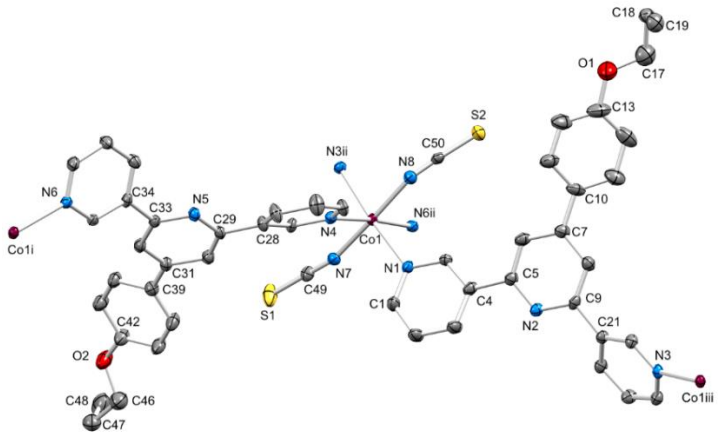

Figure 59. ORTEP representation of the asymmetric unit in $[Co(\mathbf{3})_2(NCS)_2]_n{\cdot}4nCHCl_3{\cdot}0.25nH_2O$ with symmetry-generated atoms. Ellipsoids are plotted at a 40% probability level, and H atoms are omitted. Symmetry codes: i = $^1/_2{-}x$, $-^1/_2{+}y$, $^1/_2{-}z$; ii = $^1/_2{-}x$, $^1/_2{+}y$, $^1/_2{-}z$; iii = $^1/_2{+}x$, $^3/_2{-}y$, $^1/_2{-}z$.

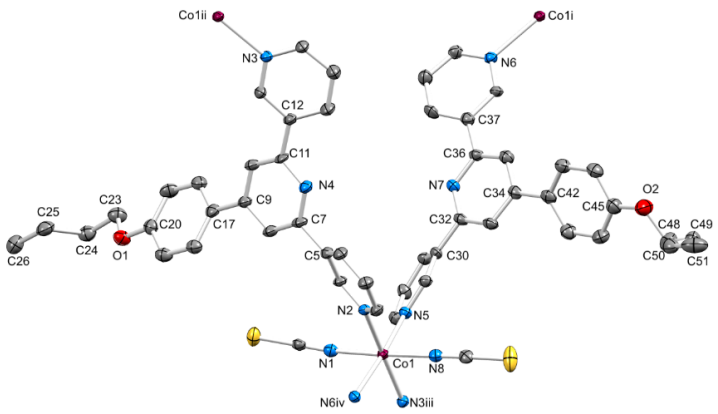

Figure 60. ORTEP representation of the asymmetric unit in $[Co(\mathbf{4})_2(NCS)_2]_n{\cdot}4n CHCl_3$ with symmetry-generated atoms. Ellipsoids are plotted at a 40% probability level, and H atoms are omitted. Symmetry codes: i = $^3/_2{-}x$, $^1/_2{+}y$, $^1/_2{-}z$; ii = $-^1/_2{+}x$, $^1/_2{-}y$, $^1/_2{-}z$; iii = $^1/_2{+}x$, $^1/_2{-}y$, $^1/_2{-}z$; iv = $^3/_2{-}x$, $-^1/_2{+}y$, $^1/_2{-}z$.

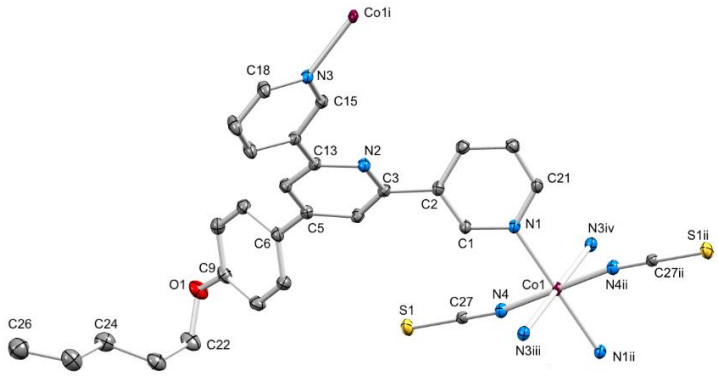

Figure 61. ORTEP representation of the asymmetric unit in $[Co_2(\mathbf{5})_4(NCS)_4]_n$ with symmetry-generated atoms. Ellipsoids are plotted at a 40% probability level, and H atoms are omitted. Symmetry codes: i = $^1/_2{-}x$, $-^1/_2{+}y$, $^3/_2{-}z$; ii = $1{-}x$, $1{-}y$, $2{-}z$; iii = $^1/_2{+}x$, $^1/_2{-}y$, $^1/_2{+}z$; iv = $^1/_2{-}x$, $^1/_2{+}y$, $^3/_2{+}z$.

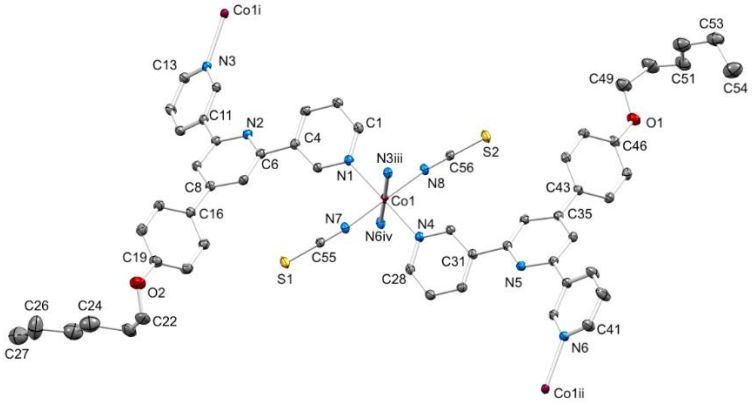

Figure 62. ORTEP representation of the asymmetric unit in $[Co(\mathbf{6})_2(NCS)_2]_n$ with symmetry-generated atoms. Ellipsoids are plotted at a 40% probability level, and H atoms are omitted. Symmetry codes: i = $2{-}x$, $-^1/_2{+}y$, $^3/_2{-}z$; ii = $1{-}x$, $^1/_2{+}y$, $^3/_2{-}z$; iii = $2{-}x$, $^1/_2{+}y$, $^3/_2{-}z$; iv = $1{-}x$, $-^1/_2{+}y$, $^3/_2{-}z$.

Table 6. Bond lengths and angles in the cobalt(II) coordination sphere.

Coordination polymer	Co–N_{tpy} / Å	Co–N_{NCS} / Å	N_{tpy}–Co–N_{tpy}[1] / °	N_{NCS}–Co–N_{NCS} / °
$[Co(\mathbf{2})_2(NCS)_2]_n \cdot 0.6n CHCl_3$	2.172(5), 2.159(5)	2.083(7)	174.4(2)	178.0(3)
$[Co(\mathbf{3})_2(NCS)_2]_n \cdot 4n CHCl_3 \cdot 0.25n H_2O$ [2]	2.211(6), 2.200(5), 2.183(6), 2.164(6)	2.067(7), 2.084(7)	175.5(2), 174.0(2)	177.0(2)
$[Co(\mathbf{4})_2(NCS)_2]_n \cdot 4n CHCl_3$ [2]	2.159(5), 2.172(5), 2.215(5), 2.229(5)	2.075(6), 2.083(6)	175.8(2), 173.78(19)	177.5(2)
$[Co_2(\mathbf{5})_4(NCS)_4]_n$	2.1693(18), 2.2175(18)	2.0870(19)	180.00(9), 180.0	180.0
$[Co(\mathbf{6})_2(NCS)_2]_n$ [2]	2.1857(19), 2.1789(19), 2.2237(18), 2.2356(18)	2.0754(18), 2.0799(18)	179.22(7), 178.59(7)	179.24(7)

[1] Only the *trans* angles are given. [2] Two independent ligands.

The (4,4) nets are produced by cobalt atoms acting as four-connecting nodes, and the 3,2′:6′,3″-tpy units bridging adjacent metal centres. This is reminiscent of the coordination networks assembled from $Co(NCS)_2$ and 4,2′:6′,4″-tpy ligands functionalized with 4′-*tert*-butyl, 4′-(4-methoxyphenyl), 4′-(4-ethoxyphenyl) and 4′-(4-*n*-propoxyphenyl) substituents.[8] However, the formation of a (4,4) net in $[Co(\mathbf{6})_2(NCS)_2]_n$ with the *n*-hexyloxy-tailed ligand **6** contrasts with the assembly of a 3D-framework when 4′-(4-*n*-hexyloxyphenyl)-4,2′:6′,4″-tpy reacts with $Co(NCS)_2$; a combination of 4′-(4-*n*-nonyloxyphenyl)-4,2′:6′,4″-tpy and $Co(NCS)_2$ also gives rise to an analogous 3D-net.[9] In $[Co(\mathbf{2})_2(NCS)_2]_n \cdot 0.6n CHCl_3$, $[Co(\mathbf{3})_2(NCS)_2]_n \cdot 4n CHCl_3 \cdot 0.25n H_2O$ and $[Co(\mathbf{4})_2(NCS)_2]_n \cdot 4n CHCl_3$, the 3,2′:6′,3″-tpy domains all adopt the conformation **A** (Scheme 27). In contrast, on going to the ligands with the *n*-pentyloxy and *n*-hexyloxy chains, the conformation switches to mode **B** (Scheme 27). The angles between the least squares planes of the pyridine rings in the 3,2′:6′,3″-tpy unit also change (Table 7). These changes are associated with a modification of the rhombi that make up the (4,4) net, as discussed below.

Table 7. Angles between the least squares planes of the rings in the 3,2′:6′,3″-tpy units.

Coordination polymer	py – py /°	py - py /°
$[Co(\mathbf{2})_2(NCS)_2]_n{\cdot}0.6n CHCl_3$	28.1	43.9
$[Co(\mathbf{3})_2(NCS)_2]_n{\cdot}4n CHCl_3{\cdot}0.25n H_2O$ [1]	22.6, 26.1	40.5, 40.6
$[Co(\mathbf{4})_2(NCS)_2]_n{\cdot}4n CHCl_3$ [1]	28.5, 23.1	37.9, 38.1
$[Co_2(\mathbf{5})_4(NCS)_4]_n$	28.5	32.8
$[Co(\mathbf{6})_2(NCS)_2]_n$ [1]	29.7, 29.9	30.8, 33.3

For conformation **B**, the two angles are defined for the left- and right-hand pairs of rings, respectively. [1]Two independent ligands.

Starting the description with the (4,4) nets assembled with $Co(NCS)_2$ and ligands **2–4**, Figure 63 shows that the net is geometrically the same in $[Co(\mathbf{2})_2(NCS)_2]_n{\cdot}0.6n CHCl_3$, $[Co(\mathbf{3})_2(NCS)_2]_n{\cdot}4n CHCl_3{\cdot}0.25n H_2O$ and $[Co(\mathbf{4})_2(NCS)_2]_n{\cdot}4n CHCl_3$. Each net comprises two geometrically distinct rhombi with Co...Co separations in the range 13.224 to 13.470(1) Å. In $[Co(\mathbf{2})_2(NCS)_2]_n{\cdot}0.6n CHCl_3$, the Co atoms are positioned along a 2-fold axis, and all Co...Co separations are 13.224 Å. Working around the circuit of each square (or near-square in the cases of $[Co(\mathbf{3})_2(NCS)_2]_n{\cdot}4n CHCl_3{\cdot}0.25n H_2O$ and $[Co(\mathbf{4})_2(NCS)_2]_n{\cdot}4n CHCl_3$), the four 4-*n*-alkyloxyphenyl substituents all point in the same direction and for adjacent corner-sharing squares, sets of four *n*-alkyloxy chains point alternately up and down. This leads to a cone-like arrangement and adjacent sheets packing with the cones nesting into one another (Figure 64a). The sheets pack in an ABAB... manner with adjacent sheets twisted through 90° with respect to the next (Figure 64b). The transition from ethoxy to *n*-propoxy to *n*-butoxy substituent has little impact on the structure, with the distances between the mean planes constructed through the cobalt atoms in a sheet increasing only from 9.07 Å in $[Co(\mathbf{2})_2(NCS)_2]_n{\cdot}0.6n CHCl_3$ to 9.56 Å in $[Co(\mathbf{4})_2(NCS)_2]_n{\cdot}4n CHCl_3$. It can be stated that π-stacking interactions play no role in the assembly.

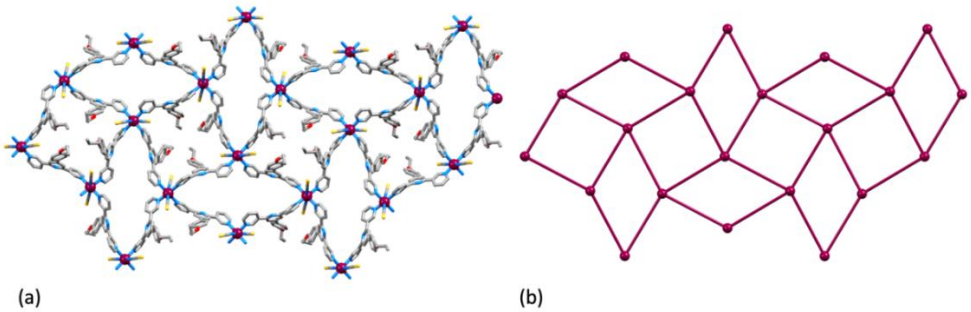

Figure 63. (**a**) Part of one (4,4) net (viewed down the crystallographic *c*-axis) in $[Co(\mathbf{4})_2(NCS)_2]_n{\cdot}4n CHCl_3$; H atoms and solvent molecules are omitted. (**b**) The same net defined by lines connecting the Co atoms.

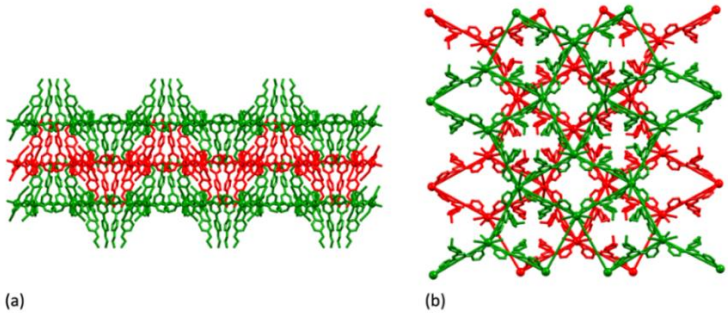

Figure 64. (**a**) Packing of (4,4) nets (viewed down the crystallographic *a*-axis) in $[Co(\mathbf{2})_2(NCS)_2]_n \cdot 0.6n CHCl_3$. (**b**) Packing of (4,4) nets (viewed down the crystallographic *c*-axis) in $[Co(\mathbf{3})_2(NCS)_2]_n \cdot 4n CHCl_3 \cdot 0.25n H_2O$, with each net defined by the lines connecting the Co atoms. Hydrogen atoms and solvent molecules are omitted.

The network common to the compounds with ligands **2**, **3** and **4** differs from that observed for the analogous compound containing ligand **1** with a methoxy substituent, which was described in the previous section. In the pseudopolymorphs $[Co(\mathbf{1})_2(NCS)_2]_n \cdot 2.2n CHCl_3$ and $[Co(\mathbf{1})_2(NCS)_2]_n \cdot 3n MeOH$, ligand **1** adopts the conformation **B**, and the network comprises identical rhombi with the ligands pointing above and below a rhombus (Figures 65a and 65b). On going from ligands **2–4** to ligands **5** and **6**, each (4,4) net in $[Co_2(\mathbf{5})_4(NCS)_4]_n$ and $[Co(\mathbf{6})_2(NCS)_2]_n$ reverts to the assembly pattern observed for ligand **1**. Figure 65c shows an overlay of the repeat units with symmetry-generated atoms in $[Co(\mathbf{1})_2(NCS)_2]_n \cdot 3n MeOH$, $[Co_2(\mathbf{5})_4(NCS)_4]_n$ and $[Co(\mathbf{6})_2(NCS)_2]_n$, revealing the similarities in the structural motifs. The (4,4) nets in $[Co_2(\mathbf{5})_4(NCS)_4]_n$ and in $[Co(\mathbf{6})_2(NCS)_2]_n$ are displayed in Figures 66a and 66b, respectively, and a comparison of these figures with Figure 65a is instructive. However, the packing of the sheets is significantly affected by the introduction of the longer alkyloxy chains. In $[Co(\mathbf{1})_2(NCS)_2]_n \cdot 3n MeOH$, the sheets are aligned with eclipsed rhombi. In contrast, in $[Co_2(\mathbf{5})_4(NCS)_4]_n$ and $[Co(\mathbf{6})_2(NCS)_2]_n$, the 2D-networks pack in an ABAB... fashion (Figure 67), allowing the *n*-pentyloxy and *n*-hexyloxy to penetrate into the cavities in an adjacent sheet.

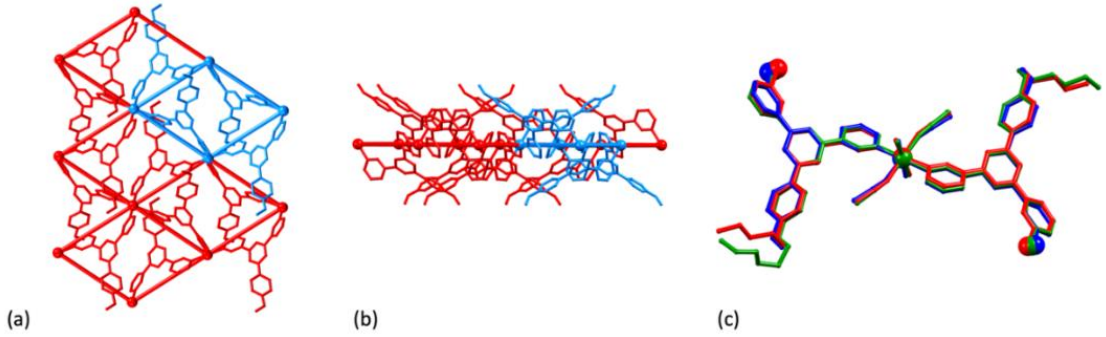

Figure 65. (**a**) Part of one (4,4) net in $[Co(\mathbf{1})_2(NCS)_2]_n \cdot 3n MeOH$ with the net defined by the lines connecting the Co atoms viewed from above and (**b**) into the plane containing the Co atoms; H atoms, thiocyanato ligands and solvent molecules are omitted. One rhombus with the four ligands **1** that link Co centers is highlighted in blue. (**c**) Overlay of the repeat units with symmetry-generated atoms in $[Co(\mathbf{1})_2(NCS)_2]_n \cdot 3n MeOH$ (in blue), $[Co_2(\mathbf{5})_4(NCS)_4]_n$ (in red) and $[Co(\mathbf{6})_2(NCS)_2]_n$ (in green).

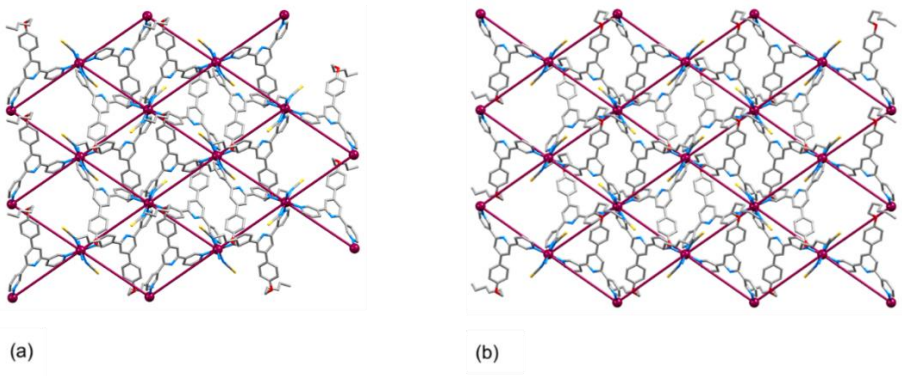

Figure 66. Part of one (4,4) net in (**a**) $[Co(\mathbf{5})_2(NCS)_2]_n$ and (**b**) $[Co(\mathbf{6})_2(NCS)_2]_n$ with the net defined by the lines connecting the Co atoms; H atoms are omitted.

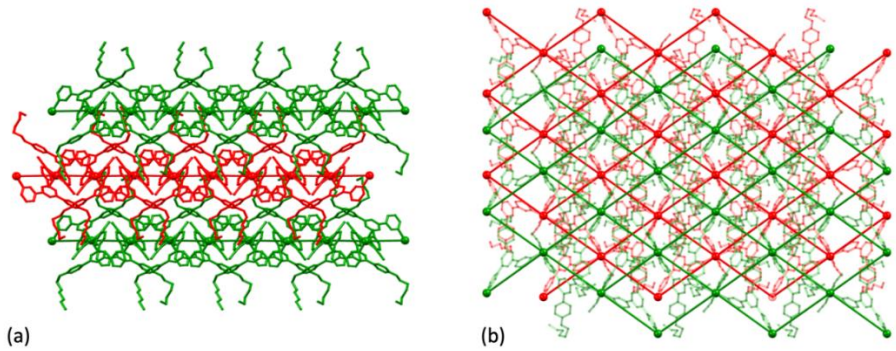

Figure 67. (**a**) Staggered 2D-sheets in $[Co(\mathbf{6})_2(NCS)_2]_n$: view down the *a*-axis, and (**b**) view down the *c*-axis. H atoms are omitted. An analogous packing of sheets occurs in $[Co_2(\mathbf{5})_4(NCS)_4]_n$.

A significant point is that in the case of the reaction of $Co(NCS)_2$ with ligand **1**, there is competition between the formation of a (4,4) net ($[Co(\mathbf{1})_2(NCS)_2]_n{\cdot}2.2n CHCl_3$ or $[Co(\mathbf{1})_2(NCS)_2]_n{\cdot}3n MeOH$) and a 1D-coordination polymer $[Co(\mathbf{1})(NCS)_2(MeOH)_2]_n$, with the 1D-coordination polymer being the dominant product (see earlier in the chapter). PXRD confirmed that this is not the case for the coordination polymers formed with ligands **5** and **6**, and the single-crystal structures of $[Co_2(\mathbf{5})_4(NCS)_4]_n$ and $[Co(\mathbf{6})_2(NCS)_2]_n$ are representative of the bulk materials. While the details of a single 2D-net are the same in each of $[Co(\mathbf{1})_2(NCS)_2]_n{\cdot}2.2n CHCl_3$, $[Co(\mathbf{1})_2(NCS)_2]_n{\cdot}3n MeOH$, $[Co_2(\mathbf{5})_4(NCS)_4]_n$ and $[Co(\mathbf{6})_2(NCS)_2]_n$, the observations suggest that longer *n*-alkyloxy chains and their penetration through voids in an adjacent layer are contributing factors to the preference for a 2D-network rather than a 1D-polymer. Another important point is that $[Co_2(\mathbf{5})_4(NCS)_4]_n$ and $[Co(\mathbf{6})_2(NCS)_2]_n$ crystallize without lattice solvent, consistent with efficient packing of the 2D-nets. In contrast, lattice solvent plays an important role in the pseudopolymorphs $[Co(\mathbf{1})_2(NCS)_2]_n{\cdot}3n MeOH$ and $[Co(\mathbf{1})_2(NCS)_2]_n{\cdot}2.2n CHCl_3$.

4.3 Reactions of **11**–**13** and **15** with $Co(NCS)_2$[10]

After investigating the effect on the assembly of supramolecular networks of the chain length of the substituent in 4′-alkyloxyphenyl-3,2′:6′,3″-terpyridines, the focus was shifted towards the effect of isomeric branched 4′-butoxyphenyl-3,2′:6′,3″-terpyridines (**11**–**13**) and of one branched 4′-pentyloxyphenyl-3,2′:6′,3″-terpyridine (**15**). In particular, the three isomeric 3,2′:6′,3″-tpy ligands, *rac*-**11**, **12** and **13** possess *rac*-4′-(4-butan-2-yloxyphenyl), 4′-(2-methylpropoxyphenyl) and 4′-(*tert*-butoxyphenyl) substituents, respectively (Scheme 29).

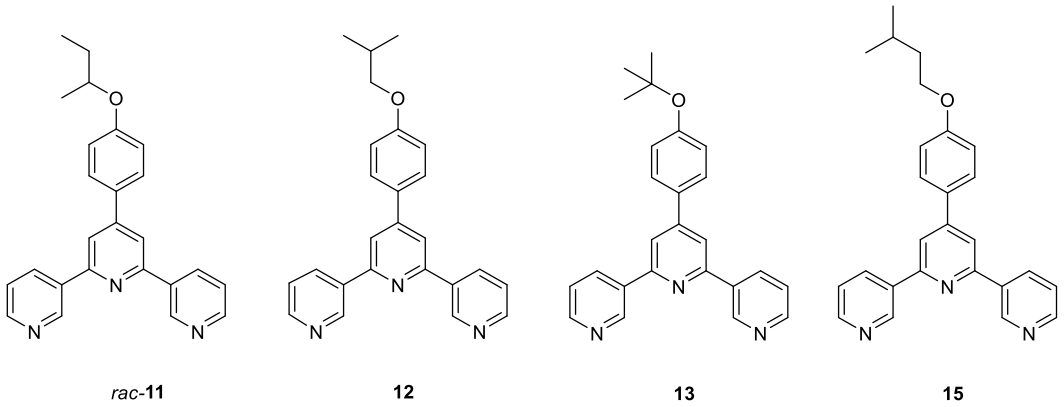

Scheme 29. The structures of ligands *rac*-**11**, **12**, **13** and **15**.

Crystals of coordination networks formed between $Co(NCS)_2$ and ligands *rac*-**11**, **12** and **13** were grown by layering a methanol solution of the cobalt(II) salt over a chloroform solution of the ligand. A suitable crystal of each product was selected for single-crystal X-ray diffraction, and the remaining pink blocks were collected, washed and analyzed by PXRD and IR spectroscopy. The strong absorption band at 2069 cm^{-1} (compound with ligand *rac*-**11**), 2061 cm^{-1} (with **12**) and 2074 cm^{-1} (with **13**) is assigned to the coordinated $[NCS]^-$ ligands. Single-crystal structure determinations revealed formulations of $[Co(rac\text{-}\mathbf{11})_2(NCS)_2]_n \cdot n CHCl_3$, $[Co(\mathbf{12})_2(NCS)_2]_n$ and $[Co(\mathbf{13})_2(NCS)_2]_n \cdot n CHCl_3$, respectively, and PXRD (Figure 68) confirmed that the single-crystal structures were representative of the bulk samples. Every peak present in the experimental plot finds a correspondence in the fit, and the differences in the intensities are mostly due to differences in the preferred orientations in the powdered bulk sample.

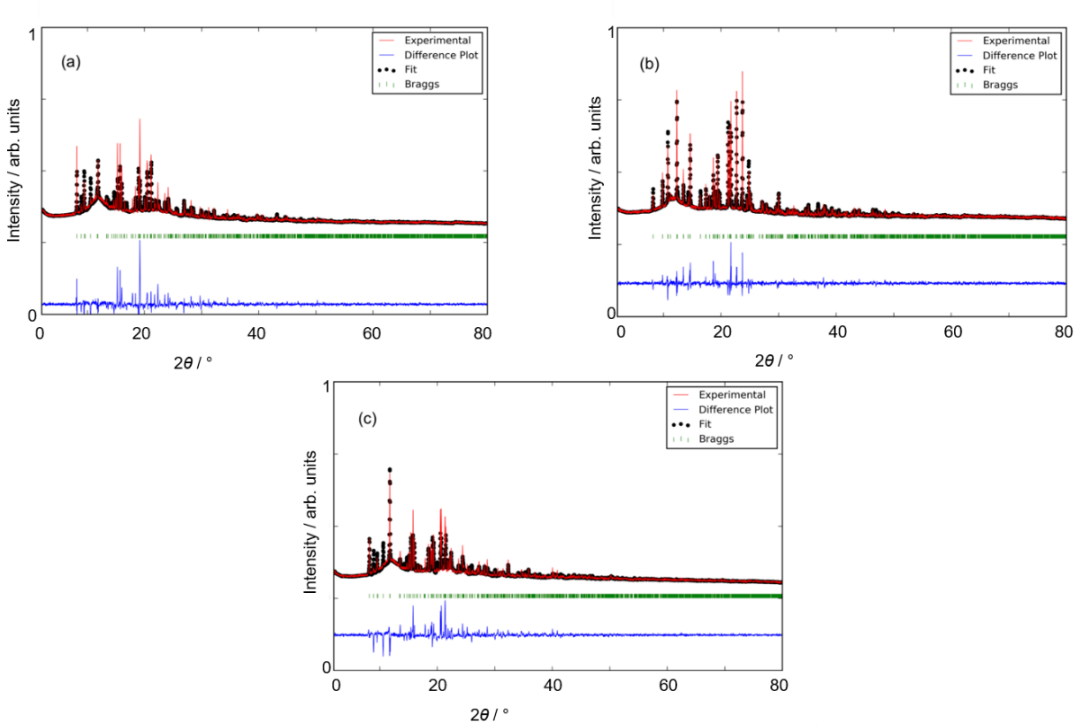

Figure 68. Laboratory powder X-ray diffraction (Cu*Kα* radiation) patterns (red lines) for (**a**) [Co(*rac*-**11**)$_2$(NCS)$_2$]$_n$·nCHCl$_3$, (**b**) [Co(**12**)$_2$(NCS)$_2$]$_n$ and (**c**) [Co(**13**)$_2$(NCS)$_2$]$_n$·nCHCl$_3$ at room temperature, compared to the fitted patterns from the single-crystal X-ray diffraction data (black dots). The green lines denote the Bragg peak positions, and the blue trace shows the difference between experimental and calculated points.

Each of [Co(*rac*-**11**)$_2$(NCS)$_2$]$_n$·nCHCl$_3$, [Co(**12**)$_2$(NCS)$_2$]$_n$ and [Co(**13**)$_2$(NCS)$_2$]$_n$·nCHCl$_3$ crystallizes in the monoclinic space group $P2_1/n$. This is in contrast to [Co(**4**)$_2$(NCS)$_2$]$_n$·4nCHCl$_3$ (reported in the previous section), which crystallizes in the tetragonal space group $P\bar{4}2_1c$. ORTEP representations of the repeat units of [Co(*rac*-**11**)$_2$(NCS)$_2$]$_n$·nCHCl$_3$, [Co(**12**)$_2$(NCS)$_2$]$_n$ and [Co(**13**)$_2$(NCS)$_2$]$_n$·nCHCl$_3$ are shown in Figure 69. The Co–N bond lengths (Table 8) are unremarkable, and the N_{tpy}-Co-N_{tpy} and N_{NCS}-Co-N_{CNS} bond angles measure 180°, due to the location of atom Co1 in each structure on an inversion center. In each structure, the 3,2′:6′,3″-tpy unit adopts conformation **B** (Scheme 27), which differs from the ligand conformation **A** observed in [Co(**4**)$_2$(NCS)$_2$]$_n$·4nCHCl$_3$.

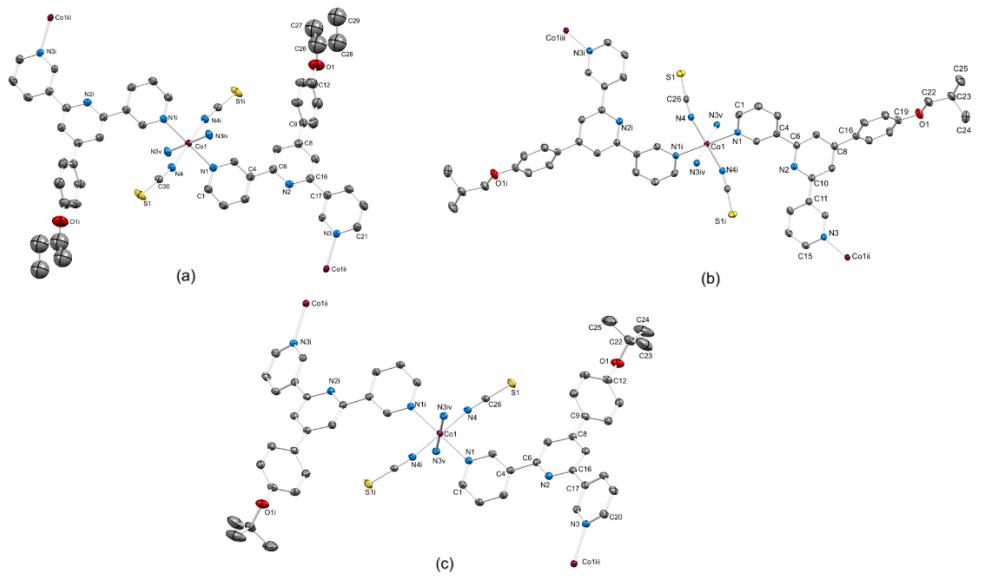

Figure 69. ORTEP representations of the coordination sphere of atom Co1 (with symmetry-generated Co centers) in (**a**) [Co(*rac*-**11**)$_2$(NCS)$_2$]$_n$·nCHCl$_3$ (symmetry codes: i = 1–x, 1–y, 1–z; ii = $^1/_2$–x, $-^1/_2$+y, $^1/_2$–z; iii = $^3/_2$–x, $^1/_2$+y, $^3/_2$–z; iv = $^1/_2$+x, $^1/_2$–y, $^1/_2$+z; v = $^1/_2$–x, $^1/_2$+y, $^1/_2$–z); (**b**) [Co(**12**)$_2$(NCS)$_2$]$_n$ (symmetry codes: i = 2–x, 2–y, 1–z; ii = $^3/_2$–x, $-^1/_2$+y, $^1/_2$–z; iii = $^5/_2$–x, $^1/_2$+y, $^3/_2$–z; iv = $^3/_2$–x, $^1/_2$+y, $^1/_2$–z; v = $^1/_2$+x, $^3/_2$–y, $^1/_2$+z); and (**c**) [Co(**13**)$_2$(NCS)$_2$]$_n$·nCHCl$_3$ (symmetry codes: i = 1–x, 1–y, –z; ii = $^1/_2$–x, $^1/_2$ + y, $-^1/_2$–z; iii = $^3/_2$–x, $-^1/_2$+y, $^1/_2$–z; iv = $-^1/_2$+x, $^1/_2$–y, $-^1/_2$+z; v = $^3/_2$–x, $^1/_2$+y, $^1/_2$–z). Ellipsoids are plotted at 40% probability level and H atoms are omitted.

Table 8. Selected bond lengths and angles[1] in [Co(*rac*-**11**)$_2$(NCS)$_2$]$_n$·nCHCl$_3$, [Co(**12**)$_2$(NCS)$_2$]$_n$ and [Co(**13**)$_2$(NCS)$_2$]$_n$·nCHCl$_3$.

Coordination polymer	Co–N$_{tpy}$/Å	Co–N$_{NCS}$/Å
[Co(*rac*-**11**)$_2$(NCS)$_2$]$_n$·nCHCl$_3$	2.185(3), 2.211(3)	2.079(3)
[Co(**12**)$_2$(NCS)$_2$]$_n$	2.217(3), 2.219(3)	2.072(3)
[Co(**13**)$_2$(NCS)$_2$]$_n$·nCHCl$_3$	2.205(3), 2.230(3)	2.066(3)

[1]Only the *trans* angles are given.

2D networks assemble for each of [Co(*rac*-**11**)$_2$(NCS)$_2$]$_n$·nCHCl$_3$, [Co(**12**)$_2$(NCS)$_2$]$_n$ and [Co(**13**)$_2$(NCS)$_2$]$_n$·nCHCl$_3$. The topology of each net is the same (Figure 70a–c, top), with *trans*-{Co(NCS)$_2$N$_4$} 4-connecting nodes, and 3,2′:6′,3″-tpy ligands bridging between adjacent of Co centers (Figure 70a–c, middle and bottom). Working sequentially around the edges of a rhombus in each network, the ligands are arranged in a down/down/up/up pattern, which contrasts with the cone-like arrangement found in [Co(**4**)$_2$(NCS)$_2$]$_n$·4nCHCl$_3$. The crystallographic symmetry dictates that both the (*R*)-**11** and (*S*)-**11** enantiomers are present is a single 2D-net of [Co(*rac*-**11**)$_2$(NCS)$_2$]$_n$·nCHCl$_3$, rendering the net heterochiral. Figures 70b and 70c illustrate that the structures of the networks in [Co(*rac*-**11**)$_2$(NCS)$_2$]$_n$·nCHCl$_3$ and [Co(**13**)$_2$(NCS)$_2$]$_n$·nCHCl$_3$ are essentially the same, and this is confirmed by inspection of the overlays depicted in Figure 71. Thus, a change in the steric effects from butan-2-yloxy to *tert*-butoxy has a negligible impact on the coordination network. However, the network deforms

on going to ligand **12** with the 2-methylpropoxy substituent (Figure 70a), and the cause can be traced to a small conformational change. The angles between the planes of pairs of bonded arene rings in each coordinated ligand are summarized in Table 9.

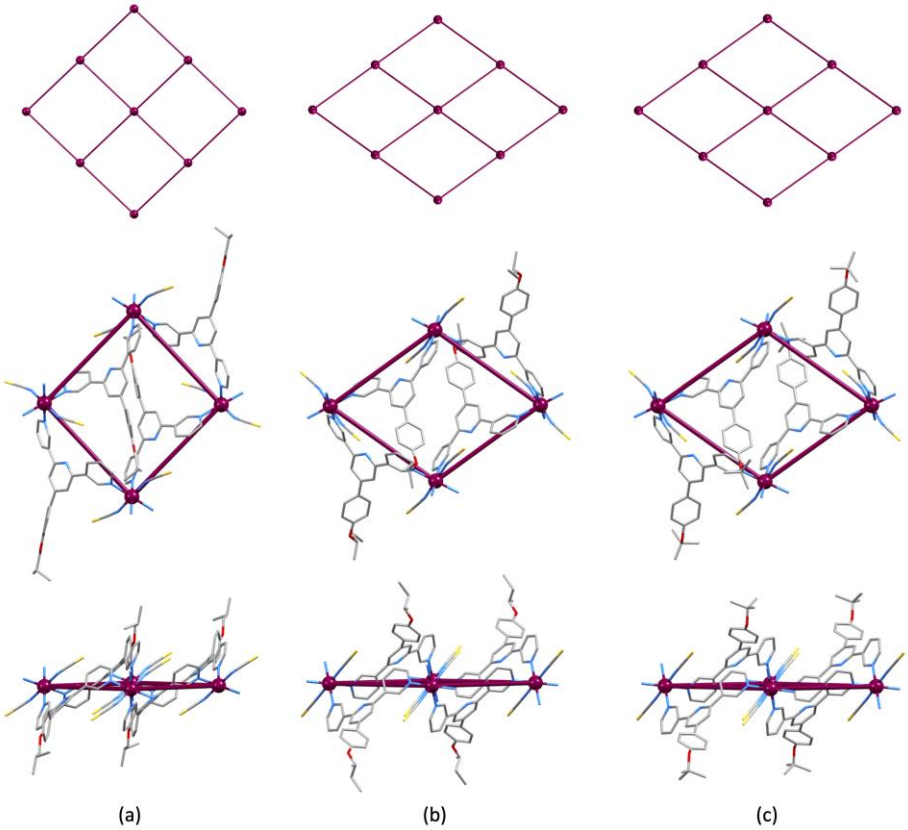

Figure 70. Comparison of the (4,4) nets in (**a**) [Co(**12**)$_2$(NCS)$_2$]$_n$ (**b**) [Co(*rac*-**11**)$_2$(NCS)$_2$]$_n$·nCHCl$_3$, and (**c**) [Co(**13**)$_2$(NCS)$_2$]$_n$·nCHCl$_3$ (top, middle and bottom diagrams for each compound). The Co…Co vectors are drawn to emphasize the (4,4) net.

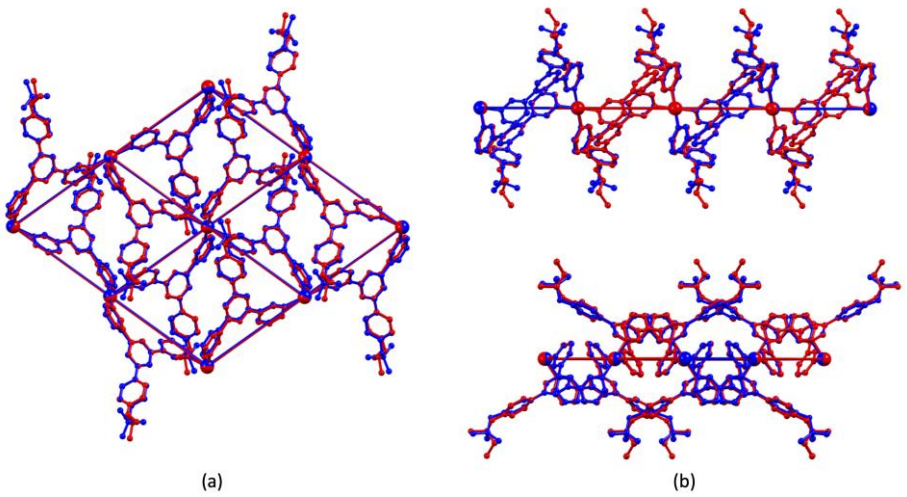

Figure 71. Overlays of parts of the (4,4) nets in [Co(*rac*-**11**)$_2$(NCS)$_2$]$_n$·nCHCl$_3$ (red) and [Co(**13**)$_2$(NCS)$_2$]$_n$·nCHCl$_3$ (blue).

Table 9. Angles between the arene ring-planes in $[Co(rac\text{-}\mathbf{11})_2(NCS)_2]_n \cdot n CHCl_3$, $[Co(\mathbf{12})_2(NCS)_2]_n$ and $[Co(\mathbf{13})_2(NCS)_2]_n \cdot n CHCl_3$. The pyridine rings are labelled as defined in Scheme 30 (see below).

Coordination polymer	ring α - ring β /°	ring β - ring γ /°	ring β - ring δ /°
$[Co(rac\text{-}\mathbf{11})_2(NCS)_2]_n \cdot n CHCl_3$	30.6	32.7	55.7
$[Co(\mathbf{12})_2(NCS)_2]_n$	37.7	27.9	48.1
$[Co(\mathbf{13})_2(NCS)_2]_n \cdot n CHCl_3$	28.0	28.9	48.3

Because the ligand is in conformation **B**, the outer pyridine rings in the coordinated 3,2′:6′,3″-tpy are distinct from each other (Scheme 30). The angles between rings β and γ are similar in all three structures, but the angle between rings α and β is larger in $[Co(\mathbf{12})_2(NCS)_2]_n$ than in $[Co(rac\text{-}\mathbf{11})_2(NCS)_2]_n \cdot n CHCl_3$ and $[Co(\mathbf{13})_2(NCS)_2]_n \cdot n CHCl_3$ (Table 9). This has a significant impact on the propagation of the 2D-structure, as can be seen from Figure 72, which displays an overlay of parts of the structures of $[Co(\mathbf{12})_2(NCS)_2]_n$ and $[Co(rac\text{-}\mathbf{11})_2(NCS)_2]_n \cdot n CHCl_3$. The Co atoms and rings γ that are labeled in Figure 72 are perfectly overlaid. The larger twist angle between rings α and β in $[Co(\mathbf{12})_2(NCS)_2]_n$ compared to $[Co(rac\text{-}\mathbf{11})_2(NCS)_2]_n \cdot n CHCl_3$ leads to a redirecting of the Co...Co vector, and, consequently, a deformation of the (4,4) network. This highlights the manner in which small conformational changes within the 3,2′:6′,3″-tpy domain can accommodate changes in the spatial properties of substituents, without leading to significant topological modifications. Note that from crystal symmetry, it follows that *trans*-arrangements must be (ring α)–Co–(ring α) or (ring γ)–Co–(ring γ) and that every Co atom is bonded to two α and two γ rings (see Scheme 30 and Figure 72 below).

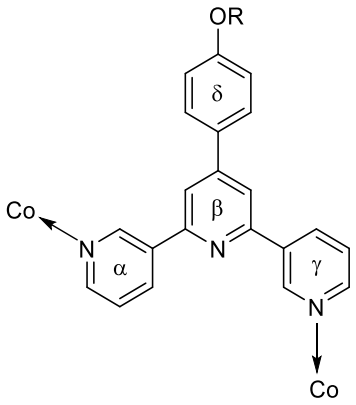

Scheme 30. In $[Co(rac\text{-}\mathbf{11})_2(NCS)_2]_n \cdot n CHCl_3$, $[Co(\mathbf{12})_2(NCS)_2]_n$ and $[Co(\mathbf{13})_2(NCS)_2]_n \cdot n CHCl_3$, the ligand adopts conformation **B** (Scheme 27) and the Co atom is on an inversion center. Pyridine rings α and γ are therefore topologically distinct.

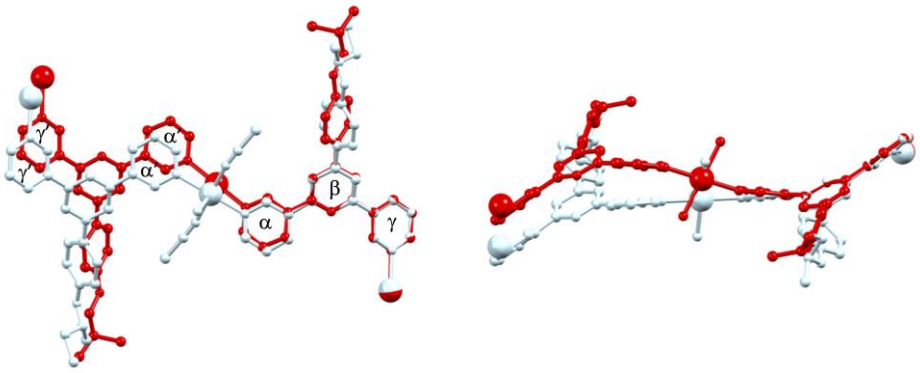

Figure 72. Overlay of parts of the structures of $[Co(\mathbf{12})_2(NCS)_2]_n$ (red) and $[Co(rac\text{-}\mathbf{11})_2(NCS)_2]_n \cdot n CHCl_3$ (pale blue). Thiocyanato ligands and H atoms are omitted. See text for details.

Following the same procedure, ligand **15** (Scheme 31) was reacted with cobalt(II) thiocyanate by layering a methanol solution of the metal salt on a chloroform solution of the terpyridine bearing a 4'-(3-methylbutoxyphenyl) substituent. The structure of $[Co(\mathbf{15})_2(NCS)_2]_n$ was determined, and PXRD confirmed that it was representative of the sample (Figure 73).

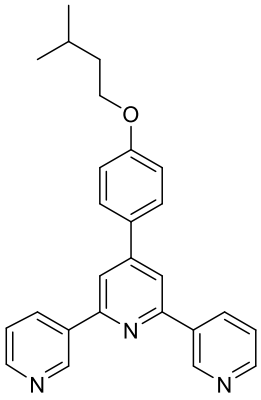

15

Scheme 31. The structures of ligand **15**.

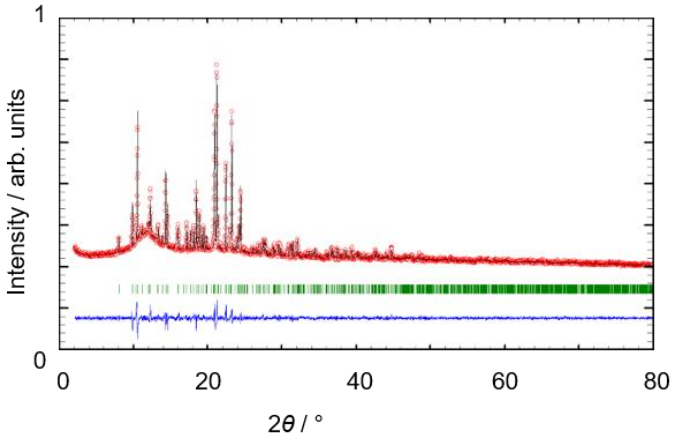

Figure 73. Laboratory powder X-ray diffraction (Cu$K\alpha$ radiation) patterns (red lines) for [Co(**15**)$_2$(NCS)$_2$]$_n$ at room temperature, compared to the fitted patterns from the single-crystal X-ray diffraction data (black dots). The green lines denote the Bragg peak positions, and the blue trace shows the difference between experimental and calculated points.

[Co(**15**)$_2$(NCS)$_2$]$_n$ crystallizes in the monoclinic space group $P2_1/n$ and the ORTEP representation of the repeat unit is shown in Figure 74. The Co–N bond lengths are unremarkable, with Co-N_{NCS} 2.0710(14) Å and Co-N_{tpy} = 2.2217(15) and 2.2505(15) Å, and the N_{tpy}-Co-N_{tpy} and N_{NCS}-Co-N_{CNS} angles fixed at 180° by symmetry since the cobalt atom lies on an inversion center.

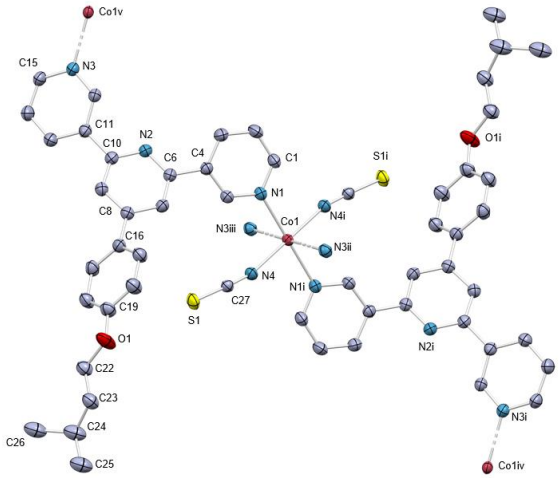

Figure 74. ORTEP representation of the coordination sphere of atom Co1 (with symmetry-generated Co centers) in [Co(**15**)$_2$(NCS)$_2$]$_n$ (symmetry codes: i = 1–x, 1–y, 2–z; ii = $^1/_2$–x, –$^1/_2$+y, $^3/_2$–z; iii = $^1/_2$+x, $^3/_2$–y, $^1/_2$+z; iv = $^3/_2$–x, –$^1/_2$+y, $^5/_2$–z; v = $^1/_2$–x, $^1/_2$+y, $^3/_2$–z). Ellipsoids are plotted at 50% probability level and H atoms are omitted.

The terminal part of the isopentyloxy chain (C24–C26) is disordered and was modelled over two positions of fractional occupancies 0.6/0.4. The net presents the same topology seen in the other structures, with *trans*-{$Co(NCS)_2N_4$} 4-connecting nodes and 3,2′:6′,3″-tpy ligands bridging between adjacent Co centers. As in the polymers of the other ligands with branched substituents (i.e. *rac*-**11**, **12** and **13**), the 3,2′:6′,3″-tpy unit adopts conformation **B** (Scheme 27) and the net comprises identical rhombi with the ligands pointing above and below a rhombus, without building the cone arrangement seen in the polymers with **2**–**4** (in the previous section). On a closer look, the structure with ligand **15** (Figure 75) resembles the one with ligand **12**, bearing a 2-methylpropoxy, more than the ones built with *rac*-**11** and **13**. An initial way to point this similarity out is to compare the internal angles in the rhombi; these are = 85.6° and 94.4° in $[Co(\mathbf{15})_2(NCS)_2]_n$, compared to 87.1° and 92.9° in $[Co(\mathbf{12})_2(NCS)_2]_n$, but they significantly differ in $[Co(rac\text{-}\mathbf{11})_2(NCS)_2]_n \cdot n CHCl_3$ and $[Co(\mathbf{13})_2(NCS)_2]_n \cdot n CHCl_3$, where they measure 71.4°, 108.6°, and 71.0°, 109.0°, respectively. A second resemblance of the two nets can be highlighted by comparing the angles between the planes of pairs of bonded arene rings in the coordinated ligands, which are summarized in Table 9 (for ligands *rac*-**11**, **12** and **13**) and in Table 10 (for ligand **15**). The angle between rings β and γ is similar in all the four structures, but the angle between rings α and β is larger in $[Co(\mathbf{15})_2(NCS)_2]_n$ and in $[Co(\mathbf{12})_2(NCS)_2]_n$, compared to the other two. As seen, this has a significant impact on the propagation of the 2D-structure.

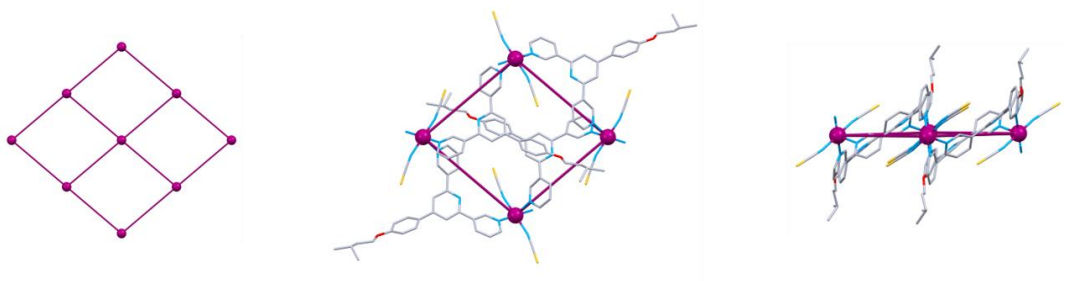

Figure 75. Structure of the (4,4) net in $[Co(\mathbf{15})_2(NCS)_2]_n$. The Co...Co vectors are drawn to emphasize the (4,4) net.

Table 10. Angles between the arene ring-planes in $[Co(\mathbf{15})_2(NCS)_2]_n$. The pyridine rings are labelled as defined in Scheme 30.

Coordination polymer	ring α - ring β /°	ring β - ring γ /°	ring β - ring δ /°
$[Co(\mathbf{15})_2(NCS)_2]_n$	36.7	31.6	46.7

Extending the comparison to the structures bearing *n*-alkyloxyphenyl substituents (described in sections 4.1 and 4.2), the network in $[Co(\mathbf{15})_2(NCS)_2]_n$ is reminiscent of those in the pseudopolymorphs $[Co(\mathbf{1})_2(NCS)_2]_n \cdot 2.2 n CHCl_3$ and $[Co(\mathbf{1})_2(NCS)_2]_n \cdot 3 n MeOH$, and in those of $[Co_2(\mathbf{5})_4(NCS)_4]_n$ and $[Co(\mathbf{6})_2(NCS)_2]_n$ (substituents: methoxy (**1**), *n*-pentyloxy (**5**), *n*-hexyloxy (**6**)). In all these cases, the tpy units adopt the conformation **B** (Scheme 27) and the nets comprise identical rhombi, without the cone-like arrangement, in contrast with the assemblies

of ligands **2**–**4**. Certainly, the packing of the sheets is significantly affected by the introduction of the different alkyloxy chains, as previously discussed on going from **1** to **5** and **6**. Among these assemblies, $[Co(\mathbf{15})_2(NCS)_2]_n$, $[Co(\mathbf{12})_2(NCS)_2]_n$, $[Co_2(\mathbf{5})_4(NCS)_4]_n$ and $[Co(\mathbf{6})_2(NCS)_2]_n$ crystallize without lattice solvent, showing a highly efficient packing, and differs from the nets of ligand **1**. Similarly to $[Co_2(\mathbf{5})_4(NCS)_4]_n$ and $[Co(\mathbf{6})_2(NCS)_2]_n$ (Figure 67, Section 4.2), the 2D-networks in $[Co(\mathbf{12})_2(NCS)_2]_n$ and $[Co(\mathbf{15})_2(NCS)_2]_n$ pack in an ABAB... fashion, allowing the alkyl chains to penetrate into the cavities in an adjacent sheet. However, the distance between neighboring planes defined by the cobalt atoms is 8.872 Å in the assembly containing ligand **15** (isopentyloxy substituent), 8.873 Å with ligand **12** (isobutyloxy), while it is 10.750 Å and 10.380 Å with ligand **5** (*n*-pentyloxy) and **6** (*n*-hexyloxy), respectively. This additional study shows that in this case, the switch from ligand **5** with the straight-chain pentyloxy substituent to ligand **15** with a branched isopentyloxy chain does not cause significant structural perturbation. Moreover, it confirms that changes in the spatial properties of the substituents are accommodated with subtle conformational changes in the 3,2′:6′,3″-tpy domain.

4.4 Reactions of **16**–**20** with $Co(NCS)_2$[11]

In Chapter 3, the 1D-polymers formed between copper(II) acetate and 3,2′:6′,3″-terpyridines with extended π–systems were described. Now, this study is extended to the coordination chemistry of cobalt(II) thiocyanate. The five 4′-substituted-[1,1′-biphenyl]-4-yl-3,2′:6′,3″-terpyridines (Scheme 32), in which the 4′-group is Me (**20**), H (**16**), F (**17**), Cl (**18**) or Br (**19**), were reacted with $Co(NCS)_2$ under crystal growth conditions by layering MeOH solution of the metal salt over $CHCl_3$ solution of each ligand, leading to the formation of five 2D-coordination networks. $[Co(\mathbf{20})_2(NCS)_2]_n{\cdot}4.5n CHCl_3$, $[Co(\mathbf{16})_2(NCS)_2]_n{\cdot}4.3n CHCl_3$, $[Co(\mathbf{17})_2(NCS)_2]_n{\cdot}4n CHCl_3$, $[Co(\mathbf{18})_2(NCS)_2]_n$, and $[Co(\mathbf{19})_2(NCS)_2]_n{\cdot}n CHCl_3$ may be categorized into three structure types, based on changes in the conformation of the 3,2′:6′,3″-tpy unit coupled with the interactions of the different peripheral substituents.

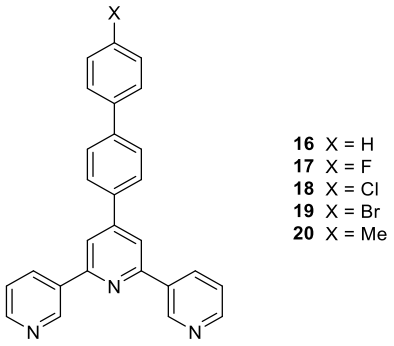

16 X = H
17 X = F
18 X = Cl
19 X = Br
20 X = Me

Scheme 32. The structures of ligands **16**–**20**.

After the selection of a crystal for single-crystal X-ray diffraction, the remaining crystals were analyzed by solid-state IR spectroscopy and powder X-ray diffraction (PXRD). The IR spectrum of [Co(**17**)$_2$(NCS)$_2$]$_n$·4*n*CHCl$_3$ is shown in Figure 76 and is representative of the whole series of compounds.

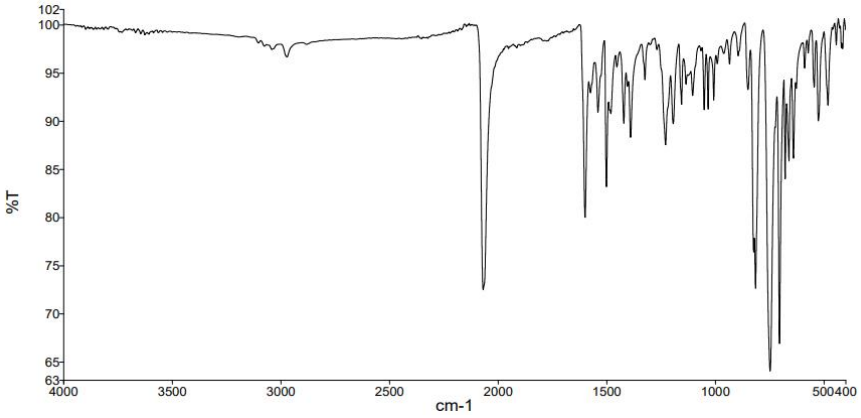

Figure 76. Solid-state IR spectrum of single crystals of [Co(**17**)$_2$(NCS)$_2$]$_n$·4*n*CHCl$_3$.

The strongest absorption band in each spectrum is assigned to the thiocyanate C≡N stretching mode (2072 cm^{-1} for [Co(**16**)$_2$(NCS)$_2$]$_n$·4.3*n*CHCl$_3$, 2070 cm^{-1} for [Co(**20**)$_2$(NCS)$_2$]$_n$·4.5*n*CHCl$_3$, 2069 cm^{-1} for [Co(**17**)$_2$(NCS)$_2$]$_n$·4*n*CHCl$_3$ and [Co(**19**)$_2$(NCS)$_2$]$_n$·*n*CHCl$_3$, and 2063 cm^{-1} for [Co(**18**)$_2$(NCS)$_2$]$_n$). Fits between the powder pattern predicted from the single-crystal structure and the experimental pattern for [Co(**17**)$_2$(NCS)$_2$]$_n$·4*n*CHCl$_3$ and [Co(**19**)$_2$(NCS)$_2$]$_n$·*n*CHCl$_3$ (Figure 77) confirmed that the single crystals were representative of the bulk materials. For the remaining compounds, it was not possible to generate a fit using the program FULLPROF.

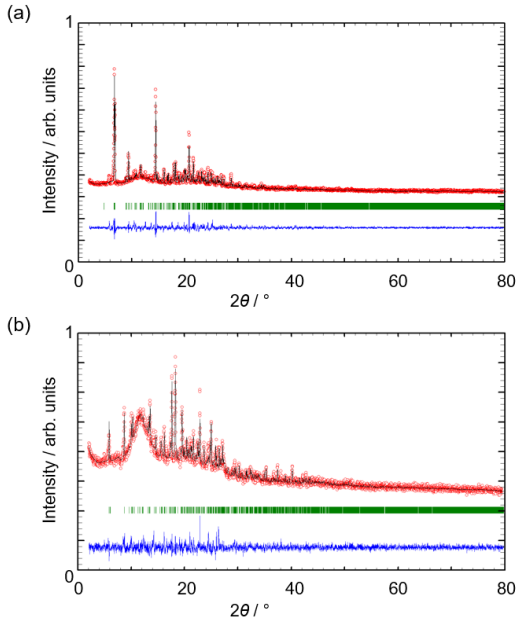

Figure 77. PXRD (Cu*Kα* radiation) patterns (red circles) of the bulk crystalline materials of (**a**) [Co(**17**)$_2$(NCS)$_2$]$_n$·4*n*CHCl$_3$, and (**b**) [Co(**19**)$_2$(NCS)$_2$]$_n$·*n*CHCl$_3$, with fitting to the predicted patterns from the single-crystal structures. The black lines are the best fits from the Rietveld refinements, and the green lines show the Bragg peak positions. Each blue plot gives the difference between calculated and experimental points, and the differences in intensities are due to differences in the preferred orientations of the crystallites in the bulk samples.

In [Co(**20**)$_2$(NCS)$_2$]$_n$·4.5*n*CHCl$_3$ and in [Co(**16**)$_2$(NCS)$_2$]$_n$·4.3*n*CHCl$_3$, part of the solvent region was treated with a solvent mask, and the electron density removed corresponded to 0.5 and to 2.3 chloroform molecules, respectively. The remaining solvent molecules were refined isotropically. [Co(**20**)$_2$(NCS)$_2$]$_n$·4.5*n*CHCl$_3$ and [Co(**16**)$_2$(NCS)$_2$]$_n$·4.3*n*CHCl$_3$ crystallize in the tetragonal space group *P*4/*ncc*, while [Co(**17**)$_2$(NCS)$_2$]$_n$·4*n*CHCl$_3$ crystallizes in the orthorhombic space group *Pccn*. The structures of the asymmetric units of these three compounds are shown with ORTEP style in Figure 78, and can be described together as a first structure type. The rings of the biphenyl unit in [Co(**16**)$_2$(NCS)$_2$]$_n$·4.3*n*CHCl$_3$ were disordered and were modelled over two positions of fractional occupancies 0.5/0.5 (for the ring containing C15) and 0.6/0.4 (for the terminal ring). In each structure, the Co atom is octahedrally sited with a *trans*-arrangement of thiocyanato ligands, and the 3,2′:6′,3″-tpy domain adopts conformation **A** (Scheme 27). Bond lengths in the cobalt(II) coordination spheres are given in Table 11.

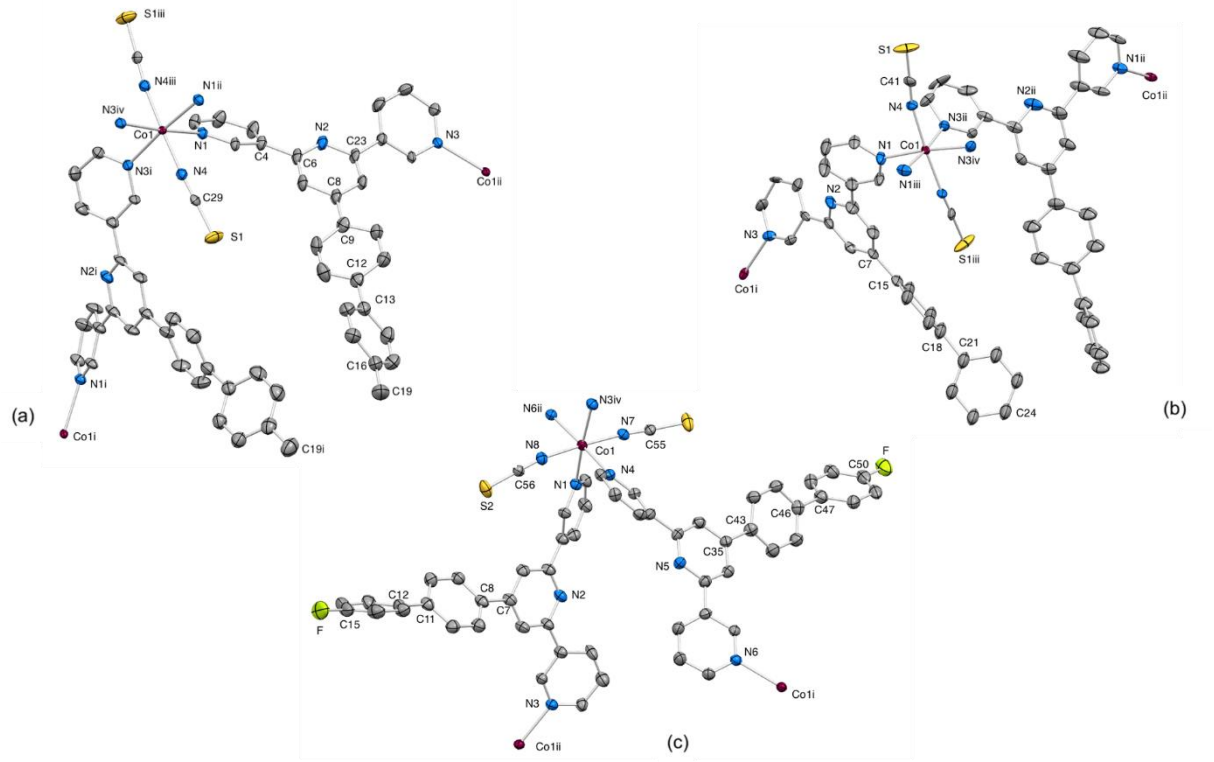

Figure 78. Structures of the asymmetric units with symmetry-related atoms in (**a**) $[Co(\mathbf{20})_2(NCS)_2]_n \cdot 4.5n CHCl_3$ (symmetry codes: i = $^3/_2-y$, x, z; ii = y, $^3/_2-x$, z; iii = $1-y$, $1-x$, $^1/_2-z$; iv = $1-x$, $-^1/_2+y$, $^1/_2-z$); (**b**) $[Co(\mathbf{16})_2(NCS)_2]_n \cdot 4.3n CHCl_3$ (symmetry codes: i = y, $^1/_2-x$, z; ii = $^1/_2-y$, x, z; iii = $-^1/_2+y$, $^1/_2+x$, $^3/_2-z$; iv = $-^1/_2+x$, $1-y$, $^3/_2-z$); and (**c**) $[Co(\mathbf{17})_2(NCS)_2]_n \cdot 4n CHCl_3$ (symmetry codes: i = $1-x$, $-^1/_2+y$, $^3/_2-z$; ii = $^1/_2+x$, $1-y$, $^3/_2-z$; iii = $1-x$, $^1/_2+y$, $^3/_2-z$; iv = $-^1/_2+x$, $1-y$, $^3/_2-z$). $[Co(\mathbf{17})_2(NCS)_2]_n \cdot 4n CHCl_3$ contains two independent ligands. Solvent molecules are omitted. Ellipsoids are plotted at 40% probability level.

Table 11. Selected bond lengths and inter-ring angles in the cobalt(II) coordination polymers containing ligands **20**, **16** and **17**. Py-py /° = angle between planes of pyridine rings, etc.

Coordination polymer	Co–N_{NCS}/Å	Co–N_{tpy}/Å	py - py /°	py - arene /°	ring C – ring D /°
$[Co(\mathbf{20})_2(NCS)_2]_n \cdot 4.5n CHCl_3$	2.066(4)	2.211(4), 2.189(4)	27.7, 28.4	17.5	55.6
$[Co(\mathbf{16})_2(NCS)_2]_n \cdot 4.3n CHCl_3$	2.067(9)	2.166(11), 2.193(10)	24.7, 35.7	35.6 [a]	79.7 [a]
$[Co(\mathbf{17})_2(NCS)_2]_n \cdot 4n CHCl_3$	2.064(7), 2.065(6)	2.164(6), 2.192(6), 2.189(6), 2.213(6)	28.3, 33.3 [b] 24.8, 37.1 [c]	40.2 [b] 15.9 [c]	48.0 [b] 58.2 [c]

[a] For one orientation of each disordered ring; [b] For one of two independent ligands; [c] For the second independent ligand. Ring C and ring D refer to the two rings of the biphenyl group.

Despite significant variation in the angles between the planes of the aromatic rings in coordinated ligands **20**, **16** and **17**, the structures of the asymmetric units in [Co(**20**)$_2$(NCS)$_2$]$_n$·4.5*n*CHCl$_3$ (Figure 78a) and [Co(**16**)$_2$(NCS)$_2$]$_n$·4.3*n*CHCl$_3$ (Figure 78b) are very similar. The structures propagate into 2D (4,4) nets with the biphenyl units arranged in cones above and below the plane containing the Co atoms. This is closely related to the structures of solvated [Co**L**$_2$(NCS)$_2$]$_n$ in which **L** is **2**, **3** or **4** (see Section 4.2); these compounds crystallize in the tetragonal space groups *P*4/*ncc* or *P*–42$_1$*c*. The cone assemblies in [Co(**20**)$_2$(NCS)$_2$]$_n$·4.5*n*CHCl$_3$ are shown in Figure 79a, and their arrangement in [Co(**16**)$_2$(NCS)$_2$]$_n$·4.3*n*CHCl$_3$ is essentially the same; hence only the structure of the compound containing ligand **20** is going to be further discussed. Each cone is built up around a 4-fold axis, and thus, in Figure 79b, the cones protrude from the square rhombi. [Co(**17**)$_2$(NCS)$_2$]$_n$·4*n*CHCl$_3$ comprises a 2D (4,4) net similar to those in [Co(**20**)$_2$(NCS)$_2$]$_n$·4.5*n*CHCl$_3$ and [Co(**16**)$_2$(NCS)$_2$]$_n$·4.3*n*CHCl$_3$, although the lower symmetry of the *Pccn* space group with respect to *P*4/*ncc* means that there are two independent terpyridine ligands in [Co(**17**)$_2$(NCS)$_2$]$_n$·4*n*CHCl$_3$ (Figure 78 and Table 11), and the cone assembly is built up around a 2-fold axis (Figure 79c,d).

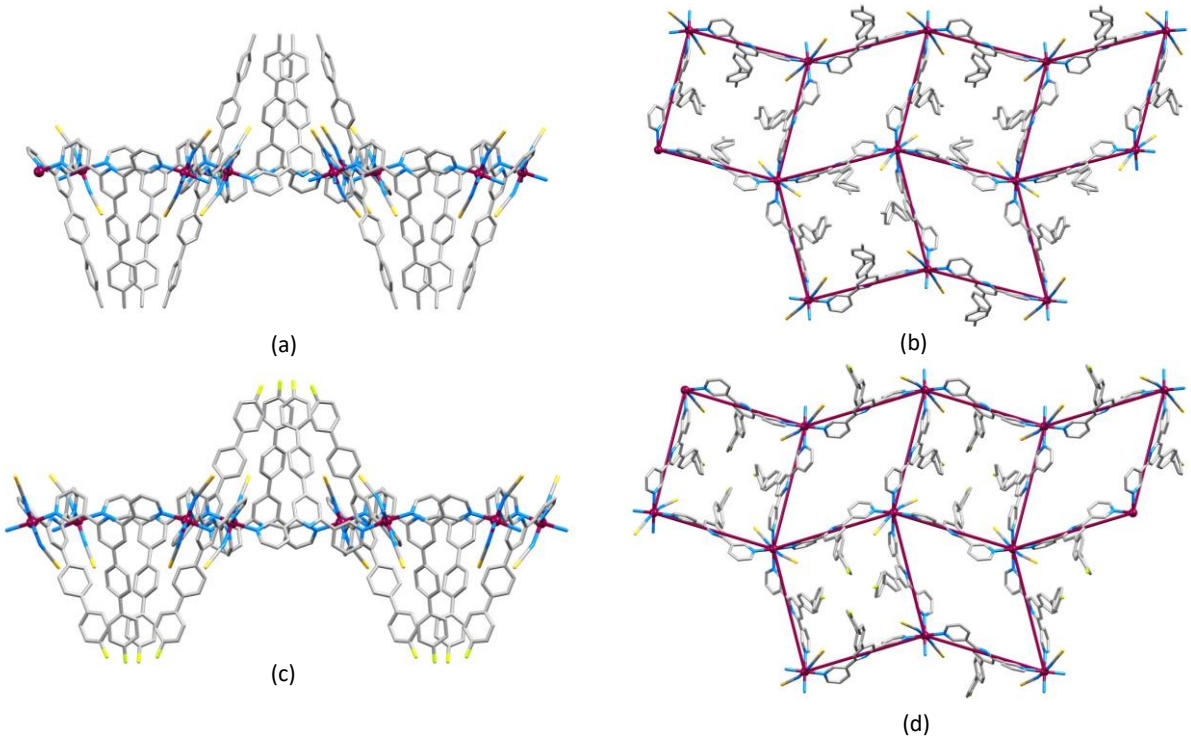

Figure 79. (**a**) Part of one 2D-sheet in [Co(**20**)$_2$(NCS)$_2$]$_n$·4.5*n*CHCl$_3$ showing cones above and below the plane containing the Co atoms, and (**b**) looking down on the sheet; the cones protrude from the square rhombi. (**c**) Part of one 2D-sheet in [Co(**17**)$_2$(NCS)$_2$]$_n$·4*n*CHCl$_3$ showing the cones which project above and below the plane and are built up around the rhombi with internal angles of 87.6° and 92.4° (**d**).

In each of $[Co(\mathbf{20})_2(NCS)_2]_n{\cdot}4.5n CHCl_3$, $[Co(\mathbf{16})_2(NCS)_2]_n{\cdot}4.3n CHCl_3$, and $[Co(\mathbf{17})_2(NCS)_2]_n{\cdot}4n CHCl_3$, adjacent sheets pack with the cones of biphenyl substituents stacked inside one another along the crystallographic *c*-axis (Figure 80a). Face-to-face π-stacking occurs between the pyridine ring containing N2 (see Figure 78 for atom numbers) in one sheet with the peripheral arene ring in the next sheet. In $[Co(\mathbf{20})_2(NCS)_2]_n{\cdot}4.5n CHCl_3$, the π-stacking interaction is characterized by a centroid distance of 3.75 Å and an angle between the ring planes of 9.6°. These parameters are 3.69 Å and 11.9° in $[Co(\mathbf{16})_2(NCS)_2]_n{\cdot}4.3n CHCl_3$ for one modelled site of the disordered phenyl ring. The cone...cone π-stacking contacts in $[Co(\mathbf{17})_2(NCS)_2]_n{\cdot}4n CHCl_3$ are effective for only one of the two independent ligands with a centroid...centroid distance of 3.63 Å and an inter-ring plane angle of 10.9°. Although the nets and their packing are similar in the compounds with ligands **20**, **16** and **17**, the number of $CHCl_3$ molecules per Co differ. Part of the solvent region in each of $[Co(\mathbf{20})_2(NCS)_2]_n{\cdot}4.5n CHCl_3$ and $[Co(\mathbf{16})_2(NCS)_2]_n{\cdot}4.3n CHCl_3$ was treated with a solvent mask because of disordering, and the small difference between the final formulations was carefully checked. There was insufficient residual electron density in the coordination network with **16** to permit a formula of $[Co(\mathbf{16})_2(NCS)_2]_n{\cdot}4.5n CHCl_3$. Further confirmation came from an analysis of the void spaces (calculated in Mercury[12] using a contact surface map with probe radius = 1.2 Å), which revealed 31.7% in $[Co(\mathbf{20})_2(NCS)_2]_n$ and 29.8% in $[Co(\mathbf{16})_2(NCS)_2]_n$. This difference may be attributed to variations in the twist angles between the arene rings of ligands **20** and **16** (Table 11) and the fact that ligand **16** is disordered over two positions. Figure 80b illustrates that the four refined $CHCl_3$ molecules (colored red and yellow in Figure 80b) per Co occupy two types of cavities. The solvent-accessible voids are illustrated in Figure 80c, which was generated in Mercury[12] using a solvent-free lattice; Figure 80d shows the residual voids after taking into account the refined $CHCl_3$ molecules. These essentially closed cavities account for 4.2% of the solvent-accessible void in the lattice and accommodate $0.5CHCl_3$ per Co. Figure 81 illustrates the lattice in $[Co(\mathbf{17})_2(NCS)_2]_n{\cdot}4n CHCl_3$. Similarities between Figure 81a and 80b are clear, and the $CHCl_3$ molecules are again distributed equally between two types of cavities in the lattice. The remaining closed voids that run along the *c*-axis account for only 1.4% of the total void and host no solvent, in contrast to analogous voids in $[Co(\mathbf{20})_2(NCS)_2]_n{\cdot}4.5n CHCl_3$ and $[Co(\mathbf{16})_2(NCS)_2]_n{\cdot}4.3n CHCl_3$.

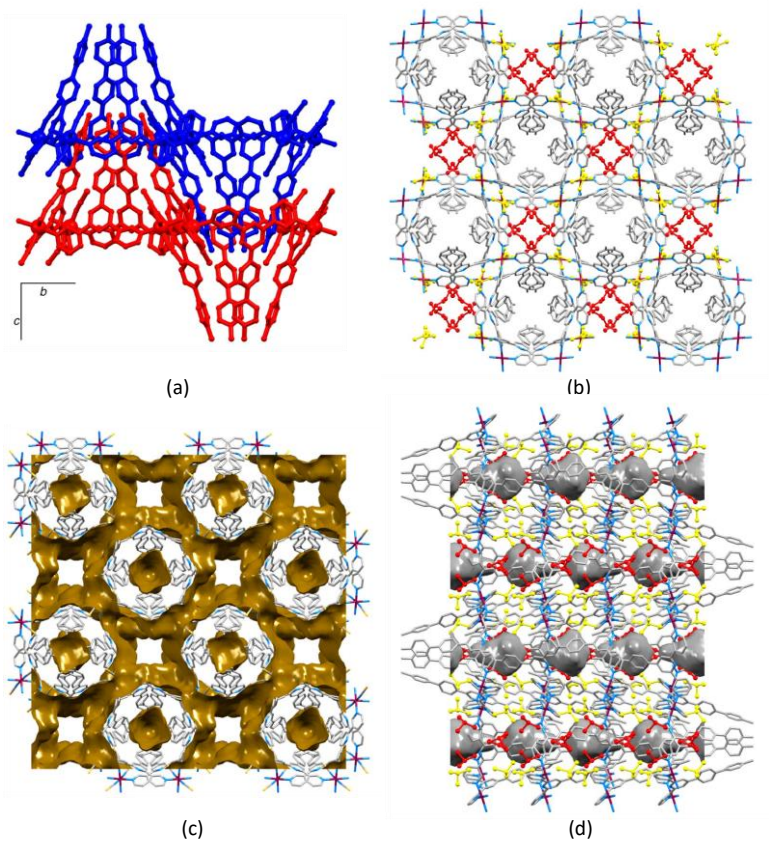

Figure 80. (**a**) $[Co(\mathbf{20})_2(NCS)_2]_n \cdot 4.5n CHCl_3$: stacking of cones of biphenyl substituents between adjacent (4,4) nets (H atoms and $CHCl_3$ molecules omitted). (**b**) Part of the lattice viewed down the *c*-axis showing that the solvent molecules that were refined (colored red and yellow) occupy two types of cavities. (**c**) The same part of the lattice as in (**b**) illustrating the voids calculated using a contact surface map with probe radius = 1.2 Å, and drawn using Mercury.[12] (**d**) A view down the *b*-axis showing the refined $CHCl_3$ molecules (red and yellow) and the residual voids (see text).

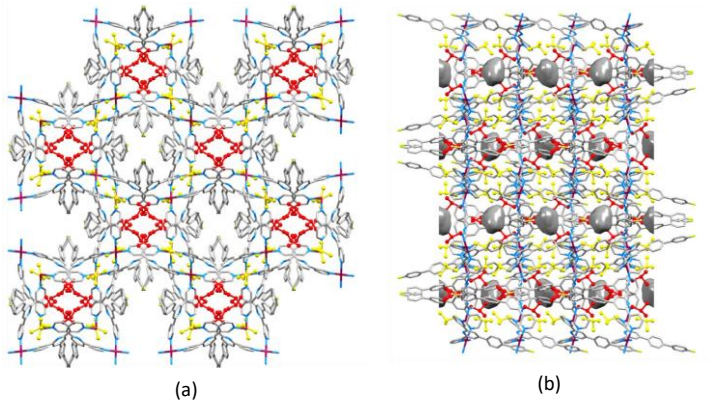

Figure 81. $[Co(\mathbf{17})_2(NCS)_2]_n \cdot 4n CHCl_3$: (**a**) part of the lattice viewed down the *c*-axis showing that the solvent molecules (colored red and yellow) occupy two types of cavities. (**b**) The same part of the lattice viewed down the *b*-axis; the residual voids (calculated using a contact surface map with probe radius = 1.2 Å, and drawn using Mercury 2020.1[12]) that are aligned along the *c*-axis account for 1.4% of the total void.

As detailed in Figure 77, PXRD confirmed that the single-crystal structure of $[Co(\mathbf{17})_2(NCS)_2]_n \cdot 4n CHCl_3$ was representative of the bulk material, and therefore this coordination network was selected for an analysis of solvent removal from, and re-entry into, the crystal lattice. Crystals of $[Co(\mathbf{17})_2(NCS)_2]_n \cdot 4n CHCl_3$ were heated to 80 °C for 30 min. Figure 82 illustrates that loss of $CHCl_3$ was detected with mass peaks at *m*/*z* 83.0, 85.0 and 87.0, corresponding to $CHCl_2^+$ as the dominant fragment.[13] In $[Co(\mathbf{17})_2(NCS)_2]_n \cdot 4n CHCl_3$, four molecules of $CHCl_3$ correspond to 32.7% of the molecular weight. The mass loss in the TGA (Figure 82 caption) corresponded to ca. 17%, indicating the loss of two $CHCl_3$ per Co atom. This is in accord with the structural data, which revealed that the solvent molecules in $[Co(\mathbf{17})_2(NCS)_2]_n \cdot 4n CHCl_3$ are equally distributed within two different types of cavities (Figure 81a).

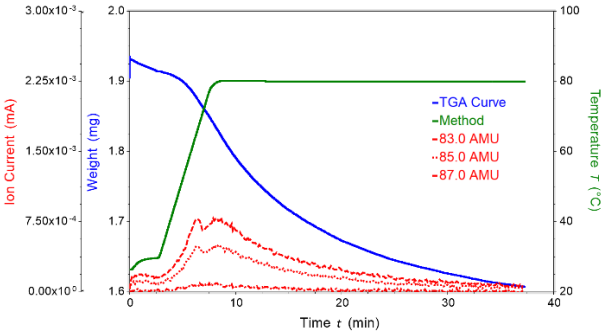

Figure 82. TGA and mass spectrometric traces for the analysis of $[Co(\mathbf{17})_2(NCS)_2]_n \cdot 4n CHCl_3$ (cycle 1). Green: temperature vs. time; blue: weight of sample vs. time; red: mass detection for *m*/*z* 83.0 (most intense peak), 85.0 and 87.0. The weight loss corresponds to ca. 17%.

After the initial TGA cycle, the sample was cooled to room temperature and was exposed to $CHCl_3$ vapor for 24 h. TGA analysis was repeated (cycle 2), and loss of $CHCl_3$ was again detected, as shown in Figure S76. A weight loss corresponding to ca. 19% was similar to that in cycle 1. In order to distinguish between the residual lattice solvent after cycle 1 and solvent re-entering the lattice during exposure to $CHCl_3$ vapor, a third cycle was carried out using $CDCl_3$. The same crystalline material was placed in contact with $CDCl_3$ vapor for 24 h and then analyzed by TGA (Figure 83). Mass peaks at *m*/*z* 84.0, 86.0 and 88.0 were detected at ca. 80 °C and were assigned to the $CDCl_2^+$ ion, and the ca. 19% weight loss (see caption to Figure 83) was consistent with the loss of ca. 2 molecules of $CDCl_3$ per Co atom. In turn, this is consistent with a formulation of $[Co(\mathbf{17})_2(NCS)_2]_n \cdot 2n CHCl_3 \cdot 2n CDCl_3$ after exposure to $CDCl_3$ vapor and before TGA cycle 3. The process was finally repeated using CH_2Cl_2 vapor. The product of cycle 3, $[Co(\mathbf{17})_2(NCS)_2]_n \cdot 2n CHCl_3$, was placed in contact with CH_2Cl_2 vapor for 24 h. TGA and mass spectrometric analysis of this material showed mass peaks at *m*/*z* 49.0, 51.0, 84.0 and 86.0 arising from CH_2Cl^+ and $CH_2Cl_2^+$ at ca. 40 °C (Figure S77), and the 12% weight loss was consistent with the removal of two molecules of CH_2Cl_2 per Co atom.

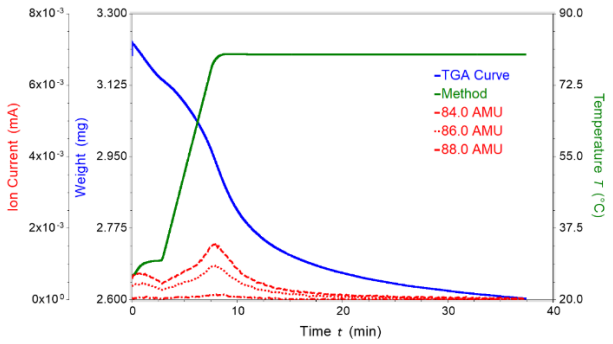

Figure 83. TGA and mass spectrometric traces for the analysis of $[Co(\mathbf{17})_2(NCS)_2]_n \cdot 2n CHCl_3 \cdot 2n CDCl_3$ (cycle 3: after 24 h exposure to $CDCl_3$ vapor). Green: temperature vs. time; blue: weight of sample vs. time; red: mass detection for *m*/*z* 84.0 (most intense peak), 86.0 and 88.0. The weight loss corresponds to ca. 19%.

The results of the TGA experiments illustrate that the coordination network in $[Co(\mathbf{17})_2(NCS)_2]_n \cdot 4n CHCl_3$ is sufficiently robust to allow half of the solvent to be reversibly removed. Inspection of Figure 81 indicates that these are most likely the molecules accommodated in the open channels, which run along the *c*-axis adjacent to the stacked cone-assemblies.

Moving forward with the description of the crystal structures, $[Co(\mathbf{18})_2(NCS)_2]_n$ and $[Co(\mathbf{19})_2(NCS)_2]_n \cdot n CHCl_3$ (X = Cl and Br, respectively) both crystallize in the monoclinic space group $P2_1/n$. The structures of the asymmetric units showing the atom numbering are displayed in Figure 84. In each, the octahedral Co(II) center exhibits a typical *trans*-arrangement of thiocyanato ligands. In $[Co(\mathbf{18})_2(NCS)_2]_n$, the Co atom lies on an inversion center, while $[Co(\mathbf{19})_2(NCS)_2]_n \cdot n CHCl_3$ contains two independent 3,2′:6′,3″-terpyridine ligands. Relevant bond lengths and twist angles between arene rings are presented in Table 12. The units shown in Figure 84 propagate into 2-dimensional (4,4) nets, consistent with the coordination networks assembled with ligands **20**, **16** and **17**. However, whereas the 3,2′:6′,3″-tpy domains in coordinated **20**, **16** and **17** exhibit conformation **A**, that in **18** possesses conformation **B** (Scheme 27 and Figure 84a), while the two independent ligands in $[Co(\mathbf{19})_2(NCS)_2]_n \cdot n CHCl_3$ adopt conformations **A** and **B**, respectively (Figure 84b). The two structures are consequently distinct from one another and from those with ligands **20**, **16** and **17**.

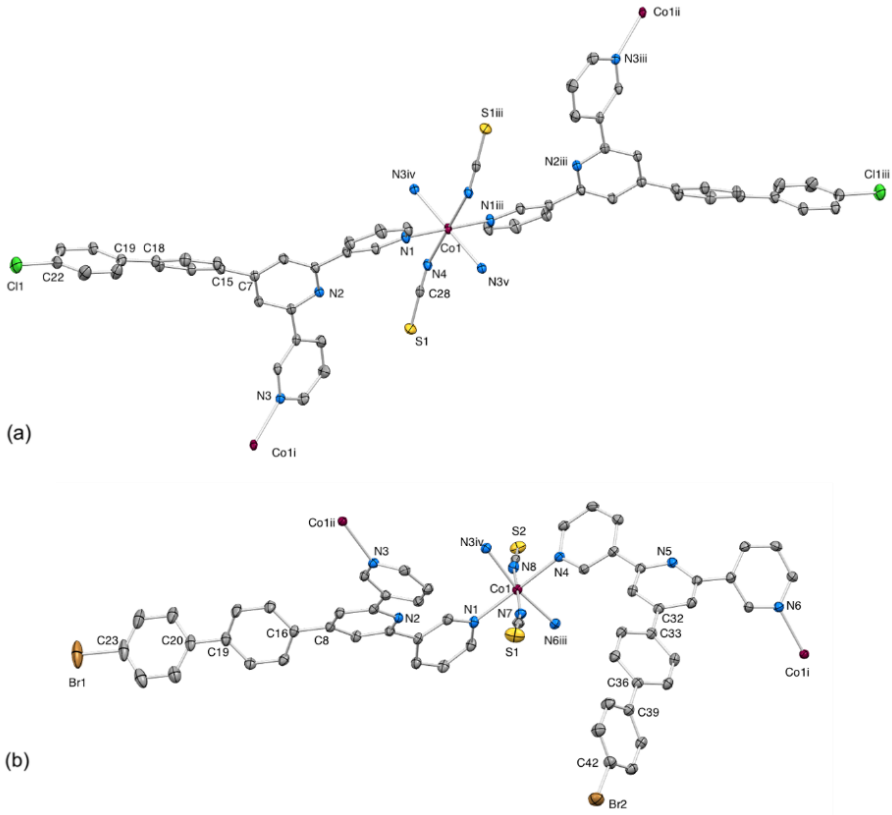

Figure 84. Structures of the asymmetric units with symmetry-related atoms in (**a**) $[Co(\mathbf{18})_2(NCS)_2]_n$ (symmetry codes: i = $^1/_2+x$, $^1/_2+y$, $^3/_2-z$; ii = $-^1/_2-x$, $-^1/_2+y$, $^1/_2-z$; iii = $-x$, $-y$, $1-z$; iv = $-^1/_2+x$, $^1/_2-y$, $-^1/_2+z$; v = $^1/_2+x$, $-^1/_2+y$, $^3/_2-z$); and (**b**) $[Co(\mathbf{19})_2(NCS)_2]_n{\cdot}n\mathrm{CHCl_3}$ (symmetry codes: i = $^5/_2-x$, $^1/_2+y$, $^1/_2-z$; ii = $^3/_2-x$, $-^1/_2+y$, $^1/_2-z$; iii = $^5/_2-x$, $-^1/_2+y$, $^1/_2-z$; iv = $^3/_2-x$, $^1/_2+y$, $^1/_2-z$). $[Co(\mathbf{19})_2(NCS)_2]_n{\cdot}n\mathrm{CHCl_3}$ contains two independent ligands. H atoms and solvent molecules are omitted. Ellipsoids are plotted at 40% probability level.

Table 12. Co–N bond lengths and inter-ring angles in the cobalt(II) coordination polymers containing ligands **18** and **19**.

Coordination polymer	Co–N_{NCS}/Å	Co–N_{tpy}/Å	py - py /°	py - arene /°	ring C – ring D /°
$[Co(\mathbf{18})_2(NCS)_2]_n$	2.0776(17)	2.1781(17), 2.2295(18)	34.1, 39.0	41.4	28.8
$[Co(\mathbf{19})_2(NCS)_2]_n{\cdot}n\mathrm{CHCl_3}$	2.061(2), 2.084(2)	2.170(2), 2.221(2), 2.175(2), 2.199(2)	29.1, 21.1 [a] 38.8, 48.3 [b]	38.9 [a] 22.1 [b]	40.9 [a] 30.6 [b]

[a] For one of two independent ligands with conformation **B**; [b] for the independent ligand with conformation **A**. Ring C and ring D refer to the two rings of the biphenyl group.

In the (4,4) net in $[Co(\mathbf{18})_2(NCS)_2]$, the Co atoms lie in a plane, and crystallographic symmetry dictates that all rhombi are identical with internal angles of 82.4° and 97.6°, and the 4′-chloro-[1,1′-biphenyl]-4-yl units are directed up/up/down/down around each rhombus. This contrasts with the cone-assemblies in the compounds containing **16**, **17** and **20**. A consequence of the conformational switch of the 3,2′:6′,3″-tpy on going from **16**, **17** and **20** to **18** is that the

4′-chloro-[1,1′-biphenyl]-4-yl domains of the ligands lie over the rhombi (Figure 85a, b) rather than projecting directly above the plane. The Cl atoms decorate the outer surfaces of the 2-dimensional sheet in [Co(**18**)$_2$(NCS)$_2$], and each Cl engages in a Cl...π interaction with a pyridine ring in the adjacent sheet (Figure 85c). The shortest contacts are Cl1...C10^{vi} = 3.422(2) and Cl1...C11^{vi} = 3.383(2) Å (symmetry code vi = $^1/_2+x$, $^3/_2-y$, $-^1/_2+z$). These distances are within the cut-off value of 3.62 Å applied by Prasanna and Row,[14] and the interaction in [Co(**18**)$_2$(NCS)$_2$], which involves the Cl atom directed at a specific arene π-bond, is classified as semi-localized.[15, 16] In contrast to the coordination networks incorporating ligands **16**–**17** and **19**–**20**, the one with ligand **18** contains no solvent of crystallization; the void (calculated using a contact surface map with probe radius = 1.2 Å) is <2%. Moreover, it is noteworthy that the network contains no face-to-face π-stacking interactions.

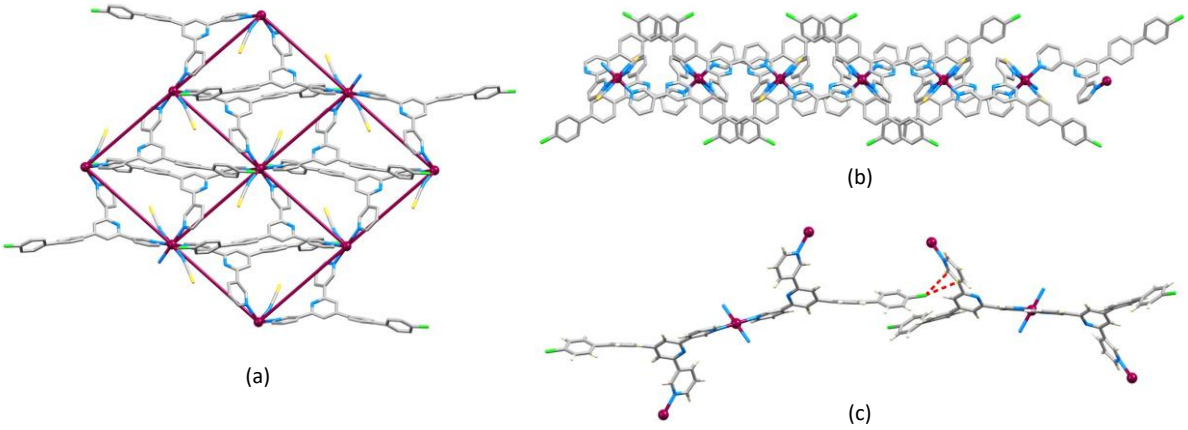

Figure 85. The structure of [Co(**18**)$_2$(NCS)$_2$]$_n$. (**a**) Part of the 2D-net showing that the ligands lie over the rhombi, and (**b**) a side view of part of one sheet. The peripheral Cl atoms engage in Cl…π interactions shown in (**c**) with arene rings in the adjacent sheet.

In contrast to the structures described above, the (4,4) net in [Co(**19**)$_2$(NCS)$_2$]$_n$·nCHCl$_3$ (Figure 86) has a corrugated profile (Figure 86b), with each rhombus adopting a folded conformation with an internal dihedral angle of 124.3°. Of the two independent terpyridine ligands, that with conformation **A** has greater twist angles between the pyridine rings (38.8° and 48.3°) than that with conformation **B** (29.1° and 21.1°). The orientations of the ligands with respect to the (4,4) net defined by the Co atoms are shown in Figure 86b. The 4′-bromo-[1,1′-biphenyl]-4-yl substituents in adjacent sheets are closely associated (Figure 86c), but there are no π-stacking interactions nor Br...π interactions. The CHCl$_3$ molecules occupy channels that follow the crystallographic *b*-axis. The difference between the coordination network on going from chloro-substituted ligand **18** to bromo-substituted **19** is striking, but the origins behind the change are unclear. It can be emphasized that the PXRD of [Co(**19**)$_2$(NCS)$_2$]$_n$·nCHCl$_3$ (Figure 77b) confirmed that the single-crystal structure was representative of the bulk sample.

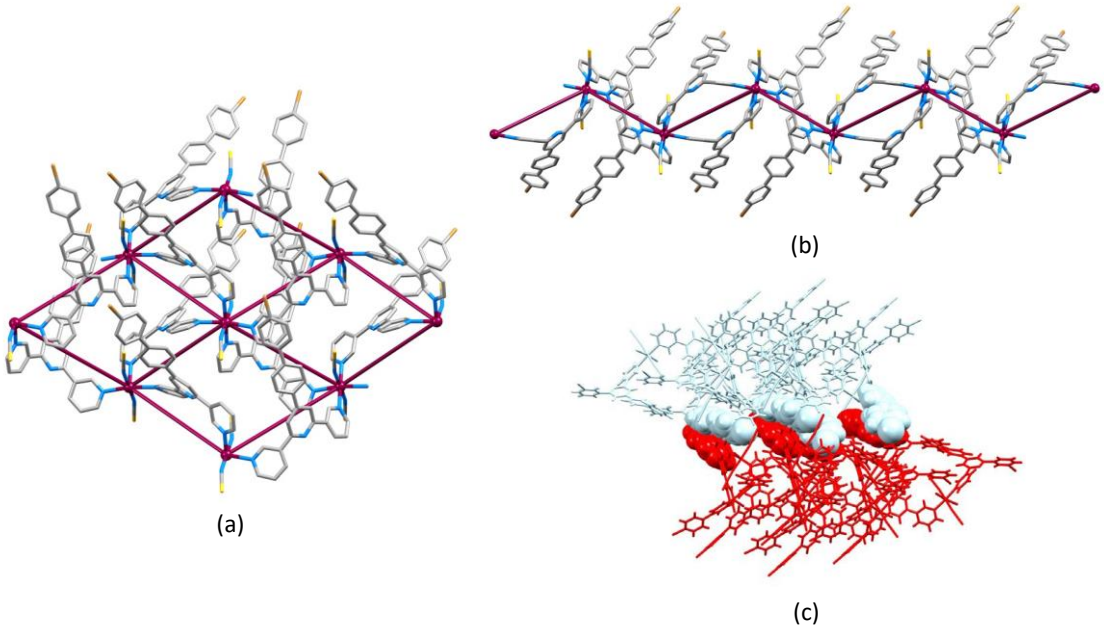

Figure 86. The structure of [Co(**19**)$_2$(NCS)$_2$]$_n$·nCHCl$_3$. (**a**) Part of one 2D-sheet, and (**b**) a side view of the sheet showing the corrugated profile with 4′-bromo-[1,1′-biphenyl]-4-yl substituents protruding above and below the sheet. (**c**) The 4′-bromo-[1,1′-biphenyl]-4-yl substituents in adjacent sheets are closely associated but not π-stacked.

The same series of five terpyridines **16**–**20** was reacted with cobalt(II) thiocyanate in methanol solution by layering it on a toluene solution of each ligand. Replacing chloroform with toluene in this new series of experiments has noticeable consequences on the assembly of the coordination polymers. $CHCl_3$ is a solvent that usually lies in cavities in the lattice without significant interactions with the net. On the other hand, toluene is a solvent that often engages in π-stacking interactions with the coordination assembly itself. It was possible to fully solve only three crystal structures *via* single-crystal XRD, and these were the assemblies containing ligands **16** (X = H), **17** (X = F) and **19** (X = Br). Once again, 2D (4,4) nets were obtained; these were [Co(**16**)$_2$(NCS)$_2$]$_n$·3nC$_6$H$_5$CH$_3$, [Co(**17**)$_2$(NCS)$_2$]$_n$·4nC$_6$H$_5$CH$_3$ and [Co(**19**)$_2$(NCS)$_2$]$_n$·4.6nC$_6$H$_5$CH$_3$. Additionally, a preliminary structure was obtained with the ligand bearing the methyl group (**20**). Besides single-crystal XRD, the products were analyzed by solid-state IR and PXRD. The IR spectrum of [Co(**19**)$_2$(NCS)$_2$]$_n$·4.6nC$_6$H$_5$CH$_3$ is shown in Figure 87 and is representative of the class of compounds.

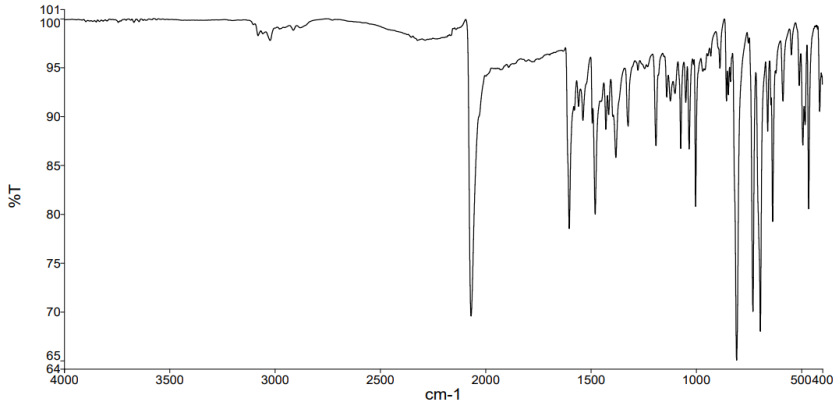

Figure 87. Solid-state IR spectrum of [Co(**19**)$_2$(NCS)$_2$]$_n$·4.6*n*C$_6$H$_5$CH$_3$.

Similarly to what was discussed earlier for the structures formed from methanol/chloroform solutions, the strongest absorption band in each spectrum can be assigned to the thiocyanate C≡N stretching mode (2070 cm^{-1} for [Co(**19**)$_2$(NCS)$_2$]$_n$·4.6*n*C$_6$H$_5$CH$_3$, 2069 cm^{-1} for [Co(**17**)$_2$(NCS)$_2$]$_n$·4*n*C$_6$H$_5$CH$_3$, and 2065 cm^{-1} for [Co(**16**)$_2$(NCS)$_2$]$_n$·3*n*C$_6$H$_5$CH$_3$). Comparisons of the experimental PXRD data were made with the patterns predicted from the single-crystal measurements; however, it was not possible to obtain a good fit. [Co(**16**)$_2$(NCS)$_2$]$_n$·3*n*C$_6$H$_5$CH$_3$, [Co(**17**)$_2$(NCS)$_2$]$_n$·4*n*C$_6$H$_5$CH$_3$ and [Co(**19**)$_2$(NCS)$_2$]$_n$·4.6*n*C$_6$H$_5$CH$_3$ crystallize in the monoclinic space groups *P*2$_1$/*n*, *C*2/*c* and *P*2$_1$/*c*, respectively. In [Co(**16**)$_2$(NCS)$_2$]$_n$·3*n*C$_6$H$_5$CH$_3$ one toluene molecule was modelled over an inversion center, with each position modelled with 50% occupancy. In [Co(**17**)$_2$(NCS)$_2$]$_n$·4*n*C$_6$H$_5$CH$_3$, the second half of a toluene molecule is generated by a C_2 axis, while another toluene molecule is disordered over an inversion center. The third toluene molecule is rotationally disordered and was modelled over two positions, each with 50% occupancy. In [Co(**19**)$_2$(NCS)$_2$]$_n$·4.6*n*C$_6$H$_5$CH$_3$, part of the solvent region was treated with a solvent mask, and the electron density removed corresponded to 2.3 toluene molecules. The remaining toluene molecules were disordered over symmetry elements and were modelled on three sites. Two of them have an arene ring in common, with a total occupancy of 60%, while the methyl groups have site occupancies of 20% and 40% each. Another toluene molecule is disordered over an inversion center, with each position modelled with 50% occupancy. All the solvent molecules were refined isotropically. The structures of the asymmetric units with symmetry-generated atoms are displayed in Figure 88a ([Co(**16**)$_2$(NCS)$_2$]$_n$·3*n*C$_6$H$_5$CH$_3$), Figure 88b ([Co(**17**)$_2$(NCS)$_2$]$_n$·4*n*C$_6$H$_5$CH$_3$) and Figure 88c ([Co(**19**)$_2$(NCS)$_2$]$_n$·4.6*n*C$_6$H$_5$CH$_3$), represented in ORTEP-style. Each of them comprises one independent ligand, and it is immediately apparent that in every structure the 3,2′:6′,3″-tpy domain adopts conformation **B** (Scheme 27), in contrast with what was observed in the polymers grown from chloroform (and methanol) with the same ligands. Bond lengths in the cobalt(II) coordination spheres are given in Table 13. Despite significant variation in the angles between the planes of the aromatic rings in coordinated ligands **16**, **17** and **19**, the structures of the asymmetric units in

$[Co(\mathbf{16})_2(NCS)_2]_n{\cdot}3n C_6H_5CH_3$, $[Co(\mathbf{17})_2(NCS)_2]_n{\cdot}4n C_6H_5CH_3$ and $[Co(\mathbf{19})_2(NCS)_2]_n{\cdot}4.6n C_6H_5CH_3$ (Figure 88) are similar.

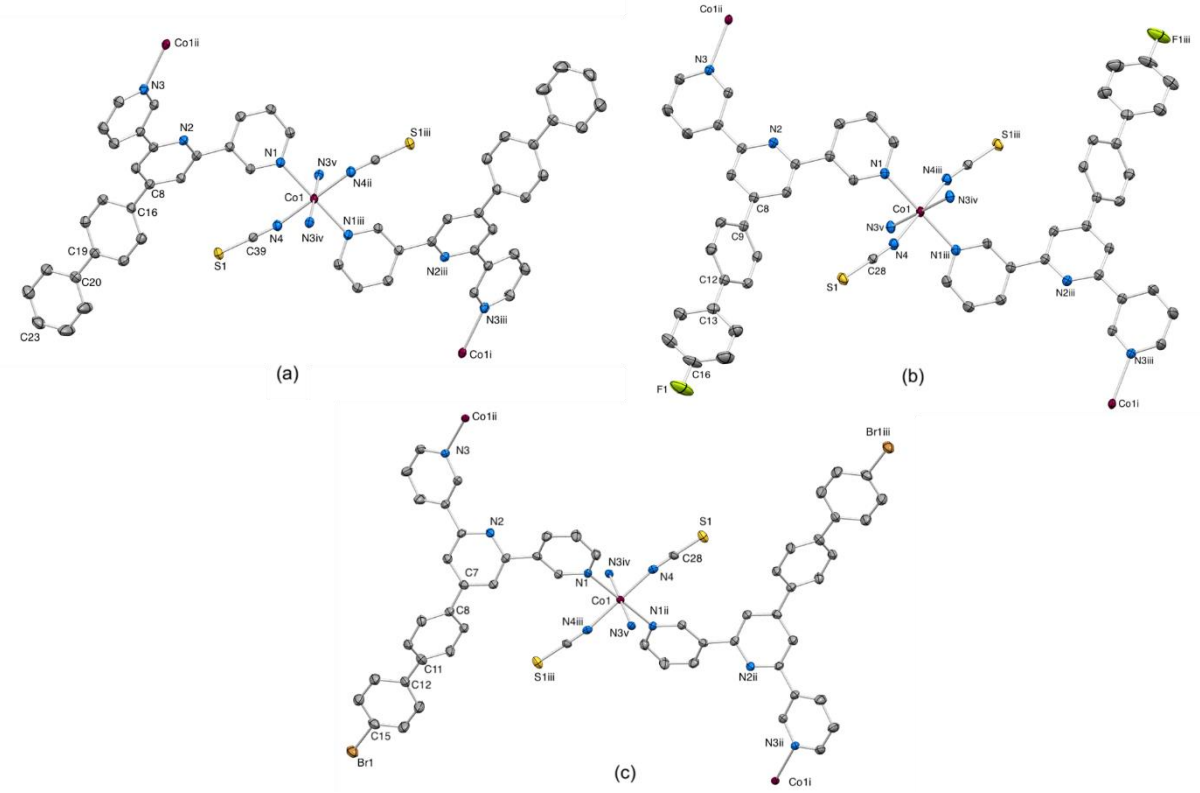

Figure 88. Structures of the asymmetric units with symmetry-related atoms in (**a**) $[Co(\mathbf{16})_2(NCS)_2]_n{\cdot}3n C_6H_5CH_3$ (symmetry codes: i = 5/2–*x*, –1/2+*y*, 5/2–*z*; ii = 3/2–*x*, 1/2+*y*, 3/2–*z*; iii = 2–*x*, 1–*y*, 2–*z*; iv = 1/2+*x*, 3/2–*y*, 1/2+*z*; v = 3/2–*x*, –1/2+*y*, 3/2–*z*); (**b**) $[Co(\mathbf{17})_2(NCS)_2]_n{\cdot}4n C_6H_5CH_3$ (symmetry codes: i = 3/2–*x*, 1/2+*y*, 5/2–*z*; ii = 3/2–*x*, –1/2+*y*, 3/2–*z*; iii = 3/2–*x*, 1/2–*y*, 2–*z*; iv = 3/2–*x*, 1/2+*y*, 3/2–*z*; v = *x*, –*y*, 1/2+*z*); and (**c**) $[Co(\mathbf{19})_2(NCS)_2]_n{\cdot}4.6n C_6H_5CH_3$ (symmetry codes: i = 1–*x*, 1/2+*y*, 3/2–*z*; ii = 1–*x*, –1/2+*y*, 1/2–*z*; iii = 1–*x*, –*y*, 1–*z*; iv = *x*, –1/2–*y*, 1/2+*z*; v = 1–*x*, 1/2+*y*, 1/2–*z*). H atoms and solvent molecules are omitted. Ellipsoids are plotted at 40% probability level.

Table 13. Selected bond lengths and inter-ring angles in the cobalt(II) coordination polymers containing ligands **16**, **17** and **19**.

Coordination polymer	Co–N_{NCS}/Å	Co–N_{tpy}/Å	py - py /°	py - arene /°	ring C – ring D /° [a]
$[Co(\mathbf{16})_2(NCS)_2]_n{\cdot}3n C_6H_5CH_3$	2.075(2)	2.2068(19), 2.224(2)	19.4, 35.9	55.3	1.8
$[Co(\mathbf{17})_2(NCS)_2]_n{\cdot}4n C_6H_5CH_3$	2.0818(12)	2.1916(13), 2.2152(13)	30.5, 31.6	43.0	45.7
$[Co(\mathbf{19})_2(NCS)_2]_n{\cdot}4.6n C_6H_5CH_3$	2.070(5)	2.200(5), 2.218(5)	18.6, 29.0	46.9	35.6

[a]Ring C and ring D refer to the two rings of the biphenyl group.

In the three polymers grown from toluene, the tpy units adopt conformation **B**, making the structures reminiscent of that seen in $[Co(\mathbf{18})_2(NCS)_2]_n$. Similarly, in $[Co(\mathbf{16})_2(NCS)_2]_n{\cdot}3n C_6H_5CH_3$, $[Co(\mathbf{17})_2(NCS)_2]_n{\cdot}4n C_6H_5CH_3$ and $[Co(\mathbf{19})_2(NCS)_2]_n{\cdot}4.6n C_6H_5CH_3$ the Co atoms lie in a plane, and crystallographic symmetry dictates that all rhombi in a given structure are identical with internal angles of 69.5° and 110.5° (in the structure with ligand **16**), 70.8° and 109.2° (with **17**), 70.3° and 109.7° (with **19**). Another analogy is that the 4′-substituted-[1,1′-biphenyl]-4-yl units are directed up/up/down/down around each rhombus; this contrasts with the cone-assemblies in the polymers containing ligands **16** and **17** that originated from chloroform. However, only the 4′-fluoro-[1,1′-biphenyl]-4-yl domains of the ligands **17** lie over the rhombi (Figure 90a) like in $[Co(\mathbf{18})_2(NCS)_2]_n$, while the 4′-bromo-[1,1′-biphenyl]-4-yl domains in $[Co(\mathbf{19})_2(NCS)_2]_n{\cdot}4.6n C_6H_5CH_3$ project directly above and below the plane. Although the nets and their packing are similar, additional differences between the three networks grown from toluene/methanol can be found by inspecting the interactions, the amount of lattice solvent and the void space in each non-solvated structure. As expected, all three coordination assemblies present molecules of toluene engaging in face-to-face π-stacking interactions; however, they involve the central pyridine ring in each case, and never the 4′-substituted-[1,1′-biphenyl]-4-yl units. In $[Co(\mathbf{16})_2(NCS)_2]_n{\cdot}3n C_6H_5CH_3$ there is a double π-stacking interaction between the pyridine ring and two different molecules of toluene (Figure 89c). The metrics for the π-π interactions are centroid...centroid = 3.69 and 3.65 Å, and angle between the ring planes = 5.4 and 9.4°. Only one toluene molecule engages in a π-stacking interaction with the central pyridine ring in $[Co(\mathbf{17})_2(NCS)_2]_n{\cdot}4n C_6H_5CH_3$ (Figure 90c), with a centroid...centroid distance = 3.87 Å, and an angle between the ring planes = 4.8°. Analogous to the compound containing ligand **16**, that comprising **19** contains two molecules of toluene involved in a double π-stacking interaction (Figure 91c), although one of these interactions is very weak; the metrics for the π-π interactions are centroid...centroid = 4.05 and 3.71 Å, and angle between the ring planes = 18.7 and 2.2°. The solvent-accessible voids (calculated in Mercury[12] using a contact surface map with probe radius = 1.2 Å after removing the lattice solvent from the crystal structure) correspond to 34.5% of the total lattice volume in $[Co(\mathbf{16})_2(NCS)_2]_n{\cdot}3n C_6H_5CH_3$, to 39.4% in $[Co(\mathbf{17})_2(NCS)_2]_n{\cdot}4n C_6H_5CH_3$ and to 43.5% in $[Co(\mathbf{19})_2(NCS)_2]_n{\cdot}4.6n C_6H_5CH_3$. In the series just described, the greater amount of toluene incorporated in the lattice is in line with the increasing percentage of void in the packing.

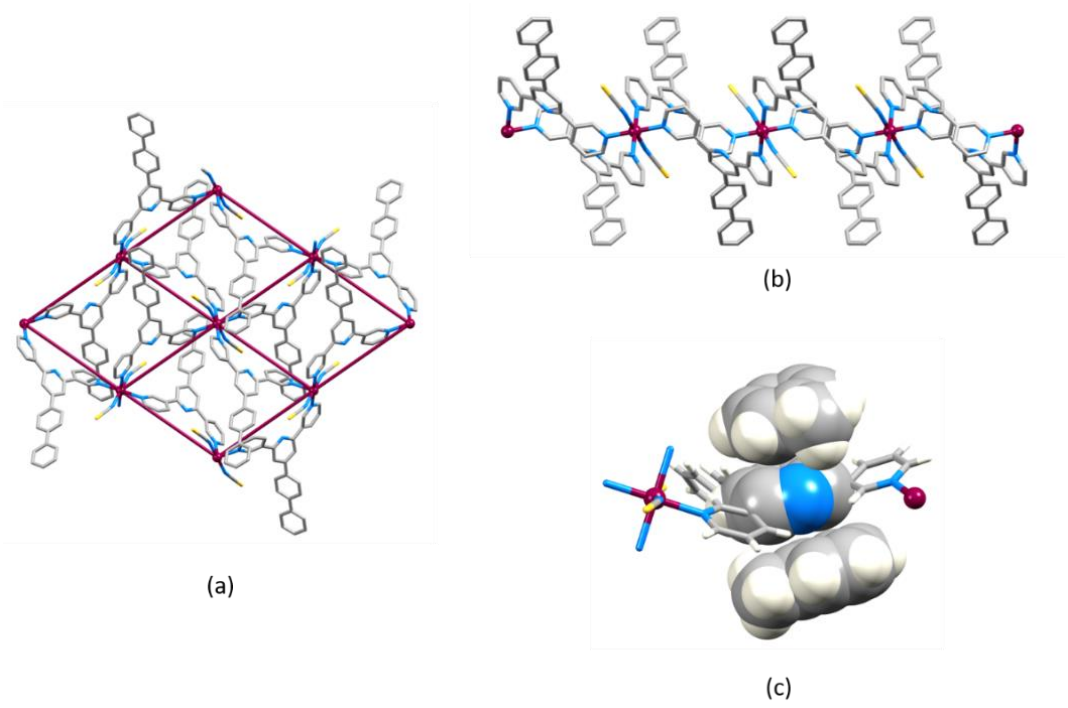

Figure 89. The structure of $[Co(\mathbf{16})_2(NCS)_2]_n \cdot 3n C_6H_5CH_3$. (**a**) Part of the 2D-net, and (**b**) a side view of part of one sheet. (**c**) Double π-stacking interactions between the central pyridine ring and two molecules of toluene.

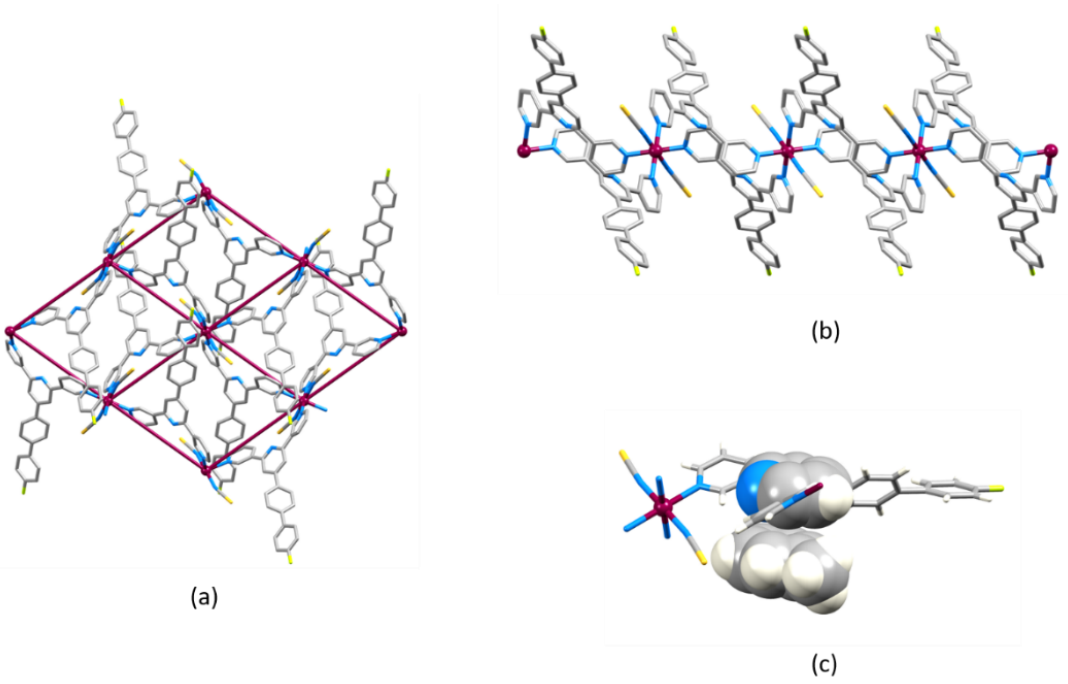

Figure 90. The structure of $[Co(\mathbf{17})_2(NCS)_2]_n \cdot 4n C_6H_5CH_3$. (**a**) Part of the 2D-net, and (**b**) a side view of part of one sheet. (**c**) Single π-stacking interaction between the central pyridine ring and one molecule of toluene.

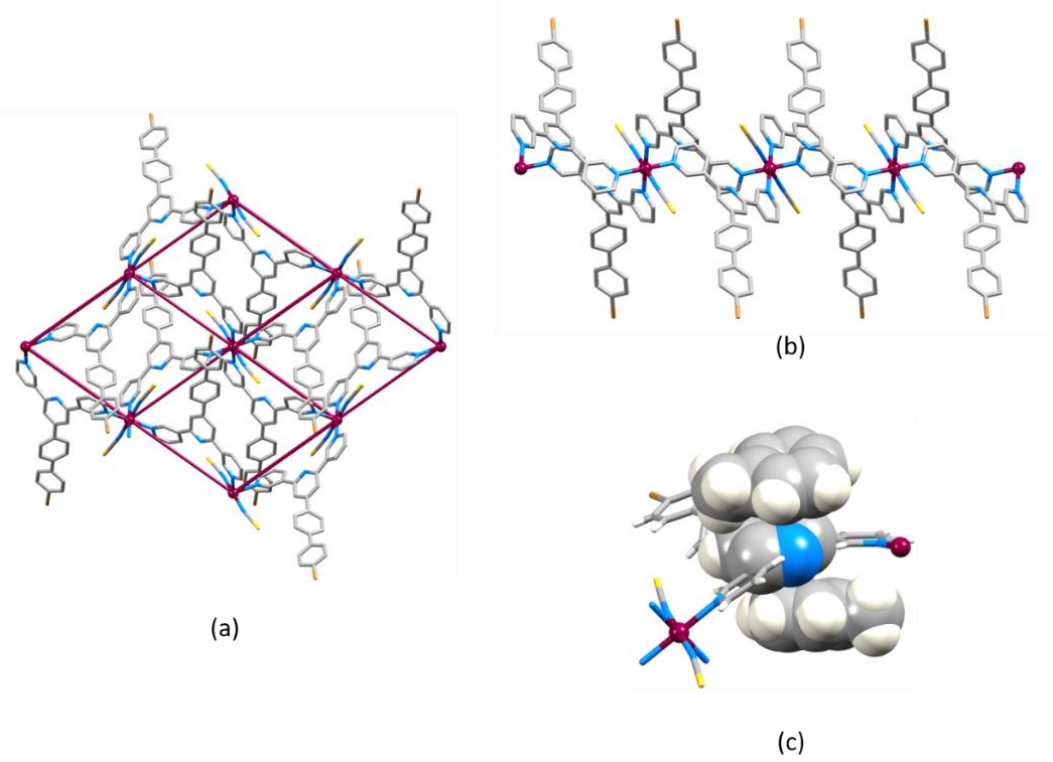

Figure 91. The structure of ([Co(**19**)$_2$(NCS)$_2$]$_n$·4.6nC$_6$H$_5$CH$_3$). (**a**) Part of the 2D-net, and (**b**) a side view of part of one sheet. (**c**) Double π-stacking interactions between the central pyridine ring and two molecules of toluene.

As mentioned above, only a preliminary structure could be obtained from the product of the reaction of ligand **20** (X = Me) with Co(NCS)$_2$ carried out in toluene/methanol. This corresponds to the formulation of [Co(**20**)$_2$(NCS)$_2$]$_n$, and the compound crystallizes in the monoclinic space group $P2_1/n$. Although this was only a preliminary structure determination, the gross structure of a 2D-network was confirmed; there is no information about the presence or absence of solvent molecules. The asymmetric unit is depicted in Figure 92 and contains one independent terpyridine ligand in conformation **B** (Scheme 27). Bond lengths and angles are unexceptional and compiled in Table 14.

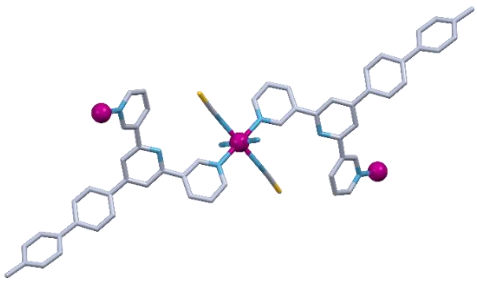

Figure 92. Structure of the asymmetric unit in [Co(**20**)$_2$(NCS)$_2$]$_n$ with symmetry-related atoms.

Table 14. Co–N bond lengths and inter-ring angles in the cobalt(II) coordination polymer containing ligand **20**.

	Co–N_{NCS}/Å	**Co–N_{tpy}/Å**	**py - py /°**	**py - arene /°**	**ring C – ring D /°** [a]
$[Co(\mathbf{20})_2(NCS)_2]_n$	2.059(10)	2.178(10), 2.253(10)	32.9, 38.2	39.7	27.1

[a]Ring C and ring D refer to the two rings of the biphenyl group, with C directly bonded to the tpy unit.

The 3,2′:6′,3″-tpy unit adopts conformation **B**, in contrast with what is seen in the polymer with the same ligand grown from chloroform/methanol, but consistent with the other ligands when reacted in toluene/methanol. Once more, the cobalt atoms lie in a plane, and crystallographic symmetry dictates that all rhombi are identical with internal angles of 81.5° and 98.5°. The 4′-methyl-[1,1′-biphenyl]-4-yl units are directed up/up/down/down around each rhombus; this contrasts with the cone-assemblies in the polymer originated from chloroform and containing the same ligand $[Co(\mathbf{20})_2(NCS)_2]_n{\cdot}4.5n CHCl_3$. Similarly to what seen in $[Co(\mathbf{18})_2(NCS)_2]_n$ and in $[Co(\mathbf{17})_2(NCS)_2]_n{\cdot}4n C_6H_5CH_3$, ligands **20** lie over the rhombi (Figure 93a).

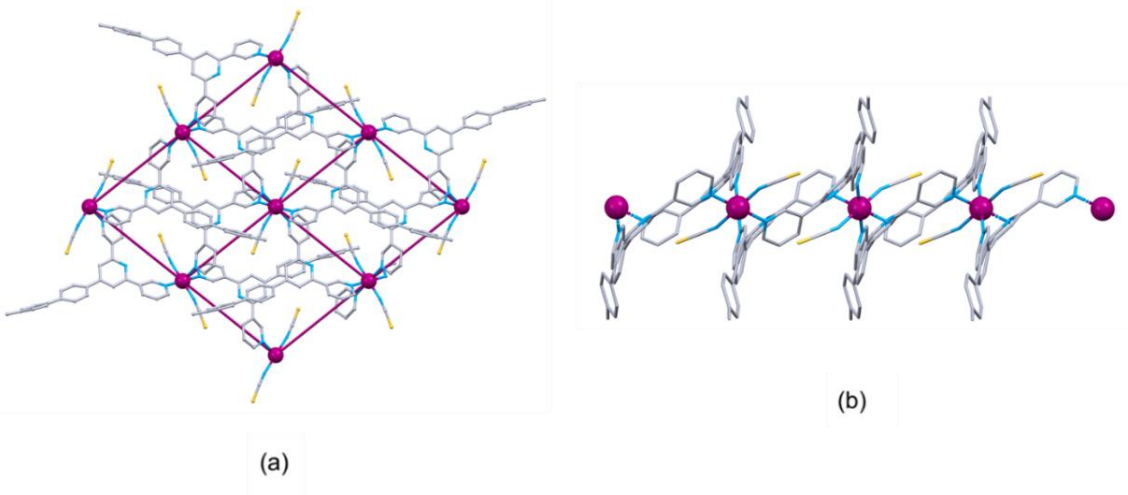

Figure 93. The structure of $[Co(\mathbf{20})_2(NCS)_2]_n$. (**a**) Part of the 2D-net showing that the ligands lie over the rhombi; (**b**) a side view of part of one sheet.

4.5 Reactions of **21** with $Co(NCS)_2$[17]

Parts of the work described in this section were carried out in collaboration with Master's candidate Samantha Novak.

To better understand the role of the solvent, a series of experiments was conducted with 4′-[4-(naphthalen-1-yl)phenyl]-3,2′:6′,3″-terpyridine (**21**) and cobalt(II) thiocyanate under conditions of crystal growth by using different solvent combinations. Single crystals of

$[Co(\mathbf{21})_2(NCS)_2]_n{\cdot}2n CHCl_3$ and $[Co(\mathbf{21})_2(NCS)_2]_n{\cdot}2n C_6H_5Me$ were grown under ambient conditions by layering a MeCN solution of $Co(NCS)_2$ over a $CHCl_3$ solution of **21**, or a MeOH solution of $Co(NCS)_2$ over a toluene solution of **21**, respectively. X-ray quality crystals were selected for XRD, and the remaining crystals were used for PXRD analysis (see below). The two compounds crystallize in the monoclinic space groups $P2_1/n$ or $P2_1/c$, and each possesses a 2D-network with the Co(II) centers acting as 4-connecting nodes. The structures of the asymmetric units with symmetry-generated atoms are shown in Figure 94. The Co atom in each structure is six-coordinate and lies on an inversion center, being bonded to four different, but crystallographically equivalent, ligands **21**. Selected bond lengths and angles in each cobalt(II) coordination sphere are given in Table 15 and are unexceptional.

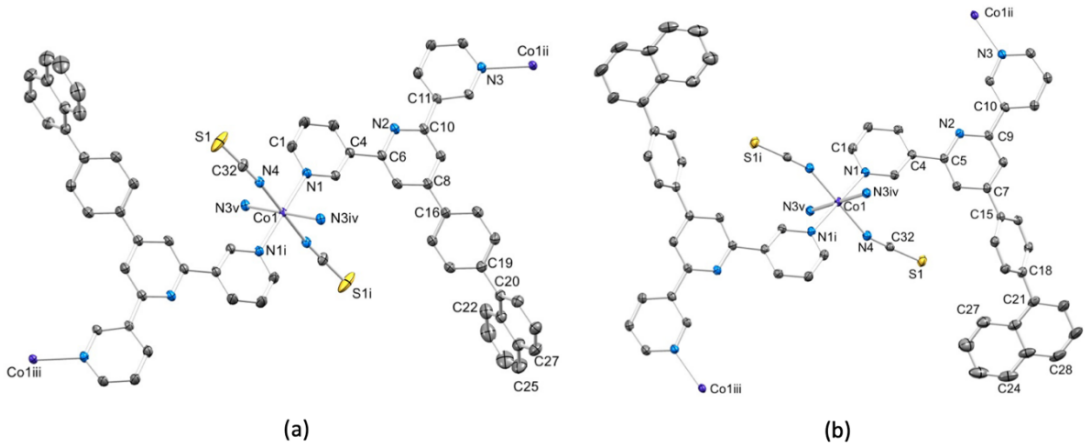

Figure 94. The structures of the asymmetric units with symmetry-generated atoms in (**a**) $[Co(\mathbf{21})_2(NCS)_2]_n{\cdot}2n CHCl_3$ (symmetry codes: i = $-x$, $1-y$, $1-z$; ii = $^1/_2-x$, $-^1/_2+y$, $^1/_2-z$; iii = $-^1/_2-x$, $^1/_2+y$, $^3/_2-z$; iv = $^1/_2-x$, $^1/_2+y$, $^1/_2-z$; v = $-^1/_2-x$, $^1/_2-y$, $^1/_2+z$), and (**b**) $[Co(\mathbf{21})_2(NCS)_2]_n{\cdot}2n C_6H_5Me$ (symmetry codes: i = $1-x$, $1-y$, $-z$; ii = $1-x$, $^1/_2+y$, $^1/_2-z$; iii = $1-x$, $-^1/_2+y$, $-^1/_2-z$; iv = x, $^3/_2-y$, $-^1/_2+z$; v = $1-x$, $-^1/_2+y$; $^1/_2-z$). H atoms and solvent molecules are omitted. Ellipsoids are plotted at a 40% probability level.

Table 15. Selected bond lengths and angles in $[Co(\mathbf{21})_2(NCS)_2]_n{\cdot}2n CHCl_3$ and $[Co(\mathbf{21})_2(NCS)_2]_n{\cdot}2n C_6H_5Me$.

Coordination polymer	Co–N_{tpy} / Å	Co–N_{NCS} / Å	N_{tpy}–Co–N_{NCS} / °	N_{tpy}–Co–N_{tpy} / °
$[Co(\mathbf{21})_2(NCS)_2]_n{\cdot}2n CHCl_3$	2.076(3)	2.188(3), 2.221(3)	90.25(13), 89.75(13), 92.38(12), 87.62(12)	91.95(12), 88.05(12)
$[Co(\mathbf{21})_2(NCS)_2]_n{\cdot}2n C_6H_5Me$	2.084(2)	2.190(2), 2.239(2)	88.26(9), 91.74(9), 87.97(9), 92.03(9)	89.60(9), 90.40(9)

In $[Co(\mathbf{21})_2(NCS)_2]_n \cdot 2n CHCl_3$, ligand **21** adopts conformation **A** (Scheme 27), whereas in $[Co(\mathbf{21})_2(NCS)_2]_n \cdot 2n C_6H_5Me$ conformation **B** is observed. This switch results in distinct differences between the 2D-assemblies, quantified by a comparison of the angles between the planes of adjacent aromatic rings in the ligand in each structure presented in Table 16. Moreover, when the terpyridine adopts conformation **A**, the vectorial properties of each N1 and N3 in each ligand are equivalent. In contrast, the different vectorial properties of the N-donor lone pairs when ligand **21** is in conformation **B** lead to three possible coordination modes for a *trans*-arrangement of ligands. Just as in the earlier discussions in the previous sections, the labels *in* and *out* can be used to describe the orientation of each N lone pair with respect to the central pyridine ring, as depicted in Scheme 33.

Table 16. Angles between planes of adjacent aromatic rings in $[Co(\mathbf{21})_2(NCS)_2]_n \cdot 2n CHCl_3$ and $[Co(\mathbf{21})_2(NCS)_2]_n \cdot 2n C_6H_5Me$.

Coordination polymer	py - py / °	py - py / °	py – phenylene / °	phenylene – naphthyl / °
$[Co(\mathbf{21})_2(NCS)_2]_n \cdot 2n CHCl_3$	15.8	15.5	34.7	52.0
$[Co(\mathbf{21})_2(NCS)_2]_n \cdot 2n C_6H_5Me$	33.2	22.4	50.5	63.1

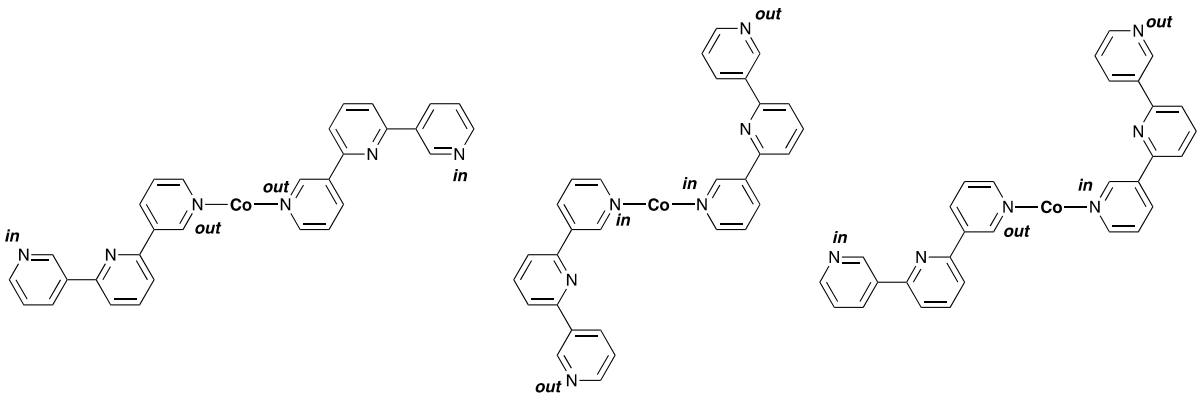

Scheme 33. Three coordination modes are possible for a *trans*-arrangement of ligands at a Co center when the 3,2′:6′:3″-tpy unit assumes conformation **B**, but only the left-hand two modes are permitted when the metal ion lies on an inversion center.

When the tpy-unit assumes conformation **A**, all motifs are *out*/*out*, as this is the only possibility (Figure 95a); on the other hand, conformation **B** allows three possible coordination modes for a *trans*-arrangement of ligands. However, since the Co atom in $[Co(\mathbf{21})_2(NCS)_2]_n \cdot 2n C_6H_5Me$ lies on a center of symmetry, only two of the three coordination modes shown in Scheme 33 are permitted. Each Co in $[Co(\mathbf{21})_2(NCS)_2]_n \cdot 2n C_6H_5Me$ is crystallographically equivalent, and both *trans out*/*out* and *in*/*in* arrangements are present at each metal center (Figure 95b). This

contrasts with the arrangement in [Co(**21**)$_2$(NCS)$_2$]$_n$·2nCHCl$_3$ leads to a significant difference between the {Co(**21**)$_4$} units in the networks (Figure 95a versus 95b).

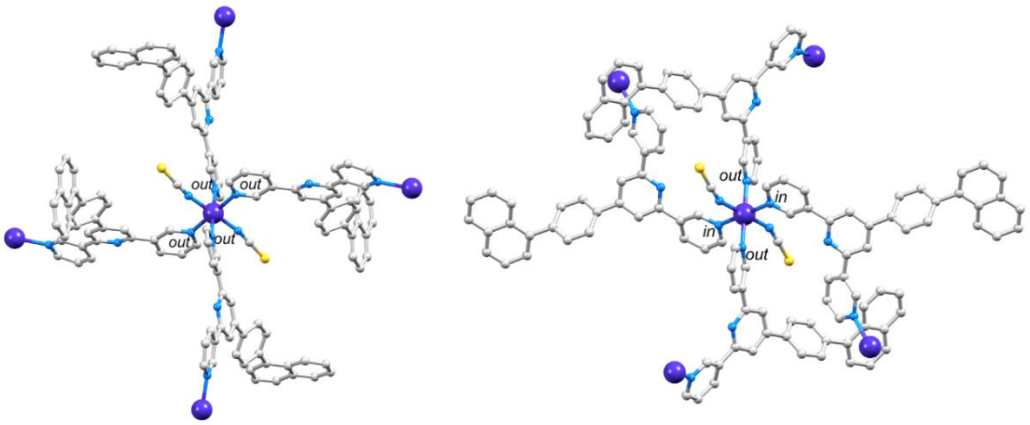

Figure 95. The arrangement of ligands **21** in the coordination sphere of the Co atom in (**a**) [Co(**21**)$_2$(NCS)$_2$]$_n$·2nCHCl$_3$, and (**b**) [Co(**21**)$_2$(NCS)$_2$]$_n$·2nC$_6$H$_5$Me. See Scheme 33 for definitions of the *in* and *out* labels.

Part of the (4,4) network in [Co(**21**)$_2$(NCS)$_2$]$_n$·2nCHCl$_3$ is shown in Figure 96a. The Co atoms are coplanar, and the 4-(naphthalen-1-yl)phenyl substituents protrude above and below the plane defined by the Co atoms. Around each rhombus in the net, the 4-(naphthalen-1-yl)phenyl groups are arranged in an up/up/down/down configuration, and adjacent 2D-sheets are locked together by face-to-face π-stacking interactions between naphthalenyl rings in one layer with the central pyridine ring of the 3,2′:6′,3″-tpy units in the neighboring sheet (Figure 96c). Metrics for the π-π interaction are centroid...centroid = 3.69 Å, and angle between the ring planes = 1.2°. The up/up/down/down configuration of the arene substituents leads to extended π-stacking interactions which interconnect all adjacent sheets in the lattice. Viewing the structure of [Co(**21**)$_2$(NCS)$_2$]$_n$·2nCHCl$_3$ down the *a*-axis without solvent molecules present reveals approximately linear channels (Figure 96d), and the solvent-accessible void space in the lattice is ca. 24% of the total volume. The disordered CHCl$_3$ molecules occupy these channels.

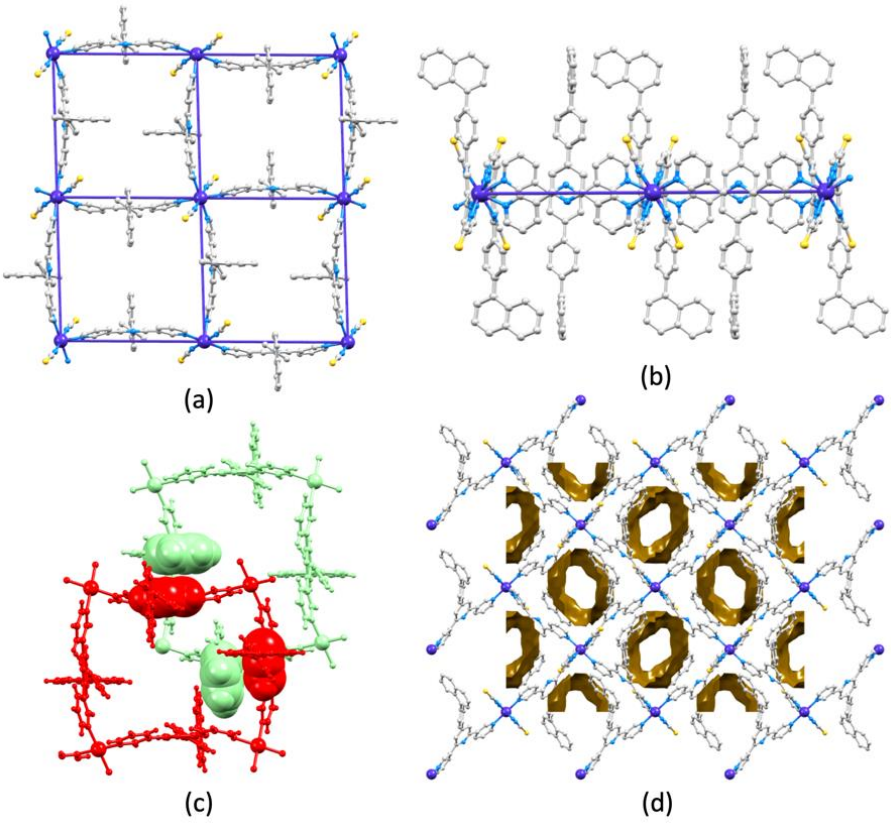

Figure 96. The structure of [Co(**21**)$_2$(NCS)$_2$]$_n$·2nCHCl$_3$. (**a**) Part of one (4,4) net with connection lines between the Co atoms to emphasize the network topology; H atoms and solvent molecules are omitted for clarity. (**b**) The network viewed from the side illustrates the positions of the peripheral naphthalenyl groups. (**c**) Stacking of naphthalenyl and 3,2′:6′,3″-domains in adjacent 2D-sheets. (**d**) View down the *a*-axis (solvent molecules omitted) showing the void (calculated using a contact surface map with probe radius = 1.2 Å); drawn using Mercury 2020.1.

In [Co(**21**)$_2$(NCS)$_2$]$_n$·2nC$_6$H$_5$Me, each toluene molecule is disordered over a symmetry element, with 50% site occupancies of head-to-tail positions. For the discussion below, one position for each toluene molecule is considered. Two views of the (4,4) net in [Co(**21**)$_2$(NCS)$_2$]$_n$·2nC$_6$H$_5$Me are depicted in Figures 97a and 97b. As in [Co(**21**)$_2$(NCS)$_2$]$_n$·2nCHCl$_3$ (Figure 96), the Co atoms in each sheet are coplanar, and terpyridine ligands adopt an up/up/down/down arrangement around each rhombus (Figure 97c). Inspection of Figures 97a and 97c reveals that ligands **21** lie over the rhombi in the net in [Co(**21**)$_2$(NCS)$_2$]$_n$·2nC$_6$H$_5$Me, in contrast to the upright positions found in [Co(**21**)$_2$(NCS)$_2$]$_n$·2nCHCl$_3$ (Figures 96a). This impacts the solvent-accessible voids in the lattice (Figures 97d) which comprise a series of interlinked cavities (ca. 24% of the total lattice volume) in contrast to the open channels in [Co(**21**)$_2$(NCS)$_2$]$_n$·2nCHCl$_3$.

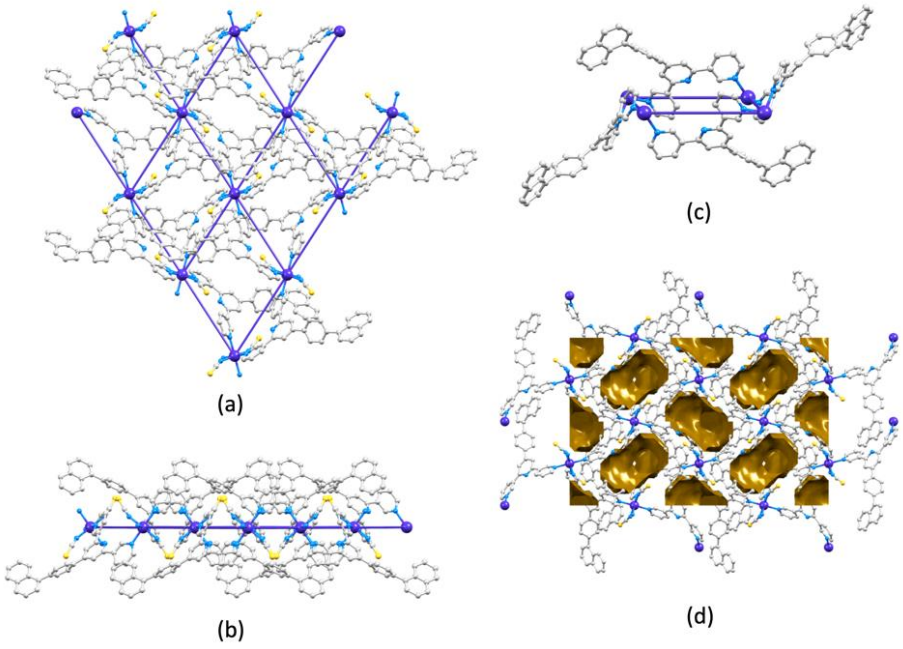

Figure 97. The structure of $[Co(\mathbf{21})_2(NCS)_2]_n \cdot 2n C_6H_5Me$. (**a**) Part of one 2D-net with connection lines between the Co atoms to highlight the (4,4) net; H atoms and solvent molecules are omitted for clarity, and (**b**) the same portion of the net viewed into the plane containing the Co atoms. (**c**) Arrangement of ligands **21** around a rhombus in the net. (**d**) View down the *a*-axis (solvent molecules omitted) showing the void space; drawn using Mercury 2020.1 and calculated using a contact surface map with a probe radius of 1.2 Å.

The toluene molecules occupying the cavities are involved in a face-to-face π-interaction with the pyridine ring containing N2 and $C–H_{py}...\pi_{toluene}$ contacts involving the pyridine rings with N2 and N3 (Figure 98). For the face-to-face contact, the distance between the ring centroids is 3.8 Å, and the angle between the ring planes is 9.8°. For the $C–H_{py}...\pi_{toluene}$ contacts, the H...centroid distances are 3.2 and 3.4 Å, and the C–H...centroid angles are 151 and 168°, respectively.

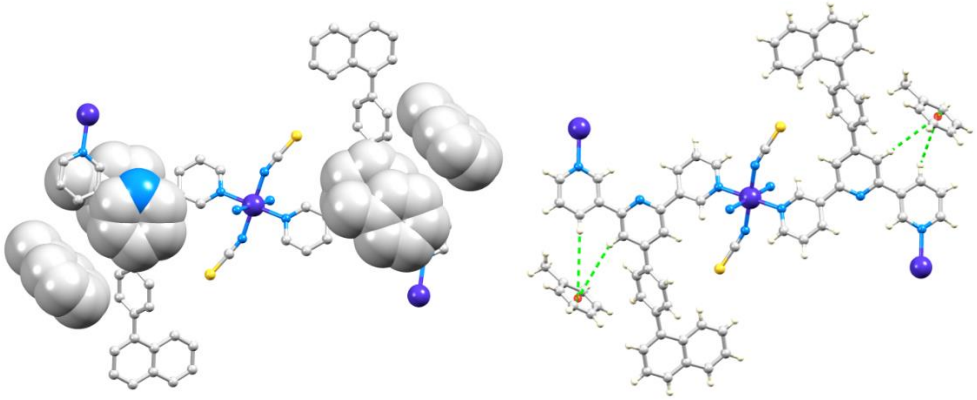

Figure 98. The structure of $[Co(\mathbf{21})_2(NCS)_2]_n \cdot 2n C_6H_5Me$: face-to-face π-interactions involving toluene molecules and the pyridine rings containing N2, and edge-to-face (C–H...π) contacts between the pyridine rings with N2 and N3 and toluene.

In order to verify that the crystals selected for single-crystal X-ray diffraction were representative of the bulk crystalline materials, PXRD was carried out on the remaining crystals in each crystallization tube. Figure 99 shows comparisons of the experimental PXRD patterns (in red) and the patterns predicted from the single-crystal structures (in black). For each compound, there was a match for every peak in the predicted pattern with those in the experimental PXRD pattern. No additional peaks were observed in the PXRD of the bulk materials.

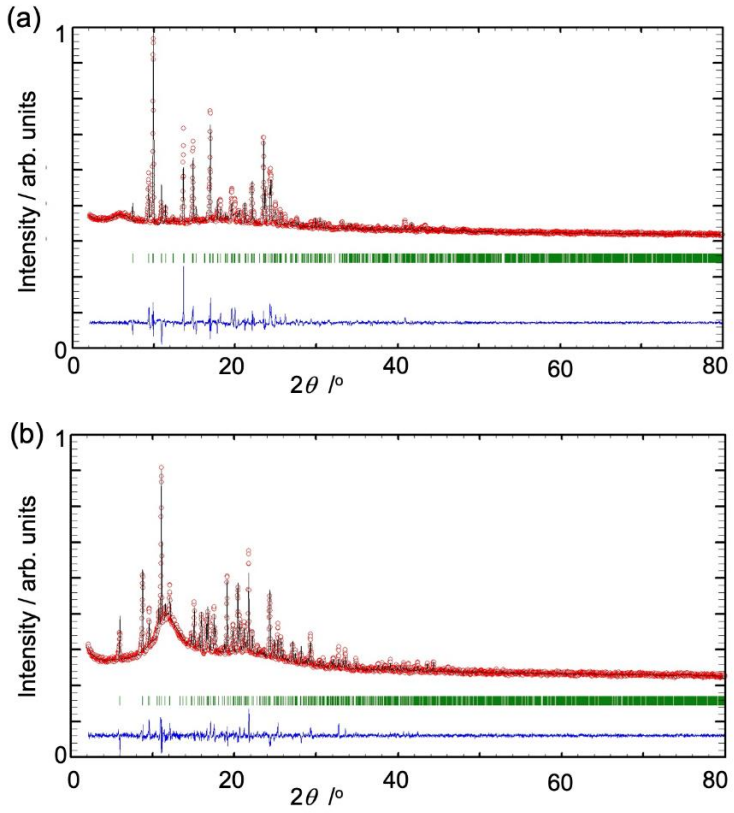

Figure 99. PXRD (Cu*Kα* radiation) patterns (red circles) of the bulk crystalline materials of (**a**) [Co(**21**)$_2$(NCS)$_2$]$_n$·2nCHCl$_3$, and (**b**) [Co(**21**)$_2$(NCS)$_2$]$_n$·2nC$_6$H$_5$Me, with fitting to the predicted patterns from the single-crystal structures. The black lines are the best fits from the Rietveld refinements, and the green lines show the Bragg peak positions. Each blue plot gives the difference between calculated and experimental points, and the differences in intensities arise from differences in the preferred orientations of the crystallites in the bulk samples.

The IR spectra of the two cobalt(II) compounds present bands in the fingerprint region, which are mainly characteristic of coordinated **21**. The dominant absorption at 2063 cm^{-1} for [Co(**21**)$_2$(NCS)$_2$]$_n$·2nCHCl$_3$ (Figure 100) and 2070 cm^{-1} for [Co(**21**)$_2$(NCS)$_2$]$_n$·2nC$_6$H$_5$Me arises from the CN stretching mode of the thiocyanato ligands.

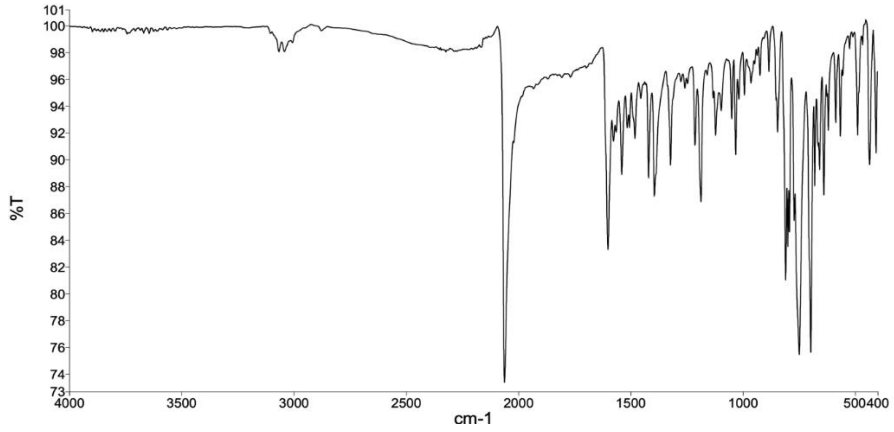

Figure 100. Solid-state IR spectrum of [Co(**21**)$_2$(NCS)$_2$]$_n$·2nCHCl$_3$.

Thermogravimetric analysis was performed on the two polymers bearing ligand **21**, with a similar procedure described in Section 4.4 for [Co(**17**)$_2$(NCS)$_2$]$_n$·4nCHCl$_3$. Crystals of [Co(**21**)$_2$(NCS)$_2$]$_n$·2nCHCl$_3$ were heated to 80 °C (and the temperature was maintained for 10 minutes) in the TGA instrument; the loss of CHCl$_3$ was detected (Figure 101) with mass peaks at m/z 83.0, 85.0 and 87.0 corresponding to CHCl$_2^+$ as the dominant fragment.[13] After cooling, the sample retained crystallinity. The weight loss of 17.1% corresponded to the loss of approximately 2 CHCl$_3$ molecules per formula unit (calculated 18.6%). In order to investigate whether the coordination network maintained its integrity, the same sample was placed in contact with CHCl$_3$ vapor for 48 h and was again analysed using TGA (Figure S78). Loss of CHCl$_3$ was again detected, confirming that, after the initial removal of solvent, the coordination assembly was able to re-absorb CHCl$_3$. A third cycle was performed with the same crystals exposed to CDCl$_3$ vapor for 24 hours and then analysed by TGA (Figure S79). Loss of CDCl$_3$ was confirmed by the presence of mass peaks at m/z 84.0, 86.0 and 88.0 corresponding to the CDCl$_2^+$ ion. In the fourth cycle, the crystalline material was recovered from the preceding TGA experiment and exposed to CH$_2$Cl$_2$ vapor for 24 hours. The TGA trace of the resultant crystal showed loss of CH$_2$Cl$_2$ (m/z 49.0, 51.0, 84.0 and 86.0 arising from CH$_2$Cl$^+$ and CH$_2$Cl$_2^+$) at around 40 °C (Figure S80). Finally, an analogous experiment was attempted using CCl$_4$, but the TGA of the crystals after exposure to CCl$_4$ vapor for 24 hours revealed no change in mass over a period of 10 minutes heating at 80 °C. This is consistent with no uptake of CCl$_4$ into the crystal lattice and suggests that CCl$_4$ is too large to enter the channels in the structure.

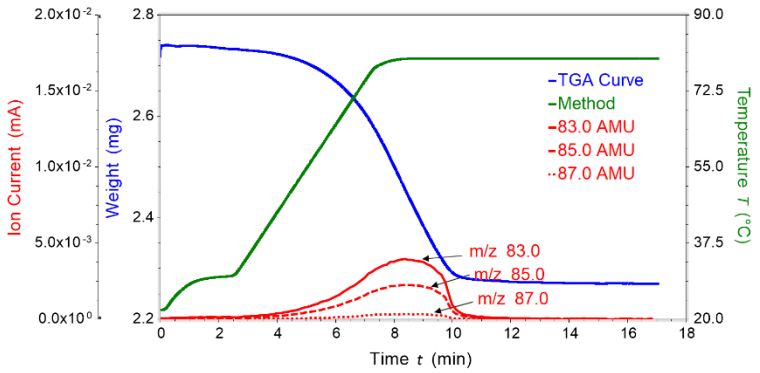

Figure 101. TGA and mass spectrometric traces for the analysis of [Co(**21**)$_2$(NCS)$_2$]$_n$·2*n*CHCl$_3$. Green: temperature vs. time; blue: weight of sample vs. time; red: mass detection for m/z 83.0 (most intense peak), 85.0 and 87.0.

Finally, [Co(**21**)$_2$(NCS)$_2$]$_n$·2*n*C$_6$H$_5$Me was analysed by TGA. It was first heated to 150 °C, and this temperature was maintained for 30 minutes. The loss of toluene was detected with peaks in the mass spectrum of the TGA-MS at *m*/*z* 92.0, 91.0 (highest intensity peak), 65.0 and 39.0 (Figure 102). The weight loss of 14.8% corresponded to the complete loss of toluene from the lattice. Visually, the sample appeared to have lost crystallinity. The same sample was then placed in contact with toluene vapor for 24 hours, and the subsequent TGA analysis showed no appreciable mass loss, consistent with the fact that once toluene had been removed from [Co(**21**)$_2$(NCS)$_2$]$_n$·2*n*C$_6$H$_5$Me, it was unable to be re-absorbed. This is consistent with the presence of the aromatic solvent in [Co(**21**)$_2$(NCS)$_2$]$_n$·2*n*C$_6$H$_5$Me playing a structural role in contrast to the CHCl$_3$ in [Co(**21**)$_2$(NCS)$_2$]$_n$·2*n*CHCl$_3$ occupying channels in a non-ordered manner. Key to the former are the π-stacking interactions, and these may template the assembly of the network in [Co(**21**)$_2$(NCS)$_2$]$_n$·2*n*C$_6$H$_5$Me and the integrity of the 2D-network is not maintained once the solvent is removed.

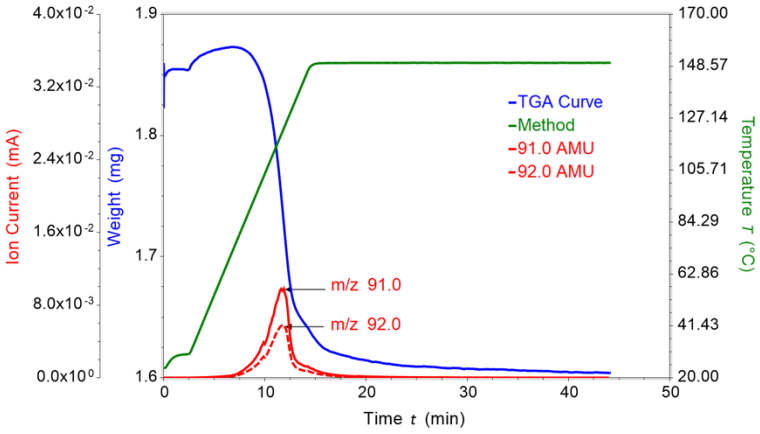

Figure 102. TGA and mass spectrometric traces for the analysis of [Co(**21**)$_2$(NCS)$_2$]$_n$·2*n*C$_6$H$_5$Me. Green: temperature vs. time; blue: weight of sample vs. time; red: mass detection for *m*/*z* 92.0, 91.0 (most intense peak), 65.0 and 39.0.

4.6 Conclusions

The characterization and the structural analysis of twenty-two coordination polymers based on cobalt(II) thiocyanate with seventeen 3,2′:6′,3″-tpy ligands have been reported. Twenty-one of these are 2D-polymers possessing the same topology: *trans*-{$Co(NCS)_2N_4$} 4-connecting nodes, and 3,2′:6′,3″-tpy ligands bridging between adjacent Co centers; while one is a 1D-polymer with a molecule of methanol coordinated on the cobalt(II) atom, reducing its connectivity. The 1D-polymer assembled from the reaction of $Co(NCS)_2$ with ligand **1**, which shows a different coordination behavior again compared to the rest of the reported terpyridine ligands. In particular, its reaction with cobalt(II) thiocyanate yielded three polymeric products in the same test tube: $[Co(\mathbf{1})(NCS)_2(MeOH)_2]_n$, consisting of 1D-chains, and the two pseudopolymorphs $[Co(\mathbf{1})_2(NCS)_2]_n{\cdot}3n$MeOH and $[Co(\mathbf{1})_2(NCS)_2]_n{\cdot}2.2n$$CHCl_3$, which possess 2D nets. PXRD confirmed that the dominant product in the bulk sample was the 1D-coordination polymer. This first investigation highlighted the interplay between thermodynamic and kinetic products from crystallization processes and illustrates once again that the full understanding of the assembly algorithms of metallo-coordination polymers involving terpyridine ligands has not yet been reached.

The focus was then moved to the effect of the *n*-alkyloxy chain length on the coordination assembly. This was studied comparing the outcome of the reactions of ligands **2**–**6** with $Co(NCS)_2$. The networks containing **2**, **3** and **4** are similar and comprise two geometrically different rhombi, with nets that pack in an ABAB... manner and cone-like arrangements of *n*-alkyloxyphenyl groups being accommodated in a similar unit in an adjacent net. An increase in the *n*-alkyloxy chain length had two consequences: a change in the conformation of the 3,2′:6′,3″-tpy metal-binding domain from **A** to **B** (Scheme 27) and the (4,4) nets comprising identical rhombi in $[Co_2(\mathbf{5})_4(NCS)_4]_n$ and $[Co(\mathbf{6})_2(NCS)_2]_n$. Although these features are reminiscent of the nets in $[Co(\mathbf{1})_2(NCS)_2]_n{\cdot}3n$MeOH and $[Co(\mathbf{1})_2(NCS)_2]_n{\cdot}2.2n$$CHCl_3$, the change from a peripheral methoxy substituent (ligand **1**) to the longer chains in **5** and **6** modifies the arrangement of adjacent sheets. In $[Co_2(\mathbf{5})_4(NCS)_4]_n$ and $[Co(\mathbf{6})_2(NCS)_2]_n$, the packing of the (4,4) nets allows the *n*-alkyloxy tails to be accommodated in cavities in an adjacent layer and no crystallization solvent is present in the lattice.

The following research aimed to understand the effect of replacing a straight alkyloxy chain as a substituent in the 3,2′:6′,3″-tpy ligands with branched ones. For this purpose, the coordination chemistry of ligands *rac*-**11**, **12** and **13**, bearing the isomeric butoxy chains, with $Co(NCS)_2$ was studied. The nets containing the branched substituents comprise identical rhombi with a down/down/up/up arrangement of four 3,2′:6′,3″-tpy linkers around a rhombus, in contrast with the cone arrangement seen in the polymer with the linear ligand **4**. This difference is undoubtedly related to the switch in the 3,2′:6′,3″-tpy domain from conformation **A** (adopted in ligand **4**) to conformation **B**, observed in *rac*-**11**, **12** and **13**. Despite the significant structural perturbation from linear to branched substituents, changes in the spatial properties of the second group of ligands are accommodated with subtle

conformational changes in the 3,2′:6′,3″-tpy domain. The 2D-polymer assembled from $Co(NCS)_2$ and **15**, bearing an isopentyloxy chain, is analogous to those obtained with the other branched ligands, in particular the network with **12**. The similarities between these two can be found both comparing the internal angles in the rhombi and the angles between the planes of pairs of bonded arene rings in the coordinated ligands. This time, the switch from the linear ligand **5** to the branched one with the same chain length, **15**, does not cause significant structural perturbation.

The subsequent study presented five (4,4) nets, each comprising a 4′-substituted-[1,1′-biphenyl]-4-yl-3,2′:6′,3″-terpyridine, in which the substituents are Me (**20**), H (**16**), F (**17**), Cl (**18**) or Br (**19**); the chosen crystallization solvents were methanol and chloroform. Changes in the conformation of the 3,2′:6′,3″-tpy unit coupled with the different peripheral substituents led to three structure types. For ligands **20**, **16** and **17**, highly symmetrical nets are formed, in which the 3,2′:6′,3″-tpy adopts conformation **A**, and the 4′-substituted-[1,1′-biphenyl]-4-yl units are once again arranged in cones pointing above and below each 2D-sheet; cone…cone π-stacking interactions contribute to the packing of sheets. These networks are porous, with $CHCl_3$ molecules occupying distinct types of cavities which can be differentiated using TGA; half of the solvent in $[Co(\mathbf{17})_2(NCS)_2]_n \cdot 4n CHCl_3$ can be reversibly removed and replaced by $CDCl_3$ or CH_2Cl_2. A second structure-type is observed for $[Co(\mathbf{18})_2(NCS)_2]_n$, in which the organic linkers lie over the rhombi in the planar (4,4) net defined by the Co atoms; the 3,2′:6′,3″-tpy exhibits conformation **B**. Each Cl atom is involved in a Cl…π interaction with a pyridine ring in the adjacent sheet. The network in $[Co(\mathbf{19})_2(NCS)_2]_n \cdot n CHCl_3$ represents a third structure-type in which the (4,4) net defined by the Co atoms is non-planar, and two independent 3,2′:6′,3″-tpy ligands adopt conformations **A** and **B**, respectively. Although adjacent sheets in this polymer are closely associated, there are no Br…π interactions. Face-to-face π-stacking interactions are not observed in either $[Co(\mathbf{18})_2(NCS)_2]_n$ or $[Co(\mathbf{19})_2(NCS)_2]_n \cdot n CHCl_3$. This investigation highlights that a combination of the conformational flexibility of the 3,2′:6′,3″-tpy metal-binding domain with a change in the peripheral group (Me, H, F, Cl or Br) leads to significant structural variation while retaining a 2D-network defined by 4-connecting Co nodes. The same ligands **16**–**20** were reacted with cobalt(II) thiocyanate in a second combination of solvents, i.e. methanol/toluene, and this proved to have consequences on the assembly of the coordination polymers. Only the structures containing ligands **16** (X = H), **17** (X = F) and **19** (X = Br) were determined and a preliminary cif file was obtained for the compound with ligand **20**. In each of these networks, the 3,2′:6′,3″-tpy domain adopts conformation **B** (Scheme 27) and the structures of the asymmetric units in $[Co(\mathbf{16})_2(NCS)_2]_n \cdot 3n C_6H_5CH_3$, $[Co(\mathbf{17})_2(NCS)_2]_n \cdot 4n C_6H_5CH_3$ and $[Co(\mathbf{19})_2(NCS)_2]_n \cdot 4.6n C_6H_5CH_3$ are similar. The Co atoms lie in a plane, and crystallographic symmetry dictates that all rhombi in a given structure are identical, with the 4′-substituted-[1,1′-biphenyl]-4-yl units directed up/up/down/down around each rhombus, in contrast with the cone-assemblies. Despite the similarities between the nets, differences emerge by inspecting the interactions in the packing, the amount of lattice solvent and the void space (calculated in each non-solvated structure). The three coordination assemblies present either

one or two molecules of toluene engaging in face-to-face π-stacking interactions with the central pyridine ring. The preliminary structure of the polymer assembled from ligand **20** is consistent with a 2D-network, once again with the 3,2′:6′,3″-tpy unit exhibiting conformation **B** and identical rhombi formed by the cobalt atoms, coherently with the other assemblies grown from the combination methanol/toluene.

To better understand the role of the lattice solvents, ligand **21** with a 4′-[4-(naphthalen-1-yl)phenyl] substituent was chosen, and a series of experiments was conducted with cobalt(II) thiocyanate under crystal growth conditions. Single crystals of $[Co(\mathbf{21})_2(NCS)_2]_n \cdot 2n CHCl_3$ and $[Co(\mathbf{21})_2(NCS)_2]_n \cdot 2n C_6H_5Me$ were isolated from a combination of acetonitrile and chloroform or from methanol and toluene, respectively. In $[Co(\mathbf{21})_2(NCS)_2]_n \cdot 2n CHCl_3$, the 3,2′:6′,3″-tpy unit in **21** adopts conformation **A** (Scheme 27) and the ligands are directed above and below the planar (4,4) net defined by the Co atoms, leading to open channels running perpendicular to the nets; whereas conformation **B** is observed in $[Co(\mathbf{21})_2(NCS)_2]_n \cdot 2n C_6H_5Me$. Concerning the solvents, molecules of chloroform lie in the channels and can be reversibly taken out of the lattice and replaced with $CDCl_3$ or CH_2Cl_2, as demonstrated by TGA-MS measurements. In stark contrast, the toluene molecules in the second net are involved in π-stacking interactions, and the solvent-accessible void-space comprises interlinked cavities; the thermogravimetric analysis showed that the removal of toluene from $[Co(\mathbf{21})_2(NCS)_2]_n \cdot 2n C_6H_5Me$ was irreversible, consistently with the aromatic solvent playing a vital role in the stabilization of the structure.

References

1. D. Rocco, A. Prescimone, Y. M. Klein, D. J. Gawryluk, E. C. Constable and C. E. Housecroft, *Polymers*, **2019**, 11, 1224.
2. D. Rocco, A. Nikoletić, A. Prescimone, E. C. Constable and C. E. Housecroft, *Crystals*, **2022**, 12, 1136.
3. E. C. Constable, C. E. Housecroft, M. Neuburger, S. Vujovic, J. A. Zampese and G. Zhang, *CrystEngComm*, **2012**, 14, 3554-3563.
4. Y. M. Klein, A. Prescimone, M. Karpacheva, E. C. Constable and C. E. Housecroft, *Polymers*, **2018**, 10, 1369.
5. C. Janiak, *J. Chem. Soc., Dalton Trans.*, **2000**, 3885-3896.
6. G. Desiraju and T. Steiner, *The Weak Hydrogen Bond*, Oxford University Press, Oxford, England, **2001**.
7. D. Rocco, A. Prescimone, E. C. Constable and C. E. Housecroft, *Molecules*, **2020**, 25, 1663.
8. Y. M. Klein, A. Prescimone, E. C. Constable and C. E. Housecroft, *Polyhedron*, **2016**, 103, 58-65.
9. Y. M. Klein, A. Prescimone, M. B. Pitak, S. J.Coles, E. C. Constable and C. E. Housecroft, *CrystEngComm*, **2016**, 18, 4704-4707.
10. D. Rocco, A. Prescimone, E. C. Constable and C. E. Housecroft, *Polymers*, **2020**, 12, 1823.
11. D. Rocco, A. Prescimone, E. C. Constable and C. E. Housecroft, *Molecules*, **2021**, 26, 6337.
12. C. F. Macrae, I. Sovago, S. J. Cottrell, P. T. A. Galek, P. McCabe, E. Pidcock, M. Platings, G. P. Shields, J. S. Stevens, M. Towler and P. A. Wood, *J. Appl. Crystallogr.*, **2020**, 53, 226-235.
13. NIST Chemistry WebBook. Available online, http://webbook.nist.gov/chemistry, (accessed November 2022).
14. M. D. Prasanna and T. N. Guru Row, *Cryst. Eng.*, **2000**, 3, 135-154.
15. E. R. T. Tiekink, *CrystEngComm*, **2021**, 23, 904-928.
16. O. V. Shishkin, *Chem. Phys. Lett.*, **2008**, 458, 96-100.
17. D. Rocco, S. Novak, A. Prescimone, E. C. Constable and C. E. Housecroft, *Polyhedron*, **2021**, 208, 115445.

Chapter 5 Expanded ligands

5.1 Introduction

The term "expanded ligands" was introduced by Constable and coworkers to designate "ditopic species in which the metal-binding domains are separated by a metal-containing unit".[1-4] This falls within the scope of metallosupramolecular chemistry, which concerns the assembly of supramolecular structures through the interaction of metal ions with metal-binding domains (as ligands).[5] To exemplify the concept, it is possible to refer to the structural and topological relationship between pairs of ligands such as pyrazine and 4,4′-bipyridine, or oxalic acid and terephthalic acid. The second ligands in each pair (i.e. 4,4′-bipyridine and terephthalic acid) can be viewed as an expanded version of the first ligand in each pair (i.e. pyrazine and oxalic acid, respectively). The second ligand offers an increased N…N or O…O distance.[6] The "expansion" of the ligands in these cases occurs through covalent bonds, but coordination chemistry can be utilized as well. The same topological relationship pointed out above for pyrazine and 4,4′-bipyridine can be extended to $\{M(\mathbf{L3})_2\}^{n+}$ complexes, **L3** being 4′-(pyridine-4-yl)-2,2′:6′,2″-terpyridine, shown in Scheme 34.

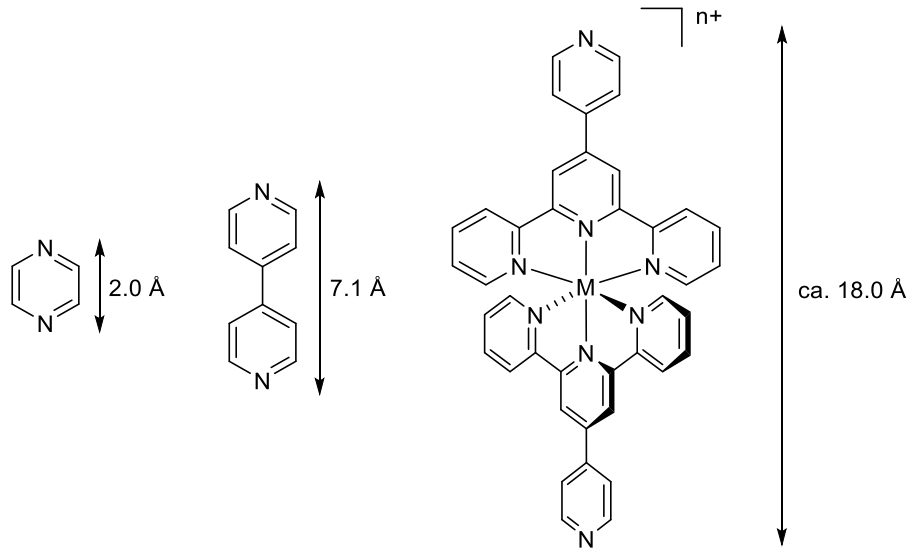

Scheme 34. The "expanded ligand" concept exemplified by the comparison of pyrazine, 4,4′-bipyridine and an $\{M(\mathbf{L3})_2\}^{n+}$ complex.

As anticipated from Scheme 34, an easy way (but not the only one) to achieve such expanded building units is by exploiting the convergent terdentate donor set and the chelating nature of 2,2′:6′,2″-terpyridine (tpy), utilizing the commonly encountered $\{M(tpy)_2\}^{n+}$ motif. The tpy unit usually presents three near-coplanar nitrogen donor atoms and tends to form pseudo-

octahedral bis(chelating) complexes, which possess higher stability than the corresponding $\{M(bpy)_3\}^{n+}$ species, rendering tpy more versatile than other oligopyridines.[5] Regarding the metal center, it plays a critical role, both in terms of the chemical and photophysical properties of the complex and with regard to the kinetics of assembly and the overall lability or inertness of the complex. For example, Co(III) has a low-spin d^6 configuration and $[Co(tpy)_2]^{3+}$ is kinetically inert. Due to the remarkably high binding affinity of tpy towards most transition-metal ions, homoleptic complexes of 4′-functionalized 2,2′:6′,2″-tpy ligands have been reported with a wide range of metal centers, including iron(II), ruthenium(II), osmium(II), cobalt(II), cobalt(III), iridium(III), copper(II), nickel(II) and zinc(II). The 4′-functionalization is needed to introduce pendant donor groups, e.g. a pyridyl or carboxylate unit. Two immediately apparent advantages of using expanded ligands as building blocks are the ease with which a broader range of ligands (hence molecular and topological variability) can be achieved without a great synthetic effort, and the facile introduction of metal-centered properties, such as redox- or photoactivity.[6] As a consequence, this area of research rapidly gained relevance and complexes containing functionalized homoleptic $\{M(tpy)_2\}^{n+}$ or heteroleptic $\{M(tpy)X_n\}$ units have been employed in several fields, including medical chemistry,[7-9] catalysis,[10, 11] enantioselective catalysis,[12] dye-sensitized solar cells,[13-17] photochemistry,[18-20] and artificial photosynthetic systems.[21] The reviews published by Newkome in 2018[22] and by Housecroft and Constable in 2021[23] provide comprehensive overviews of recent developments in terpyridine-based 2D- and 3D-fractals, as well as discrete metallosupramolecular architectures, including 3D-metallocages and metallomacrocycles (or metallopolygons), using functionalized ditopic bis(tpy) ligands with predetermined internal angles rather than linear ones.[22, 23] The first crystallographically characterized coordination polymer based on an expanded 4,4′-bipyridine ligand was reported in 2007 by Beves *et.al*.[24] This assembly consists of 1D chains in which $\{Ru(\mathbf{L3})_2\}^{2+}$ (**L3** = 4′-(4-pyridyl)-2,2′:6′,2″-terpyridine, Scheme 35a) metalloligands are linked by $\{Ag(NO_3)(MeCN)\}$ units. Not long after, they also reported a 1D-CP of the iron(II) homoleptic complex of **L3** (as a ditopic expanded ligand) with $Cu(NO_3)_2$,[25] and a work in which one pendant pyridyl group of $[Fe(\mathbf{L3})_2]^{2+}$ is protonated and the conjugate acid $[Fe(\mathbf{L3})(H\mathbf{L3})]^{3+}$ assembles into a 1D hydrogen-bonded polymer, i.e. where H^+ acts in place of a metal ion linking the expanded ligands.[26] Searches of the Cambridge Structural Database (CSD, v. 2022.2.0) reveal 74 hits for $\{M[\mathbf{L3}]_2\}^{n+}$, including any metal (Scheme 35c). However, moving from ditopic to tetratopic expanded ligands, far fewer examples have been reported. Considering ligand **L4** (Scheme 35b), where the functionalization of the 2,2′:6′,2″-tpy unit is with a pyrimidin-2-yl ring rather than a pyridin-4-yl substituent, searches of the CSD (v. 2022.2.0) show only 3 hits, comprising one coordination polymer.[27] This is a 2D-network assembled from the homoleptic ruthenium(II) complex $\{Ru(\mathbf{L4})_2\}^{2+}$ as tetratopic metalloligand and copper(II) chloride acting as a 2-connecting linker. The other two structures correspond to the homoleptic iron(II) and ruthenium(II) complexes of **L4**, in both cases with PF_6^- as counterion and different amounts of water and acetonitrile incorporated in the lattice.

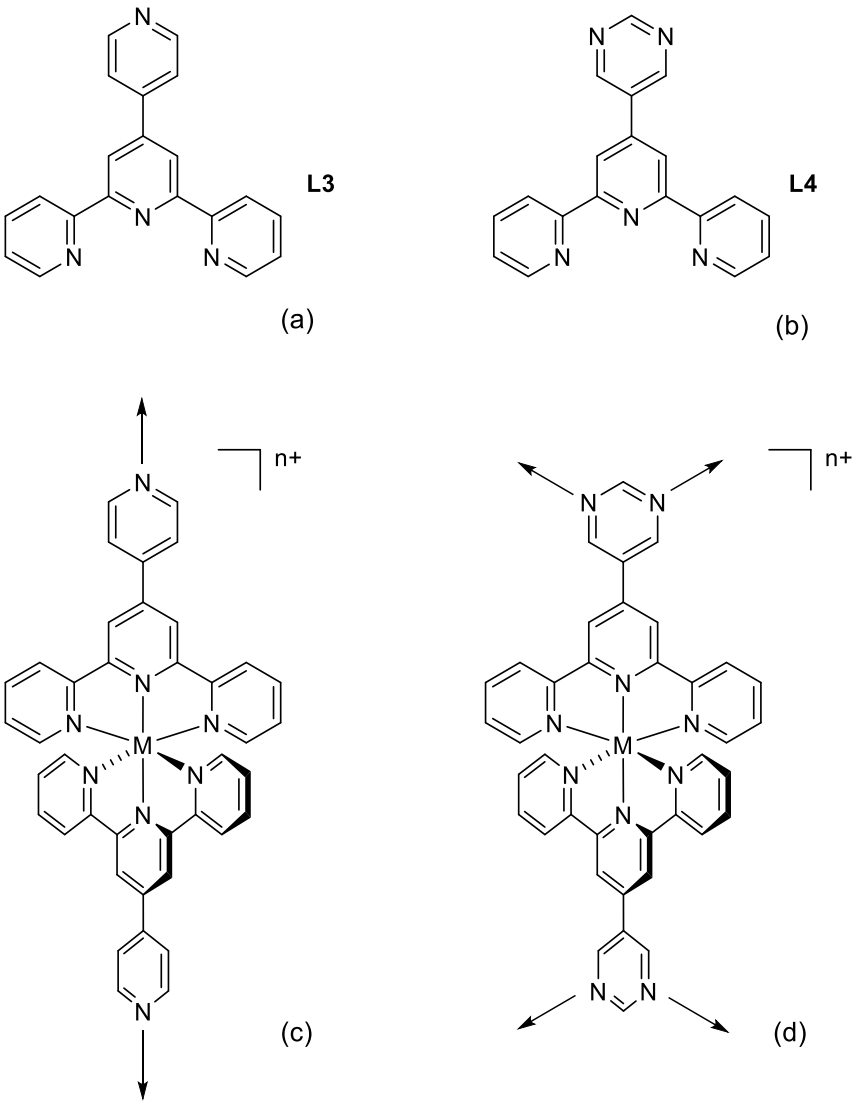

Scheme 35. Structures of (**a**) **L3** and (**b**) **L4**; (**c**) a ditopic expanded ligand, i.e. $\{M(\mathbf{L3})_2\}^{n+}$, and (**d**) a tetratopic expanded ligand, i.e. $\{M(\mathbf{L4})_2\}^{n+}$.

In contrast to the small number of tetratopic metalloligands, a number of purely organic, tetratopic bis(terpyridine) ligands have been synthesized and studied. As discussed for 4,2′:6′,4″- and 3,2′:6′,3″-tpy ligands in Chapter 1 (rigidity versus flexibility), the coordination chemistry of tetratopic bis(4,2′:6′,4″-tpy) ligands has been investigated more than that of the analogous bis(3,2′:6′,3″-tpy) ligands (Scheme 36).

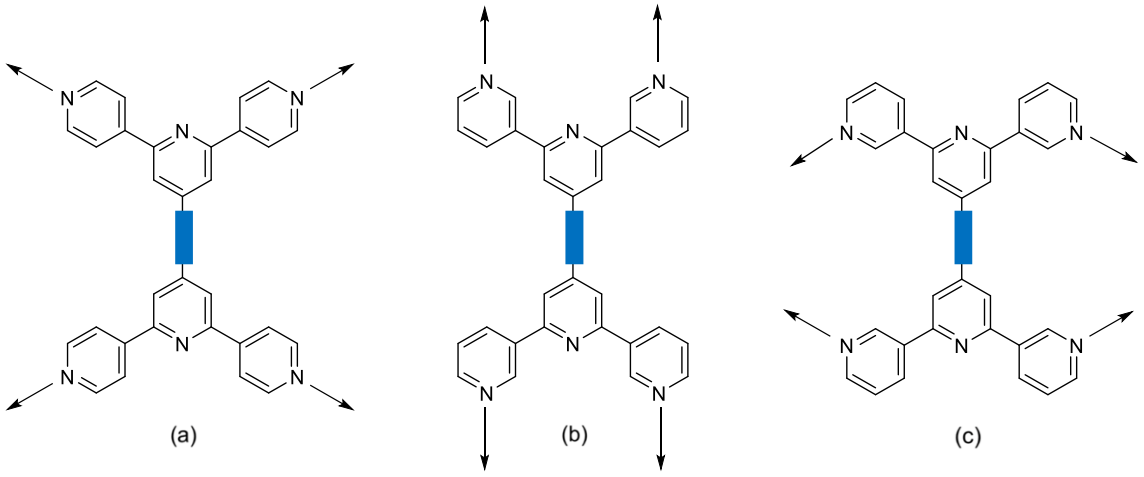

Scheme 36. Comparison between (**a**) bis(4,2′:6′,4″-tpy) ligands: tetratopic with fixed directionality, and (**b**), (**c**) bis(3,2′:6′,3″-tpy) ligands: tetratopic with variable directionalities (only two possible limiting planar conformations are shown). The blue rectangle represents a general organic spacer.

Many examples of these complexes have been synthesized in the Constable/Housecroft research group in recent years.[28] The ligands incorporate different spacers between the two 4,2′:6′,4″- or 3,2′:6′,3″-tpy units. These are often 1,4-phenylene rings functionalized with alkyloxy groups, both with linear[29-33] or branched chains,[34] which have been chosen to enhance the solubility of the ligands in organic solvents. These studies showed once again how the length of the chains in the substituent groups can affect the topological outcome of the assembled polymers. Other selected spacers bear a pendant aryl group to facilitate face-to-face π-interactions within the solid structure.[29] The Mukherjee group reported "self-assembled Pd(II) barrels" built from the tetratopic ligand showed in Scheme 37a.[35] All the cited examples include spacers that constitute a linear connection between the two 4,2′:6′,4″- or 3,2′:6′,3″-tpy units; however, this is not the only possibility, and angular bis(3,2′:6′,3″-tpy) and bis(4,2′:6′,4″-tpy) ligands have also been prepared. Yoshida *et al.* in 2013[36] were the first ones to use a bis(3,2′:6′,3″-tpy) ligand as a 4-connecting node for the assembly of a 2D-network; the ligand is shown in Scheme 37b.

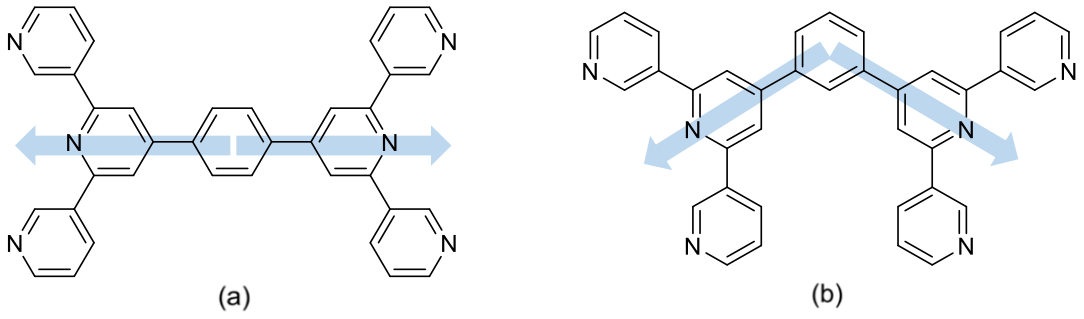

Scheme 37. Comparison between examples of (**a**) a linear and (**b**) an angular bis(3,2′:6′,3″-tpy) ligands.

Additional searches of the Cambridge Structural Database (CSD, v. 2022.2.0) show only a few results where the spacer consists of a [1,1′-(biphenyl-4,4′-diyl] moiety. Specifically, a compound reported by Chen and coworkers[37] (Scheme 38a), and one published by Schröder *et.al*,[38] (Scheme 38b).

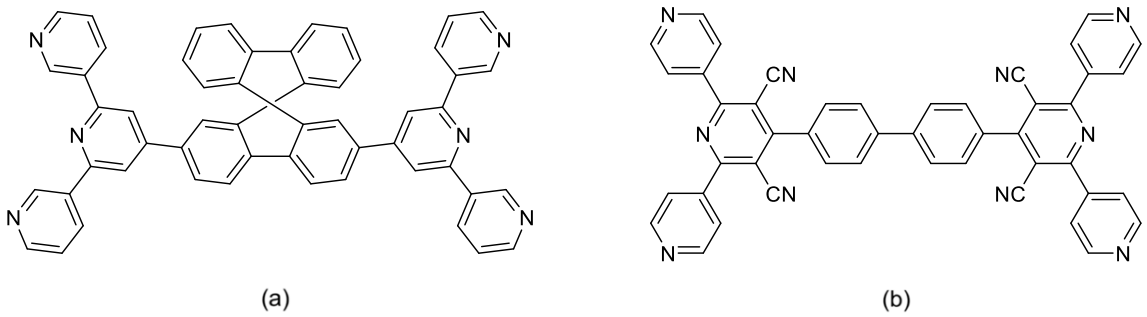

Scheme 38. Examples of (**a**) a bis(3,2′:6′,3″-tpy) and (**b**) a bis(4,2′:6′,4″-tpy) compounds containing a [1,1′-(biphenyl-4,4′-diyl] moiety as a spacer.

However, as of October 2022, the CSD (v. 2022.2.0) contained no examples of metal-centered expanded ligands containing bis(4,2′:6′,4″-tpy) and bis(3,2′:6′,3″-tpy) domains (Scheme 39). Hence, the aim of the last part of this thesis was the synthesis, characterization and investigation of the coordination chemistry of iron(II)-based tetratopic expanded ligands, possessing divergent 3,2′:6′,3″- or 4,2′:6′,4″-tpy units as donor groups available for reactions with additional metal centers.

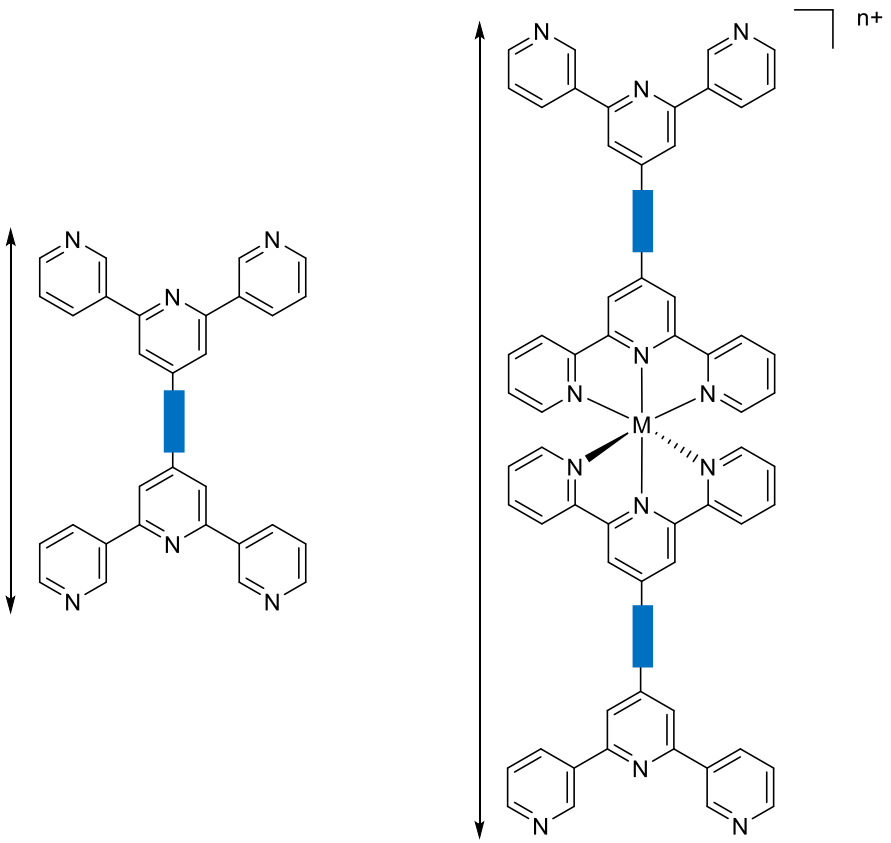

Scheme 39. Comparison of a purely organic bis(3,2′:6′,3″-tpy) ligand with a metal-centered expanded analog. The blue rectangle represents a general organic spacer.

5.2 Ligand synthesis and characterization

The iron(II) complexes [Fe(**26**)$_2$][NO_3]$_2$ and [Fe(**27**)$_2$][BF_4]$_2$ are reported here, where **26** and **27** are novel asymmetric bisterpyridines, each containing two different terpyridine isomers. In particular, they both contain the 2,2′:6′,2″-tpy domain, suited to behaving as a bis(chelate), and the 3,2′:6′,3″- or the 4,2′:6′,4″-tpy domain (**26** and **27**, respectively), apt to behave as a divergent ligand. [Fe(**26**)$_2$][NO_3]$_2$ and [Fe(**27**)$_2$][BF_4]$_2$, the homoleptic iron(II) complexes of **26** and **27**, represent the first two examples of this kind of expanded ligands. The synthetic approach to **26** and **27** (Scheme 40) with full characterization of all the intermediate compounds is first described.

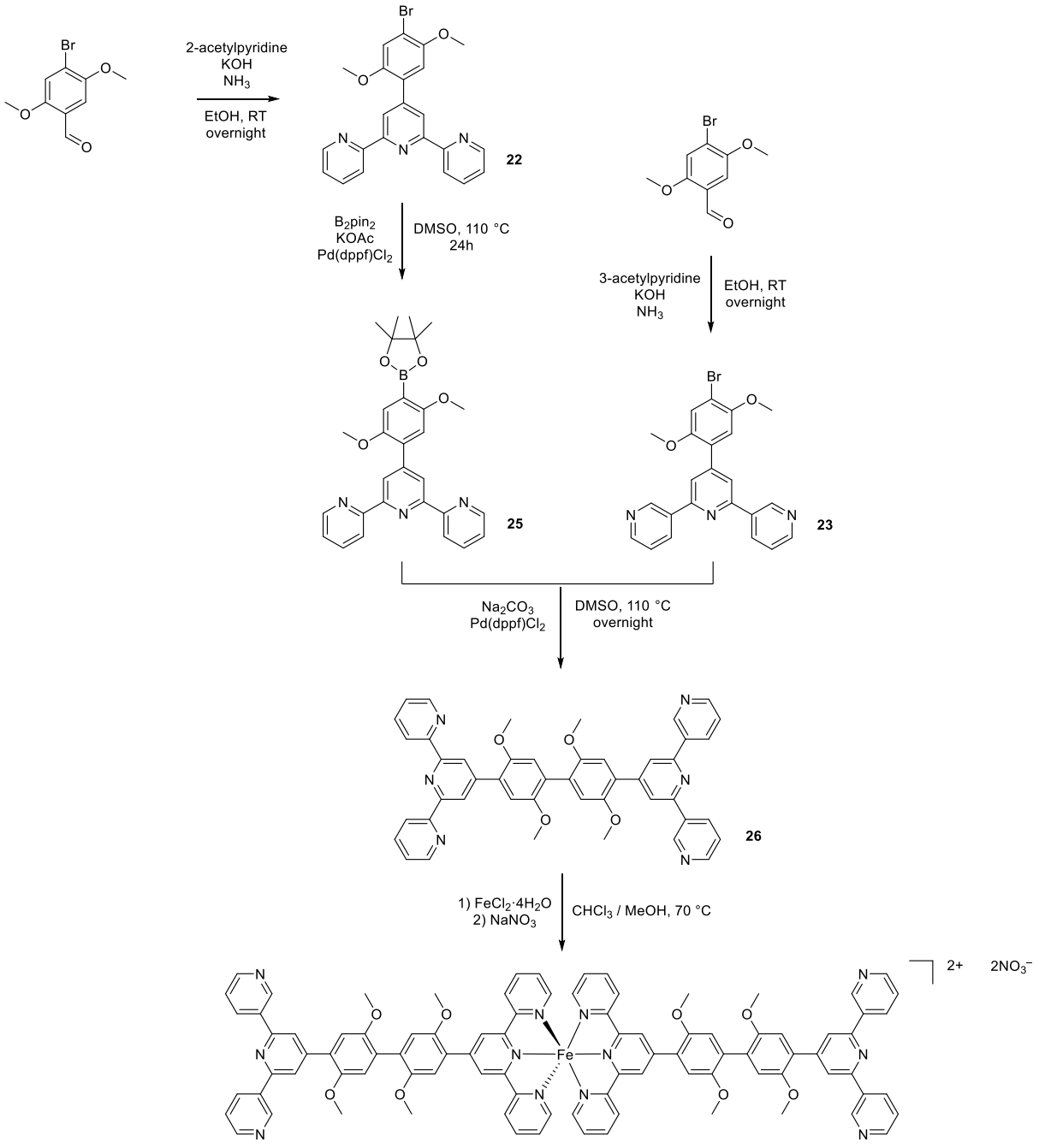

Scheme 40. Multi-step synthetic approach to [Fe(**26**)$_2$][NO$_3$]$_2$. An analogous route was followed to prepare **27**; the last step to [Fe(**27**)$_2$][BF$_4$]$_2$ is slightly different and is detailed below.

In the first step, three isomeric terpyridines were prepared following the one-pot synthesis by Wang and Hanan.[39] Thus, 4-bromo-2,5-dimethoxybenzaldehyde was reacted with two equivalents of 2-, 3- or 4-acetylpyridine, in basic EtOH solution, followed by the addition of aqueous ammonia in excess. Compound **22** (4′-(4-bromo-2,5-dimethoxyphenyl)-2,2′:6′,2″-tpy), **23** (bearing a 3,2′:6′,3″-tpy unit with the same functionalization in 4′-position) and **24** (4,2′:6′,4″-tpy with the same functionalization, Scheme 41) were isolated in 43.3%, 29.2% and 38.0% yields after recrystallization, respectively.

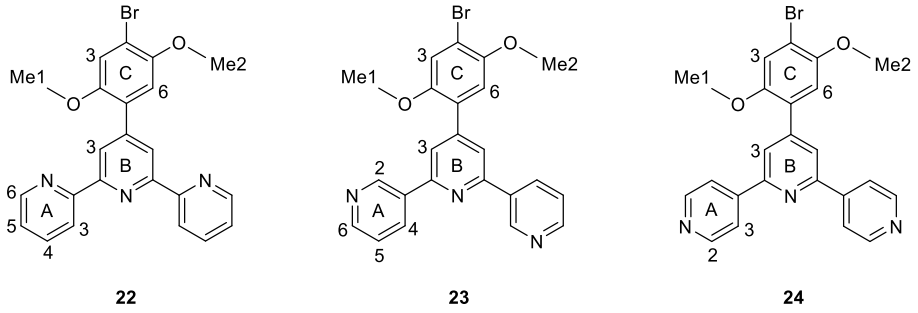

Scheme 41. Structures of compounds **22**–**24**, with atom labelling used for NMR spectroscopic assignments.

The three terpyridines **22**–**24**, as well as all the intermediate compounds described below, were fully characterized by ^{1}H and ^{13}C{^{1}H} NMR spectroscopy, ESI-MS, elemental analysis or HR-ESI-MS, melting point and solution UV-Vis and solid-state FT-IR spectroscopies. Figure 103 shows a comparison of the ^{1}H NMR spectra of (a) **22**, (b) **23** and (c) **24**, highlighting the characteristics peaks for each of the three tpy isomers; see Scheme 41 for atom labelling.

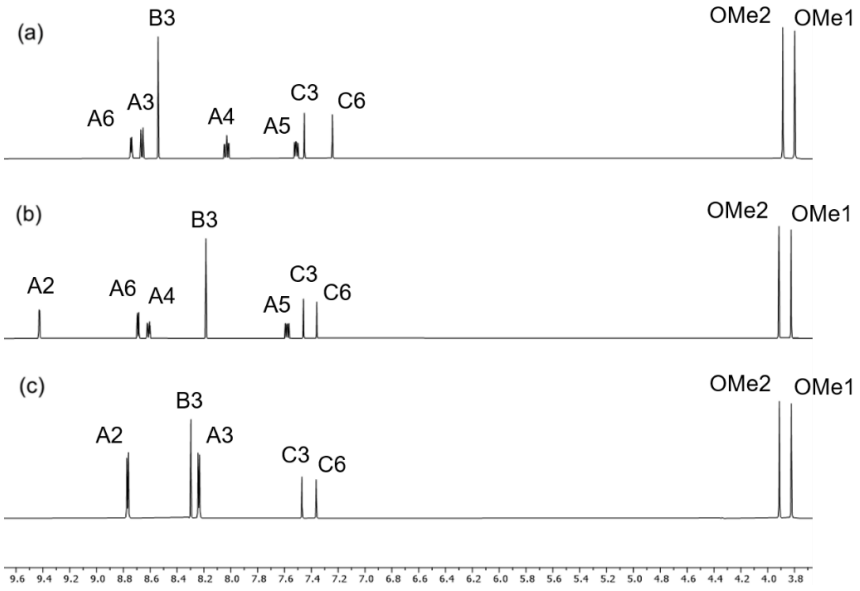

Figure 103. ^{1}H NMR spectra for compounds (**a**) **22**, (**b**) **23** and (**c**) **24** (500 MHz, DMSO-d_6, 298 K).

The electrospray (ESI-MS) mass spectra were recorded in acetonitrile solution, with the addition of a few drops of formic acid; in each case they show a base peak arising from the $[M+H]^+$ ion.

The solution absorption spectra of **22**–**24** exhibit intense absorptions in the UV region arising from spin-allowed π*←n and π*←π transitions. Figure 104 shows an overlay of the recorded spectra.

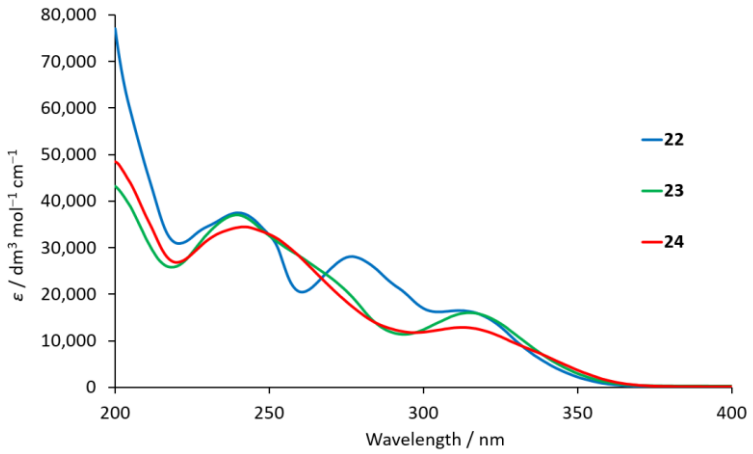

Figure 104. Solution absorption spectra (MeCN, 2.0 × 10^{-5} mol dm^{-3}) of compounds **22**–**24**.

The second step consisted of the borylation of compound **22**, to give 4′-(2,5-dimethoxy-4-(4,4,5,5-tetramethyl-1,3,2-dioxaborolan-2-yl)phenyl)-2,2′:6′,2″-terpyridine, **25** (Scheme 42).

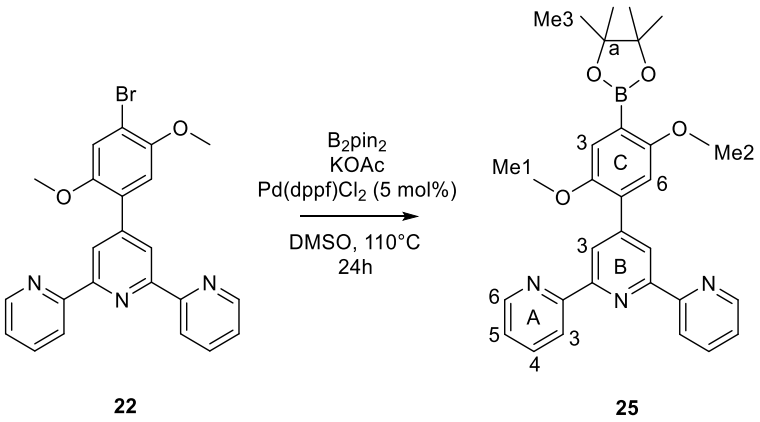

22 **25**

Scheme 42. Step II: borylation of **22**; see text and Section 6.3.2 for the experimental details. Structure of **25** with atom labelling used for NMR spectroscopic assignments.

In order to achieve this, **22** was reacted with bis(pinacolato)diboron in degassed DMSO solution, using potassium acetate as a base and [Pd(dppf)Cl_2] as a catalyst; **25** was isolated in 50.2% yield as a white, crystalline solid. The aromatic region of the ^{1}H NMR spectrum is not significantly affected by the replacement in 4′ position of the bromo-substituent by the boron-containing group. The effect is only visible on the signals assigned to protons H^{C6}, H^{C3} and the

methyl substituents; this is clearly highlighted in Figure 105, which shows a comparison of the ^{1}H NMR spectra of compounds **22** and **25**.

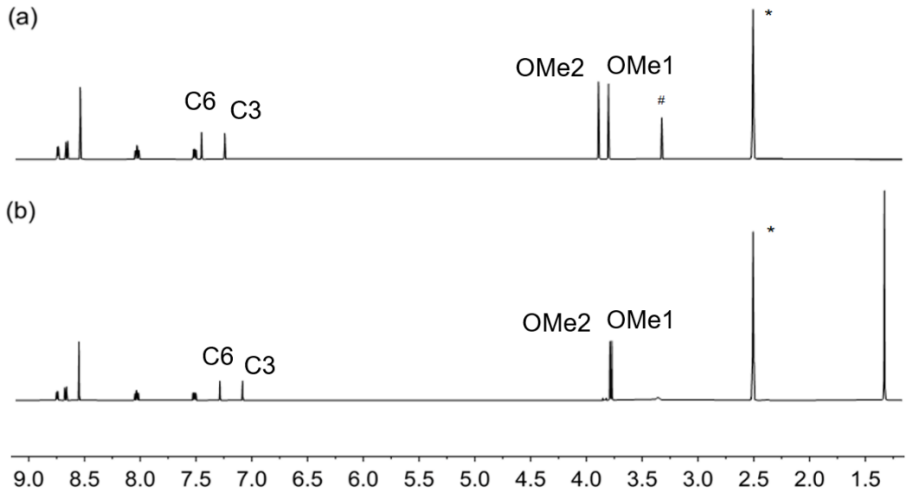

Figure 105. Comparison of the ^{1}H NMR spectra of compounds (a) **22** and (b) **25** (500 MHz, DMSO-d_6, 298 K). * = residual DMSO-d_5; # = H_2O.

The UV-Vis spectrum of **25** is dominated by intense absorptions below 350 nm, which are assigned mainly to π*←π transition (Figure 106).

The electrospray (ESI-MS) mass spectrum of **25**, recorded in acetonitrile solution with the addition of a few drops of formic acid, shows a base peak arising from the $[2M+Na]^+$ ion at *m*/*z* 1013.40, and a second peak at *m*/*z* 518.21 corresponding to the $[M+Na]^+$ ion (Figure 107).

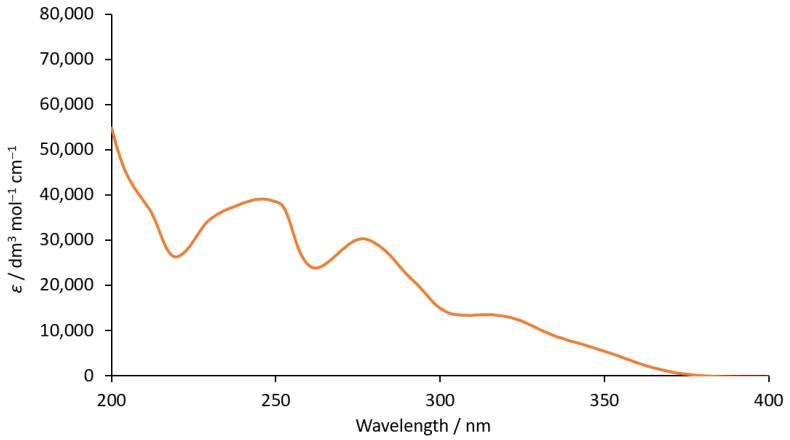

Figure 106. Solution absorption spectra (MeCN, 2.0 × 10^{-5} mol dm^{-3}) of compounds **22** and **25**.

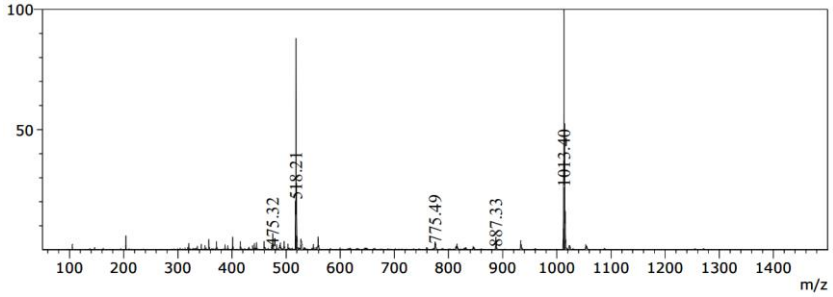

Figure 107. Electrospray mass spectrum of **25**.

Palladium-catalyzed cross-coupling reactions were carried out in parallel on **25**, reacting the boronic ester with the two bromo-compounds **23** (as shown in Scheme 43) and with **24**, to yield the asymmetric bisterpyridines **26** and **27**, respectively.

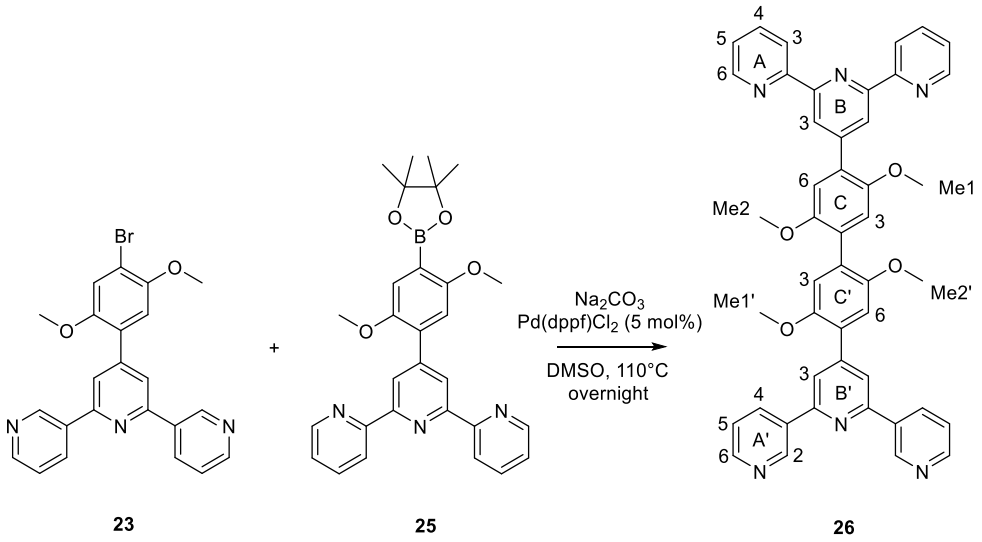

Scheme 43. Step III: Cross-coupling reaction between **23** and **25**, to yield the asymmetric bisterpyridine **26**; see text and Section 6.3.3 of the experimental part for additional details. Structure of **26** with atom labelling used for NMR spectroscopic assignments.

The two reactions were performed in Schlenk tubes under nitrogen atmosphere in degassed DMSO solution, heating the mixtures at 110 °C overnight (ca. 14 h). A purification step by column chromatography on basic Al_2O_3 with Brockmann activity II was necessary to isolate the desired bisterpyridines (see details in the Experimental Section 6.3.3). **26** and **27** were obtained in 57.4% and 36.2% yield, respectively. Once again, no effort was invested in optimizing the reaction conditions. The compounds were fully characterized and Figure 108 displays a comparison of the ^{1}H NMR spectra.

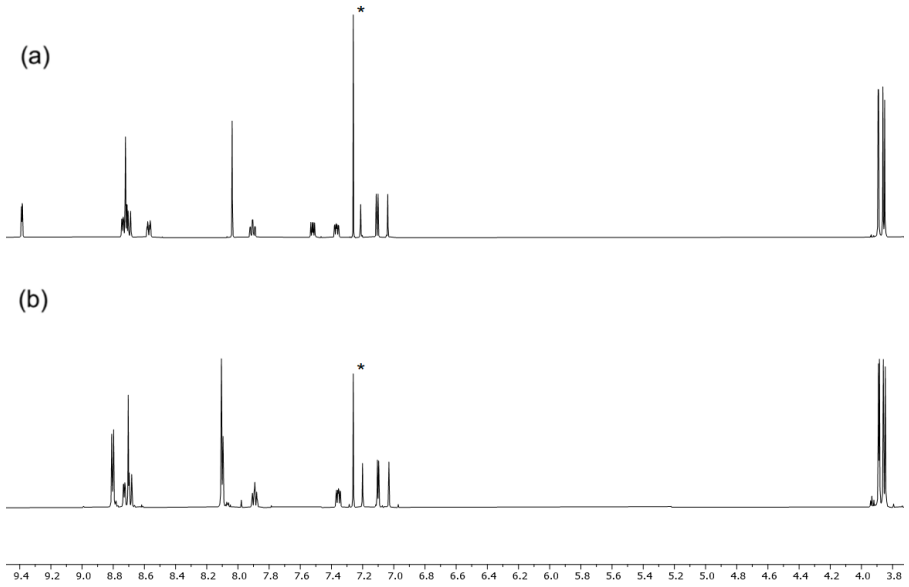

Figure 108. ^{1}H NMR spectra for compounds (a) **26** and (b) **27** (500 MHz, $CDCl_3$, 298 K). * = residual $CHCl_3$.

The full assignment was made with the aid of 2D experiments, and by comparing the spectra of the asymmetric bisterpyridines with those of compounds **23** (or **24**) and **25** it was possible to distinguish the two tpy moieties in each of compounds **26** and **27**. NOESY crosspeaks between H^{B3} and H^{C6}, H^{C6} and H^{OMe2} and between H^{C3} and H^{OMe1} (in the 2,2′:6′,2″-tpy unit) were useful for the assignment, together with the corresponding signals in the 3,2′:6′,3″- or in the 4,2′:6′,4″-tpy units. Additionally, critical HMBC correlation peaks were H^{C3}/C^{C2}, $H^{C3'}/C^{C2'}$, H^{C6}/C^{C5}, $H^{C6'}/C^{C5'}$, $H^{C6'}/C^{B4'}$, H^{B3}/C^{C1} and $H^{B3'}/C^{C1'}$.

The ESI-MS spectra, recorded in acetonitrile solutions with the addition of a few drops of formic acid, showed a base peak arising from the $[M+H]^+$ ion at *m*/*z* 737.23 in the case of **26**, and at *m*/*z* 737.31 for **27** .

Finally, the two expanded ligands $[Fe(\mathbf{26})_2][NO_3]_2$ and $[Fe(\mathbf{27})_2][BF_4]_2$ were prepared (Scheme 44). The complexation reactions were carried out by adding a methanol/water solution of an appropriate iron(II) salt (see below) to a hot solution of the asymmetric bisterpyridine in methanol/chloroform, while stirring. The solutions of **26** and **27** were prepared by heating at 70 °C. The immediate formation of the intensely colored iron(II) complexes was clearly observed in solution: in both cases, the reaction mixture turned purple as soon as the two colorless solutions were mixed. The preparative details are given below.

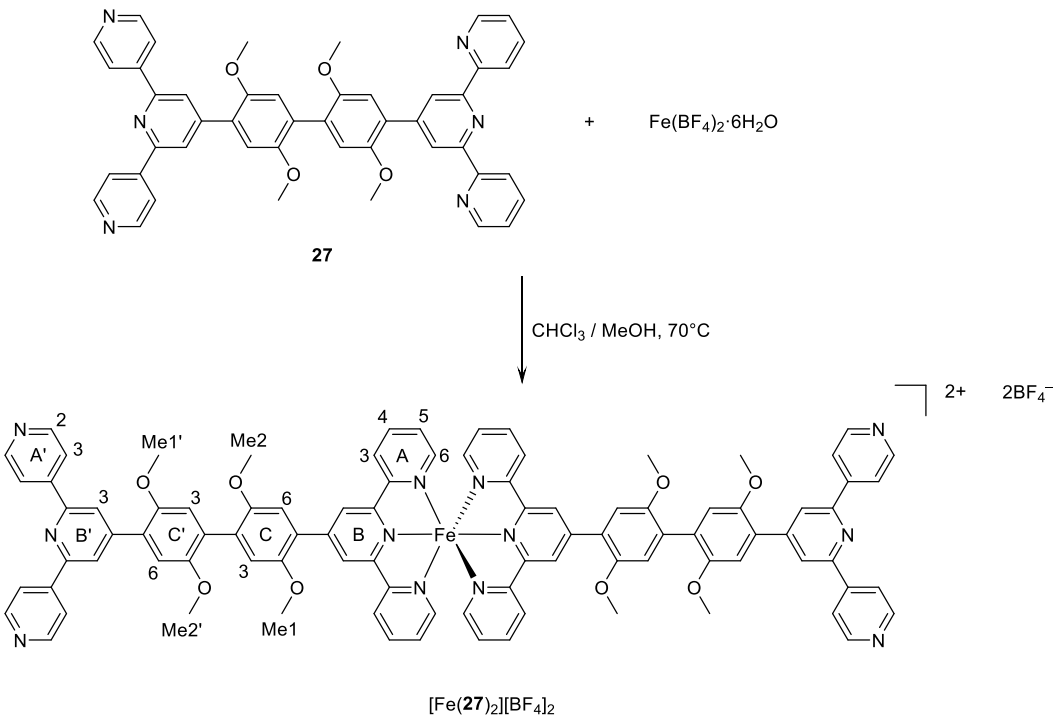

Scheme 44. Step IV: Complexation of **27** with iron(II) tetrafluoroborate hexahydrate, to yield the bis-chelating complex [Fe(**27**)$_2$][BF$_4$]$_2$; see text and Section 6.3.4 of the experimental part for further details. Structure of [Fe(**27**)$_2$][BF$_4$]$_2$ with atom labelling used for NMR spectroscopic assignments. A similar method was used to prepare [Fe(**26**)$_2$][NO$_3$]$_2$, starting with **26** and FeCl$_2$·4H$_2$O, followed by aqueous NaNO$_3$.

The salt [Fe(**26**)$_2$][NO$_3$]$_2$ was prepared from the corresponding chloride. After being dissolved in MeOH/CHCl$_3$ (1:3), **26** was reacted with FeCl$_2$·4H$_2$O and the purple solution so-obtained was stirred for 30 minutes. CHCl$_3$ was then removed under vacuum and the remaining solution treated with an excess of aqueous NaNO$_3$, the mixture stirred for additional 10 minutes, after which, the precipitation of a purple solid was observed. The latter was collected on celite, washed with H$_2$O and dissolved in MeCN. [Fe(**26**)$_2$][NO$_3$]$_2$ was isolated as a purple solid in 82.4% yield. Compound **27** was directly reacted with Fe(BF$_4$)$_2$·6H$_2$O under similar conditions, and [Fe(**27**)$_2$][BF$_4$]$_2$ was isolated as a purple solid in 78.0% yield. Both iron(II) complexes were fully characterized. The NMR spectra were recorded in CD$_3$CN because of solubility reasons, and with the addition of a small amount of K$_2$CO$_3$ to the NMR tubes. It was possible to fully assign the spectra with the help of 2D experiments and by comparison with the corresponding uncoordinated **26** and **27** (Figure 108). The comparisons of coordinated and free compounds are shown in Figure 109 for **26** and in Figure 110 for **27**. The shift of the signals attributable to the use of different solvents was relatively little. As expected, the positions of some signals of the 2,2′:6′,2″-tpy moiety were affected by coordination, and this impact was particularly significant for protons H^{A6}, H^{B3} and H^{C6} due to the switch of the 2,2′:6′,2″-tpy unit from conformation **I** (*trans*,*trans*) to conformation **II** (*cis*,*cis*) in Scheme 45.

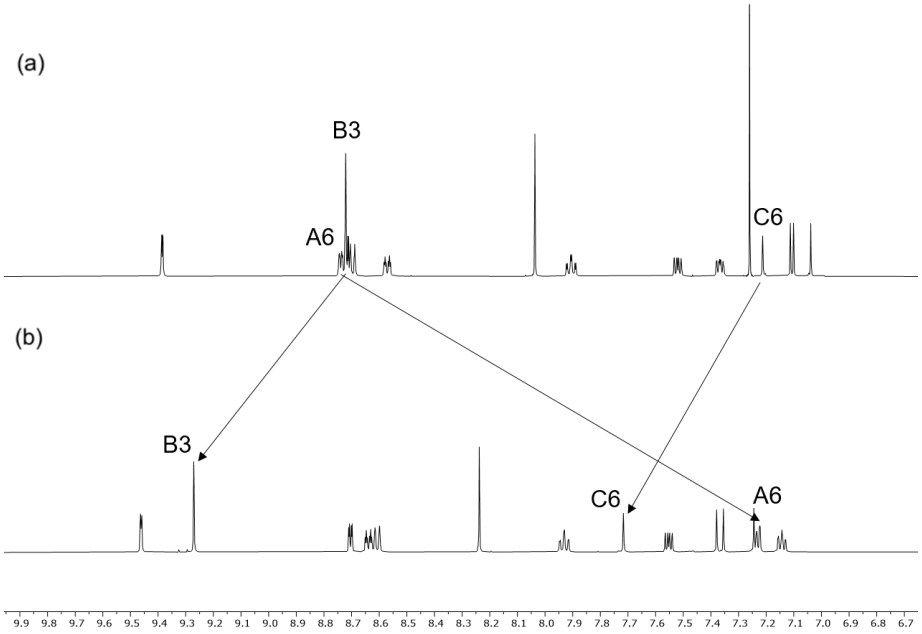

Figure 109. Comparison of the ^{1}H NMR spectra (aromatic region) for (**a**) compound **26** and (**b**) its bis-chelating iron(II) complex [Fe(**26**)$_2$][NO$_3$]$_2$. The arrows point out the effect of the coordination of the 2,2′:6′,2″-tpy unit to the Fe^{2+} on the chemical shifts of protons H^{A6}, H^{B3} and H^{C6}.

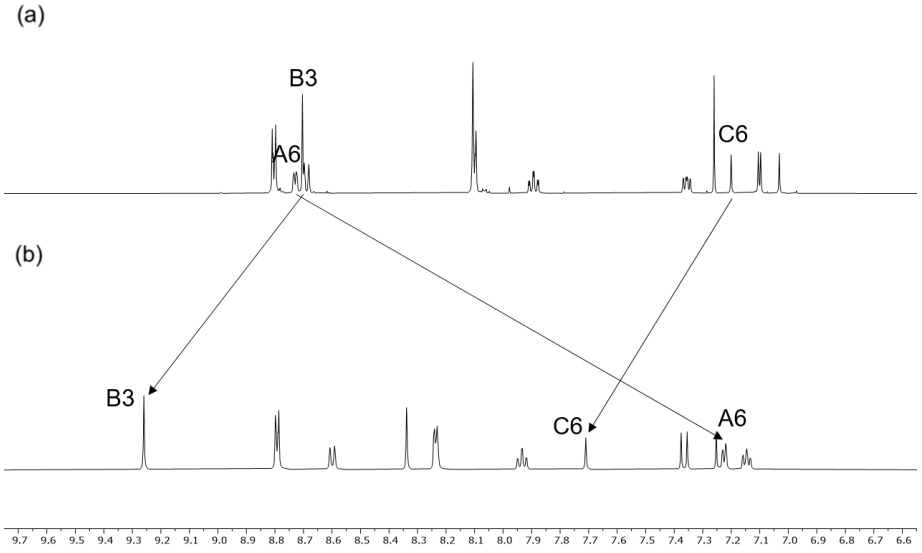

Figure 110. Comparison of the ^{1}H NMR spectra (aromatic region) for (**a**) compound **27** and (**b**) its iron(II) complex [Fe(**27**)$_2$][BF$_4$]$_2$. The arrows point out the effect of the coordination of the 2,2′:6′,2″-tpy unit to the Fe^{2+} on the chemical shifts of protons H^{A6}, H^{B3} and H^{C6}.

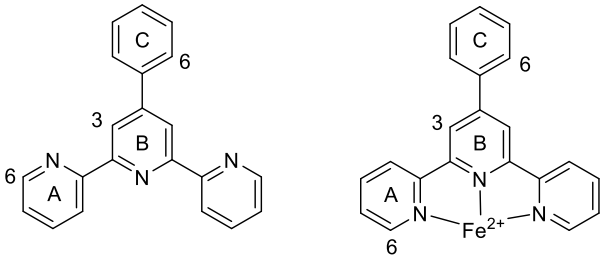

Scheme 45. Two conformations of the 2,2′:6′,2″-tpy unit: uncoordinated (**I**) and coordinated (**II**).

Figure 111 shows an overlay of the solution absorption spectra of the two bisterpyridines **26** and **27** and their complexes. Due to solubility reasons, the absorption spectrum of **26** was measured in MeCN/$CHCl_3$ 9:1, instead of neat MeCN, while the other three measurements were performed on MeCN solutions of the compounds.

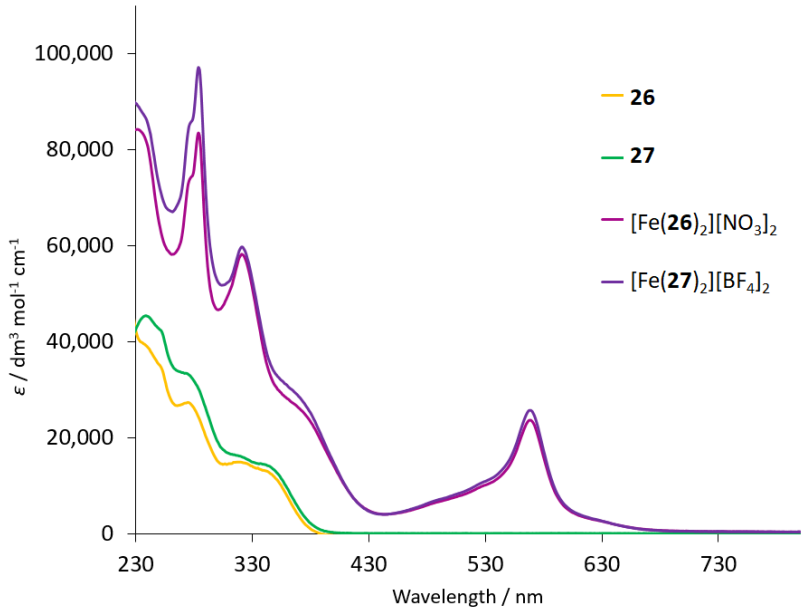

Figure 111. Solution absorption spectra (MeCN or MeCN/$CHCl_3$ 9:1, 1.0 × 10^{-5} mol dm^{-3}) of compounds **26**, **27** and their iron(II) complexes.

From the comparison, the appearance of the MLCT bands in the visible region at 568 nm is immediately evident. These can be assigned to the d-π* transition,[40] terpyridines being good π-acceptor ligands. The values of the molar extinction coefficient are ε = 23,700 dm^3 mol^{-1} cm^{-1} in the case of [Fe(**26**)$_2$][NO_3]$_2$ and 25,700 dm^3 mol^{-1} cm^{-1} for [Fe(**27**)$_2$][BF_4]$_2$. A second observation is the approximate doubling of the extinction coefficients in the high-energy region for the $[FeL_2]^{2+}$ complexes, compared to the uncoordinated ligands, L. The intense absorptions exhibited in the UV region arise mainly from spin-allowed π*←π transitions. The ESI-MS spectra were recorded on acetonitrile solutions of the bis-chelating complexes, this

time without the addition of formic acid, and each showed a peak arising from the $[M]^{2+}$ ion at *m*/*z* 764.67 in both cases. To date, single crystals of the expanded ligands $[Fe(\mathbf{26})_2][NO_3]_2$ or $[Fe(\mathbf{27})_2][BF_4]_2$ have not been obtained. However, a modelled structure of the $[Fe(\mathbf{27})_2]^{2+}$ unit was prepared using Spartan 18 (v. 1.4.8) and is displayed in Figure 112. The two N…N distances marked in the figure correspond to 38.7 and 39.5 Å. The $[Fe(\mathbf{27})_2]^{2+}$ moiety can be seen as the expanded, metal-binding version of the tetratopic bisterpyridine ligand reported by Schröder and coworkers.[38] As mentioned in Section 5.1, this compound is the only example of a bis(4,2′:6′,4″-tpy) ligand containing a [1,1′-(biphenyl-4,4′-diyl] spacer. The corresponding N…N distances were measured in the purely organic compound using the coordinates from the CSD, refcode: BUHLIB, and they are 19.5 and 20.9 Å (Scheme 46).

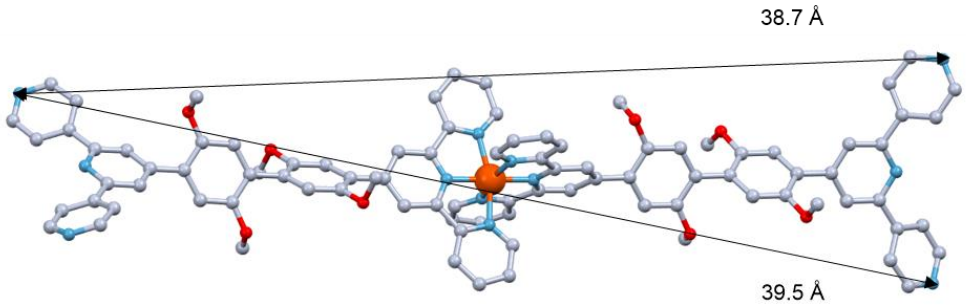

Figure 112. Modelled structure of $[Fe(\mathbf{27})_2]^{2+}$. Geometry optimized using molecular mechanics in the program Spartan 18 (v. 1.4.8).

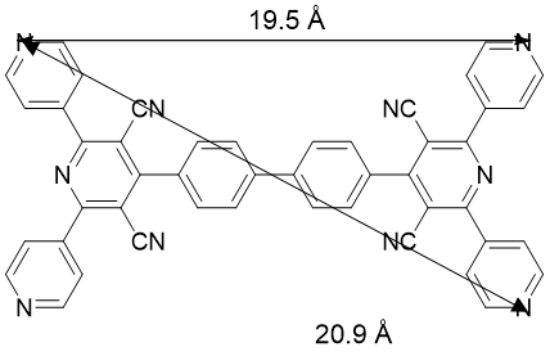

Scheme 46. Structure of 1,4-bis(4-(3,5-dicyano-2,6-dipyridyl)pyridyl)phenylbenzene (reported by Schröder and coworkers), drawn using the coordinates from the CSD, refcode BUHLIB.[38]

Unfortunately, the crystals that grew so far from the reactions of $[Fe(\mathbf{26})_2][NO_3]_2$ or $[Fe(\mathbf{27})_2][BF_4]_2$ with a variety of metal salts were not suitable for XRD structural determination. Several metal salts have been employed, including $AgNO_3$, $Cu(OAc)_2{\cdot}H_2O$, $CuCl_2$, $Cu(hfacac)_2{\cdot}H_2O$, $Cu(NO_3)_2{\cdot}3H_2O$ and $Co(NCS)_2$, and different crystallization set-ups have

been tried. The most promising ones involved the solution layering technique; in particular, layering an acetonitrile solution of the metal salt over a MeCN/H_2O solution of the metalloligand in a test tube, sealing it, and letting the two solutions diffuse into one another. The use of neat water or other solvents to dissolve the metal salt led to quick precipitation of the iron(II) complex as an amorphous solid. The reaction between [Fe(**27**)$_2$][BF_4]$_2$ and $Cu(NO_3)_2 \cdot 3H_2O$ under crystal growth conditions afforded small violet plate-like crystals. However, only low angle data could be collected and the quality was not good enough for a complete X-ray analysis.

5.3 Structures of compounds **23**–**25**

Crystal structures were obtained for the bromo-compounds **23** and **24**, and for the boronic ester **25**. Single crystals of **23** were obtained upon recrystallization from EtOH/$CHCl_3$ and storing the solutions at 2–5 °C for three days; **24** was isolated as a crystalline solid directly after it was filtered from the reaction mixture and was simply washed with H_2O (3 × 10 mL) and EtOH (3 × 10 mL); single crystals of **25** formed from the colorless solution obtained upon filtration of a brown CH_2Cl_2 solution through a celite pad. Compound **23** crystallizes in the triclinic space group *P*–1, **24** in the monclinic space group $P2_1/n$, while **25** crystallizes in the orthorhombic space group *Pbca*. The asymmetric unit in each structure contains one independent molecule, depicted in Figure 113. Bond lengths and angles are unexceptional. In **23**: C11–Br1 = 1.895(2) Å, C12–O1 = 1.365(2) Å, C9–O2 = 1.367(2) Å, C12–O1–C22 = 116.4(1)° and C9–O2–C23 = 117.2(2)°. In **24**: C10–Br1 = 1.898(2) Å, C11–O1 = 1.358(3) Å, C8–O2 = 1.370(3) Å, C11–O1–C22 = 117.9(2)° and C8–O2–C23 = 117.1(2)°. In **25**: C19–B1 = 1.561(2) Å, C17–O1 = 1.372(2) Å, C20–O2 = 1.368(2) Å, C17–O1–C28 = 117.3(1)° and C20–O2–C29 = 117.6(1)°. A *trans,trans*-conformation of the 2,2′:6′,2″-tpy unit is observed in **25**, typical of non-coordinated tpy ligands. The angles between the least squares planes through adjacent pairs of aromatic rings are compiled in Table 17.

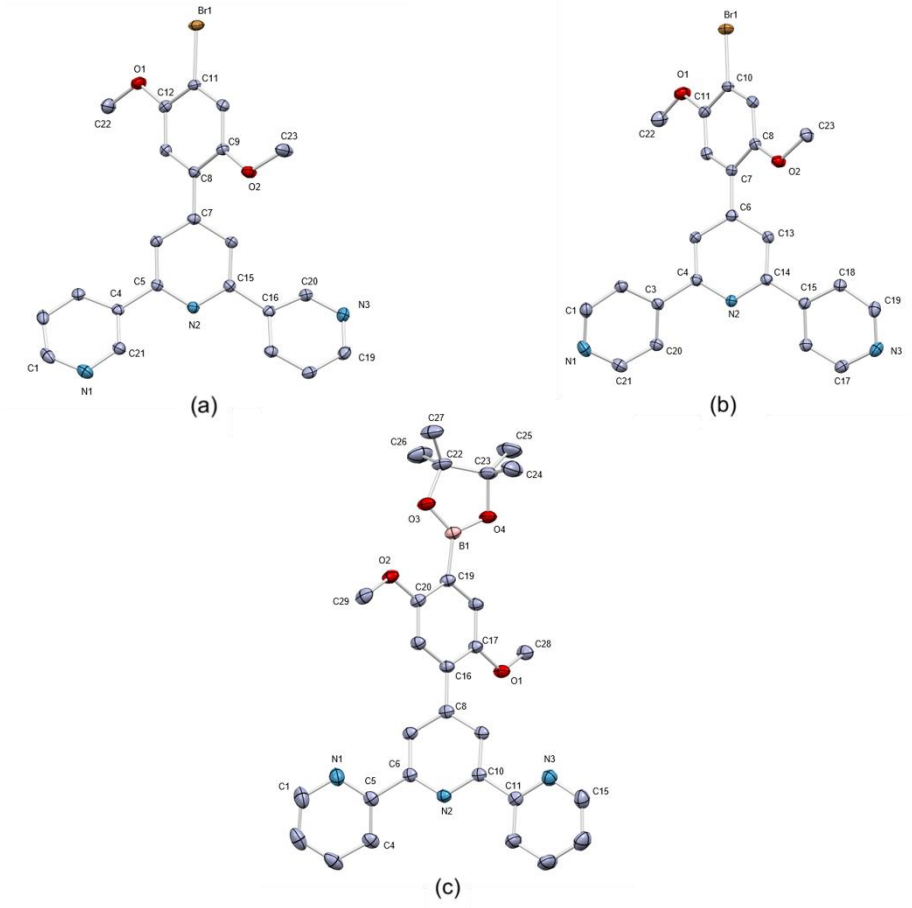

Figure 113. ORTEP representations of (**a**) **23**, (**b**) **24** and (**c**) **25** (ellipsoids are plotted at a 40% probability level, and H atoms are omitted for clarity).

Table 17. Selected structural parameters in compounds **23**–**25**. Angles between the least squares planes of pairs of aromatic rings; between outer and central pyridine rings, and between the central pyridine ring and the phenylene.

Compound	py - py /°	py - py /°	py - phenylene /°
23	28.1	25.9	44.1
24	30.3	21.6	43.5
25	26.2	9.5	50.3

Molecules of **23** interact through weak face-to-face π-stacking between centrosymmetric pairs of central pyridine rings (rings with N2 and N2^{i}, symmetry code i = 1–*x*, 1–*y*, 1–*z*), with inter-plane separation = 3.610 Å and a centroid…centroid distance = 4.073 Å (Figure 114a). Additionally, the terpyridine unit engages in a second π-stacking interaction involving the rings containing N1/N3^{ii}, and N3/N1^{ii} (symmetry code ii = 2–*x*, 1–*y*, 1–*z*, centroid...centroid = 3.93 Å, angle between ring planes = 17.9° (Figure 114b). There is also a net of weak hydrogen bonds. First of all, the nitrogen atoms of the outer pyridine rings (N1 and N3) are involved in C–H...N hydrogen bonded interactions, with different molecules. In particular, the C...N separation between C23ii and N1 corresponds to 3.518(4) Å, and the one between C23iii and

N3 to 3.426(4) Å; the H...N distances are in the range 2.63–2.74 Å, the H atom being in calculated positions (Figure 114c). Furthermore, a C–H…Br interaction presents a C...Br separation of 3.586(2) Å and a H...Br distance of 2.99 Å. (Figure 114d). Lastly, C–H…O interactions contribute to the packing, with a C...O separation of 3.597(3) Å and H...O distance = 2.68 Å. (Note that the H atoms are in crystallographically calculated positions.)

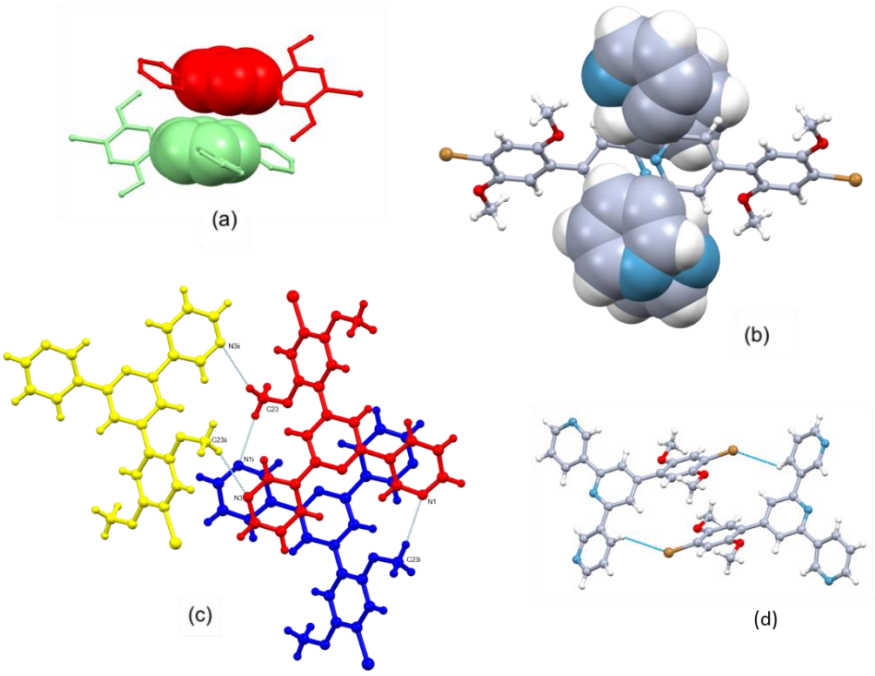

Figure 114. Packing of molecules of **23**. (**a**) Weak face-to-face π-stacking between centrosymmetric pairs of central pyridine rings. (**b**) Second π-stacking interaction involving the rings containing N1/N3^{ii}, and N3/N1^{ii}. (**c**) Net of C–H...N interactions (symmetry codes: ii = 2–*x*, 1–*y*, 1–*z*; iii = 2–*x*, –*y*, 1–*z*). (**d**) C–H...Br interaction.

In contrast, in the packing of **24** there are no π-stacking interactions. The molecules interact through weak hydrogen bonds. Similarly, both N1 and N3 are involved in C–H...N hydrogen bonded interactions, each with a different molecule. Metrics of the interaction involving N1 are a C...N separation of 3.468(3) Å with C9i, and H...N distance = 2.59 Å, while N3 is involved in a bifurcated hydrogen interaction, with C...N separations of 3.396(3) Å with C2ii and 3.558(3) Å with C5ii; H...N distances are in the range 2.61–2.74 Å, the H atoms being in calculated positions (Figure 115). Differently from the packing of **23**, there are no short contacts involving the bromine atom. However, there are C–H…O interactions, with C...O separation of 3.360(3) Å and H...O distance = 2.64 Å.

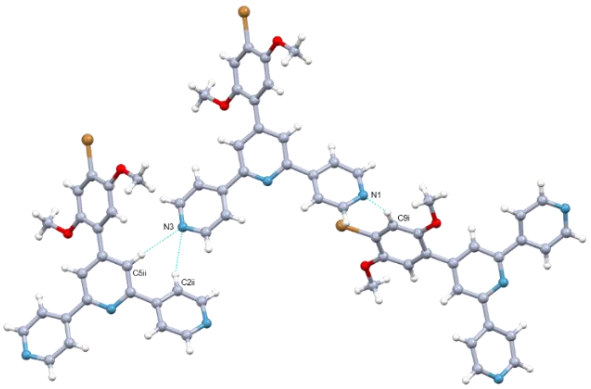

Figure 115. Packing of molecules of **24**. Net of C–H…N interactions (symmetry codes: i = x, $-1/2+y$, $3/2-z$; ii = x, y, $-1+z$).

The boronic ester **25** comprises a 2,2′:6′,2″-unit, which adopts conformation **I** (Scheme 45), as expected for a non-coordinated 2,2′:6′,2″-tpy. The main interaction in the packing is a C12^{i}–H12^{i}…B1 contact (sym. code i = 2–x, 1–y, 1–z), with a B…C separation of 3.660(3) Å and a B…H distance of 2.94 Å, with C12 and H12, belonging to the pyridine ring containing N3^{i}. On a closer inspection, the relative orientation of the C–H vector with respect to the plane of the BO_2C_2 ring is consistent with the interaction involving the electron density in the 2p orbital of the boron atom, with an angle of 89.2° between the least squares planes through the pyridine ring and through the trigonal planar system centered on B (Figure 116). Evidence for the occupancy of 2p orbital can be found by inspecting the B–O distance, which is 1.361(2) Å. In fact, the solid state B–O distance in the trigonal planar BO_3 groups is typically ca. 1.36 Å, while in tetrahedral BO_4 units it increases to 1.48 Å, suggesting that B–O π-bonding involving O lone pairs is present in planar BO_3 units.[41] This is also the case in molecules of **25**.

Additionally, the boron atom interacts weakly with another C–H unit of the pyridine ring containing N3^{ii} (sym. code ii = $3/2-x$, $1-y$, $1/2+z$); in this case, the B…C distance is 3.889(3) Å and the B…H distance = 3.04 Å. Other interactions that contribute to the packing include C–H…O, involving both the oxygen atoms of the methoxy groups, and one oxygen of the ester group. C...O separations are 3.410 (2) and 3.418(2) Å in the first case, with H...O distance = 2.67 and 2.57 Å. The oxygen atom of the ester group presents a C...O separation of 3.476(2) Å and H...O distance = 2.57 Å. The nitrogen atoms N1 and N3 do not engage in short contacts.

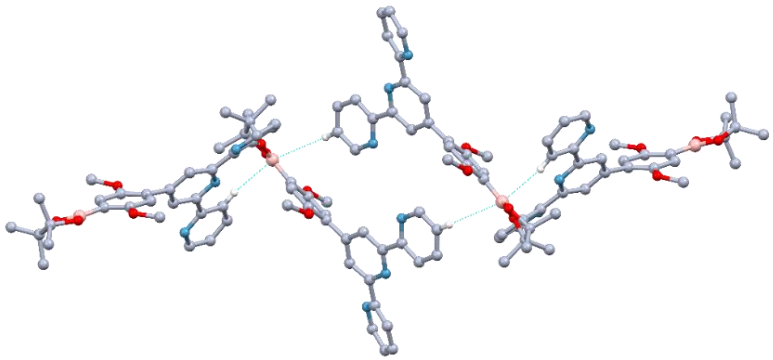

Figure 116. Packing of molecules of **25**. C–H...B interaction involving the electron density in the p orbital of the boron atom.

5.4 Conclusions

Two new homoleptic iron(II) complexes, $[Fe(\mathbf{26})_2][NO_3]_2$ and $[Fe(\mathbf{27})_2][BF_4]_2$ have been synthesized and fully characterized. These metalloligands represent the expanded version of bis(3,2′:6′,3″-tpy) and bis(4,2′:6′,4″-tpy) ligands, respectively, and are potential tetratopic building blocks for the assembly of coordination polymers. The compounds **26** and **27** were obtained *via* cross-coupling reactions and each of them consists of two different terpyridine isomers bonded together. Specifically, they both contain the bis(chelating) 2,2′:6′,2″-tpy domain on one side, and the divergent 3,2′:6′,3″- or 4,2′:6′,4″-tpy moiety on the other, thus representing unprecedented asymmetric bisterpyridines. The synthetic approach to **26**, **27** and their complexes is described, with the full characterization of all the intermediate compounds. ^{1}H NMR and solution absorption spectra of intermediate and final compounds are reported and compared. The cross-coupling reactions involved the boronic ester of the 4′-substituted-2,2′:6′,2″-tpy **25** with the 4′-(4-bromo-2,5-dimethoxyphenyl)-3,2′:6′,3″-tpy **23** in one case, or the corresponding 4,2′:6′,4″-tpy **24**. The three 4′-bromo compounds (**22**–**24**) were successfully synthesized following the one-pot approach by Hanan. Two bromo compounds, **23** and **24**, and the boronic ester **25** were additionally characterized by single-crystal XRD. Selected angles and bond distances are listed, and the dominant packing interactions in each structure are described. Unfortunately, no single crystals of the bis(chelating) complexes could be obtained up to now, and the quality of the crystals of their coordination polymers was unsatisfactory and did not allow a structural determination.

References

1. E. C. Constable and E. Schofield, *Chem. Commun.*, **1998**, 403-404.
2. E. C. Constable, C. E. Housecroft, M. Neuburger, S. Schaffner and F. Schaper, *Inorg. Chem. Commun.*, **2006**, 9, 433-436.
3. E. C. Constable, C. E. Housecroft, M. Neuburger, S. Schaffner and F. Schaper, *Inorg. Chem. Commun.*, **2006**, 9, 616-619.
4. E. C. Constable, E. L. Dunphy, C. E. Housecroft, M. Neuburger, S. Schaffner, F. Schaper and S. R. Batten, *Dalton Trans.*, **2007**, 4323-4332.
5. E. C. Constable, *Chem. Soc. Rev.*, **2007**, 36, 246-253.
6. E. C. Constable, *Coord. Chem. Rev.*, **2008**, 252, 842-855.
7. S. Rajalakshmi, T. Weyhermüller, M. Dinesh and B. U. Nair, *J. Inorg. Biochem.*, **2012**, 117, 48-59.
8. X. Liang, J. Jiang, X. Xue, L. Huang, X. Ding, D. Nong, H. Chen, L. Pan and Z. Ma, *Dalton Trans.*, **2019**, 48, 10488-10504.
9. E. M. Hahn, N. Estrada-Ortiz, J. Han, V. F. C. Ferreira, T. G. Kapp, J. D. G. Correia, A. Casini and F. E. Kühn, *Eur. J. Inorg. Chem.*, **2017**, 1667-1672.
10. Y. Zhang, X. Sun, H. Zhang and J. Zhao, *Appl. Organomet. Chem.*, **2016**, 30, 645-652.
11. G. Zhang, H. Zeng, S. Li, J. Johnson, Z. Mo, M. C. Neary and S. Zheng, *Dalton Trans.*, **2020**, 49, 2610-2615.
12. H.-L. Kwong, W.-L. Wong, W.-S. Lee, L.-S. Cheng and W.-T. Wong, *Tetrahedron: Asymmetry*, **2001**, 12, 2683-2694.
13. K. C. D. Robson, B. D. Koivisto, A. Yella, B. Sporinova, M. K. Nazeeruddin, T. Baumgartner, M. Grätzel and C. P. Berlinguette, *Inorg. Chem.*, **2011**, 50, 5494-5508.
14. H. Ozawa, T. Sugiura, T. Kuroda, K. Nozawa and H. Arakawa, *J. Mater. Chem. A*, **2016**, 4, 1762-1770.
15. S. Caramori, J. Husson, M. Beley, C. A. Bignozzi, R. Argazzi and P. C. Gros, *Chem. - Eur. J.*, **2010**, 16, 2611-2618.
16. T. Duchanois, T. Etienne, C. Cebrián, L. Liu, A. Monari, M. Beley, X. Assfeld, S. Haacke and P. C. Gros, *Eur. J. Inorg. Chem.*, **2015**, 2015, 2469-2477.
17. H. Ozawa, K. Fukushima, A. Urayama and H. Arakawa, *Inorg. Chem.*, **2015**, 54, 8887-8889.
18. E. R. Schofield, J.-P. Collin, N. Gruber and J.-P. Sauvage, *Chem. Commun.*, **2003**, 188-189.
19. P. Labra-Vázquez, M. Bocé, M. Tassé, S. Mallet-Ladeira, P. G. Lacroix, N. Farfán and I. Malfant, *Dalton Trans.*, **2020**, 49, 3138-3154.
20. C. K. Jang, Y. H. Lee, S. Y. Han and J. Y. Jaung, *Dyes Pigm.*, **2008**, 79, 101-104.
21. E. Baranoff, J.-P. Collin, L. Flamigni and J.-P. Sauvage, *Chem. Soc. Rev.*, **2004**, 33, 147-155.
22. S. Chakraborty and G. R. Newkome, *Chem. Soc. Rev.*, **2018**, 47, 3991-4016.
23. C. E. Housecroft and E. C. Constable, in *Comprehensive Coordination Chemistry III*, eds. E. C. Constable, G. Parkin and L. Que Jr, Elsevier, Oxford, **2021**, pp. 121-173.
24. J. E. Beves, E. C. Constable, C. E. Housecroft, C. J. Kepert and D. J. Price, *CrystEngComm*, **2007**, 9, 456-459.
25. J. E. Beves, E. C. Constable, C. E. Housecroft, M. Neuburger and S. Schaffner, *CrystEngComm*, **2008**, 10, 344-348.
26. J. E. Beves, E. C. Constable, C. E. Housecroft, C. J. Kepert, M. Neuburger, D. J. Price and S. Schaffner, *CrystEngComm*, **2007**, 9, 1073-1077.
27. J. E. Beves, E. C. Constable, S. Decurtins, E. L. Dunphy, C. E. Housecroft, T. D. Keene, M. Neuburger and S. Schaffner, *CrystEngComm*, **2008**, 10, 986-990.
28. C. E. Housecroft and E. C. Constable, *Chem. Commun.*, **2020**, 56, 10786-10794.
29. Y. M. Klein, A. Prescimone, M. Neuburger, E. C. Constable and C. E. Housecroft, *CrystEngComm*, **2017**, 19, 2894-2902.
30. E. C. Constable, C. E. Housecroft, S. Vujovic and J. A. Zampese, *CrystEngComm*, **2014**, 16, 3494-3497.

31. S. Vujovic, E. C. Constable, C. E. Housecroft, C. D. Morris, M. Neuburger and A. Prescimone, *Polyhedron*, **2015**, 92, 77-83.
32. Y. M. Klein, A. Prescimone, E. C. Constable and C. E. Housecroft, *Materials*, **2017**, 10, 728.
33. S. S. Capomolla, G. Manfroni, A. Prescimone, E. C. Constable and C. E. Housecroft, *Polyhedron*, **2022**, 224, 116005.
34. G. Manfroni, A. Prescimone, S. R. Batten, Y. M. Klein, D. J. Gawryluk, E. C. Constable and C. E. Housecroft, *Crystals*, **2019**, 9, 529.
35. P. Howlader, B. Mondal, P. C. Purba, E. Zangrando and P. S. Mukherjee, *J. Am. Chem. Soc.*, **2018**, 140, 7952-7960.
36. J. Yoshida, S.-i. Nishikiori and H. Yuge, *J. Coord. Chem.*, **2013**, 66, 2191-2200.
37. X. Guo, M. Bian, F. Lv, Y. Wang, Z. Zhao, Z. Bian, B. Qu, L. Xiao and Z. Chen, *J. Mater. Chem. C*, **2019**, 7, 11581-11587.
38. J. Lü, L.-W. Han, N. H. Alsmail, A. J. Blake, W. Lewis, R. Cao and M. Schröder, *Cryst. Growth Des.*, **2015**, 15, 4219-4224.
39. J. H. Wang, G. S., *Synlett*, **2005**, 8, 1251-1254.
40. C. W. Machan, M. Adelhardt, A. A. Sarjeant, C. L. Stern, J. Sutter, K. Meyer and C. A. Mirkin, *J. Am. Chem. Soc.*, **2012**, 134, 16921-16924.
41. C. E. Housecroft and A. G. Sharpe, *Inorganic Chemistry*, Pearson, Harlow, 5th edn., **2018**.

Chapter 6 Experimental part

6.1 Materials and methods

Synthetic reactions were carried out under ambient conditions, unless otherwise specified. Commercial chemicals were purchased from Acros Organics, Alfa Aesar, Apollo Sci., Combi-Blocks, Fluka, Fluorochem, Sigma Aldrich, and used as received. Chromatographic separations were carried out on columns of basic alumina (Brockmann activity II) or silica. Filtrations were conducted on silica or celite. ^{1}H, ^{13}C{^{1}H}, ^{19}F{^{1}H} and 2D NMR spectra were recorded on a Bruker Avance III-500 spectrometer equipped with a BBFO probehead at 298 K. The chemical shifts (expressed in parts per million) were referenced to residual solvent peaks (δ TMS = 0). The ^{1}H and ^{13}C{^{1}H} NMR spectra were assigned with the assistance of 2D NMR experiments (COSY, NOESY, HMBC and HMQC). Coupling constants (*J*) are reported in Hertz (Hz) and the multiplicity is described as follows: s (singlet), d (doublet), dd (doublet of doublets), t (triplet), dt (doublet of triplets), tt (triplet of triplets), q (quartet), and m (multiplet). Shimadzu LCMS-2020 and Bruker maXis 4G QTOF instruments were used to record electrospray ionization (ESI-MS) and high-resolution (HR-MS) mass spectra, respectively. MALDI-TOF mass spectra were recorded using a Shimadzu MALDI-8020 with α-cyano-4-hydroxycinnamic acid (CHCA) as matrix. FT-infrared (FT-IR) spectra were recorded using a PerkinElmer UATR Two instrument on solid samples at 298 K; the position of the peaks is given in cm^{-1}. UV-Vis absorption spectra were recorded on a Shimadzu UV2600 spectrophotometer and the samples were introduced as acetonitrile solutions with a drop of formic acid added when needed. Melting points were determined using a Bibby Melting Point Apparatus MP30. Thermogravimetric analysis (TGA) was performed on a TGA5500 instrument (TA Instruments) coupled to a Discovery II MS, Cirrus 3, Mass Spectrometer, DMS. The analysis was carried out under nitrogen, using a Barchart scanning method in the mass range 10–125. In all the experiments, the temperature of the TGA instrument was initially stabilized at 30 °C. The samples were then heated to the appropriate temperature, which was then maintained for 10–30 min. During this time, it was possible to detect the solvent being released from the coordination network and solvents were identified through mass spectrometry. Organic compounds were analyzed by the service of elemental analyses (CHN) of the Department of Chemistry of the University of Basel.

Single-crystal data were collected either on a STOE StadiVari Eulerian 4-circle diffractometer with Cu$K\alpha$ radiation and a Dectris Eiger2 1M detector, or on a STOE StadiVari diffractometer equipped with a Metaljet D2 source (Ga$K\alpha$ radiation) and a Dectris Pilatus300K detector, or on a Bruker APEX-II diffractometer. Data reduction, solution and refinement were performed using the programs Superflip,[1, 2] APEX,[3] ShelXT,[4] Olex2[5] and ShelXL v. 2014/7.[6] All H atoms were included at geometrically calculated positions and refined using a riding model with Uiso = 1.2 of the parent atom. Structure analysis and structural diagrams used the

program Mercury.[7] SQUEEZE[8] or a solvent mask was used in some cases to treat the solvent regions. Powder X-Ray Diffraction (PXRD) patterns were either collected at 295 K in transmission mode using a Stoe Stadi P diffractometer equipped with Cu$K\alpha_1$ radiation (Ge(111)) monochromator and a DECTRIS MYTHEN 1K detector or in the Debye-Scherrer geometry using a Bruker AXS D8 Advance diffractometer equipped with a Ni-filtered Cu$K\alpha$ radiation and a 1D LynxEye PSD detector. Whole-pattern profile-matching analysis[9-11] of the diffraction patterns was carried out using FULLPROF SUITE[11, 12] and applying a previously determined instrument resolution function based on a NIST640d standard. The structural models were derived from the single-crystal X-ray diffraction data. The refined parameters in the Rietveld analysis were scale factor, zero shift, lattice parameters, background points, peak shapes as a Thompson-Cox-Hastings pseudo-Voigt function and in some cases atomic positions of the heavy atoms in the structure. Preferred orientations were included in the analysis as a March-Dollase multi-axial phenomenological model.

6.2 Synthesis of 3,2′:6′,3″-terpyridines

6.2.1 General procedure

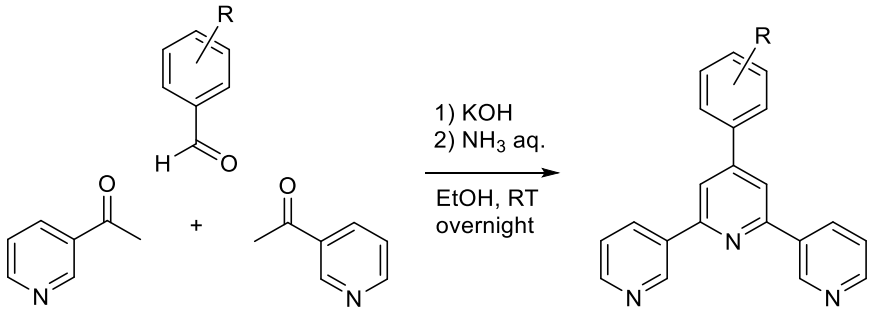

The appropriate substituted benzaldehyde was dissolved in EtOH, then 3-acetylpyridine (2 eq.) and crushed KOH (2 eq.) were added to the solution. Upon addition, a color change to orange was observed. An excess of aqueous NH_3 (32%) was then slowly added and the reaction mixture stirred at room temperature (ca. 22 °C) overnight. The solid that formed was collected by filtration, washed and recrystallized from the appropriate solvent (see below), and then dried *in vacuo*.

6.2.1.1 4′-(4-Methoxyphenyl)-3,2′:6′,3″-terpyridine, **1**

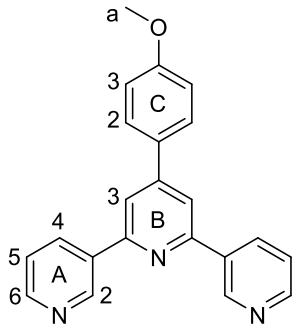

4-Methoxybenzaldehyde (1.36 g, 1.22 mL, 10.0 mmol), 3-acetylpyridine (2.42 g, 2.20 mL, 20.0 mmol), crushed KOH (1.12 g, 20.0 mmol) and aqueous NH_3 (32%, 38.5 mL) were combined in EtOH (50 mL) according to the general procedure. The solid was washed with water (3 × 10 mL) and EtOH (3 × 10 mL) and then recrystallized from EtOH. Compound **1** was isolated as a white powder (0.888 g, 2.62 mmol, 26.2%). M.p. = 157 °C. ^{1}H NMR (500 MHz, $CDCl_3$): δ / ppm 9.38 (d, J = 2.1 Hz, 2H, H^{A2}), 8.71 (dd, J = 4.8, 1.5 Hz, 2H, H^{A6}), 8.55 (m, 2H, H^{A4}), 7.94 (s, 2H, H^{B3}), 7.72 (m, 2H, H^{C2}), 7.50 (m, 2H, H^{A5}), 7.08 (m, 2H, H^{C3}), 3.90 (s, 3H, H^{a}). ^{13}C{^{1}H} NMR (126 MHz, $CDCl_3$): δ / ppm 161.1 (C^{C4}), 155.2 (C^{A3}), 150.7 (C^{B4}), 149.6 (C^{A6}), 147.9 (C^{A2}), 135.3 (C^{A4}), 135.2 (C^{B2}), 130.4 (C^{C1}), 128.5 (C^{C2}), 124.0 (C^{A5}), 117.5 (C^{B3}), 114.9 (C^{C3}), 55.6 (C^{a}). UV-Vis (CH_3CN, 5.0 × 10^{-5} mol dm^{-3}) λ / nm (ε/dm^3 mol^{-1} cm^{-1}): 228 (24,400), 274 (30,000). ESI-MS *m*/*z* 340.10 $[M+H]^+$ (calc. 340.14). Found C 77.74, H 5.05, N 12.36; required for $C_{22}H_{17}N_3O$: C 77.86, H 5.05, N 12.38.

6.2.1.2 4′-(4-Ethoxyphenyl)-3,2′:6′,3″-terpyridine, **2**

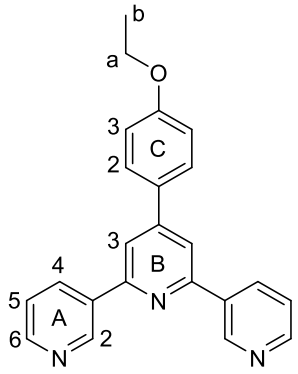

4-Ethoxybenzaldehyde (1.50 g, 1.39 mL, 10.0 mmol), 3-acetylpyridine (2.42 g, 2.20 mL, 20.0 mmol), crushed KOH (1.12 g, 20.0 mmol) and aqueous NH_3 (32%, 38.5 mL) were combined in EtOH (50 mL) according to the general procedure. The solid was washed with water (3 × 10 mL) and EtOH (3 × 10 mL) and then recrystallized from EtOH. Compound **2** was isolated as a white powder (0.591 g, 1.67 mmol, 16.7%). M.p. = 120 °C. ^{1}H NMR (500 MHz, $CDCl_3$): δ / ppm 9.37 (m, 2H, H^{A2}), 8.70 (m, 2H, H^{A6}), 8.51 (8.51 (dt, *J* = 8.0, 1.9 Hz, 2H, H^{A4}), 7.91 (s, 2H, H^{B3}), 7.70 (m, 2H, H^{C2}), 7.47 (m, 2H, H^{A5}), 7.05 (m, 2H, H^{C3}), 4.12 (q, *J* = 7.0 Hz, 2H, H^{a}), 1.47 (t, *J* = 7.0 Hz,

3H, H^{b}). $^{13}C\{^{1}H\}$ NMR (126 MHz, $CDCl_3$): δ / ppm 160.1 (C^{C4}), 155.0 (C^{A3}), 150.3 (C^{B4}), 149.7 (C^{A6}), 148.0 (C^{A2}), 134.8 (C^{A4}), 134.6 (C^{B2}), 130.0 (C^{C1}), 128.2 (C^{C2}), 123.6 (C^{A5}), 117.1 (C^{B3}), 115.1 (C^{C3}), 63.6 (C^{a}), 14.7 (C^{b}). UV-Vis (CH_3CN, 3.3×10^{-5} mol dm^{-3}) λ / nm (ε/dm^3 mol^{-1} cm^{-1}): 229 (29,700), 272 (33,800). ESI–MS *m*/*z* 354.08 $[M+H]^+$ (calc. 354.08). Found C 77.38, H 5.30, N 11.91; required for $C_{23}H_{19}N_3O$: C 78.16, H 5.42, N 11.89.

6.2.1.3 3:2 Ketone-aldehyde condensation product **2a**

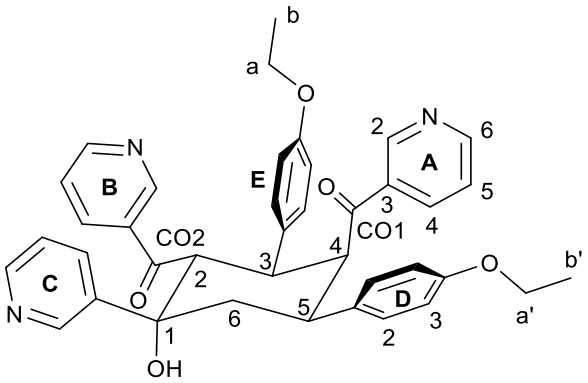

4-Ethoxybenzaldehyde (0.75 g, 0.70 ml, 5.0 mmol) was dissolved in EtOH (25 mL), then 3–acetylpyridine (1.21 g, 1.10 ml, 10.0 mmol) and crushed KOH (0.56 g, 10 mmol) were added to the solution. After five minutes a white precipitate began to form. The reaction mixture was stirred at room temperature overnight. The solid that formed was collected by filtration, washed with water (3 × 10 mL) then EtOH (3 × 10 mL), recrystallized from EtOH and dried *in vacuo*. **2a** was isolated as a white powder (0.27 g, 0.43 mmol, 17.1%). M.p. = 210 °C. ^{1}H NMR (500 MHz, $CDCl_3$): δ / ppm 9.06 (d, J = 1.9 Hz, 1H, H^{C2}), 8.76 (d, J = 1.8 Hz, 1H, H^{B2}), 8.54 (dd, J = 4.8, 1.6 Hz, 1H, H^{B6}), 8.44 (dd, J = 4.8, 1.6 Hz, 1H, H^{A6}), 8.41 (dd, J = 4.9, 1.3 Hz, 1H, H^{C6}), 8.34 (d, J = 1.8 Hz, 1H, H^{A2}), 8.25 (m, 1H, H^{C4}), 7.72 (dt, J = 8.0, 1.9 Hz, 1H, H^{B4}), 7.43 (dt, J = 8.0, 1.9 Hz, 1H, H^{A4}), 7.37 (m, 1H, H^{C5}), 7.13 (m, 1H, H^{B5}), 7.05 (m, 2H, H^{D2}), 7.02 (m, 1H, H^{A5}), 6.95 (m, 2H, H^{E2}), 6.61 (m, 2H, H^{D3}), 6.39 (m, 2H, H^{E3}), 5.62 (d, J = 11.9 Hz, 1H, H^{2}), 5.18 (d, J = 2.1 Hz, 1H, H^{OH}), 4.29 (dd, J = 4.6, 4.6 Hz, 1H, H^{4}), 4.08 (overlapping m, 2H, H^{3+5}), 3.85 (m, 2H, $H^{a'}$), 3.71 (m, 2H, H^{a}), 3.19 (ddd, J = 13.6, 13.6, 2.1 Hz, 1H, H^{6ax}), 2.04 (dd, J = 13.7, 3.4 Hz, 1H, H^{6eq}), 1.29 (t, J = 7.0 Hz, 3H, $H^{b'}$), 1.20 (t, J = 7.0 Hz, 3H, H^{b}). $^{13}C\{^{1}H\}$ NMR (126 MHz, $CDCl_3$): δ / ppm 206.6 (C^{CO2}), 206.1 (C^{CO1}), 158.2 (C^{E4}), 158.0 (C^{D4}), 153.9 (C^{B6}), 152.6 (C^{A6}), 149.6 (C^{B2}), 149.1 (C^{A2}), 146.2 (C^{C6}), 144.8 (C^{C2}), 143.2 (C^{C3}), 135.3 (C^{C4}), 134.8 (C^{A3}), 134.9 (C^{B4}), 134.8 (C^{A4}), 132.8 (C^{B3}), 132.6 (C^{D1}), 130.1 (C^{E1}), 129.7 (C^{E2}), 128.6 (C^{D2}), 123.5 (C^{C5}), 123.4 (C^{B5}), 123.0 (C^{A5}), 114.7 (C^{D3}), 114.6 (C^{E3}), 75.1 (C^{1}), 63.5 ($C^{a'}$), 63.2 (C^{a}), 53.4 (C^{4}), 50.8 (C^{2}), 46.9 (C^{3}), 41.2 (C^{5}), 38.9 (C^{6}), 14.8 ($C^{b'}$), 14.7 (C^{b}). ESI-MS *m*/*z* 628.29 $[M+H]^+$ (calc. 628.28). Found C 74.26, H 5.88, N 6.53; required for $C_{39}H_{37}N_3O_5$ C 74.62, H 5.94, N 6.69.

6.2.1.4 4′-(4-*n*-Propyloxyphenyl)-3,2′:6′,3″-terpyridine, **3**

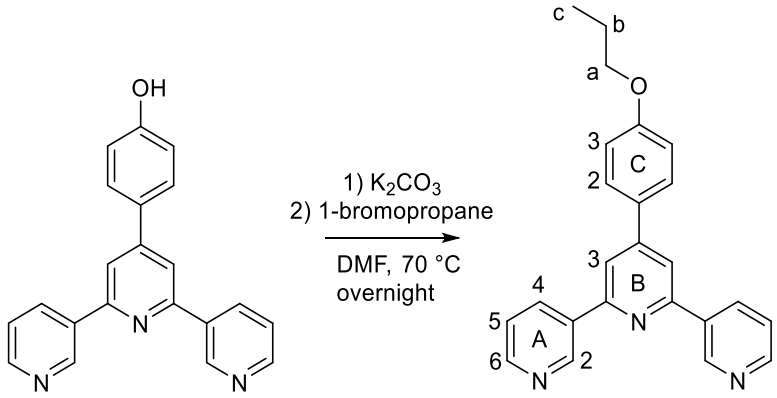

4-Hydroxybenzaldehyde (3.05 g, 25.0 mmol), 3-acetylpyridine (6.06 g, 5.51 ml, 50.0 mmol), crushed KOH (2.81 g, 50.0 mmol) and aqueous NH_3 (32%, 80.0 mL) were combined in EtOH (50 mL) according to the general procedure, and the reaction mixture was stirred at room temperature overnight. The excess of NH_3 was removed under vacuum, then water (100 mL) was added to the reaction mixture and CH_2Cl_2 was used to extract impurities. Aqueous HCl (ca. 4%) was added to the aqueous phase until the pH = 8 and the formation of a solid was observed. The yellow solid was collected by filtration, washed with water (3 × 10 mL) and dried *in vacuo*. The ^{1}H NMR spectrum of the product was in agreement with that previously reported[13] for 4-(3,2′:6′,3′′-terpyridin-4′-yl)phenol (3.10 g, 9.53 mmol, 38.1%). The intermediate (3.10 g, 9.53 mmol) was dissolved in DMF (40 mL) and the solution was heated to 70 °C. Then, anhydrous K_2CO_3 (3.95 g, 28.6 mmol) was added, and the color changed from yellow to red-brown. After 5 min, 1-bromopropane (1.29 g, 0.96 ml, 10.5 mmol) was added to the reaction mixture. This was stirred at 70°C overnight, then it was cooled to room temperature and poured into ice water and stirred for 20 min. The brown solid that formed was dissolved in $CHCl_3$ and was washed with aqueous K_2CO_3 solution. The organic layers were dried over $MgSO_4$ and the solvent was then removed. The solid product was purified by column chromatography (SiO_2, ethyl acetate : cyclohexane 1:1, R_f = 0.16). Ligand **3** was obtained as a pale yellow solid (1.32 g, 3.60 mmol, 37.8%). M.p. = 83 °C. ^{1}H NMR (500 MHz, $CDCl_3$): δ / ppm 9.37 (d, J = 0.8 Hz, 2H, H^{A2}), 8.70 (dd, J = 4.8, 1.7 Hz, 2H, H^{A6}), 8.50 (dt, J = 7.9, 2.0 Hz, 2H, H^{A4}), 7.92 (s, 2H, H^{B3}), 7.71 (m, 2H, H^{C2}), 7.46 (m, 2H, H^{A5}), 7.07 (m, 2H, H^{C3}), 4.01 (t, J = 6.6 Hz, 2H, H^a), 1.86 (m, 2H, H^b), 1.08 (t, J = 7.4 Hz, 3H, H^c). ^{13}C{^{1}H} NMR (126 MHz, $CDCl_3$): δ / ppm 160.6 (C^{C4}), 155.4 (C^{A3}), 150.6 (C^{B4}), 150.2 (C^{A6}), 148.5 (C^{A2}), 135.0 (C^{B2}), 134.7 (C^{A4}), 130.3 (C^{C1}), 128.5 (C^{C2}), 123.8 (C^{A5}), 117.3 (C^{B3}), 115.4 (C^{C3}), 69.9 (C^a), 22.7 (C^b), 10.7 (C^c). UV-Vis (CH_3CN, 2.0 × 10^{-5} mol dm^{-3}) λ / nm (ε/dm^3 mol^{-1} cm^{-1}): 227 (26,500), 275 (31,700). ESI-MS m/z 368.15 $[M+H]^+$ (calc. 368.18). HR-MS m/z 368.1764 $[M+H]^+$ (calc. 368.1757).

6.2.1.5 3:2 Ketone-aldehyde condensation product **3a**

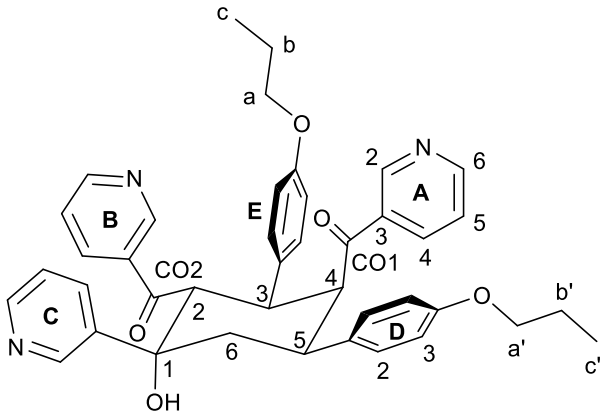

Method 1

4-*n*-Propoxybenzaldehyde (1.64 g, 1.58 ml, 10.0 mmol) was dissolved in EtOH (50 mL), then 3-acetylpyridine (2.42 g, 2.20 ml, 20.0 mmol) and crushed KOH (1.12 g, 20.0 mmol) were added to the solution. At this stage, a white precipitate began to form. Aqueous NH_3 (32%, 38.5 mL) was slowly added to the reaction mixture which was then stirred at room temperature overnight. The solid that formed was collected by filtration, washed with water (3 × 10 mL), EtOH (3 × 10 mL), recrystallized from EtOH and dried *in vacuo*. Compound **3a** was isolated as a white powder (0.495 g, 0.755 mmol, 15.1%). M.p. = 208 °C. ^{1}H NMR (500 MHz, $CDCl_3$): δ / ppm 9.04 (d, J = 1.9 Hz, 1H, H^{C2}), 8.75 (d, J = 1.8 Hz, 1H, H^{B2}), 8.52 (dd, J = 4.8, 1.6 Hz, 1H, H^{B6}), 8.42 (dd, J = 4.8, 1.6 Hz, 1H, H^{A6}), 8.38 (dd, J = 4.8, 1.5 Hz, 1H, H^{C6}), 8.34 (d, J = 1.7 Hz, 1H, H^{A2}), 8.11 (dt, J = 8.1, 1.8 Hz, 1H, H^{C4}), 7.71 (dt, J = 8.1, 2.0 Hz, 1H, H^{B4}), 7.42 (dt, J = 8.1, 2.0 Hz, 1H, H^{A4}), 7.25 (m, 1H, H^{C5}), 7.11 (m, 1H, H^{B5}), 7.06 (m, 2H, H^{D2}), 7.01 (m, 1H, H^{A5}), 6.95 (m, 2H, H^{E2}), 6.61 (m, 2H, H^{D3}), 6.39 (m, 2H, H^{E3}), 5.62 (d, J = 11.9 Hz, 1H, H^2), 5.08 (d, J = 2.1 Hz, 1H, H^{OH}), 4.29 (dd, J = 4.7, 4.7 Hz, 1H, H^4), 4.08 (overlapping m, 2H, H^{3+5}), 3.73 (m, 2H, $H^{a'}$), 3.60 (m, 2H, H^a), 3.20 (ddd, J = 13.0, 13.0, 2.5 Hz, 1H, H^{6ax}), 2.03 (dd, J = 13.7, 3.4 Hz, 1H, H^{6eq}), 1.67 (m, 2H, $H^{b'}$), 1.59 (m, 2H, H^b), 0.94 (t, J = 7.4 Hz, 3H, $H^{c'}$), 0.87 (t, J = 7.4 Hz, 3H, H^c). ^{13}C{^{1}H} NMR (126 MHz, $CDCl_3$): δ / ppm 206.8 (C^{CO2}), 206.1 (C^{CO1}), 158.3 (C^{E4}), 158.1 (C^{D4}), 153.7 (C^{B6}), 152.5 (C^{A6}), 149.6 (C^{B2}), 149.1 (C^{A2}), 147.9 (C^{C6}), 146.4 (C^{C2}), 142.6 (C^{C3}), 135.2 (C^{B4}), 135.0 (C^{A3}), 134.8 (C^{A4}), 133.8 (C^{C4}), 133.0 (C^{B3}), 132.7 (C^{D1}), 130.2 (C^{E1}), 129.7 (C^{E2}), 128.6 (C^{D2}), 123.5 (C^{C5}), 123.2 (C^{B5}), 122.9 (C^{A5}), 114.7 (C^{D3}), 114.6 (C^{E3}), 75.0 (C^1), 69.6 ($C^{a'}$), 69.4 (C^a), 53.5 (C^4), 51.0 (C^2), 46.8 (C^3), 41.2 (C^5), 38.8 (C^6), 22.6 ($C^{b'}$), 22.5 (C^b), 10.6 ($C^{c'}$), 10.5 (C^c). UV-Vis (CH_3CN, 3.3 × 10^{-5} mol dm^{-3}) λ / nm (ε / dm^3 mol^{-1} cm^{-1}): 228 (38,100), 264 (10,400). ESI-MS m/z 656.31 $[M+H]^+$ (calc. 656.31). Found C 74.67, H 6.77, N 6.73; required for $C_{41}H_{41}N_3O_5$ C 75.09, H 6.30, N 6.41.

Method 2

The reaction was carried out as in method 1 without the addition of NH_3. Reagents and solvent: 4-propoxybenzaldehyde (0.82 g, 0.79 ml, 5.0 mmol), EtOH (25 mL), 3-acetylpyridine (1.21 g, 1.10 ml, 10.0 mmol) and crushed KOH (0.56 g, 10 mmol). **3a** was isolated as a white powder

(0.690 g, 1.05 mmol, 42.0%). Characterization data matched those for the product reported in the previous Section.

6.2.1.6 4′-(4-n-Butoxyphenyl)-3,2′:6′,3″-terpyridine, **4**

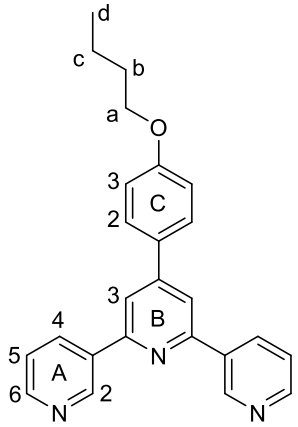

4-*n*-Butoxybenzaldehyde (1.78 g, 1.73 ml, 10.0 mmol), 3-acetylpyridine (2.42 g, 2.20 mL, 20.0 mmol), crushed KOH (1.12 g, 20.0 mmol) and aqueous NH_3 (32%, 38.5 mL) were combined in EtOH (50 mL) according to the general procedure. The solid was washed with water (3 × 10 mL) and EtOH (3 × 10 mL) and then recrystallized from EtOH. Compound **4** was isolated as a white powder (1.19 g, 3.11 mmol, 31.1%). M.p. = 113 °C. ^{1}H NMR (500 MHz, $CDCl_3$): δ / ppm 9.39 (d, J = 2.2 Hz, 2H, H^{A2}), 8.72 (dd, J = 4.9, 1.6 Hz, 2H, H^{A6}), 8.59 (dt, J = 8.1, 2.0 Hz, 2H, H^{A4}), 7.95 (s, 2H, H^{B3}), 7.71 (m, 2H, H^{C2}), 7.53 (m, 2H, H^{A5}), 7.07 (m, 2H, H^{C3}), 4.06 (t, J = 6.5 Hz, 2H, H^{a}), 1.83 (m, 2H, H^{b}), 1.54 (m, 2H, H^{c}), 1.01 (t, J = 7.4 Hz, 3H, H^{d}). ^{13}C{^{1}H} NMR (126 MHz, $CDCl_3$): δ / ppm 160.8 (C^{C4}), 154.9 (C^{A3}), 150.9 (C^{B4}), 149.0 (C^{A6}), 147.4 (C^{A2}), 135.8 (C^{A4}), 135.4 (C^{B2}), 129.9 (C^{C1}), 128.5 (C^{C2}), 124.2 (C^{A5}), 117.6 (C^{B3}), 115.5 (C^{C3}), 68.1 (C^{a}), 31.4 (C^{b}), 19.4 (C^{c}), 14.0 (C^{d}). UV-Vis (CH_3CN, 3.3 × 10^{-5} mol dm^{-3}) λ / nm (ε / dm^3 mol^{-1} cm^{-1}): 228 (30,100), 274 (33,700). ESI-MS m/z 382.16$[M+H]^+$ (calc. 382.19). Found C 78.37, H 5.93, N 11.05; required for $C_{25}H_{23}N_3O$: C 78.71, H 6.08, N 11.02.

6.2.1.7 3:2 Ketone-aldehyde condensation product **4a**

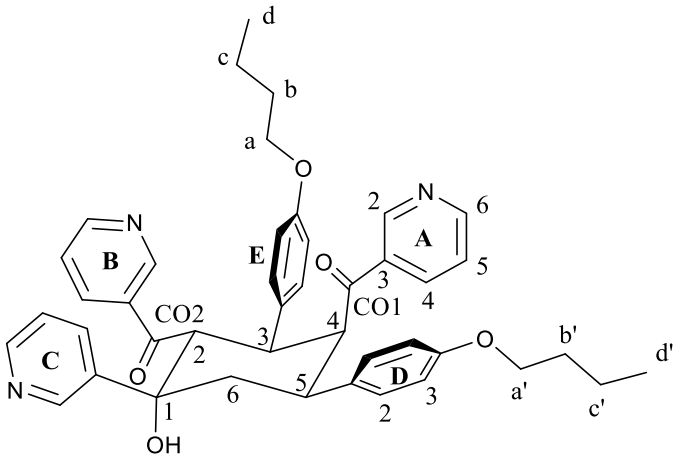

4-*n*-Butyloxybenzaldehyde (0.89 g, 0.87 ml, 5.0 mmol) was dissolved in EtOH (25 mL), then 3-acetylpyridine (1.21 g, 1.10 ml, 10.0 mmol) and crushed KOH (0.56 g, 10 mmol) were added to the solution. After five minutes, a white precipitate began to form. The reaction mixture was stirred at room temperature overnight. The precipitate was collected by filtration, washed with water (3 × 10 mL) and EtOH (3 × 10 mL), then recrystallized from EtOH and dried *in vacuo*. **4a** was isolated as a white powder (0.40 g, 0.59 mmol, 11.7%). M.p. = 185 °C. ^{1}H NMR (500 MHz, $CDCl_3$): δ / ppm 9.06 (d, J = 1.8 Hz, 1H, H^{C2}), 8.77 (d, J = 1.8 Hz, 1H, H^{B2}), 8.54 (dd, J = 4.8, 1.6 Hz, 1H, H^{B6}), 8.43 (dd, J = 4.8, 1.7 Hz, 1H, H^{A6}), 8.42 (dd, J = 5.0, 1.4 Hz, 1H, H^{C6}), 8.35 (d, J = 1.7 Hz, 1H, H^{A2}), 8.27 (m, 1H, H^{C4}), 7.72 (dt, J = 8.0, 1.9 Hz, 1H, H^{B4}), 7.44 (dt, J = 8.0, 2.0 Hz, 1H, H^{A4}), 7.39 (m, 1H, H^{C5}), 7.13 (m, 1H, H^{B5}), 7.05 (m, 2H, H^{D2}), 7.02 (m, 1H, H^{A5}), 6.95 (m, 2H, H^{E2}), 6.61 (m, 2H, H^{D3}), 6.39 (m, 2H, H^{E3}), 5.63 (d, J = 11.9 Hz, 1H, H^{2}), 5.18 (d, J = 2.1 Hz, 1H, H^{OH}), 4.29 (dd, J = 4.6, 4.6 Hz, 1H, H^{4}), 4.08 (overlapping m, 2H, H^{3+5}), 3.77 (m, 2H, $H^{a'}$), 3.64 (m, 2H, H^{a}), 3.18 (ddd, J = 13.7, 13.7, 2.0 Hz, 1H, H^{6ax}), 2.04 (dd, J = 13.7, 3.4 Hz, 1H, H^{6eq}), 1.63 (m, 2H, $H^{b'}$), 1.55 (m, 2H, H^{b}), 1.39 (m, 2H, $H^{c'}$), 1.32 (m, 2H, H^{c}), 0.91 (t, J = 7.4 Hz, 3H, $H^{d'}$), 0.86 (t, J = 7.4 Hz, 3H, H^{d}). ^{13}C{^{1}H} NMR (126 MHz, $CDCl_3$): δ / ppm 207.4 (C^{CO2}), 206.8 (C^{CO1}), 158.3 (C^{D4}), 158.1 (C^{E4}), 153.9 (C^{B6}), 152.4 (C^{A6}), 149.4 (C^{B2}), 149.0 (C^{A2}), 145.9 (C^{C6}), 144.5 (C^{C2}), 143.8 (C^{C3}), 135.6 (C^{C4}), 135.2 (C^{B4}), 134.9 (C^{A3}), 134.8 (C^{A4}), 132.9 (C^{B3}), 132.3 (C^{D1}), 130.0 (C^{E1}), 129.7 (C^{E2}), 128.5 (C^{D2}), 124.1 (C^{C5}), 123.3 (C^{B5}), 122.7 (C^{A5}), 114.8 (C^{D3}), 114.6 (C^{E3}), 75.4 (C^{1}), 67.7 ($C^{a'}$), 67.5 (C^{a}), 53.3 (C^{4}), 50.6 (C^{2}), 46.7 (C^{3}), 41.2 (C^{5}), 38.8 (C^{6}), 31.3 ($C^{b'}$), 31.2 (C^{b}), 19.3 ($C^{c'}$), 19.2 (C^{c}), 13.8 ($C^{d'}$), 13.7 (C^{d}). ESI-MS m/z 684.35 $[M+H]^+$ (calc. 684.34). Found C 75.31, H 6.67, N 6.11; required for $C_{43}H_{45}N_3O_5$ C 75.52, H 6.63, N 6.14.

6.2.1.8 4′-(4-*n*-Pentyloxyphenyl)-3,2′:6′,3″-terpyridine, **5**

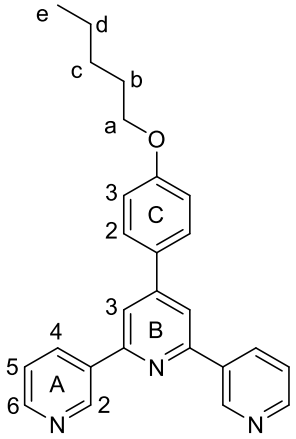

4-*n*-Pentyloxybenzaldehyde (1.92 g, 1.88 mL, 10.0 mmol), 3-acetylpyridine (2.42 g, 2.20 mL, 20.0 mmol), crushed KOH (1.12 g, 20.0 mmol) and aqueous NH_3 (32%, 38.5 mL) were combined in EtOH (50 mL) according to the general procedure. The solid was washed with EtOH (3 × 10 mL), then recrystallized from EtOH. Compound **5** was isolated as a white powder (0.928 g, 2.23 mmol, 23.5%). M.p. = 116 °C. ^{1}H NMR (500 MHz, $CDCl_3$): δ / ppm 9.37 (dd, J = 2.3, 0.9 Hz, 2H, H^{A2}), 8.70 (dd, J = 4.8, 1.7 Hz, 2H, H^{A6}), 8.51 (dt, J = 7.9, 2.3 Hz, 2H, H^{A4}), 7.93 (s, 2H, H^{B3}), 7.71 (m, 2H, H^{C2}), 7.46 (ddd, J = 7.9, 4.8, 0.9 Hz, 2H, H^{A5}), 7.07 (m, 2H, H^{C3}), 4.05 (t, J = 6.6 Hz, 2H, H^{a}), 1.84 (m, 2H, H^{b}), 1.49 (m, 2H, H^{c}), 1.42 (m, 2H, H^{d}), 0.96 (t, J = 7.2 Hz 3H, H^{e}). ^{13}C{^{1}H} NMR (126 MHz, $CDCl_3$): δ / ppm 160.6 (C^{C4}), 155.4 (C^{A3}), 150.6 (C^{B4}), 150.2 (C^{A6}), 148.5 (C^{A2}), 135.0 (C^{A4}), 134.7 (C^{B2}), 130.3 (C^{C1}), 128.5 (C^{C2}), 123.8 (C^{A5}), 117.3 (C^{B3}), 115.4 (C^{C3}), 68.4 (C^{a}), 29.1 (C^{b}), 28.4 (C^{c}), 22.6 (C^{d}), 14.2 (C^{e}). UV-Vis (CH_3CN, 2.5 × 10^{-5} mol dm^{-3}) λ / nm (ε / dm^3 mol^{-1} cm^{-1}): 227 (36,500), 272 (34,400). ESI-MS m/z 396.20 $[M+H]^+$ (calc. 396.20). Found C 78.37, H 6.34, N 10.25; required for $C_{26}H_{25}N_3O$ C 78.96, H 6.37, N 10.62.

6.2.1.9 4′-(4-*n*-Hexyloxyphenyl)-3,2′:6′,3″-terpyridine,[14] **6**

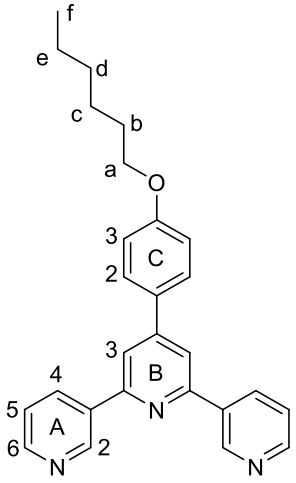

4-*n*-Hexyloxybenzaldehyde (2.06 g, 2.08 mL, 10.0 mmol), 3-acetylpyridine (2.42 g, 2.20 mL, 20.0 mmol), crushed KOH (1.12 g, 20.0 mmol) and aqueous NH_3 (32%, 38.5 mL) were combined in

EtOH (50 mL) according to the general procedure. The solid was washed with EtOH (3 × 10 mL), then recrystallized from EtOH. Compound **6** was isolated as a white powder (1.20 g, 2.92 mmol, 29.2%). X-ray quality crystals of **6** were obtained upon storing the solution at 2–5 °C for one day. M.p. = 126 °C. ^{1}H NMR (500 MHz, $CDCl_3$): δ / ppm 9.38 (d, J = 0.8 Hz, 2H, H^{A2}), 8.70 (dd, J = 4.9, 1.7 Hz, 2H, H^{A6}), 8.55 (dt, J = 8.0, 1.9 Hz, 2H, H^{A4}), 7.93 (s, 2H, H^{B3}), 7.71 (m, 2H, H^{C2}), 7.50 (ddd, J = 8.0, 4.8, 0.8 Hz, 2H, H^{A5}), 7.07 (m, 2H, H^{C3}), 4.05 (t, J = 6.6 Hz, 2H, H^{a}), 1.83 (m, 2H, H^{b}), 1.49 (m, 2H, H^{c}), 1.41-1.33 (overlapping m, 4H, H^{d+e}), 0.92 (m, 3H, H^{f}). ^{13}C{^{1}H} NMR (126 MHz, $CDCl_3$): δ / ppm 160.7 (C^{C4}), 155.2 (C^{A3}), 150.7 (C^{B4}), 149.6 (C^{A6}), 148.0 (C^{A2}), 135.3 + 135.2 (C^{A4+B2}), 130.1 (C^{C1}), 128.5 (C^{C2}), 124.0 (C^{A5}), 117.4 (C^{B3}), 115.4 (C^{C3}), 68.4 (C^{a}), 31.7 (C^{d}), 29.3 (C^{b}), 25.9 (C^{c}), 22.8 (C^{e}), 14.2 (C^{f}). UV-Vis (CH_3CN, 5.0 × 10^{-5} mol dm^{-3}) λ / nm (ε / dm^3 mol^{-1} cm^{-1}): 228 (31,600), 270 (35,500). ESI-MS m/z 410.18 $[M+H]^+$ (calc. 410.22).

6.2.1.10 4′-(4-*n*-Heptyloxyphenyl)-3,2′:6′,3″-terpyridine, **7**

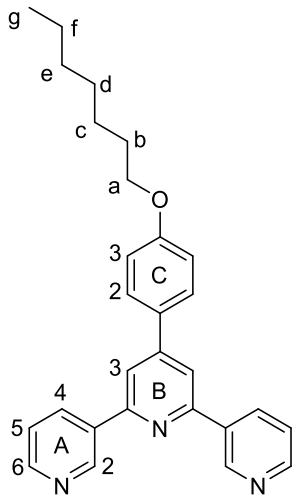

4-*n*-Heptyloxybenzaldehyde (2.20 g, 2.23 mL, 10.0 mmol), 3-acetylpyridine (2.42 g, 2.20 mL, 20.0 mmol), crushed KOH (1.12 g, 20.0 mmol) and aqueous NH_3 (32%, 38.5 mL) were combined in EtOH (50 mL) according to the general procedure. The solid was washed with EtOH (3 × 10 mL), then recrystallized from EtOH. Compound **7** was isolated as a pale yellow crystalline material (1.22 g, 2.89 mmol, 28.9%). X-ray quality crystals of **7** immediately formed from the warm EtOH solution, upon recrystallization. M.p. = 124 °C. ^{1}H NMR (500 MHz, $CDCl_3$): δ / ppm 9.38 (dd, J = 2.3, 0.8 Hz, 2H, H^{A2}), 8.71 (dd, J = 4.9, 1.7 Hz, 2H, H^{A6}), 8.56 (dt, J = 8.0, 2.3 Hz, 2H, H^{A4}), 7.94 (s, 2H, H^{B3}), 7.71 (m, 2H, H^{C2}), 7.50 (ddd, J = 8.0, 4.9, 0.8 Hz, 2H, H^{A5}), 7.06 (m, 2H, H^{C3}), 4.05 (t, J = 6.6 Hz, 2H, H^{a}), 1.84 (m, 2H, H^{b}), 1.49 (m, 2H, H^{c}), 1.39 (m, 2H, H^{d}), 1.33 (overlapping m, 4H, H^{e+f}), 0.91 (m, 3H, H^{g}). ^{13}C{^{1}H} NMR (126 MHz, $CDCl_3$): δ / ppm 160.7 (C^{C4}), 155.1 (C^{A3}), 150.7 (C^{B4}), 149.5 (C^{A6}), 147.9 (C^{A2}), 135.3 (C^{A4}), 135.2 (C^{B2}), 130.1 (C^{C1}), 128.5 (C^{C2}), 124.0 (C^{A5}), 117.5 (C^{B3}), 115.4 (C^{C3}), 68.4 (C^{a}), 31.9 (C^{e}), 29.4 (C^{b}), 29.2 (C^{d}), 26.2 (C^{c}), 22.8 (C^{f}), 14.2 (C^{g}). UV-Vis (CH_3CN, 2.0 × 10^{-5} mol dm^{-3}) λ / nm (ε / dm^3 mol^{-1} cm^{-1}): 226 (35,400), 272 (32,500). ESI-MS m/z 424.26 $[M+H]^+$ (calc. 424.23). Found C 79.23, H 6.85, N 9.90; required for $C_{28}H_{29}N_3O$: C 79.40, H 6.90, N 9.92.

6.2.1.11 4′-(4-*n*-Octyloxyphenyl)-3,2′:6′,3″-terpyridine, **8**

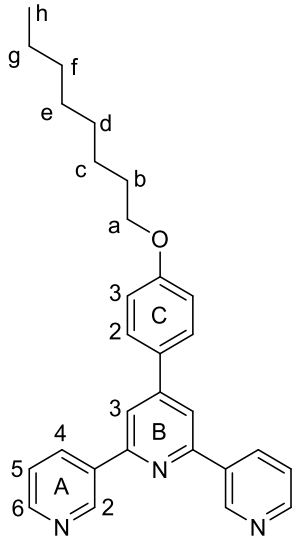

4-*n*-Octyloxybenzaldehyde (2.34 g, 2.39 mL, 10.0 mmol), 3-acetylpyridine (2.42 g, 2.20 mL, 20.0 mmol), crushed KOH (1.12 g, 20.0 mmol) and aqueous NH_3 (32%, 38.5 mL) were combined in EtOH (50 mL) according to the general procedure. The solid was washed with EtOH (3 × 10 mL), then recrystallized from EtOH. Compound **8** was isolated as a white powder (0.942 g, 2.15 mmol, 21.5 %). X-ray quality crystals of **8** were obtained upon recrystallization from EtOH and storing the solution for a few days at 2–5 °C. M.p. = 99 °C. ^{1}H NMR (500 MHz, $CDCl_3$): δ / ppm 9.37 (dd, J = 2.2, 0.6 Hz, 2H, H^{A2}), 8.70 (dd, J = 4.8, 1.6 Hz, 2H, H^{A6}), 8.50 (dt, J = 8.0, 1.8 Hz, 2H, H^{A4}), 7.92 (s, 2H, H^{B3}), 7.70 (m, 2H, H^{C2}), 7.45 (ddd, J = 8.0, 4.8, 0.7 Hz, 2H, H^{A5}), 7.06 (m, 2H, H^{C3}), 4.04 (t, J = 6.6 Hz, 2H, H^{a}), 1.83 (m, 2H, H^{b}), 1.49 (m, 2H, H^{c}), 1.41–1.26 (overlapping m, 8H, $H^{d+e+f+g}$), 0.90 (m, 3H, H^{h}). ^{13}C{^{1}H} NMR (126 MHz, $CDCl_3$): δ / ppm 160.6 (C^{C4}), 155.5 (C^{A3}), 150.5 (C^{A6}), 150.3 (C^{B4}), 148.6 (C^{A2}), 135.0 (C^{A4}), 134.7 (C^{B2}), 130.3 (C^{C1}), 128.4 (C^{C2}), 123.7 (C^{A5}), 117.3 (C^{B3}), 115.4 (C^{C3}), 68.4 (C^{a}), 32.0 (C^{d}), 29.5, 29.4 (C^{e} + C^{f}), 29.3 (C^{b}), 26.2 (C^{c}), 22.8 (C^{g}), 14.3 (C^{h}). UV-Vis (CH_3CN, 5.0 × 10^{-5} mol dm^{-3}) λ / nm (ε / dm^3 mol^{-1} cm^{-1}): 227 (31,300), 271 (33,400). ESI-MS m/z 438.25 $[M+H]^+$ (calc. 438.25). Found C 79.31, H 7.12, N 9.52; required for $C_{29}H_{31}N_3O$: C 79.60, H 7.14, N 9.60.

6.2.1.12 4′-(4-*n*-Nonyloxyphenyl)-3,2′:6′,3″-terpyridine, **9**

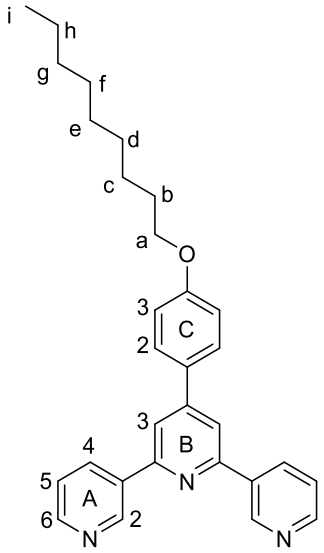

4-*n*-Nonyloxybenzaldehyde (2.48 g, 2.57 mL, 10.0 mmol), 3-acetylpyridine (2.42 g, 2.20 mL, 20.0 mmol), crushed KOH (1.12 g, 20.0 mmol) and aqueous NH_3 (32%, 38.5 mL) were combined in EtOH (50 mL) according to the general procedure. The solid was washed with EtOH (3 × 10 mL), then recrystallized from EtOH. Compound **9** was isolated as a white powder (0.757 g, 1.68 mmol, 16.8 %). X-ray quality crystals of **9** were obtained upon recrystallization from EtOH and storing the solution for a few days at 2–5 °C. M.p. = 106 °C. ^{1}H NMR (500 MHz, $CDCl_3$): δ / ppm 9.37 (d, J = 2.0 Hz, 2H, H^{A2}), 8.70 (dd, J = 4.7, 1.2 Hz, 2H, H^{A6}), 8.50 (m, 2H, H^{A4}), 7.92 (s, 2H, H^{B3}), 7.71 (m, 2H, H^{C2}), 7.46 (m, 2H, H^{A5}), 7.06 (m, 2H, H^{C3}), 4.04 (t, J = 6.6 Hz, 2H, H^{a}), 1.83 (m, 2H, H^{b}), 1.49 (m, 2H, H^{c}), 1.41–1.24 (overlapping m, 10H, $H^{d+e+f+g+h}$), 0.89 (m, 3H, H^{i}). ^{13}C{^{1}H} NMR (126 MHz, $CDCl_3$): δ / ppm 160.6 (C^{C4}), 155.4 (C^{A3}), 150.6 (C^{B4}), 150.3 (C^{A6}), 148.5 (C^{A2}), 135.0 (C^{A4}), 134.7 (C^{B2}), 130.2 (C^{C1}), 128.4 (C^{C2}), 123.8 (C^{A5}), 117.3 (C^{B3}), 115.4 (C^{C3}), 68.4 (C^{a}), 32.0 ($C^{b/d/e/f/g/h}$), 29.7 ($C^{b/d/e/f/g/h}$), 29.6 ($C^{b/d/e/f/g/h}$), 29.4 ($C^{b/d/e/f/g/h}$), 29.3 ($C^{b/d/e/f/g/h}$), 22.8 ($C^{b/d/e/f/g/h}$), 26.2 (C^{c}), 14.3 (C^{i}). UV-Vis (CH_3CN, 2.0 × 10^{-5} mol dm^{-3}) λ / nm (ε / dm^3 mol^{-1} cm^{-1}): 227 (28,900), 273 (31,400). ESI-MS m/z 452.21 $[M+H]^+$ (calc. 452.27). Found C 79.70, H 7.22, N 9.38; required for $C_{30}H_{33}N_3O$: C 79.79, H 7.37, N 9.30.

6.2.1.13 4′-(4-*n*-Decyloxyphenyl)-3,2′:6′,3″-terpyridine, **10**

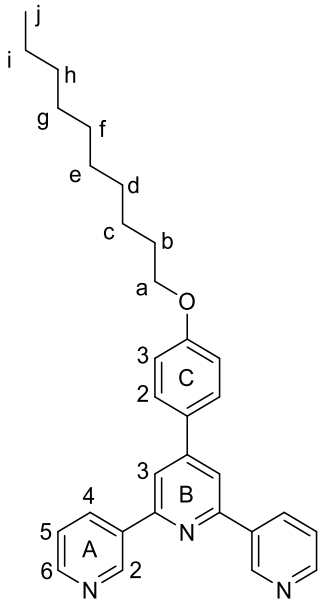

4-*n*-Decyloxybenzaldehyde (2.62 g, 2.73 mL, 10.0 mmol), 3-acetylpyridine (2.42 g, 2.20 mL, 20.0 mmol), crushed KOH (1.12 g, 20.0 mmol) and aqueous NH_3 (32%, 38.5 mL) were combined in EtOH (50 mL) according to the general procedure. The solid was washed with EtOH (3 × 10 mL), then recrystallized from EtOH. Compound **10** was isolated as a white powder (0.452 g, 0.971 mmol, 9.71 %). M.p. = 97 °C. ^{1}H NMR (500 MHz, $CDCl_3$): δ / ppm 9.37 (d, J = 0.9 Hz, 2H, H^{A2}), 8.70 (d, J = 4.6 Hz, 2H, H^{A6}), 8.50 (m, 2H, H^{A4}), 7.92 (s, 2H, H^{B3}), 7.71 (m, 2H, H^{C2}), 7.45 (m, 2H, H^{A5}), 7.06 (m, 2H, H^{C3}), 4.04 (t, J = 6.5 Hz, 2H, H^{a}), 1.83 (m, 2H, H^{b}), 1.49 (m, 2H, H^{c}), 1.41–1.25 (overlapping m, 12H, $H^{d+e+f+g+h+i}$), 0.89 (m, 3H, H^{j}). ^{13}C{^{1}H} NMR (126 MHz, $CDCl_3$): δ / ppm 160.6 (C^{C4}), 155.4 (C^{A3}), 150.5 (C^{A6}), 150.2 (C^{B4}), 148.5 (C^{A2}), 135.0 (C^{A4}), 134.7 (C^{B2}), 130.2 (C^{C1}), 128.4 (C^{C2}), 123.8 (C^{A5}), 117.3 (C^{B3}), 115.4 (C^{C3}), 68.4 (C^{a}), 32.0 ($C^{d/e/f/g/h/i}$), 29.71 ($C^{d/e/f/g/h/i}$), 29.70 ($C^{d/e/f/g/h/i}$), 29.54 ($C^{d/e/f/g/h/i}$), 29.46 ($C^{d/e/f/g/h/i}$), 22.8 ($C^{d/e/f/g/h/i}$), 29.36 (C^{b}), 26.2 (C^{c}), 14.3 (C^{j}). UV-Vis (CH_3CN, 2.0 × 10^{-5} mol dm^{-3}) λ / nm (ε / dm^3 mol^{-1} cm^{-1}): 227 (32,200), 274 (32,200). ESI-MS m/z 466.27 $[M+H]^+$ (calc. 466.29). Found C 79.92, H 7.43, N 9.10; required for $C_{31}H_{35}N_3O$: C 79.96, H 7.58, N 9.02.

6.2.1.14 4′-(4-*sec*-Butoxyphenyl)-3,2′:6′,3″-terpyridine, *rac*-**11**

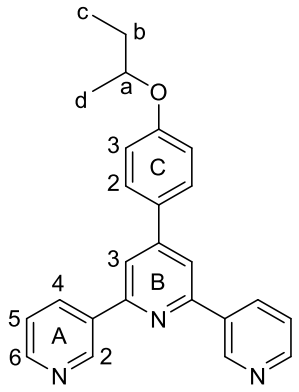

rac-4-(Butan-2-yloxy)benzaldehyde (1.00 g, 5.61 mmol), 3-acetylpyridine (1.36 g, 1.24 mL, 11.2 mmol), crushed KOH (0.630 g, 11.2 mmol) and aqueous NH_3 (32%, 20.0 mL) were combined in EtOH (40 mL) according to the general procedure. The reaction mixture was stirred at room temperature overnight, during which time a small amount of solid formed. The solvent was removed under vacuum, and the solid residue was washed with water (3 × 10 mL), recrystallized from MeOH/H_2O and dried *in vacuo*. Compound *rac*-**11** was isolated as a white powder (0.531 g, 1.39 mmol, 24.8%). M.p. = 97 °C. ^{1}H NMR (500 MHz, $CDCl_3$): δ / ppm 9.37 (d, J = 1.7 Hz, 2H, H^{A2}), 8.70 (dd, J = 4.7, 1.4 Hz, 2H, H^{A6}), 8.51 (dt, J = 9.8, 1.8 Hz, 2H, H^{A4}), 7.92 (s, 2H, H^{B3}), 7.69 (m, 2H, H^{C2}), 7.46 (m, 2H, H^{A5}), 7.05 (m, 2H, H^{C3}), 4.41 (m, 1H, H^{a}), 1.81 (m, 1H, H^{b1}), 1.68 (m, 1H, H^{b2}), 1.36 (m, 3H, H^{d}), 1.02 (t, J = 7.5 Hz, 3H, H^{c}). ^{13}C{^{1}H} NMR (126 MHz, $CDCl_3$): δ / ppm 159.8 (C^{C4}), 155.4 (C^{A3}), 150.6 (C^{B4}), 150.2 (C^{A6}), 148.5 (C^{A2}), 135.0 (C^{A4}), 134.7 (C^{B2}), 130.1 (C^{C1}), 128.5 (C^{C2}), 123.8 (C^{A5}), 117.3 (C^{B3}), 116.6 (C^{C3}), 75.4 (C^{a}), 29.3 (C^{b}), 19.4 (C^{d}), 9.9 (C^{c}). UV-Vis (CH_3CN, 2.0 × 10^{-5} mol dm^{-3}) λ / nm (ε / dm^3 mol^{-1} cm^{-1}): 227 (35,100), 273 (33,100). ESI-MS m/z 382.19 $[M+H]^+$ (calc. 382.19). Found C 78.65, H 6.13, N 10.85; required for $C_{25}H_{23}N_3O$: C 78.71, H 6.08, N 11.02.

6.2.1.15 4′-(2-Methylpropoxyphenyl)-3,2′:6′,3″-terpyridine, **12**

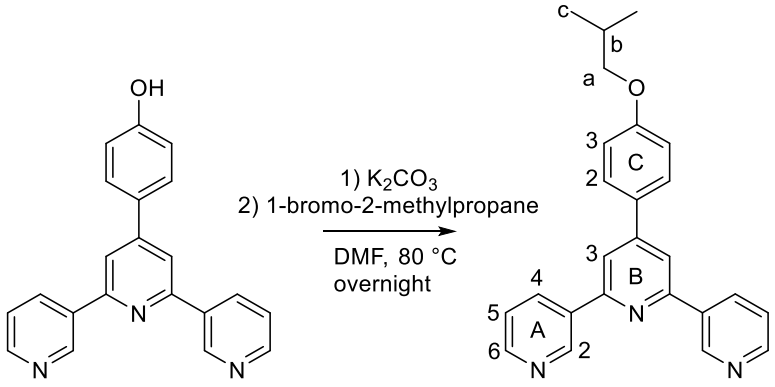

4-(3,2′:6′,3′′-terpyridin-4′-yl)phenol (1.26 g, 3.86 mmol) was dissolved in DMF (40 mL) and the solution was heated to 80 °C. Then, anhydrous K_2CO_3 (1.60 g, 11.6 mmol) was added, and the color changed from yellow to red-brown. After 5 min, 1-bromo-2-methylpropane (0.582 g, 0.46

mL, 4.25 mmol) was added to the reaction mixture. This was stirred at 80°C overnight, then it was cooled to room temperature and poured into ice water and stirred for 20 min, but no solid was formed. The product was extracted with $CHCl_3$ and washed with aqueous K_2CO_3 solution, then the organic layer was dried over $MgSO_4$, and the solvent was removed. The solid product was purified by column chromatography (SiO_2, ethyl acetate: cyclohexane 3:1, R_f = 0.25). Compound **12** was obtained as a pale yellow solid (0.282 g, 0.739 mmol, 19.2%). M.p. = 115 °C. ^{1}H NMR (500 MHz, $CDCl_3$): δ / ppm 9.33 (d, J = 1.5 Hz, 2H, H^{A2}), 8.65 (dd, J = 4.8, 1.7 Hz, 2H, H^{A6}), 8.44 (dt, J = 8.0, 2.0 Hz, 2H, H^{A4}), 7.84 (s, 2H, H^{B3}), 7.64 (m, 2H, H^{C2}), 7.40 (m, 2H, H^{A5}), 7.01 (m, 2H, H^{C3}), 3.76 (d, J = 6.5 Hz, 2H, H^{a}), 2.11 (m, 1H, H^{b}), 1.04 (d, J = 6.7 Hz, 6H, H^{c}). ^{13}C{^{1}H} NMR (126 MHz, $CDCl_3$): δ / ppm 160.6 (C^{C4}), 155.2 (C^{A3}), 150.3 (C^{B4}), 150.1 (C^{A6}), 148.4 (C^{A2}), 134.8 (C^{B2}), 134.5 (C^{A4}), 130.0 (C^{C1}), 128.3 (C^{C2}), 123.6 (C^{A5}), 117.1 (C^{B3}), 115.3 (C^{C3}), 74.6 (C^{a}), 28.3 (C^{b}), 19.3 (C^{c}). UV-Vis (CH_3CN, 2.0 × 10^{-5} mol dm^{-3}) λ / nm (ε / dm^3 mol^{-1} cm^{-1}): 227 (39,700), 269 (37,500). ESI-MS m/z 382.14 $[M+H]^+$ (calc. 382.19). Found C 78.40, H 5.99, N 10.88; required for $C_{25}H_{23}N_3O$ C 78.71, H 6.08, N 11.02.

6.2.1.16 3:2 Ketone- aldehyde condensation product **12a**

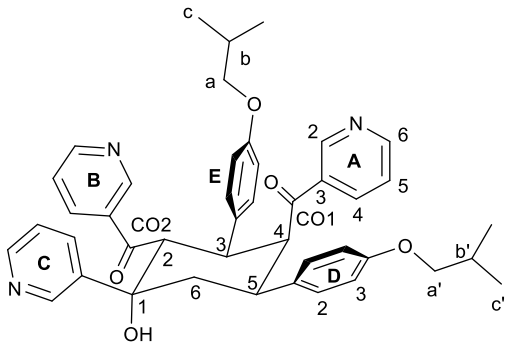

4-(2-Methylpropoxy)benzaldehyde (1.78 g, 1.75 ml, 10.0 mmol) was dissolved in EtOH (40 mL), then 3-acetylpyridine (2.42 g, 2.20 ml, 20.0 mmol) and crushed KOH (1.12 g, 20.0 mmol) were added to the solution. Aqueous NH_3 (32%, 38.5 mL) was slowly added to the reaction mixture, which was then stirred at room temperature overnight. The solid that formed was collected by filtration, washed with water (3 × 10 mL), EtOH (3 × 10 mL), recrystallized from EtOH and dried *in vacuo*. Compound **12a** was isolated as a white powder (0.167 g, 0.244 mmol, 4.9 %). M.p. = 203 °C. ^{1}H NMR (500 MHz, $CDCl_3$): δ / ppm 9.04 (d, J = 2.3 Hz, 1H, H^{C2}), 8.76 (d, J = 2.3 Hz, 1H, H^{B2}), 8.52 (dd, J = 4.8, 1.7 Hz, 1H, H^{B6}), 8.42 (dd, J = 4.8, 1.7 Hz, 1H, H^{A6}), 8.38–8.34 (overlapping m, 2H, H^{C6+A2}), 8.04 (dt, J = 8.0, 2.0 Hz, 1H, H^{C4}), 7.71 (dt, J = 8.1, 2.0 Hz, 1H, H^{B4}), 7.42 (dt, J = 8.1, 2.0 Hz, 1H, H^{A4}), 7.20 (m, 1H, H^{C5}), 7.10 (m, 1H, H^{B5}), 7.06 (m, 2H, H^{D2}), 7.00 (m, 1H, H^{A5}), 6.96 (m, 2H, H^{E2}), 6.61 (m, 2H, H^{D3}), 6.39 (m, 2H, H^{E3}), 5.62 (d, J = 11.9 Hz, 1H, H^{2}), 5.03 (d, J = 2.4 Hz, 1H, H^{OH}), 4.29 (dd, J = 4.7, 4.7 Hz, 1H, H^{4}), 4.12-4.03 (m, 2H, H^{3}+H^{5}), 3.53 (m, 2H, $H^{a'}$), 3.39 (m, 2H, H^{a}), 3.21 (m, 1H, H^{6ax}), 2.03 (dd, J = 13.8, 3.5 Hz, 1H, H^{6eq}), 1.93 (m, 1H, $H^{b'}$), 1.85 (m, 1H, H^{b}), 0.93 (d, J = 6.7 Hz, 6H, $H^{c'}$), 0.86 (d, J = 6.7 Hz, 6H, H^{c}). ^{13}C{^{1}H} NMR (126

MHz, $CDCl_3$): δ / ppm 206.9 (C^{CO2}), 206.1 (C^{CO1}), 158.5 (C^{E4}), 158.3 (C^{D4}), 153.6 (C^{B6}), 152.5 (C^{A6}), 149.7 (C^{B2}), 149.2 (C^{A2}), 148.7 (C^{C6}), 147.1 (C^{C2}), 142.1 (C^{C3}), 135.2 (C^{B4}), 135.0 (C^{A3}), 134.8 (C^{A4}), 133.1 (overlapping C^{C4+B3}), 132.7 (C^{D1}), 130.3 (C^{E1}), 129.7 (C^{E2}), 128.6 (C^{D2}), 123.3 (C^{C5}), 123.2 (C^{B5}), 122.9 (C^{A5}), 114.7 (C^{D3}), 114.6 (C^{E3}), 75.0 (C^{1}), 74.5 ($C^{a'}$), 74.3 (C^{a}), 53.6 (C^{4}), 51.1 (C^{2}), 46.8 (C^{3}), 41.2 (C^{5}), 38.8 (C^{6}), 28.3 ($C^{b'}$), 28.2 (C^{b}), 19.3 ($C^{c'}$), 19.2 (C^{c}). UV-Vis (CH_3CN, 2.0×10^{-5} mol dm^{-3}) λ / nm (ε / dm^3 mol^{-1} cm^{-1}): 228 (53,300), 263 (14,000). ESI-MS *m*/*z* 684.28 $[M+H]^+$ (calc. 684.34). Found C 75.08, H 6.54, N 5.97; required for $C_{43}H_{45}N_3O_5$ C 75.52, H 6.63, N 6.14.

6.2.1.17 4′-(*tert*-Butoxyphenyl)-3,2′:6′,3″-terpyridine, **13**

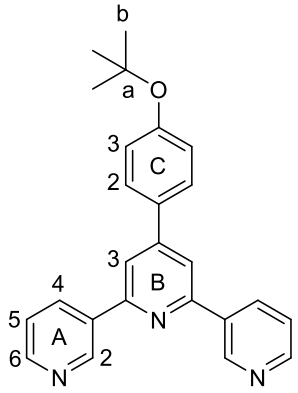

4′-(*tert*-Butoxy)benzaldehyde (1.78 g, 1.75 mL, 10.0 mmol), 3-acetylpyridine (2.42 g, 2.20 mL, 20.0 mmol), crushed KOH (1.12 g, 20.0 mmol) and aqueous NH_3 (32%, 38.5 mL) were combined in EtOH (50 mL) according to the general procedure. The solid was washed with H_2O (3 × 10 mL) and EtOH (3 × 10 mL) and then recrystallized from EtOH. Compound **13** was isolated as a white powder (0.781 g, 2.05 mmol, 20.5%). M.p. = 207 °C. ^{1}H NMR (500 MHz, $CDCl_3$): δ / ppm 9.37 (d, 2H, H^{A2}), 8.70 (dd, J = 4.8, 1.6 Hz, 2H, H^{A6}), 8.51 (m, 2H, H^{A4}), 7.93 (s, 2H, H^{B3}), 7.67 (m, 2H, H^{C2}), 7.45 (m, 2H, H^{A5}), 7.16 (m, 2H, H^{C3}), 1.43 (s, 9H, H^{b}). ^{13}C{^{1}H} NMR (126 MHz, $CDCl_3$): δ / ppm 157.2 (C^{C4}), 155.4 (C^{A3}), 150.6 (C^{B4}), 150.3 (C^{A6}), 148.5 (C^{A2}), 134.9 (C^{A4}), 134.7 (C^{B2}), 132.9 (C^{C1}), 127.9 (C^{C2}), 124.6 (C^{A5}), 123.7 (C^{B3}), 117.5 (C^{C3}), 79.4 (C^{a}), 29.1 (C^{b}). UV-Vis (CH_3CN, 2.0×10^{-5} mol dm^{-3}) λ / nm (ε / dm^3 mol^{-1} cm^{-1}): 224 (32,600), 264 (38,600), 315 *sh* (10,800). ESI-MS *m*/*z* 382.17 $[M+H]^+$ (calc. 382.19). Found C 78.60, H 5.98, N 10.94; required for $C_{25}H_{23}N_3O$ C 78.71, H 6.08, N 11.02.

6.2.1.18 4′-(4-(Isopropoxyphenyl)-3,2′:6′,3″-terpyridine, **14**

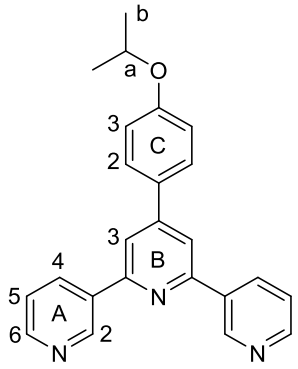

4′-Isopropoxybenzaldehyde (1.64 g, 1.58 mL, 10.0 mmol), 3-acetylpyridine (2.42 g, 2.20 mL, 20.0 mmol), crushed KOH (1.12 g, 20.0 mmol) and aqueous NH_3 (32%, 38.5 mL) were combined in EtOH (40 mL) according to the general procedure. The solid was washed with EtOH (3 × 10 mL), then recrystallized from EtOH. Compound **14** was isolated as a white powder (0.456 g, 1.24 mmol, 12.4%). M.p. = 137 °C. ^{1}H NMR (500 MHz, $CDCl_3$): δ / ppm 9.37 (d, J = 2.3 Hz, 2H, H^{A2}), 8.70 (dd, J = 4.9, 1.7 Hz, 2H, H^{A6}), 8.51 (dt, J = 8.0, 2.0 Hz, 2H, H^{A4}), 7.93 (s, 2H, H^{B3}), 7.70 (m, 2H, H^{C2}), 7.46 (m, 2H, H^{A5}), 7.05 (m, 2H, H^{C3}), 4.66 (m, 1H, H^{a}), 1.40 (d, J = 6.0 Hz, 6H, H^{b}). ^{13}C{^{1}H} NMR (126 MHz, $CDCl_3$): δ / ppm 159.4 (C^{C4}), 155.4 (C^{A3}), 150.6 (C^{B4}), 150.2 (C^{A6}), 148.5 (C^{A2}), 135.0 (C^{B2}), 134.8 (C^{A4}), 130.2 (C^{C1}), 128.5 (C^{C2}), 123.8 (C^{A5}), 117.3 (C^{B3}), 116.6 (C^{C3}), 70.3 (C^{a}), 22.2 (C^{b}). UV-Vis (CH_3CN, 2.0 × 10^{-5} mol dm^{-3}) λ / nm (ε / dm^3 mol^{-1} cm^{-1}): 227 (32,100), 268 (31,900). ESI-MS m/z 368.17 $[M+H]^+$ (calc. 368.18). Found C 77.39, H 5.71, N 11.74; required for $C_{24}H_{21}N_3O$ C 78.45, H 5.76, N 11.44.

6.2.1.19 4′-(4-(Isopentyloxyphenyl)-3,2′:6′,3″-terpyridine, **15**

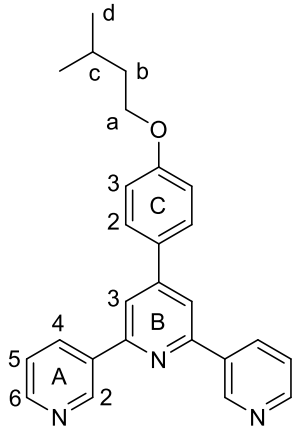

4-(3-Methyl-butoxy)-benzaldehyde (1.00 g, 5.19 mmol), 3-acetylpyridine (1.26 g, 1.14 mL, 10.4 mmol), crushed KOH (0.582 g, 10.4 mmol) and aqueous NH_3 (32%, 20.0 mL) were combined in EtOH (50 mL) according to the general procedure. The reaction mixture was stirred at room temperature overnight, during which time a small amount of solid formed. Most of the solvent was removed under vacuum, the mixture was filtered and the solid was washed with H_2O (3

× 10 mL), affording an orange oil. After washing with Et_2O, compound **15** was isolated as a white powder (0.305 g, 0.771 mmol, 14.9 %). M.p. = 130 °C. ^{1}H NMR (500 MHz, $CDCl_3$): δ / ppm 9.37 (d, J = 2.3 Hz, 2H, H^{A2}), 8.70 (dd, J = 4.8, 1.7 Hz, 2H, H^{A6}), 8.50 (dt, J = 8.0, 2.0 Hz, 2H, H^{A4}), 7.92 (s, 2H, H^{B3}), 7.71 (m, 2H, H^{C2}), 7.46 (m, 2H, H^{A5}), 7.07 (m, 2H, H^{C3}), 4.08 (t, J = 6.6 Hz, 2H, C^a), 1.88 (m, 1H, C^c), 1.73 (m, 2H, C^b), 1.00 (d, J = 6.6 Hz, 6H, C^d). ^{13}C{^{1}H} NMR (126 MHz, $CDCl_3$): δ / ppm 160.6 (C^{C4}), 155.4 (C^{A3}), 150.6 (C^{B4}), 150.3 (C^{A6}), 148.5 (C^{A2}), 135.0 (C^{A4}), 134.7 (C^{B2}), 130.3 (C^{C1}), 128.5 (C^{C2}), 123.8 (C^{A5}), 117.3 (C^{B3}), 115.4 (C^{C3}), 66.8 (C^a), 38.1 (C^b), 25.2 (C^c), 22.7 (C^d). UV-Vis (CH_3CN, 2.0 × 10^{-5} mol dm^{-3}) λ / nm (ε / dm^3 mol^{-1} cm^{-1}): 227 (29,900), 271 (31,500). ESI-MS m/z 396.17 $[M+H]^+$ (calc. 396.21). Found C 77.42, H 7.45, N 10.76; required for $C_{26}H_{25}N_3O$ C 78.96, H 6.37, N 10.62.

6.2.1.20 4′-([1,1′-Biphenyl-4-yl)-3,2′:6′,3″-terpyridine, **16**

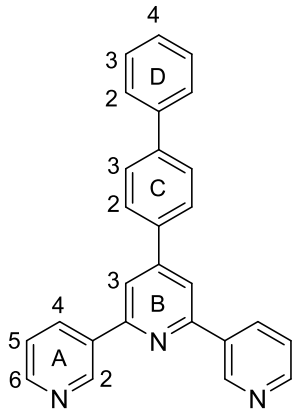

[1,1′-Biphenyl]-4-carbaldehyde (1.84 g, 10.0 mmol), 3-acetylpyridine (2.42 g, 2.20 mL, 20.0 mmol), crushed KOH (1.12 g, 20.0 mmol) and aqueous NH_3 (32%, 38.5 mL) were combined in EtOH (50 mL) according to the general procedure. The solid was washed with water (3 × 10 mL) and EtOH (3 × 10 mL), then recrystallized from MeOH. Compound **16** was isolated as a white powder (1.54 g, 4.00 mmol, 40.0%). M.p. = 218 °C. ^{1}H NMR (500 MHz, $CDCl_3$): δ / ppm 9.40 (d, J = 2.2 Hz, 2H, H^{A2}), 8.72 (dd, J = 4.7, 1.7 Hz, 2H, H^{A6}), 8.53 (dt, J = 7.9, 2.2 Hz, 2H, H^{A4}), 8.01 (s, 2H, H^{B3}), 7.85 (d, J = 8.4 Hz, 2H, H^{C2}), 7.79 (d, J = 8.4 Hz, 2H, H^{C3}), 7.68 (m, 2H, H^{D2}), 7.50 (m, 2H, H^{D3}), 7.47 (m, 2H, H^{A5}), 7.42 (m, 1H, H^{D4}). ^{13}C{^{1}H} NMR (126 MHz, $CDCl_3$): δ / ppm 155.6 (C^{A3}), 150.6 (C^{B4}), 150.4 (C^{A6}), 148.6 (C^{A2}), 142.6 (C^{C4}), 140.3 (C^{D1}), 137.1 (C^{C1}), 134.8 (C^{B2}), 134.7 (C^{A4}), 129.1 (C^{D3}), 128.2 (C^{C3}), 128.0 (C^{D4}), 127.7 (C^{C2}), 127.3 (C^{D2}), 123.8 (C^{A5}), 117.7 (C^{B3}). UV-Vis (CH_3CN, 2.0 × 10^{-5} mol dm^{-3}) λ / nm (ε / dm^3 mol^{-1} cm^{-1}): 228 (28,400), 265 *sh* (34,600), 284 (41,100). ESI-MS m/z 386.13 $[M+H]^+$ (calc. 386.17). Found C 83.91, H 4.81, N 11.04; required for $C_{27}H_{19}N_3$ C 84.13, H 4.97, N 10.90.

6.2.1.21 4′-(4′-Fluoro-[1,1′-biphenyl-4-yl)-3,2′:6′,3″-terpyridine, **17**

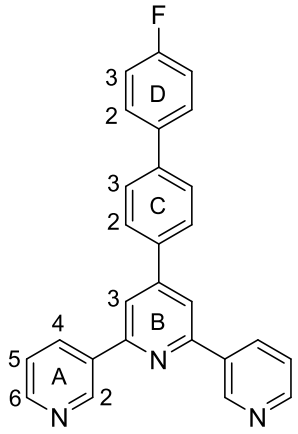

4′-Fluoro-[1,1′-biphenyl]-4-carbaldehyde (2.00 g, 10.0 mmol), 3-acetylpyridine (2.42 g, 2.20 mL, 20.0 mmol), crushed KOH (1.12 g, 20.0 mmol) and aqueous NH_3 (32%, 38.5 mL) were combined in EtOH (50 mL) according to the general procedure. The solid was washed with water (3 × 10 mL) and EtOH (3 × 10 mL), then recrystallized from MeOH. Compound **17** was isolated as a white powder (1.62 g, 4.03 mmol, 40.3%). M.p. = 215 °C. ^{1}H NMR (500 MHz, $CDCl_3$): δ / ppm 9.39 (d, J = 2.2 Hz, 2H, H^{A2}), 8.71 (dd, J = 4.7, 1.5 Hz, 2H, H^{A6}), 8.53 (dt, J = 8.0, 2.2 Hz, 2H, H^{A4}), 8.00 (s, 2H, H^{B3}), 7.84 (m, 2H, H^{C2}), 7.74 (m, 2H, H^{C3}), 7.63 (m, 2H, H^{D2}), 7.48 (ddd, J = 8.0, 4.7, 0.9 Hz, 2H, H^{A5}), 7.18 (m, 2H, H^{D3}). ^{13}C{^{1}H} NMR (126 MHz, $CDCl_3$): δ / ppm 162.9 (d, J_{CF} = 239 Hz, C^{D4}), 155.6 (C^{A3}), 150.5 (C^{B4}), 150.3 (C^{A6}), 148.5 (C^{A2}), 141.6 (C^{C4}), 137.1 (C^{C1}), 136.4 (d, J_{CF} = 2.5 Hz, C^{D1}), 134.85 (C^{B2}), 134.8 (C^{A4}), 128.9 (d, J_{CF} = 7.6 Hz, C^{D2}), 128.0 (C^{C3}), 127.8 (C^{C2}), 123.8 (C^{A5}), 117.7 (C^{B3}), 116.1 (d, J_{CF} = 22.5 Hz, C^{D3}). ^{19}F{^{1}H} NMR (470 MHz, $CDCl_3$): δ / ppm –114.6. UV-Vis (CH_3CN, 2.0 × 10^{-5} mol dm^{-3}) λ / nm (ε / dm^3 mol^{-1} cm^{-1}): 227 (28,200), 264 *sh* (33,100), 284 (38,800). ESI-MS *m*/*z* 404.12 $[M+H]^+$ (calc. 404.16). Found C 79.08, H 4.59, N 10.42; required for $C_{27}H_{18}FN_3$ C 80.38, H 4.50, N 10.42.

6.2.1.22 4′-(4′-Chloro-[1,1′-biphenyl-4-yl)-3,2′:6′,3″-terpyridine, **18**

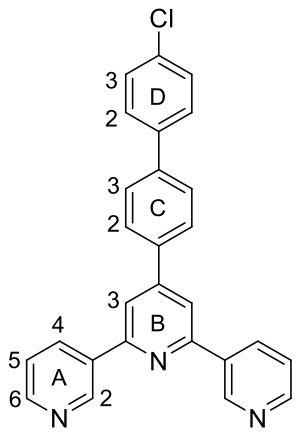

4′-Chloro-[1,1′-biphenyl]-4-carbaldehyde (2.17 g, 10.0 mmol), 3-acetylpyridine (2.42 g, 2.20 mL, 20.0 mmol), crushed KOH (1.12 g, 20.0 mmol) and aqueous NH_3 (32%, 38.5 mL) were

combined in EtOH (50 mL) according to the general procedure. The solid was washed with water (3 × 10 mL) and EtOH (3 × 10 mL), then recrystallized from EtOH. Compound **18** was isolated as a white powder (1.43 g, 3.40 mmol, 34.0%). M.p. = 240 °C. ^{1}H NMR (500 MHz, $CDCl_3$): δ / ppm 9.40 (dd, J = 2.2, 0.9 Hz, 2H, H^{A2}), 8.72 (dd, J = 4.8, 1.6 Hz, 2H, H^{A6}), 8.54 (dt, J = 8.1, 2.2 Hz, 2H, H^{A4}), 8.00 (s, 2H, H^{B3}), 7.84 (m, 2H, H^{C2}), 7.75 (m, 2H, H^{C3}), 7.60 (m, 2H, H^{D2}), 7.50-7.44 (overlapping m, 4H, H^{A5+D3}). ^{13}C{^{1}H} NMR (126 MHz, $CDCl_3$): δ / ppm 155.6 (C^{A3}), 150.4 (C^{B4}), 150.3 (C^{A6}), 148.5 (C^{A2}), 141.3 (C^{C4}), 138.7 (C^{D4}), 137.5 (C^{C1}), 134.84 (C^{B2}), 134.8 (C^{A4}), 134.2 (C^{D1}), 129.3 (C^{D3}), 128.5 (C^{D2}), 128.0 (C^{C3}), 127.8 (C^{C2}), 123.8 (C^{A5}), 117.7 (C^{B3}). UV-Vis (CH_3CN, 2.0 × 10^{-5} mol dm^{-3}) λ / nm (ε / dm^3 mol^{-1} cm^{-1}): 228 (29,000), 264 *sh* (35,800), 288 (45,900). ESI-MS *m*/*z* 420.09 $[M+H]^+$ (calc. 420.13). Found C 76.58, H 4.12, N 9.87; required for $C_{27}H_{18}ClN_3$ C 77.23, H 4.32, N 10.01.

6.2.1.23 4′-(4′-Bromo-[1,1′-biphenyl-4-yl)-3,2′:6′,3″-terpyridine, **19**

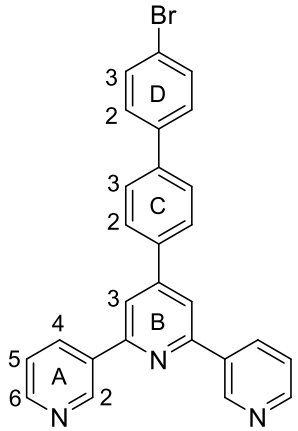

4′-Bromo-[1,1′-biphenyl]-4-carbaldehyde (0.809 g, 3.10 mmol), 3-acetylpyridine (0.751 g, 0.683 mL, 6.20 mmol), crushed KOH (0.348 g, 6.20 mmol) and aqueous NH_3 (32%, 11.9 mL) were combined in EtOH (50 mL) according to the general procedure. The solid was washed with water (3 × 10 mL) and EtOH (3 × 10 mL), then dried. Compound **19** was isolated as a white powder (0.645 g, 1.39 mmol, 44.8%). M.p. = 248 °C. ^{1}H NMR (500 MHz, $CDCl_3$): δ / ppm 9.40 (dd, J = 2.3, 0.9 Hz, 2H, H^{A2}), 8.72 (dd, J = 4.8, 1.7 Hz, 2H, H^{A6}), 8.54 (dt, J = 8.0, 2.3 Hz, 2H, H^{A4}), 8.00 (s, 2H, H^{B3}), 7.84 (m, 2H, H^{C2}), 7.75 (m, 2H, H^{C3}), 7.62 (m, 2H, H^{D3}), 7.54 (m, 2H, H^{D2}), 7.44 (m, 2H, H^{A5}). ^{13}C{^{1}H} NMR (126 MHz, $CDCl_3$): δ / ppm 155.6 (C^{A3}), 150.4 (C^{B4}), 150.3 (C^{A6}), 148.5 (C^{A2}), 141.3 (C^{C4}), 139.2 (C^{D1}), 137.5 (C^{C1}), 134.83 (C^{B2}), 134.81 (C^{A4}), 132.3 (C^{D3}), 128.9 (C^{D2}), 128.0 (C^{C3}), 127.9 (C^{C2}), 123.9 (C^{A5}), 122.4 (C^{D4}), 117.7 (C^{B3}). UV-Vis (CH_3CN, 2.0 × 10^{-5} mol dm^{-3}) λ / nm (ε / dm^3 mol^{-1} cm^{-1}): 228 (29,000), 264 *sh* (35,800), 292 (47,000). ESI-MS *m*/*z* 464.05 $[M+H]^+$ (calc. 464.08). Found C 69.55, H 3.76, N 8.89; required for $C_{27}H_{18}BrN_3$ C 69.84, H 3.91, N 9.05.

6.2.1.24 4′-(4′-Methyl-[1,1′-biphenyl-4-yl)-3,2′:6′,3″-terpyridine, **20**

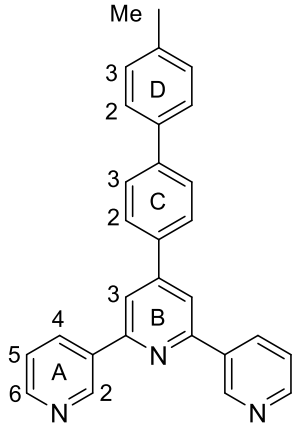

4′-Methyl-[1,1′-biphenyl]-4-carbaldehyde (1.00 g, 5.09 mmol), 3-acetylpyridine (1.23 g, 1.12 mL, 10.2 mmol), crushed KOH (0.571 g, 10.2 mmol) and aqueous NH_3 (32%, 19.6 mL) were combined in EtOH (50 mL) according to the general procedure. The solid was washed with water (3 × 10 mL) and EtOH (3 × 10 mL), then recrystallized from EtOH. Compound **20** was isolated as a white powder (0.670 g, 1.68 mmol, 32.9%). M.p. = 191 °C. ^{1}H NMR (500 MHz, $CDCl_3$): δ / ppm 9.40 (d, J = 0.9 Hz, 2H, H^{A2}), 8.72 (dd, J = 4.8, 1.7 Hz, 2H, H^{A6}), 8.53 (dt, J = 8.0, 2.0 Hz, 2H, H^{A4}), 8.01 (s, 2H, H^{B3}), 7.83 (d, J = 8.2 Hz, 2H, H^{C2}), 7.78 (d, J = 8.2 Hz, 2H, ^{HC3}), 7.58 (d, J = 8.0 Hz, 2H, H^{D2}), 7.48 (m, 2H, H^{A5}), 7.31 (d, J = 8.0 Hz, 2H, H^{D3}), 2.43 (s, 3H, CH_3). $^{13}C\{^1H\}$ NMR (126 MHz, $CDCl_3$): δ / ppm 155.6 (C^{A3}), 150.7 (C^{B4}), 150.3 (C^{A6}), 148.5 (C^{A2}), 142.5 (C^{C4}), 138.0 (C^{D4}), 137.3 (C^{D1}), 136.8 (C^{C1}), 134.9 (C^{B2}), 134.8 (C^{A4}), 129.8 (C^{D3}), 127.9 (C^{C3}), 127.7 (C^{C2}), 127.1 (C^{D2}), 123.8 (C^{A5}), 117.7 (C^{B3}), 21.3 (C^{Me}). UV-Vis (CH_3CN, 2.0 × 10^{-5} mol dm^{-3}) λ / nm (ε / dm^3 mol^{-1} cm^{-1}): 230 (30,500), 261 *sh* (31,100), 295 (38,000). ESI-MS m/z 400.16 $[M+H]^+$ (calc. 400.18). Found C 83.89, H 5.30, N 10.39; required for $C_{28}H_{21}N_3$ C 84.18, H 5.30, N 10.52.

6.2.1.25 4′-(4′-Napththalen-1-yl)phenyl)-3,2′:6′,3″-terpyridine, **21**

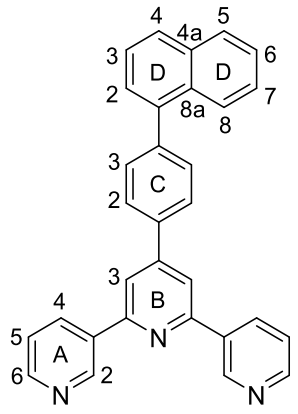

4-(Naphthalen-1-yl)benzaldehyde (1.00 g, 4.31 mmol), 3-acetylpyridine (1.04 g, 0.95 ml, 8.62 mmol), crushed KOH (0.484 g, 8.62 mmol) and aqueous NH_3 (32%, 16.6 mL) were combined in EtOH (50 mL) according to the general procedure. The solid was washed with water (3 × 10

mL) and EtOH (3 × 10 mL), then recrystallized from EtOH. Compound **21** was isolated as a white powder (0.789 g, 1.81 mmol, 42.0%). M.p. = 225 °C. ^{1}H NMR (500 MHz, $CDCl_3$): δ / ppm 9.46 (dd, J = 2.3, 0.9 Hz, 2H, H^{A2}), 8.75 (dd, J = 4.9, 1.6 Hz, 2H, H^{A6}), 8.68 (dt, J = 8.0, 2.0 Hz, 2H, H^{A4}), 8.11 (s, 2H, H^{B3}), 7.94 (overlapping m, 5H, H^{C2} + 3H^{D}), 7.72 (m, 2H, H^{C3}), 7.62-7.47 (overlapping m, 6H, H^{A5} + 4H^{D}). ^{13}C{^{1}H} NMR (126 MHz, $CDCl_3$): δ / ppm 155.0 (C^{A3}), 151.2 (C^{B4}), 148.8 (C^{A6}), 147.1 (C^{A2}), 142.6 (C^{C4}), 139.2 (C^{D1}), 136.8 (C^{C1}), 136.1 (C^{A4}), 135.4 (C^{B2}), 134.0 ($C^{D4a/D8a}$), 131.6 ($C^{D4a/D8a}$), 131.3 (C^{C3}), 128.6 (C^{D}), 128.4 (C^{D}), 127.3 (C^{C2}), 127.2 (C^{D}), 126.5 (C^{D}), 126.1 (C^{D}), 125.8 (C^{D}), 125.6 (C^{D}), 124.4 (C^{A5}), 118.3 (C^{B3}). UV-Vis (CH_3CN, 2.0 × 10^{-5} mol dm^{-3}) λ / nm (ε / dm^3 mol^{-1} cm^{-1}): 222 (62,600), 258 (35,500), 294 (25,900). ESI-MS m/z 436.17 $[M+H]^+$ (calc. 436.18). Found C 85.51, H 4.81, N 9.79; required for $C_{31}H_{21}N_3$ C 85.49, H 4.86, N 9.65.

6.3 Synthesis of expanded ligands

6.3.1 Synthesis of 4′-substituted 2,2′:6′,2″-, 3,2′:6′,3″-, and 4,2′:6′,4″-terpyridines

The following compounds were prepared according to the general procedure described in the previous section for 3,2′:6′,3″-tpys, combining in each case 4-bromo-2,5-dimethoxybenzaldehyde with the appropriate isomer of the acetylpyridine.

6.3.1.1 4′-(4-Bromo-2,5-dimethoxyphenyl)-2,2′:6′,2″-terpyridine, **22**

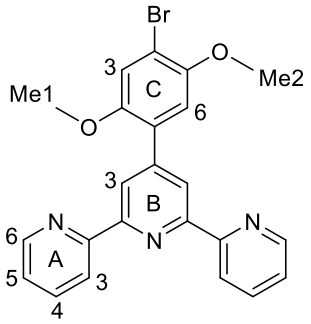

4-Bromo-2,5-dimethoxybenzaldehyde (5.00 g, 20.4 mmol) was dissolved in EtOH (60 mL), then 2-acetylpyridine (4.94 g, 4.57 ml, 40.8 mmol) and crushed KOH (2.29 g, 40.8 mmol) were added to the solution. Aqueous NH_3 (32%, 78.6 mL) was slowly added to the reaction mixture and this was stirred at room temperature overnight. The solid that formed was collected by filtration, washed with H_2O (3 × 10 mL) and EtOH (3 × 10 mL), recrystallized from EtOH/$CHCl_3$ and dried *in vacuo*. Compound **22** was isolated as a white powder (3.96 g, 8.84 mmol, 43.3%). M.p. = 175 °C. ^{1}H NMR (500 MHz, DMSO-d_6): δ / ppm 8.74 (ddd, J = 4.8, 1.8, 0.9 Hz, 2H, H^{A6}), 8.66 (dt, J = 8.0, 1.1 Hz, 2H, H^{A3}), 8.54 (s, 2H, H^{B3}), 8.03 (td, 2H, J = 7.6, 1.8 Hz, H^{A4}), 7.51 (ddd, 2H, J = 7.6, 4.8, 1.1 Hz, H^{A5}), 7.45 (s, 1H, H^{C3}), 7.24 (s, 1H, H^{C6}), 3.89 (s, 3H, H^{OMe2}), 3.80 (s, 3H, H^{OMe1}). ^{13}C{^{1}H} NMR (126 MHz, DMSO-d_6): δ / ppm 155.1 ($C^{B2/A2}$), 154.9 ($C^{B2/A2}$), 150.5 ($C^{C2/C5}$), 150.0 ($C^{C2/C5}$), 149.4 (C^{A6}), 147.3 (C^{B4}), 137.4 (C^{A4}), 127.5 (C^{C1}), 124.4 (C^{A5}), 121.0 ($C^{A3/B3}$), 120.9

($C^{A3/B3}$), 117.2 (C^{C3}), 114.2 (C^{C6}), 111.7 (C^{C4}), 56.9 ($C^{OMe1/OMe2}$), 56.7 ($C^{OMe1/OMe2}$). UV-Vis (CH_3CN, 2.0×10^{-5} mol dm^{-3}) λ / nm (ε / dm^3 mol^{-1} cm^{-1}): 240 (37,500), 277 (28,100), 311 *sh* (16,500). ESI-MS *m*/*z* 448.02 $[M+H]^+$ (calc. 448.06). Found C 61.04, H 3.99, N 9.42; required for $C_{23}H_{18}BrN_3O_2$ C 61.62, H 4.05, N 9.37.

6.3.1.2 4′-(4-Bromo-2,5-dimethoxyphenyl)-3,2′:6′,3″-terpyridine, **23**

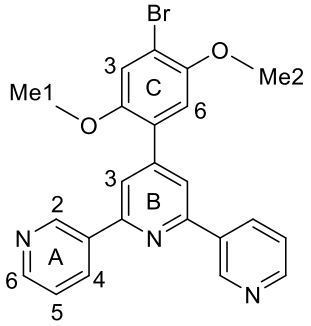

4-Bromo-2,5-dimethoxybenzaldehyde (2.50 g, 10.2 mmol) was dissolved in EtOH (40 mL), then 3-acetylpyridine (2.47 g, 2.25 ml, 20.4 mmol) and crushed KOH (1.15 g, 20.4 mmol) were added to the solution. Aqueous NH_3 (32%, 39.3 mL) was slowly added to the reaction mixture and this was stirred at room temperature overnight. The solid that formed was collected by filtration, washed with H_2O (3 × 10 mL) and EtOH (3 × 10 mL), recrystallized from EtOH/$CHCl_3$ and dried *in vacuo*. Compound **23** was isolated as a white crystalline material (1.33 g, 2.98 mmol, 29.2%). M.p. = 198 °C. ^{1}H NMR (500 MHz, DMSO-d_6): δ / ppm 9.43 (dd, J = 2.4, 0.9 Hz, 2H, H^{A2}), 8.69 (dd, J = 4.8, 1.6 Hz, 2H, H^{A6}), 8.61 (ddd, J = 8.0, 2.4, 1.6 Hz, 2H, H^{A4}), 8.19 (s, 2H, H^{B3}), 7.58 (ddd, J = 8.0, 4.8, 0.9 Hz, 2H, H^{A5}), 7.46 (s, 1H, H^{C3}), 7.36 (s, 1H, H^{C6}), 3.92 (s, 3H, H^{OMe2}), 3.83 (s, 3H, H^{OMe1}). ^{13}C{^{1}H} NMR (126 MHz, DMSO-d_6): δ / ppm 154.0 (C^{B2}), 150.6 (C^{C2}), 150.1 (C^{C5}), 149.9 (C^{A6}), 148.2 (C^{A2}), 147.6 (C^{B4}), 134.4 (C^{A4}), 134.0 (C^{A3}), 127.0 (C^{C1}), 123.9 (C^{A5}), 120.4 (C^{B3}), 117.1 (C^{C3}), 114.9 (C^{C6}), 111.8 (C^{C4}), 56.9 (C^{OMe2}), 56.7 (C^{OMe1}). UV-Vis (CH_3CN, 2.0×10^{-5} mol dm^{-3}) λ / nm (ε / dm^3 mol^{-1} cm^{-1}): 240 (37,000), 315 (16,000). ESI-MS *m*/*z* 448.03 $[M+H]^+$ (calc. 448.06). Found C 61.18, H 4.03, N 9.42; required for $C_{23}H_{18}BrN_3O_2$ C 61.62, H 4.05, N 9.37.

6.3.1.3 4′-(4-Bromo-2,5-dimethoxyphenyl)-4,2′:6′,4″-terpyridine, **24**

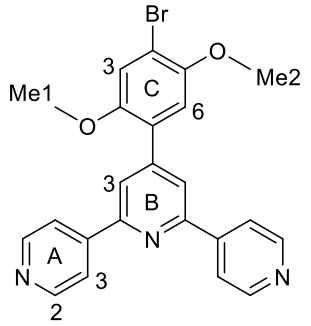

4-Bromo-2,5-dimethoxybenzaldehyde (2.50 g, 10.2 mmol) was dissolved in EtOH (40 mL), then 4-acetylpyridine (2.47 g, 2.27 ml, 20.4 mmol) and crushed KOH (1.15 g, 20.4 mmol) were added to the solution. Aqueous NH_3 (32%, 39.3 mL) was slowly added to the reaction mixture, which was stirred at room temperature overnight. The crystalline solid that formed was collected by filtration, washed with H_2O (3 × 10 mL) and EtOH (3 × 10 mL), and dried *in vacuo*. Compound **24** was isolated as a white crystalline solid (1.74 g, 3.87 mmol, 38.0%). M.p. = 242 °C. ^{1}H NMR (500 MHz, DMSO-d_6): δ / ppm 8.77 (m, 4H, H^{A2}), 8.30 (s, 2H, H^{B3}), 8.24 (m, 4H, H^{A3}), 7.47 (s, 1H, H^{C3}), 7.36 (s, 1H, H^{C6}), 3.91 (s, 3H, H^{OMe2}), 3.82 (s, 3H, H^{OMe1}). ^{13}C{^{1}H} NMR (126 MHz, DMSO-d_6): δ / ppm 153.7 (C^{B2}), 150.6 (C^{C2}), 150.4 (C^{A2}), 150.0 (C^{C5}), 147.9 (C^{B4}), 145.3 (C^{A4}), 126.7 (C^{C1}), 121.8 (C^{B3}), 121.1 (C^{A3}), 117.1 (C^{C3}), 114.9 (C^{C6}), 112.0 (C^{C4}), 56.9 (C^{OMe2}), 56.7 (C^{OMe1}). UV-Vis (CH_3CN, 2.0 × 10^{-5} mol dm^{-3}) λ / nm (ε / dm^3 mol^{-1} cm^{-1}): 242 (34,400), 313 (12,800). ESI-MS *m*/*z* 448.03 $[M+H]^+$ (calc. 448.06). Found C 60.93, H 3.99, N 9.36; required for $C_{23}H_{18}BrN_3O_2$ C 61.62, H 4.05, N 9.37.

6.3.2 Synthesis of a boronic ester

6.3.2.1 4′-(2,5-dimethoxy-4-(4,4,5,5-tetramethyl-1,3,2-dioxaborolan-2-yl)phenyl)-2,2′:6′,2″-terpyridine, **25**

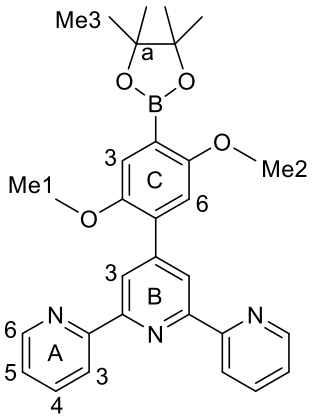

A 100 mL Schlenk tube was charged with compound **22** (1.00 g, 2.23 mmol), B_2pin_2 (0.680 g, 2.68 mmol), KOAc (0.657 g, 6.69 mmol) and $[Pd(dppf)Cl_2]$ (0.049 g, 0.067 mmol). The reaction vessel was flushed with nitrogen, then degassed DMSO (25 mL) was added and the mixture was stirred and heated at 110 °C for 24h. After allowing it to cool down to room temperature, the mixture was diluted with toluene (100 mL) and washed with brine (4 x 50 mL). The toluene layer was dried over Na_2SO_4, then filtered. The solvent was removed by rotary evaporation yielding a brown residue, which was redissolved in CH_2Cl_2 and filtered through a celite pad. The brown portion was retained by the celite, while the colorless solution was dried, giving **25** (0.555 g, 1.12 mmol, 50.2%) as a crystalline, white solid. M.p. = 211 °C. ^{1}H NMR (500 MHz, DMSO-d_6): δ / ppm 8.75 (ddd, J = 4.8, 1.8, 0.9 Hz, 2H, H^{A6}), 8.67 (dt, J = 8.0, 1.1 Hz, 2H, H^{A3}), 8.55 (s, 2H, H^{B3}), 8.04 (td, 2H, J = 7.6, 1.8 Hz, H^{A4}), 7.52 (ddd, 2H, J = 7.6, 4.8, 1.1 Hz, H^{A5}), 7.29 (s, 1H, H^{C3}), 7.08 (s, 1H, H^{C6}), 3.78 (s, 3H, H^{OMe2}), 3.77 (s, 3H, H^{OMe1}), 1.32 (s, 12H, H^{OMe3}). ^{13}C{^{1}H}

NMR (126 MHz, DMSO-d_6): δ / ppm 158.3 (C^{C5}), 155.1 (C^{B2}), 154.8 (C^{A2}), 149.7 (C^{C2}), 149.4 (C^{A6+B4}), 147.9 (C^{C4}), 137.5 (C^{A4}), 131.1 (C^{C1}), 124.4 (C^{A5}), 121.0 ($C^{B3/A3}$), 120.9 ($C^{B3/A3}$), 119.3 (C^{C3}), 113.2 (C^{C6}), 83.4 (C^{a}), 56.3 ($C^{OMe1+OMe2}$), 24.7 (C^{OMe3}). UV-Vis (CH_3CN, 2.0 × 10^{-5} mol dm^{-3}) λ / nm (ε / dm^3 mol^{-1} cm^{-1}): 246 (39,200), 276 (30,300), 315 *sh* (13,500). ESI-MS *m/z* 518.21 $[M+Na]^+$ (calc. 518.22), 1013.40 $[2M+Na]^+$ (calc. 1013.46). Found C 69.66, H 6.07, N 8.55; required for $C_{29}H_{30}BN_3O_4$ C 70.31, H 6.10, N 8.48.

6.3.3 Synthesis of asymmetric bisterpyridines

6.3.3.1 4′-(4′-([3,2′:6′,3″-Terpyridin]-4′-yl)-2,2′,5,5′-tetramethoxy-[1,1′-biphenyl]-4-yl)-2,2′:6′,2″-terpyridine, **26**

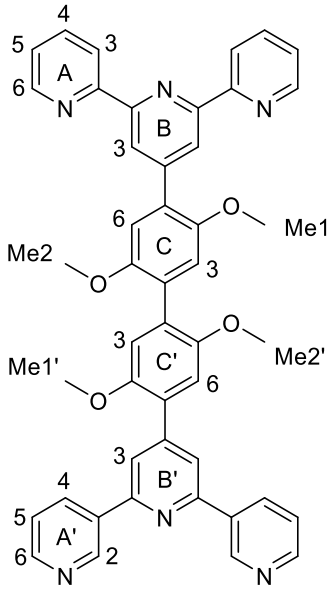

A 100 mL Schlenk tube was charged with **25** (500 mg, 1.01 mmol), **23** (498 mg, 1.11 mmol), Na_2CO_3 (321 mg, 3.03 mmol) and [Pd(dppf)Cl_2] (37.0 mg, 0.05 mmol). The reaction vessel was flushed with nitrogen, then degassed DMSO (20 mL) was added and the mixture stirred at 110 °C under nitrogen overnight (ca. 14h). The reaction mixture was then cooled to room temperature, leading to some precipitation. The solid was removed by filtration and washed with toluene. The filtrate was diluted with additional toluene (70 mL), and washed with brine (5 x 100 mL), then the organic layer was dried over Na_2SO_4, filtered, and the solvent partially removed by rotary evaporation. While removing the solvent, part of the desired product precipitated as an off-white solid. This was collected by filtration and washed with acetone, yielding a first batch of the product. The filtrate was then further concentrated and purified by column chromatography on basic Al_2O_3 with Brockmann activity II (ethyl acetate : cyclohexane 1:2). Compound **26** was isolated as a white solid (428 mg, 0.58 mmol, 57.4%). M.p. = 294 °C. ^{1}H NMR (500 MHz, $CDCl_3$): δ / ppm 9.39 (dd, *J* = 2.3, 0.9 Hz, 2H, $H^{A'2}$), 8.74 (ddd, *J* = 4.8, 1.8, 0.9 Hz, 2H, H^{A6}), 8.73-8.71 (m, 4H, $H^{A'6+B3}$), 8.70 (dt, *J* = 8.0, 1.1 Hz, 2H, H^{A3}), 8.57 (ddd, *J* = 8.0, 2.3, 1.7 Hz, 2H, $H^{A'4}$), 8.04 (s, 2H, $H^{B'3}$), 7.91 (td, 2H, *J* = 7.7, 1.8 Hz, H^{A4}), 7.52 (ddd, 2H, *J* = 8.0, 4.8,

0.8 Hz, $H^{A'5}$), 7.37 (ddd, 2H, J = 7.6, 4.8, 1.2 Hz, H^{A5}), 7.21 (s, 1H, H^{C6}), 7.11 (s, 1H, $H^{C'6}$), 7.10 (s, 1H, $H^{C'3}$), 7.04 (s, 1H, H^{C3}), 3.89 (m, 6H, $H^{OMe1'+OMe2}$), 3.86 (s, 3H, $H^{OMe2'}$), 3.85 (s, 3H, H^{OMe1}). $^{13}C\{^1H\}$ NMR (126 MHz, $CDCl_3$): δ / ppm 156.5 ($C^{B2/A2}$), 155.4 ($C^{B2/A2}$), 154.7 ($C^{B'2}$), 151.7 ($C^{C'5}$), 151.4 (C^{C2}), 150.8 (C^{C5}), 150.6 ($C^{C'2}$), 149.7 ($C^{A'6}$), 149.2 (C^{A6}), 148.9 ($C^{C'4}$), 148.6 (C^{C4}), 148.2 ($C^{A'2}$), 137.1 (C^{A4}), 135.3 ($C^{A'3}$), 135.2 ($C^{A'4}$), 129.7 (C^{C4}), 128.7 (C^{C1}), 128.1 ($C^{C'4}$), 127.3 ($C^{C'1}$), 124.0 ($C^{A'5}$), 123.9 (C^{A5}), 122.0 (C^{B3}), 121.6 (C^{A3}), 120.6 ($C^{B'3}$), 115.6 ($C^{C'3}$), 115.4 (C^{C3}), 114.4 (C^{C6}), 114.3 ($C^{C'6}$), 57.05 ($C^{OMe1/OMe1'/OMe2/OMe2'}$), 57.0 ($C^{OMe1/OMe1'/OMe2/OMe2'}$), 56.7 ($C^{OMe1/OMe1'/OMe2/OMe2'}$), 56.6 ($C^{OMe1/OMe1'/OMe2/OMe2'}$). UV-Vis ($CH_3CN/CHCl_3$ 9:1, 2.0 × 10^{-5} mol dm^{-3}) λ / nm (ε / dm^3 mol^{-1} cm^{-1}): 275 (28,900), 318 (15,600). ESI-MS m/z 737.23 $[M+H]^+$ (calc. 737.29). HR–MS m/z 737.2869 $[M+H]^+$ (calc. 737.2871), 759.2687 $[M+Na]^+$ (calc. 759.2690).

6.3.3.2 4′-(4′-([4,2′:6′,4″-Terpyridin]-4′-yl)-2,2′,5,5′-tetramethoxy-[1,1′-biphenyl]-4-yl)-2,2′:6′,2″-terpyridine, **27**

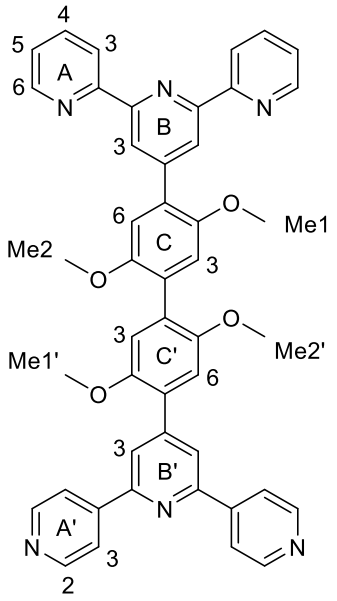

A 100 mL Schlenk tube was charged with **25** (750 mg, 1.67 mmol), **24** (753 mg, 1.52 mmol), Na_2CO_3 (483 mg, 4.56 mmol) and $[Pd(dppf)Cl_2]$ (55.6 mg, 0.076 mmol). The reaction vessel was flushed with nitrogen, then degassed DMSO (20 mL) was added and the mixture stirred at 110 °C under nitrogen overnight (ca. 14h). The reaction mixture was then cooled to room temperature, leading to some precipitation. The solid was removed by filtration and washed with toluene. The filtrate was diluted with additional toluene (70 mL), and washed with brine (5 x 100 mL), then the organic layer was dried over Na_2SO_4, filtered, and the solvent partially removed by rotary evaporation. A first batch of the product (174 mg) was obtained by washing the brown residue with acetone and recrystallizing it from acetone/chloroform. The rest of the compound was purified by column chromatography on basic Al_2O_3 with Brockmann activity II (ethyl acetate : cyclohexane 2:1). Compound **27** was isolated as a white solid (407 mg, 0.55 mmol, 36.2%). M.p. = 227 °C. ^1H NMR (500 MHz, $CDCl_3$): δ / ppm 8.80 (d, J = 6.12 Hz, 4H, $H^{A'2}$),

8.73 (ddd, J = 4.7, 1.9, 0.9 Hz, 2H, H^{A6}), 8.71-8.67 (m, 4H, H^{A3+B3}), 8.12-8.09 (m, 6H, $H^{A'3+B'3}$), 7.89 (td, 2H, J = 7.7, 1.8 Hz, H^{A4}), 7.36 (ddd, 2H, J = 7.5, 4.7, 1.2 Hz, H^{A5}), 7.20 (s, 1H, H^{C6}), 7.11 (s, 1H, $H^{C'3}$), 7.10 (s, 1H, $H^{C'6}$), 7.03 (s, 1H, H^{C3}), 3.89 (s, 3H, $H^{OMe1'}$), 3.88 (s, 3H, H^{OMe2}), 3.86 (s, 3H, $H^{OMe2'}$), 3.85 (s, 3H, H^{OMe1}). $^{13}C\{^1H\}$ NMR (126 MHz, $CDCl_3$): δ / ppm 156.6 (C^{B2}), 155.5 (C^{A2}), 154.7 ($C^{B'2}$), 151.7 ($C^{C'5}$), 151.3 (C^{C2}), 150.8 (C^{C5}), 150.6 ($C^{C'2}$), 150.4 ($C^{A'2}$), 149.3 (C^{A6}), 149.1 ($C^{B'4}$), 148.5 (C^{B4}), 146.7 ($C^{A'4}$), 137.0 (C^{A4}), 129.8 ($C^{C'4}$), 128.8 (C^{C1}), 128.0 (C^{C4}), 127.1 ($C^{C'1}$), 123.9 (C^{A5}), 121.9 (C^{B3}), 121.8 ($C^{A'3/B'3/A3}$), 121.6 ($C^{A'3/B'3/A3}$), 121.5 ($C^{A'3/B'3/A3}$), 115.6 ($C^{C'3}$), 115.3 (C^{C3}), 114.4 (C^{C6}), 114.3 ($C^{C'6}$), 57.1 ($C^{OMe1/OMe2/OMe1'/OMe2'}$), 57.0 ($C^{OMe1/OMe2/OMe1'/OMe2'}$), 56.7 ($C^{OMe1/OMe2/OMe1'/OMe2'}$), 56.6 ($C^{OMe1/OMe2/OMe1'/OMe2'}$). UV-Vis ($CH_3CN$, 2.0 × 10^{-5} mol dm^{-3}) λ / nm (ε / dm^3 mol^{-1} cm^{-1}): 238 (44,500), 254 *sh* (40,500), 275 *sh* (32,900), 343 *sh* (14,000). ESI-MS m/z 737.31 $[M+H]^+$ (calc. 737.29). HR-MS m/z 369.1476 $[M+2H]^{2+}$ (calc. 369.1472), 737.2869 $[M+H]^+$ (calc. 737.2871).

6.3.4 Synthesis of iron(II) complexes of asymmetric bisterpyridines

6.3.4.1 $[Fe(\mathbf{26})_2][NO_3]_2$

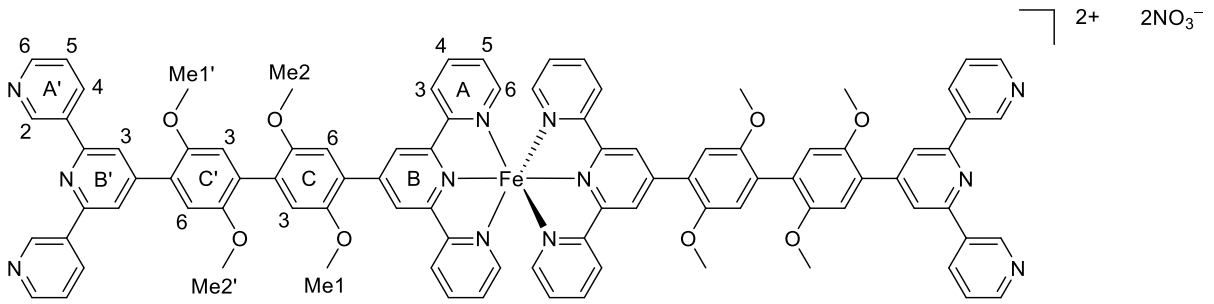

A methanol solution of $FeCl_2{\cdot}4H_2O$ (3.37 mg, 0.017 mmol) was added dropwise to a warm stirred solution (70 °C) of **26** (25 mg, 0.034 mmol) in 40 mL MeOH/$CHCl_3$ (1:3). The mixture immediately turned purple. After 30 minutes, $CHCl_3$ was removed under vacuum and the purple methanol solution was treated with an excess of aqueous $NaNO_3$ and the mixture stirred for additional 10 minutes; immediate precipitation of the purple solid was observed. The mixture was cooled to 2–5 °C in a refrigerator. When the solution became colorless and all the fine solid had precipitated, it was collected on celite, washed with H_2O and dissolved in MeCN. The solvent was removed by rotary evaporation, affording $[Fe(\mathbf{26})_2][NO_3]_2$ as a purple solid (23.2 mg, 0.014 mmol, 82.4%). ^1H NMR (500 MHz, CD_3CN): δ / ppm 9.46 (dd, J = 2.3, 0.9 Hz, 4H, $H^{A'2}$), 9.27 (s, 4H, H^{B3}), 8.70 (dd, J = 4.7, 1.6 Hz, 4H, $H^{A'6}$), 8.64 (dt, J = 7.9, 1.9 Hz, 4H, $H^{A'4}$), 8.61 (m, 4H, H^{A3}), 8.24 (s, 4H, $H^{B'3}$), 7.93 (td, J = 7.7, 1.5 Hz, 4H, H^{A4}), 7.72 (s, 2H, H^{C6}), 7.55 (ddd, J = 8.1, 4.8, 0.9 Hz, 4H, $H^{A'5}$), 7.38 (s, 2H, $H^{C'6}$), 7.35 (s, 2H, H^{C3}), 7.24 (s, 2H, $H^{C'3}$), 7.23 (dd, J = 6.2, 1.2 Hz, 4H, H^{A6}), 7.14 (ddd, J = 7.1, 5.6, 1.3 Hz, 4H, H^{A5}), 4.10 (s, 6H, H^{OMe1}), 4.03 (s, 6H, H^{OMe2}), 3.95 (s, 6H, $H^{OMe1'}$), 3.93 (s, 6H, $H^{OMe2'}$). $^{13}C\{^1H\}$ NMR (126 MHz, CD_3CN): δ / ppm 160.7 (C^{B2}), 159.2 (C^{A2}), 155.6 ($C^{B'2}$), 154.0 (C^{A6}), 152.8 (C^{C5}), 152.5 ($C^{C'5}$), 151.9 (C^{C2}), 151.5 ($C^{C'2}$), 151.1 ($C^{A'6}$), 149.4 ($C^{A'2}$), 149.1 (C^{B4}), 139.7 (C^{A4}), 135.6 ($C^{A'3}$), 135.4 ($C^{A'4}$), 131.7 (C^{C4}), 129.7 ($C^{C'4}$), 128.4 ($C^{C'1}$), 128.2 (C^{A5}), 126.3 (C^{C1}), 125.1 (C^{B3}), 124.7 ($C^{A'5}$), 124.6 (C^{A3}), 121.5 ($C^{B'3}$), 116.8 (C^{C3}), 116.5 ($C^{C'3}$), 115.3 (C^{C6}), 115.1 ($C^{C'6}$), 57.4 ($C^{OMe2+OMe1}$), 57.2 ($C^{OMe2'+OMe1'}$).

UV-Vis (CH_3CN, 1.0×10^{-5} mol dm^{-3}) λ / nm (ε / dm^3 mol^{-1} cm^{-1}): 284 (83,600), 321 (58,300), 568 (23,700). ESI-MS *m*/*z* 764.67 $[M]^{2+}$ (calc. 764.25). HR-MS *m*/*z* 764.2479 $[M]^{2+}$ (calc. 764.2469).

6.3.4.2 $[Fe(\mathbf{27})_2][BF_4]_2$

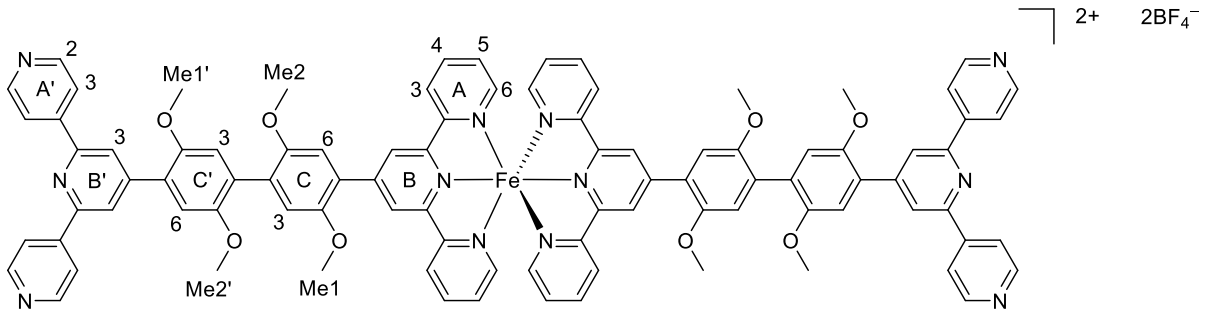

A methanol solution of $Fe(BF_4)_2{\cdot}6H_2O$ (23.0 mg, 0.068 mmol) was added dropwise to a hot stirred solution (70 °C) of **27** (100.0 mg, 0.136 mmol) in MeOH/$CHCl_3$ (ca. 1:3). The mixture immediately turned purple. After 1h, an excess of aqueous $NaBF_4$ was added and the mixture was stirred for additional 10 minutes; immediate precipitation of a purple solid was observed. The mixture was cooled to 2–5 °C. When the solution became colorless and all the fine solid had precipitated, it was collected on celite, washed with H_2O and dissolved in MeCN. The solvent was removed by rotary evaporation, affording $[Fe(\mathbf{27})_2][BF_4]_2$ as a purple solid (90.3 mg, 0.053 mmol, 78.0%). ^{1}H NMR (500 MHz, CD_3CN with a small amount of added K_2CO_3): δ / ppm 9.26 (s, 4H, H^{B3}), 8.79 (d, J = 6.0 Hz, 8H, $H^{A'2}$), 8.60 (d, J = 8.0 Hz, 4H, H^{A3}), 8.34 (s, 4H, $H^{B'3}$), 8.24 (dd, 8H, $H^{A'3}$), 7.93 (td, 4H, J = 7.7, 1.5 Hz, H^{A4}), 7.71 (s, 2H, H^{C6}), 7.38 (s, 2H, $H^{C'6}$), 7.35 (s, 2H, H^{C3}), 7.25 (s, 2H, $H^{C'3}$), 7.22 (m, 4H, H^{A6}), 7.15 (ddd, J = 7.1, 5.6, 1.3 Hz, 4H, H^{A5}), 4.11 (s, 6H, H^{OMe1}), 4.03 (s, 6H, H^{OMe2}), 3.95 (s, 6H, $H^{OMe1'}$), 3.93 (s, 6H, $H^{OMe2'}$). ^{13}C{^{1}H} NMR (126 MHz, CD_3CN, with a small amount of added K_2CO_3): δ / ppm 160.7 (C^{B2}), 159.2 (C^{A2}), 155.4 ($C^{B'2}$), 154.0 (C^{A6}), 152.8 (C^{C5}), 152.6 ($C^{C'5}$), 151.9 (C^{C2}), 151.5 ($C^{C'2}$), 151.4 ($C^{A'2}$), 149.7 ($C^{B'4}$), 149.0 (C^{B4}), 146.9 ($C^{A'4}$), 139.7 (C^{A4}), 131.6 (C^{C4}), 129.9 ($C^{C'4}$ + $C^{C'1}$), 128.2 (C^{A5}), 126.3 (C^{C1}), 125.1 (C^{B3}), 124.7 (C^{A3}), 122.8 ($C^{B'3}$), 122.2 ($C^{A'3}$), 116.8 (C^{C3}), 116.5 ($C^{C'3}$), 115.3 (C^{C6}), 115.0 ($C^{C'6}$), 57.4 ($C^{OMe2+OMe1}$), 57.2 ($C^{OMe2'+OMe1'}$). UV-Vis (CH_3CN, 1.0×10^{-5} mol dm^{-3}) λ / nm (ε / dm^3 mol^{-1} cm^{-1}): 284 (97,200), 321 (59,800), 568 (25,700). ESI-MS *m*/*z* 764.67 $[M]^{2+}$ (calc. 764.25). HR-MS *m*/*z* 764.2466 $[M]^{2+}$ (calc. 764.2469).

6.4 Coordination Polymers

6.4.1 General procedure

A solution of the chosen metal salt in methanol or acetonitrile was layered over a chloroform, dichloromethane or toluene solution of the ligand. The test tube was then sealed with a septum and left to stand at room temperature until visible crystals had formed. If no crystals were visible after two weeks, the septum was pierced with a needle to allow slow evaporation and optimum crystal growth. X-ray quality crystals grew within a period of time between 1 day

and 6 months; although crystal growth was not complete within this period, crystals were removed for X-ray diffraction purposes and the yield of the product was not determined. A single crystal was selected for X-ray diffraction and the remaining crystals were filtered, washed with the crystallization solvents and analyzed by PXRD, FT-IR spectroscopy and sometimes TGA-MS. All single-crystal growth experiments were carried out using identical crystallization tubes (i.d. = 13.6 mm, volume = 24 mL). In a few representative cases, when more than one coordination polymer was identified in the same crystallization experiment, a preparative scale reaction was also performed. These reactions were carried out in a round-bottomed flask, by adding the solid metal salt to a solution of the ligand, while stirring. In all cases, the formation of a suspension was immediately observed. The product was either collected by filtration or centrifugation and dried under vacuum up to constant weight. Elemental analysis and/or PXRD were measured in order to confirm the correspondence between the compound and one of the species identified *via* single-crystal XRD.

6.4.2 Coordination polymers with copper(II) acetate

6.4.2.1 $[Cu_2(\mu\text{-}OAc)_4(\mathbf{1})]_n$

A solution of $Cu(OAc)_2{\cdot}H_2O$ (12.0 mg, 0.060 mmol) in MeOH (3 mL) was layered over a $CHCl_3$ solution (3 mL) of **1** (10.2 mg, 0.030 mmol). Blue block-like crystals were obtained after 2 months.

Preparative scale reaction: compound **1** (70.0 mg, 0.206 mmol) was dissolved in MeOH (25 mL), then solid $Cu(OAc)_2{\cdot}H_2O$ (82.3 mg, 0.412 mmol) was added to the colorless solution. A blue solution was obtained and immediately produced a fine light blue suspension. The solid that formed was collected by filtration and then dried *in vacuo* up to constant weight (4 h). The product was isolated as a light blue powder. Yield for $[Cu_2(OAc)_4(\mathbf{1})]_n$ (79.3 mg, 0.11 mmol, 55%). Found C 50.94, H 4.13, N 5.75; required for $C_{30}H_{29}N_3O_9$: C 51.28, H 4.16, N 5.98. PXRD confirmed the product to be $[Cu_2(OAc)_4(\mathbf{1})]_n$.

6.4.2.1 $[Cu_4(\mu\text{-}OAc)_8(\mathbf{4})_2]_n{\cdot}1.25n$MeOH

A solution of $Cu(OAc)_2{\cdot}H_2O$ (12.0 mg, 0.060 mmol) in MeOH (8 mL) was layered over a $CHCl_3$ solution (5 mL) of **4** (11.4 mg, 0.030 mmol). Green block-like crystals grew after 2 months.

6.4.2.2 $[Cu_2(\mu\text{-}OAc)_4(\mathbf{5})]_n$

A solution of $Cu(OAc)_2{\cdot}H_2O$ (12.0 mg, 0.060 mmol) in MeOH (3 mL) was layered over a $CHCl_3$ solution (3 mL) of **5** (11.9 mg, 0.030 mmol). Blue block-like crystals grew after 20 days.

6.4.2.3 $[Cu_2(\mu\text{-}OAc)_4(\mathbf{7})]_n \cdot 0.2n CHCl_3$

A solution of $Cu(OAc)_2 \cdot H_2O$ (12.0 mg, 0.060 mmol) in MeOH (6 mL) was layered over a $CHCl_3$ solution (4 mL) of **7** (12.7 mg, 0.030 mmol). Blue plate-like crystals grew after 6 months.

6.4.2.4 $[Cu_2(\mu\text{-}OAc)_4(\mathbf{16})]_n$

A solution of $Cu(OAc)_2 \cdot H_2O$ (12.0 mg, 0.060 mmol) in MeOH (5 mL) was layered over a $CHCl_3$ solution (4 mL) of **16** (11.6 mg, 0.030 mmol). Blue block-like crystals grew after 11 days.

6.4.2.5 $[Cu_2(\mu\text{-}OAc)_4(\mathbf{17})]_n$

A solution of $Cu(OAc)_2 \cdot H_2O$ (12.0 mg, 0.060 mmol) in MeOH (5 mL) was layered over a $CHCl_3$ solution (4 mL) of **17** (12.1 mg, 0.030 mmol). Blue block-like crystals grew within 20 days.

6.4.2.6 $[Cu_2(\mu\text{-}OAc)_4(\mathbf{18})]_n$

A solution of $Cu(OAc)_2 \cdot H_2O$ (12.0 mg, 0.060 mmol) in MeOH (4 mL) was layered over a $CHCl_3$ solution (4 mL) of **18** (12.6 mg, 0.030 mmol). Green plate-like crystals grew after 8 days.

6.4.2.7 $[Cu_2(\mu\text{-}OAc)_4(\mathbf{19})]_n$

A solution of $Cu(OAc)_2 \cdot H_2O$ (12.0 mg, 0.060 mmol) in MeOH (4 mL) was layered over a $CHCl_3$ solution (4 mL) of **19** (13.9 mg, 0.030 mmol). Green plate-like crystals grew within 20 days.

6.4.2.8 $[Cu_2(\mu\text{-}OAc)_4(\mathbf{20})]_n \cdot n MeOH$

A solution of $Cu(OAc)_2 \cdot H_2O$ (12.0 mg, 0.060 mmol) in MeOH (4 mL) was layered over a $CHCl_3$ solution (4 mL) of **20** (11.9 mg, 0.030 mmol). Green plate-like crystals grew within 25 days.

6.4.3 Coordination polymers with cobalt(II) thiocyanate

6.4.3.1 $[Co(\mathbf{1})(NCS)_2(MeOH)_2]_n$

Experiment I: a solution of $Co(NCS)_2$ (5.3 mg, 0.030 mmol) in MeOH (6 mL) was layered over a $CHCl_3$ solution (4 mL) of **1** (10.2 mg, 0.030 mmol). Pink block-like crystals were obtained after 17 days.

Experiment II: a solution of $Co(NCS)_2$ (5.3 mg, 0.030 mmol) in MeOH (6 mL) was layered over a $CHCl_3$ solution (4 mL) of **1** (10.2 mg, 0.030 mmol). Pink block-like crystals were obtained after 1 week.

Experiment III: a solution of $Co(NCS)_2$ (10.5 mg, 0.060 mmol) in MeOH (6 mL) was layered over a $CHCl_3$ solution (4 mL) of **1** (10.2 mg, 0.030 mmol). Pink block-like crystals were obtained after 17 days.

Experiment IV: a solution of $Co(NCS)_2$ (2.6 mg, 0.015 mmol) in MeOH (5 mL) was layered over a $CHCl_3$ solution (5 mL) of **1** (10.2 mg, 0.030 mmol). Pink plate-like crystals were obtained after 15 days.

Preparative scale reaction: solid $Co(NCS)_2$ (51.7 mg, 0.295 mmol) was added to a colorless solution of **1** (100 mg, 0.295 mmol) in MeOH (40 mL). Immediate precipitation of a pale pink solid was observed and the mixture was left stirring at room temperature for 15 h. The product was separated by centrifuge followed by decantation of the supernatant liquid. The solid was washed with MeOH (2 × 10 mL) and with $CHCl_3$ (10 mL) to remove unreacted reagents and was then dried under vacuum. The procedure was repeated with 1:2 molar ratio, starting with $Co(NCS)_2$ (25.7 mg, 0.147 mmol) and **1** (100 mg, 0.295 mmol). PXRD confirmed the product to be $[Co(\mathbf{1})(NCS)_2(MeOH)_2]_n$.

6.4.3.2 $[Co(\mathbf{1})_2(NCS)_2]_n \cdot 3n MeOH$

A solution of $Co(NCS)_2$ (5.3 mg, 0.030 mmol) in MeOH (6 mL) was layered over a $CHCl_3$ solution (4 mL) of **1** (10.2 mg, 0.030 mmol). Pink block-like crystals were obtained after 1 week.

6.4.3.3 $[Co(\mathbf{1})_2(NCS)_2]_n \cdot 2.2n CHCl_3$

A solution of $Co(NCS)_2$ (5.3 mg, 0.030 mmol) in MeOH (6 mL) was layered over a $CHCl_3$ solution (4 mL) of **1** (10.2 mg, 0.030 mmol). Pink block-like crystals were obtained after 1 week.

6.4.3.4 $[Co(\mathbf{2})_2(NCS)_2]_n \cdot 0.6n CHCl_3$

Experiment I: a solution of $Co(NCS)_2$ (5.3 mg, 0.030 mmol) in MeOH (6 mL) was layered over a $CHCl_3$ solution (4 mL) of **2** (10.6 mg, 0.030 mmol). Pink block-like crystals were obtained after 4 days.

Experiment II: a solution of $Co(NCS)_2$ (10.6 mg, 0.060 mmol) in MeOH (6 mL) was layered over a $CHCl_3$ solution (4 mL) of **2** (10.6 mg, 0.030 mmol). Pink block-like crystals were obtained after 4 days.

Experiment III: a solution of $Co(NCS)_2$ (2.7 mg, 0.015 mmol) in MeOH (6 mL) was layered over a $CHCl_3$ solution (4 mL) of **2** (10.6 mg, 0.030 mmol). Pink block-like crystals were obtained after 5 days.

6.4.3.5 $[Co(\mathbf{3})_2(NCS)_2]_n \cdot 4n CHCl_3 \cdot 0.25n H_2O$

Experiment I: a solution of $Co(NCS)_2$ (5.3 mg, 0.030 mmol) in MeOH (5 mL) was layered over a $CHCl_3$ solution (4 mL) of **3** (11.0 mg, 0.030 mmol). Pink block-like crystals grew after 1 day.

Experiment II: a solution of $Co(NCS)_2$ (10.6 mg, 0.060 mmol) in MeOH (5 mL) was layered over a $CHCl_3$ solution (4 mL) of **3** (11.0 mg, 0.030 mmol). Pink block-like crystals grew after 1 day.

6.4.3.6 $[Co(\mathbf{4})_2(NCS)_2]_n \cdot 4n CHCl_3$

Experiment I: a solution of $Co(NCS)_2$ (5.3 mg, 0.030 mmol) in MeOH (6 mL) was layered over a $CHCl_3$ solution (4 mL) of **4** (11.4 mg, 0.030 mmol). Pink plate-like crystals grew after 5 days.

Experiment II: a solution of $Co(NCS)_2$ (10.6 mg, 0.060 mmol) in MeOH (5 mL) was layered over a $CHCl_3$ solution (4 mL) of **4** (11.4 mg, 0.030 mmol). Pink plate -like crystals grew after 4 days.

6.4.3.7 $[Co_2(\mathbf{5})_4(NCS)_4]_n$

A solution of $Co(NCS)_2$ (10.6 mg, 0.060 mmol) in MeOH (6 mL) was layered over a $CHCl_3$ solution (4 mL) of **5** (11.9 mg, 0.030 mmol). Pink plate-like crystals grew after 3 months.

6.4.3.8 $[Co(\mathbf{6})_2(NCS)_2]_n$

A solution of $Co(NCS)_2$ (5.3 mg, 0.030 mmol) in MeOH (6 mL) was layered over a CH_2Cl_2 solution (4 mL) of **6** (12.3 mg, 0.030 mmol). Pink plate-like crystals were obtained after 6 days.

6.4.3.9 $[Co(rac\text{-}\mathbf{11})_2(NCS)_2]_n \cdot n CHCl_3$

A solution of $Co(NCS)_2$ (5.3 mg, 0.030 mmol) in MeOH (5 mL) was layered over a $CHCl_3$ solution (4 mL) of *rac*-**11** (11.4 mg, 0.030 mmol). Pink block-like crystals were obtained after 6 days.

6.4.3.10 $[Co(\mathbf{12})_2(NCS)_2]_n$

A solution of $Co(NCS)_2$ (5.3 mg, 0.030 mmol) in MeOH (6 mL) was layered over a $CHCl_3$ solution (6 mL) of **12** (11.4 mg, 0.030 mmol). Pink plate-like crystals grew within a period of 15 days.

6.4.3.11 $[Co(\mathbf{13})_2(NCS)_2]_n \cdot n CHCl_3$

A solution of $Co(NCS)_2$ (5.3 mg, 0.030 mmol) in MeOH (8 mL) was layered over a $CHCl_3$ solution (8 mL) of **13** (11.4 mg, 0.030 mmol). Pink plate-like crystals grew over a period of 40 days.

6.4.3.12 $[Co(\mathbf{15})_2(NCS)_2]_n$

A solution of $Co(NCS)_2$ (5.3 mg, 0.030 mmol) in MeOH (5 mL) was layered over a $CHCl_3$ solution (6 mL) of **15** (11.9 mg, 0.030 mmol). Pink block-like crystals grew within 1 week.

6.4.3.13 $[Co(\mathbf{20})_2(NCS)_2]_n \cdot 4.5 n CHCl_3$

A solution of $Co(NCS)_2$ (5.3 mg, 0.030 mmol) in MeOH (5 mL) was layered over a $CHCl_3$ solution (4 mL) of **20** (11.9 mg, 0.030 mmol). Pink block-like crystals grew within 2 weeks.

6.4.3.14 $[Co(\mathbf{20})_2(NCS)_2]_n$

A solution of $Co(NCS)_2$ (2.7 mg, 0.015 mmol) in MeOH (6 mL) was layered over a toluene solution (6 mL) of **20** (6.0 mg, 0.015 mmol). Pink crystals grew within 10 days.

6.4.3.15 $[Co(\mathbf{16})_2(NCS)_2]_n \cdot 4.3 n CHCl_3$

A solution of $Co(NCS)_2$ (5.3 mg, 0.030 mmol) in MeOH (5 mL) was layered over a $CHCl_3$ solution (5 mL) of **16** (11.6 mg, 0.030 mmol). Pink plate-like crystals grew within 2 weeks.

6.4.3.16 $[Co(\mathbf{16})_2(NCS)_2]_n \cdot 3 n C_6H_5CH_3$

A solution of $Co(NCS)_2$ (5.3 mg, 0.030 mmol) in MeOH (5 mL) was layered over a toluene solution (6 mL) of **16** (11.6 mg, 0.030 mmol). Pink plate-like crystals grew within 2 weeks.

6.4.3.17 $[Co(\mathbf{17})_2(NCS)_2]_n \cdot 4 n CHCl_3$

A solution of $Co(NCS)_2$ (5.3 mg, 0.030 mmol) in MeOH (5 mL) was layered over a $CHCl_3$ solution (4 mL) of **17** (12.1 mg, 0.030 mmol). Pink plate-like crystals grew after 1 day.

6.4.3.18 $[Co(\mathbf{17})_2(NCS)_2]_n \cdot 4n C_6H_5CH_3$

A solution of $Co(NCS)_2$ (2.7 mg, 0.015 mmol) in MeOH (4 mL) was layered over a toluene solution (6 mL) of **17** (6.0 mg, 0.015 mmol). Pale pink plate-like crystals grew within 2 weeks.

6.4.3.19 $[Co(\mathbf{18})_2(NCS)_2]_n$

A solution of $Co(NCS)_2$ (5.3 mg, 0.030 mmol) in MeOH (6 mL) was layered over a $CHCl_3$ solution (6 mL) of **18** (12.6 mg, 0.030 mmol). Pink block-like crystals grew after 5 days.

6.4.3.20 $[Co(\mathbf{19})_2(NCS)_2]_n \cdot n CHCl_3$

A solution of $Co(NCS)_2$ (5.3 mg, 0.030 mmol) in MeOH (5 mL) was layered over a $CHCl_3$ solution (4 mL) of **19** (13.9 mg, 0.030 mmol). Pale pink plate-like crystals grew within 2 weeks.

6.4.3.21 $[Co(\mathbf{19})_2(NCS)_2]_n \cdot 4.6n C_6H_5CH_3$

A solution of $Co(NCS)_2$ (5.3 mg, 0.030 mmol) in MeOH (6 mL) was layered over a toluene solution (6 mL) of **19** (13.9 mg, 0.030 mmol). Pale pink plate-like crystals grew within 2 weeks.

6.4.3.22 $[Co(\mathbf{21})_2(NCS)_2]_n \cdot 2n CHCl_3$

A solution of $Co(NCS)_2$ (5.3 mg, 0.030 mmol) in MeCN (6 mL) was layered over a $CHCl_3$ solution (5 mL) of **21** (13.1 mg, 0.030 mmol). Pink block-like crystals grew after 10 days.

6.4.3.23 $[Co(\mathbf{21})_2(NCS)_2]_n \cdot 2n C_6H_5Me$

A solution of $Co(NCS)_2$ (5.3 mg, 0.030 mmol) in MeOH (6 mL) was layered over a toluene solution (6 mL) of **21** (13.1 mg, 0.030 mmol). Pink plate-like crystals grew after 7 days.

6.5 Crystallographic data

6.5.1 Ligands and precursors

6.5.1.1 4′-(4-*n*-Hexyloxyphenyl)-3,2′:6′,3″-terpyridine, **6**

$C_{27}H_{27}N_3O$, M_r = 409.51, colorless block, monoclinic, space group $P2_1/n$, a = 18.8773(3), b = 11.3154(2), c = 21.6453(3) Å, β = 105.985(1)°, V = 4444.75(12) Å^3, D_c = 1.224 g cm^{-3}, T = 300 K, Z = 8, μ(Ga$K\alpha$) = 0.378 mm^{-1}. Total 34613 reflections, 8962 unique (R_{int} = 0.0210). Refinement of 7622 reflections (562 parameters) with $I > 2\sigma(I)$ converged at final R_1 = 0.0537 (R_1 all data = 0.0606), wR_2 = 0.1586 (wR_2 all data = 0.1702), gof = 1.055. CCDC 2009745.

6.5.1.2 4′-(4-*n*-Heptyloxyphenyl)-3,2′:6′,3″-terpyridine, **7**

$C_{28}H_{29}N_3O$, M_r = 423.54, colorless block, monoclinic, space group $P2_1/c$, a = 23.1434(10), b = 10.8165(5), c = 18.7860(9) Å, β = 108.115(3)°, V = 4469.6(4) Å^3, D_c = 1.259 g cm^{-3}, T = 130 K, Z = 8, μ(Cu$K\alpha$) = 0.601 mm^{-1}. Total 30119 reflections, 8165 unique (R_{int} = 0.0366). Refinement of 6195 reflections (579 parameters) with $I > 2\sigma(I)$ converged at final R_1 = 0.0429 (R_1 all data = 0.0615), wR_2 = 0.1090 (wR_2 all data = 0.1205), gof = 1.025. CCDC 2009746.

6.5.1.3 4′-(4-*n*-Octyloxyphenyl)-3,2′:6′,3″-terpyridine, **8**

$C_{29}H_{31}N_3O$, M_r = 437.57, colorless block, monoclinic, space group $P2_1/c$, a = 13.8447(15), b = 14.1626(16), c = 24.757(3) Å, β = 102.213(4)°, V = 4744.4(9) Å^3, D_c = 1.225 g cm^{-3}, T = 130 K, Z = 8, μ(Cu$K\alpha$) = 0.582 mm^{-1}. Total 31983 reflections, 8603 unique (R_{int} = 0.0286). Refinement of 7947 reflections (597 parameters) with $I > 2\sigma(I)$ converged at final R_1 = 0.0378 (R_1 all data = 0.0407), wR_2 = 0.1038 (wR_2 all data = 0.1067), gof = 1.035. CCDC 2009748.

6.5.1.4 4′-(4-*n*-Nonyloxyphenyl)-3,2′:6′,3″-terpyridine, **9**

$C_{30}H_{33}N_3O$, M_r = 451.59, colorless block, triclinic, space group $P\bar{1}$, a = 11.6102(4), b = 13.9680(5), c = 16.4766(6) Å, α = 95.198(3), β = 99.538(3), γ = 108.195(3)°, V = 2474.27(16) Å^3, D_c = 1.212 g cm^{-3}, T = 130 K, Z = 4, μ(Ga$K\alpha$) = 0.368 mm^{-1}. Total 39623 reflections, 9703 unique (R_{int} = 0.0728). Refinement of 7683 reflections (615 parameters) with $I > 2\sigma(I)$ converged at final R_1 = 0.0739 (R_1 all data = 0.0962), wR_2 = 0.2154 (wR_2 all data = 0.2374), gof = 1.133. CCDC 2009747.

6.5.1.5 4′-(4-Bromo-2,5-dimethoxyphenyl)-3,2′:6′,3″-terpyridine, **23**

$C_{23}H_{18}BrN_3O_2$, M_r = 448.31, colorless block, triclinic, space group $P\bar{1}$, a = 8.4228(7), b = 11.1275(9), c = 11.1387(9) Å, α = 69.054(3), β = 86.557(3), γ = 81.212(4)°, V = 963.52(14) Å^3, D_c = 1.545 g cm^{-3}, T = 150 K, Z = 2, μ(Cu$K\alpha$) = 3.115 mm^{-1}. Total 10442 reflections, 3414 unique (R_{int} = 0.0205). Refinement of 3377 reflections (264 parameters) with $I > 2\sigma(I)$ converged at final R_1 = 0.0252 (R_1 all data = 0.0254), wR_2 = 0.0677 (wR_2 all data = 0.0679), gof = 1.051. CCDC 2203620.

6.5.1.6 4′-(4-Bromo-2,5-dimethoxyphenyl)-4,2′:6′,4″-terpyridine, **24**

$C_{23}H_{18}BrN_3O_2$, M_r = 448.31, colorless plate, monoclinic, space group $P2_1/n$, a = 8.3527(5), b = 23.5829(14), c = 10.5854(7) Å, β = 112.567(3)°, V = 1925.5(2) Å^3, D_c = 1.547 g cm^{-3}, T = 150 K, Z = 4, μ(Cu$K\alpha$) = 3.117 mm^{-1}. Total 12341 reflections, 3462 unique (R_{int} = 0.0231). Refinement of 3210 reflections (264 parameters) with $I > 2\sigma(I)$ converged at final R_1 = 0.0321 (R_1 all data = 0.0347), wR_2 = 0.0817 (wR_2 all data = 0.0840), gof = 1.053. CCDC 2203619.

6.5.1.7 4′-(2,5-Dimethoxy-4-(4,4,5,5-tetramethyl-1,3,2-dioxaborolan-2-yl)phenyl)-2,2′:6′,2″-terpyridine, **25**

$C_{29}H_{30}BN_3O4$, M_r = 495.37, colorless block, orthorhombic, space group *Pbca*, a = 15.2294(7), b = 17.9085(7), c = 19.3318(8) Å, V = 5272.5(4) Å^3, D_c = 1.248 g cm^{-3}, T = 150 K, Z = 8, μ(Cu$K\alpha$) = 0.668 mm^{-1}. Total 65360 reflections, 4886 unique (R_{int} = 0.0460). Refinement of 4044 reflections (340 parameters) with $I > 2\sigma(I)$ converged at final R_1 = 0.0414 (R_1 all data = 0.0527), wR_2 = 0.1006 (wR_2 all data = 0.1074), gof = 1.040. CCDC 2203621.

6.5.2 Coordination polymers with copper(II) acetate

6.5.2.1 $[Cu_2(\mu\text{-}OAc)_4(\mathbf{1})]_n$

$C_{30}H_{29}Cu_2N_3O_9$, M_r = 702.64, blue block, triclinic, space group *P*–1, a = 8.4817(5), b = 13.7510(10), c = 15.3776(10) Å, α = 115.153(5), β = 104.720(5), γ = 92.942(5)°, V = 1543.94(19) Å^3, D_c = 1.511 g cm^{-3}, T = 130 K, Z = 2, μ(Ga$K\alpha$) = 7.754 mm^{-1}. Total 23704 reflections, 6163 unique (R_{int} = 0.1083). Refinement of 3838 reflections (402 parameters) with $I > 2\sigma(I)$ converged at final R_1 = 0.1432 (R_1 all data = 0.2081), wR_2 = 0.3804 (wR_2 all data = 0.4385), gof = 1.601. CCDC 1967918.

6.5.2.2 $[Cu_4(\mu\text{-}OAc)_8(\mathbf{4})_2]_n \cdot 1.25n$MeOH

$C_{67.25}H_{75}Cu_4N_6O_{19.25}$, M_r = 1529.49, green block, triclinic, space group *P*–1, a = 14.2771(16), b = 16.0424(18), c = 17.258(2) Å, α = 109.126(3), β = 92.317(3), γ = 110.953(3)°, V = 3431.5(7) Å^3, D_c = 1.480 g cm^{-3}, T = 130 K, Z = 2, μ(Cu$K\alpha$) = 2.032 mm^{-1}. Total 61235 reflections, 12421 unique (R_{int} = 0.0237). Refinement of 12194 reflections (886 parameters) with $I > 2\sigma(I)$ converged at final R_1 = 0.0347 (R_1 all data = 0.0352), wR_2 = 0.0977 (wR_2 all data = 0.0980), gof = 1.049. CCDC 1967920.

6.5.2.3 $[Cu_2(\mu\text{-}OAc)_4(\mathbf{5})]_n$

$C_{34}H_{37}Cu_2N_3O_9$, M_r = 758.74, blue block, monoclinic, space group $P2_1/n$, a = 11.0414(3), b = 21.6148(5), c = 14.4787(3) Å, β = 106.004(2)°, V = 3321.53(14) Å^3, D_c = 1.517 g cm^{-3}, T = 130 K, Z = 4, μ(Ga$K\alpha$) = 7.237 mm^{-1}. Total 52984 reflections, 6665 unique (R_{int} = 0.0729). Refinement of 6294 reflections (438 parameters) with $I > 2\sigma(I)$ converged at final R_1 = 0.0805 (R_1 all data = 0.0867), wR_2 = 0.1549 (wR_2 all data = 0.1578), gof = 1.163. CCDC 1967919.

6.5.2.4 $[Cu_2(\mu\text{-}OAc)_4(\mathbf{7})]_n \cdot 0.2n$CHCl$_3$

$C_{36.2}H_{41.2}Cl_{0.6}Cu_2N_3O_9$, M_r = 810.67, blue plate, triclinic, space group *P*–1, a = 8.3686(6), b = 14.7025(11), c = 16.4640(13) Å, α = 73.217(4), β = 78.314(4), γ = 73.555(4)°, V = 1843.9(2)^o, Å^3, D_c = 1.460 g cm^{-3}, T = 130 K, Z = 2, μ(Cu$K\alpha$) = 2.302 mm^{-1}. Total 21215 reflections, 6656 unique (R_{int} =

0.0353). Refinement of 5906 reflections (492 parameters) with $I > 2\sigma(I)$ converged at final R_1 = 0.0514 (R_1 all data = 0.0566), wR_2 = 0.1495 (wR_2 all data = 0.1553), gof = 1.048. CCDC 1967917.

6.5.2.5 $[Cu_2(\mu\text{-}OAc)_4(\mathbf{16})]_n$

$C_{35}H_{31}Cu_2N_3O_8$, M_r = 748.71, blue block, monoclinic, space group *C*2/*c*, *a* = 27.7823(14), *b* = 15.4445(11), *c* = 7.9423(4) Å, β = 102.301(4)°, *V* = 3329.7(3) Å^3, D_c = 1.494 g cm^{-3}, *T* = 150 K, *Z* = 4, μ(Ga*K*α) = 7.203 mm^{-1}. Total 20589 reflections, 3485 unique (R_{int} = 0.0693). Refinement of 2756 reflections (222 parameters) with $I > 2\sigma(I)$ converged at final R_1 = 0.0656 (R_1 all data = 0.0979), wR_2 = 0.1287 (wR_2 all data = 0.1526), gof = 1.212. CCDC 2042171.

6.5.2.6 $[Cu_2(\mu\text{-}OAc)_4(\mathbf{17})]_n$

$C_{35}H_{30}Cu_2FN_3O_8$, M_r = 766.70, blue block, monoclinic, space group *C*2/*c*, *a* = 27.6940(16), *b* = 15.9902(7), *c* = 7.8753(6) Å, β = 102.343(5)°, *V* = 3406.8(4) Å^3, D_c = 1.495 g cm^{-3}, *T* = 150 K, *Z* = 4, μ(Ga*K*α) = 7.077 mm^{-1}. Total 26608 reflections, 3531 unique (R_{int} = 0.0845). Refinement of 2854 reflections (227 parameters) with $I > 2\sigma(I)$ converged at final R_1 = 0.0907 (R_1 all data = 0.1116), wR_2 = 0.2310 (wR_2 all data = 0. 2590), gof = 1.151. CCDC 2042172.

6.5.2.7 $[Cu_2(\mu\text{-}OAc)_4(\mathbf{18})]_n$

$C_{35}H_{30}Cu_2ClN_3O_8$, M_r = 783.15, green plate, triclinic, space group *P*–1, *a* = 8.0001(3), *b* = 9.3586(3), *c* = 23.7240(7) Å, α = 99.3320(10), β = 96.370(2), γ = 98.442(2)°, *V* = 1717.11(10) Å^3, D_c = 1.515 g cm^{-3}, *T* = 150 K, *Z* = 2, μ(Cu*K*α) = 2.714 mm^{-1}. Total 20409 reflections, 6355 unique (R_{int} = 0.0293). Refinement of 5729 reflections (446 parameters) with $I > 2\sigma(I)$ converged at final R_1 = 0.0457 (R_1 all data = 0.0502), wR_2 = 0.1286 (wR_2 all data = 0.1340), gof = 1.054. CCDC 2042175.

6.5.2.8 $[Cu_2(\mu\text{-}OAc)_4(\mathbf{19})]_n$

$C_{70}H_{60}Cu_4Br_2N_6O_{16}$, M_r = 1655.22, green plate, triclinic, space group *P*–1, *a* = 7.9898(5), *b* = 9.3656(5), *c* = 23.6072(13) Å, α = 98.626(2), β = 96.301(2), γ = 97.555(2)°, *V* = 1716.19(17) Å^3, D_c = 1.602 g cm^{-3}, *T* = 150 K, *Z* = 1, μ(Cu*K*α) = 3.363 mm^{-1}. Total 27701 reflections, 6338 unique (R_{int} = 0.0236). Refinement of 6120 reflections (446 parameters) with $I > 2\sigma(I)$ converged at final R_1 = 0.0482 (R_1 all data = 0.0493), wR_2 = 0.1317 (wR_2 all data = 0.1328), gof = 1.072. CCDC 2042174.

6.5.2.9 $[Cu_2(\mu\text{-}OAc)_4(\mathbf{20})]_n{\cdot}n$MeOH

$C_{74}H_{74}Cu_4N_6O_{18}$, M_r = 1589.55, green plate, triclinic, space group *P*–1, *a* = 8.0240(4), *b* = 9.4295(5), *c* = 23.8856(11) Å, α = 100.7670(10), β = 95.673(2), γ = 97.244(2)°, *V* = 1747.30(15) Å^3, D_c = 1.511 g

cm^{-3}, T = 150 K, Z = 1, μ(Cu$K\alpha$) = 2.008 mm^{-1}. Total 21488 reflections, 6397 unique (R_{int} = 0.0280). Refinement of 6197 reflections (477 parameters) with $I > 2\sigma(I)$ converged at final R_1 = 0.0366 (R_1 all data = 0.0374), wR_2 = 0.1030 (wR_2 all data = 0.1038), gof = 1.053. CCDC 2042173.

6.5.3 Coordination polymers with cobalt(II) thiocyanate

6.5.3.1 [Co(**1**)(NCS)$_2$(MeOH)$_2$]$_n$

$C_{26}H_{25}CoN_5O_3S_2$, M_r = 578.56, pink block, orthorhombic, space group *Pbca*, a = 14.0281(3), b = 14.3649(3), c = 26.0077(6) Å, V = 5240.9(2) Å^3, D_c = 1.467 g cm^{-3}, T = 130 K, Z = 8, μ(GaKα) = 4.713 mm^{-1}. Total 98166 reflections, 5359 unique (R_{int} = 0.3579). Refinement of 3094 reflections (343 parameters) with $I > 2\sigma(I)$ converged at final R_1 = 0.0639 (R_1 all data = 0.1341), wR_2 = 0.1376 (wR_2 all data = 0.1728), gof = 1.006. CCDC 1922228.

6.5.3.2 [Co(**1**)$_2$(NCS)$_2$]$_n$·3nMeOH

$C_{49}H_{46}CoN_8O_5S_2$, M_r = 949.99, pink plate, monoclinic, space group $P2_1/n$, a = 13.2570(6), b = 12.1980(5), c = 15.0937(6) Å, β = 98.675(2)°, V = 2412.86(18) Å^3, D_c = 1.308 g cm^{-3}, T = 130 K, Z = 2, μ(CuKα) = 4.069 mm^{-1}. Total 15819 reflections, 4303 unique (R_{int} = 0.0336). Refinement of 3963 reflections (269 parameters) with $I > 2\sigma(I)$ converged at final R_1 = 0.0386 (R_1 all data = 0.0420), wR_2 = 0.1092 (wR_2 all data = 0.1118), gof = 1.062. CCDC 1922226.

6.5.3.3 [Co(**1**)$_2$(NCS)$_2$]$_n$·2.2nCHCl$_3$

$C_{48.2}H_{36.6}Cl_{6.6}CoN_8O_2S_2$, Mr = 1116.87, pink block, monoclinic, space group $P2_1/c$, a = 11.0555(8), b = 13.2414(10), c = 18.5561(13) Å, β = 96.956(3)°, V = 2696.4(3) Å^3, D_c = 1.376 g cm^{-3}, T = 130 K, Z = 2, μ(CuKα) = 6.592 mm^{-1}. Total 23049 reflections, 4886 unique (R_{int} = 0.0313). Refinement of 4652 reflections (341 parameters) with $I > 2\sigma(I)$ converged at final R_1 = 0.1177 (R_1 all data = 0.1199), wR_2 = 0.4012 (wR_2 all data = 0.4131), gof = 1.096. CCDC 1922227.

6.5.3.4 [Co(**2**)$_2$(NCS)$_2$]$_n$·0.6nCHCl$_3$

$C_{50.40}H_{40.40}Cl_{7.20}CoN_8O_2S_2$, M_r = 1168.39, pink block, tetragonal, space group $P4/ncc$, a = b = 25.3093(5), c = 18.1347(5) Å, V = 11616.4(6) Å^3, D_c = 1.336 g cm^{-3}, T = 130 K, Z = 8, μ(Ga$K\alpha$) = 4.267 mm^{-1}. Total 81455 reflections, 6020 unique (R_{int} = 0.1459). Refinement of 3155 reflections (330 parameters) with $I > 2\sigma(I)$ converged at final R_1 = 0.0963 (R_1 all data = 0.1675), wR_2 = 0.2722 (wR_2 all data = 0.3398), gof = 1.028. CCDC 1982103.

6.5.3.5 $[Co(\mathbf{3})_2(NCS)_2]_n \cdot 4n CHCl_3 \cdot 0.25n H_2O$

$C_{54}H_{46.50}Cl_{12}CoN_8O_{2.25}S_2$, M_r = 1391.94, pink block, tetragonal, space group $P\text{–}42_1c$, $a = b$ = 25.6618(13), c = 18.709(1) Å, V = 12320.4(14) Å^3, D_c = 1.501 g cm^{-3}, T = 130 K, Z = 8, μ(Cu$K\alpha$) = 7.998 mm^{-1}. Total 68222 reflections, 11345 unique (R_{int} = 0.0469). Refinement of 10789 reflections (720 parameters) with $I > 2\sigma(I)$ converged at final R_1 = 0.0684 (R_1 all data = 0.0712), wR_2 = 0.1962 (wR_2 all data = 0.1998), gof = 1.115. CCDC 1982101.

6.5.3.6 $[Co(\mathbf{4})_2(NCS)_2]_n \cdot 4n CHCl_3$

$C_{56}H_{50}Cl_{12}CoN_8O_2S_2$, M_r = 1417.50, pink plate, tetragonal, space group $P\text{–}42_1c$, $a = b$ = 25.7185(3), c = 19.1253(3) Å, V = 12650.3(4) Å^3, D_c = 1.489 g cm^{-3}, T = 130 K, Z = 8, μ(Ga$K\alpha$) = 5.173 mm^{-1}. Total 87950 reflections, 12678 unique (R_{int} = 0.0925). Refinement of 9999 reflections (733 parameters) with $I > 2\sigma(I)$ converged at final R_1 = 0.0626 (R_1 all data = 0.0789), wR_2 = 0.1655 (wR_2 all data = 0.1710), gof = 1.030. CCDC 1982105.

6.5.3.7 $[Co_2(\mathbf{5})_4(NCS)_4]_n$

$C_{108}H_{100}Co_2N_{16}O_4S_4$, Mr = 1932.13, pink plate, monoclinic, space group $P2_1/n$, a = 13.1357(4), b = 12.4666(3), c = 15.1441(4) Å, β = 100.148(2)°, V = 2441.16(12) Å^3, Dc = 1.314 g cm^{-3}, T = 130 K, Z = 1, μ(GaKα) = 2.675 mm^{-1}. Total 36315 reflections, 4983 unique (R_{int} = 0.0621). Refinement of 4596 reflections (305 parameters) with $I > 2\sigma(I)$ converged at final R_1 = 0.0500 (R_1 all data = 0.0555), wR_2 = 0.1376 (wR_2 all data = 0.1453), gof = 1.113. CCDC 1982104.

6.5.3.8 $[Co(\mathbf{6})_2(NCS)_2]_n$

$C_{56}H_{54}CoN_8O_2S_2$, M_r = 994.12, pink plate, monoclinic, space group $P2_1/c$, a = 18.3988(14), b = 12.9419(10), c = 21.7046(17) Å, β = 98.421(4)°, V = 5112.5(7) Å^3, D_c = 1.292 g cm^{-3}, T = 130 K, Z = 4, μ(Cu$K\alpha$) = 3.787 mm^{-1}. Total 61349 reflections, 9388 unique (R_{int} = 0.0353). Refinement of 8264 reflections (624 parameters) with $I > 2\sigma(I)$ converged at final R_1 = 0.0467 (R_1 all data = 0.0534), wR_2 = 0.1241 (wR_2 all data = 0.1298), gof = 1.047. CCDC 1982102.

6.5.3.9 $[Co(rac\text{-}\mathbf{11})_2(NCS)_2]_n \cdot n CHCl_3$

$C_{53}H_{47}Cl_3CoN_8O_2S_2$, M_r = 1057.38, colorless block, monoclinic, space group $P2_1/n$, a = 13.2404(9), b = 13.2088(9), c = 15.0375(10) Å, β = 99.261(3)°, V = 2595.6(3) Å^3, D_c = 1.353 g cm^{-3}, T = 150 K, Z = 2, μ(Cu$K\alpha$) = 5.151 mm^{-1}. Total 17402 reflections, 4804 unique (R_{int} = 0.0309). Refinement of 4518 reflections (277 parameters) with $I > 2\sigma(I)$ converged at final R_1 = 0.0772 (R_1 all data = 0.0801), wR_2 = 0.2350 (wR_2 all data = 0.2394), gof = 1.097. CCDC 2013944.

6.5.3.10 $[Co(\mathbf{12})_2(NCS)_2]_n$

$C_{52}H_{46}CoN_8O_2S_2$, M_r = 938.02, pink block, monoclinic, space group $P2_1/n$, a = 9.6250(5), b = 16.3159(6), c = 14.7532(7) Å, β = 104.178(4)°, V = 2246.28(18) Å^3, D_c = 1.387 g cm^{-3}, T = 150 K, Z = 2, μ(Ga$K\alpha$) = 2.896 mm^{-1}. Total 30956 reflections, 4723 unique (R_{int} = 0.0465). Refinement of 4086 reflections (297 parameters) with $I > 2\sigma(I)$ converged at final R_1 = 0.0702 (R_1 all data = 0.0869), wR_2 = 0.1608 (wR_2 all data = 0.1763), gof = 1.168. CCDC 2013945.

6.5.3.11 $[Co(\mathbf{13})_2(NCS)_2]_n \cdot n CHCl_3$

$C_{53}H_{47}Cl_3CoN_8O_2S_2$, M_r = 1057.44, pink plate, monoclinic, space group $P2_1/n$, a = 13.0484(7), b = 13.1230(5), c = 15.3008(8) Å, β = 99.454(4)°, V = 2584.4(2) Å^3, D_c = 1.359 g cm^{-3}, T = 150 K, Z = 2, μ(Ga$K\alpha$) = 3.470 mm^{-1}. Total 33416 reflections, 5439 unique (R_{int} = 0.0756). Refinement of 5002 reflections (298 parameters) with $I > 2\sigma(I)$ converged at final R_1 = 0.0733 (R_1 all data = 0.0798), wR_2 = 0.1593 (wR_2 all data = 0.1626), gof = 1.0505. CCDC 2013946.

6.5.3.12 $[Co(\mathbf{15})_2(NCS)_2]_n$

$C_{54}H_{50}CoN_8O_2S_2$, M_r = 966.07, pink block, monoclinic, space group $P2_1/n$, a = 9.7282(4), b = 17.01180(7), c = 14.7303(6) Å, β = 102.807(3)°, V = 2377.13(17) Å^3, D_c = 1.350 g cm^{-3}, T = 150 K, Z = 2, μ(Ga$K\alpha$) = 2.747 mm^{-1}. Total 32534 reflections, 5001 unique (R_{int} = 0.0470). Refinement of 4785 reflections (311 parameters) with $I > 2\sigma(I)$ converged at final R_1 = 0.0406 (R_1 all data = 0.0425), wR_2 = 0.1057 (wR_2 all data = 0.1093), gof = 1.039. CCDC 2203530.

6.5.3.13 $[Co(\mathbf{20})_2(NCS)_2]_n \cdot 4.5 n CHCl_3$

$C_{62.50}H_{46.50}Cl_{13.50}CoN_8S_2$, M_r = 1511.20, pink block, tetragonal, space group $P4/ncc$, a = 26.1874(12), b = 26.1874(12), c = 19.0189(10) Å, V = 13042.8(14) Å^3, D_c = 1.539 g cm^{-3}, T = 150 K, Z = 8, μ(Cu$K\alpha$) = 8.134 mm^{-1}. Total 106826 reflections, 5933 unique (R_{int} = 0.0511). Refinement of 5227 reflections (385 parameters) with $I > 2\sigma(I)$ converged at final R_1 = 0.0949 (R_1 all data = 0.1027), wR_2 = 0.2926 (wR_2 all data = 0.3016), gof = 1.075. CCDC 2111729.

6.5.3.14 $[Co(\mathbf{16})_2(NCS)_2]_n \cdot 4.3 n CHCl_3$

$C_{60.3}Cl_{12.9}CoH_{42.3}N_8S_2$, M_r = 1459.27, pink plate, tetragonal, space group $P4/ncc$, a = 25.8136(8), b = 25.8136(8), c = 18.8776(6) Å, V = 12578.9(9) Å^3, D_c = 1.541 g cm^{-3}, T = 150 K, Z = 8, μ(Cu$K\alpha$) = 8.183 mm^{-1}. Total 63834 reflections, 5852 unique (R_{int} = 0.1506). Refinement of 5020 reflections (318 parameters) with $I > 2\sigma(I)$ converged at final R_1 = 0.1858 (R_1 all data = 0.1963), wR_2 = 0.4219 (wR_2 all data = 0.4271), gof = 1.125. CCDC 2111727.

6.5.3.15 $[Co(\mathbf{16})_2(NCS)_2]_n \cdot 3n C_6H_5CH_3$

$C_{77}H_{62}CoN_8S_2$, M_r = 1222.39, light pink plate, monoclinic, space group $P2_1/n$, a = 16.0266(4), b = 12.8020(4), c = 16.7374(5) Å, β = 111.519(2)°, V = 3194.69(16) Å^3, D_c = 1.271 g cm^{-3}, T = 150 K, Z = 2, μ(Ga$K\alpha$) = 2.103 mm^{-1}. Total 21999 reflections, 6684 unique (R_{int} = 0.0360). Refinement of 5648 reflections (386 parameters) with $I > 2\sigma(I)$ converged at final R_1 = 0.0534 (R_1 all data = 0.0655), wR_2 = 0.1400 (wR_2 all data = 0.1508), gof = 1.060. CCDC 2111728.

6.5.3.16 $[Co(\mathbf{17})_2(NCS)_2]_n \cdot 4n CHCl_3$

$C_{60}H_{40}Cl_{12}CoF_2N_8S_2$, M_r = 1459.45, light pink plate, orthorhombic, space group $Pccn$, a = 25.5390(17), b = 26.0947(18), c = 18.6994(12) Å, V = 12461.9(14) Å^3, D_c = 1.556 g cm^{-3}, T = 150 K, Z = 8, μ(Cu$K\alpha$) = 7.962 mm^{-1}. Total 147886 reflections, 11731 unique (R_{int} = 0.0739). Refinement of 9492 reflections (766 parameters) with $I > 2\sigma(I)$ converged at final R_1 = 0.1449 (R_1 all data = 0.1556), wR_2 = 0.4596 (wR_2 all data = 0.4825), gof = 0.979. CCDC 2111726.

6.5.3.17 $[Co(\mathbf{17})_2(NCS)_2]_n \cdot 4n C_6H_5CH_3$

$C_{84}H_{68}CoF_2N_8S_2$, M_r = 1350.51, light pink plate, monoclinic, space group $C2/c$, a = 30.9817(6) , b = 12.9061(3), c = 18.1752(4) Å, β = 99.634(2)°, V = 7164.9(3) Å^3, D_c = 1.252 g cm^{-3}, T = 150 K, Z = 4, μ(Ga$K\alpha$) = 1.957 mm^{-1}. Total 38406 reflections, 7197 unique (R_{int} = 0.0319). Refinement of 6443 reflections (457 parameters) with $I > 2\sigma(I)$ converged at final R_1 = 0.0392 (R_1 all data = 0.0463), wR_2 = 0.1013 (wR_2 all data = 0.1067), gof = 1.071. CCDC 2111725.

6.5.3.18 $[Co(\mathbf{18})_2(NCS)_2]_n$

$C_{56}H_{36}Cl_2CoN_8S_2$, M_r = 1014.88, pink block, monoclinic, space group $P2_1/n$, a = 9.96970(10), b = 17.2090(2), c = 14.3819(2) Å, β = 105.999(2)°, V = 2371.91(5) Å^3, D_c = 1.421 g cm^{-3}, T = 150 K, Z = 2, μ(Ga$K\alpha$) = 3.411 mm^{-1}. Total 46926 reflections, 5023 unique (R_{int} = 0.1144). Refinement of 4752 reflections (313 parameters) with $I > 2\sigma(I)$ converged at final R_1 = 0.0507 (R_1 all data = 0.0527), wR_2 = 0.1383 (wR_2 all data = 0.1399), gof = 1.050. CCDC 2111724.

6.5.3.19 $[Co(\mathbf{19})_2(NCS)_2]_n \cdot n CHCl_3$

$C_{57}H_{37}Br_2Cl_3CoN_8S_2$, M_r = 1223.17, light pink plate, monoclinic, space group $P2_1/n$, a = 17.1095(12), b = 10.7555(7), c = 28.8062(19) Å, β = 91.434(3)°, V = 5299.3(6) Å^3, D_c = 1.533 g cm^{-3}, T = 150 K, Z = 4, μ(Cu$K\alpha$) = 6.808 mm^{-1}. Total 70610 reflections, 9840 unique (R_{int} = 0.0370). Refinement of 9183 reflections (658 parameters) with $I > 2\sigma(I)$ converged at final R_1 = 0.0453 (R_1 all data = 0.0483), wR_2 = 0.1140 (wR_2 all data = 0.1163), gof = 1.051. CCDC 2111731.

6.5.3.20 [Co(**19**)$_2$(NCS)$_2$]$_n$·4.6*n*C$_6$H$_5$CH$_3$

$C_{88.2}H_{72.8}Br_2CoN_8S_2$, M_r = 1527.61, pink plate, monoclinic, space group $P2_1/c$, a = 16.7073(8), b = 12.7934(6), c = 18.1545(9) Å, β = 91.934(4)°, V = 3878.2(3) Å^3, D_c = 1.308 g cm^{-3}, T = 150 K, Z = 2, μ(Cu$K\alpha$) = 3.832 mm^{-1}. Total 49970 reflections, 7311 unique (R_{int} = 0.1058). Refinement of 5514 reflections (370 parameters) with $I > 2\sigma(I)$ converged at final R_1 = 0.0838 (R_1 all data = 0.1053), wR_2 = 0.2313 (wR_2 all data = 0.2463), gof = 1.045. CCDC 2111730.

6.5.3.21 [Co(**21**)$_2$(NCS)$_2$]$_n$·2*n*CHCl$_3$

$C_{66}H_{44}Cl_6CoN_8S_2$, M_r = 1284.919, pink block, monoclinic, space group $P2_1/n$, a = 10.9048(6), b = 18.5289(10), c = 15.4837(8) Å, β = 91.214(3)°, V = 3127.8(3) Å^3, D_c = 1.364 g cm^{-3}, T = 150 K, Z = 2, μ(Cu$K\alpha$) = 5.508 mm^{-1}. Total 18857 reflections, 5644 unique (R_{int} = 0.0327). Refinement of 5210 reflections (340 parameters) with $I > 2\sigma(I)$ converged at final R_1 = 0.0442 (R_1 all data = 0.0474), wR_2 = 0.1226 (wR_2 all data = 0.1261), gof = 1.0431. CCDC 2087183.

6.5.3.22 [Co(**21**)$_2$(NCS)$_2$]$_n$·2*n*C$_6$H$_5$Me

$C_{78}H_{58}CoN_8S_2$, M_r = 1230.37, pink plate, monoclinic, space group $P2_1/c$, a = 14.6063(5), b = 11.8567(5), c = 18.3485(6) Å, β = 92.912(2)°, V = 3173.5(2) Å^3, D_c = 1.288 g cm^{-3}, T = 150 K, Z = 2, μ(Cu$K\alpha$) = 3.137 mm^{-1}. Total 20072 reflections, 5706 unique (R_{int} = 0.0368). Refinement of 5130 reflections (375 parameters) with $I > 2\sigma(I)$ converged at final R_1 = 0.0583 (R_1 all data = 0.0646), wR_2 = 0.1557 (wR_2 all data = 0.1612), gof = 1.050. CCDC 2087184.

References

1. L. Palatinus, S. J. Prathapa and S. van Smaalen, *J. Appl. Crystallogr.*, **2012**, 45, 575-580.
2. L. Palatinus and G. Chapuis, *J. Appl. Crystallogr.*, **2007**, 40, 786-790.
3. Bruker axs. Software for the Integration of CCD Detector System Bruker Analytical X-ray Systems; Bruker AXS: Madison, WI, USA.
4. G. Sheldrick, *Acta Crystallogr., Sect. A: Found. Adv.*, **2015**, 71, 3-8.
5. O. V. Dolomanov, L. J. Bourhis, R. J. Gildea, J. A. K. Howard and H. Puschmann, *J. Appl. Crystallogr.*, **2009**, 42, 339-341.
6. G. Sheldrick, *Acta Crystallogr., Sect. C: Struct. Chem.*, **2015**, 71, 3-8.
7. C. F. Macrae, I. Sovago, S. J. Cottrell, P. T. A. Galek, P. McCabe, E. Pidcock, M. Platings, G. P. Shields, J. S. Stevens, M. Towler and P. A. Wood, *J. Appl. Crystallogr.*, **2020**, 53, 226-235.
8. A. Spek, *Acta Crystallogr., Sect. C: Struct. Chem.*, **2015**, 71, 9-18.
9. G. Pawley, *J. Appl. Crystallogr.*, **1981**, 14, 357-361.
10. A. Le Bail, H. Duroy and J. L. Fourquet, *Mater. Res. Bull.*, **1988**, 23, 447-452.
11. J. Rodríguez-Carvajal, *Phys. B*, **1993**, 192, 55-69.
12. T. Roisnel and J. Rodríguez-Carvajal, In Proceedings of the Seventh European Powder Diffraction Conference (EPDIC 7), Barcelona, Spain, **2000**, 118-123.
13. G. W. V. Cave and C. L. Raston, *J. Chem. Soc., Perkin Trans. 1*, **2001**, 3258-3264.
14. L. Li, Y. Z. Zhang, C. Yang, E. Liu, J. A. Golen and G. Zhang, *Polyhedron*, **2016**, 105, 115-122.

Chapter 7 Summary and outlook

In the main part of this PhD thesis, systematic studies of the assembly of coordination polymers based on several homologous series of ditopic 4′-functionalized-3,2′:6′,3″-terpyridine ligands have been presented. In particular, the investigation involved series of organic compounds differing in the length, the branching type, the nature of the substituent groups or the extent of conjugation. The synthetic approach to these organic building blocks is the one-pot procedure from Wang and Hanan, starting from commercially available benzaldehydes. This strategy proved to be successful in the majority of the cases, with the exceptions of compounds **3** and **12**. Under the usual conditions, cyclohexanol derivatives (**3a** and **12a**) were obtained, and the alternative route involving the intermediate 4-(3,2′:6′,3″-terpyridin-4′-yl)phenol was adopted to achieve the desired products. All the organic compounds were fully characterized by NMR, IR and absorption spectroscopies, mass spectrometry, melting point and elemental analysis or high-resolution mass spectrometry and the main features of each were discussed. Additionally, the crystal structures of compounds **6**–**9** were obtained and analyzed in detail, highlighting similarities and differences in the 3,2′:6′,3″-tpy unit conformation and in the packing interactions.

The coordination chemistry of the newly-prepared ligands was studied, and they proved to be responsive (i.e. adopting different conformations) linkers, suitable for the assembly of 1D- and 2D-architectures. Naturally, the topology of the resulting polymers strongly depends on the choice of the metal salt as well as the ligand. Copper(II) acetate and cobalt(II) thiocyanate were selected to carry out the systematic investigations. The former tends to crystallize in the paddle-wheel $\{Cu_2(OAc)_4\}$ unit, thus directing the assembly of 1D-chains when reacting with ditopic ligands. This expectation was largely fulfilled, and polymers with the general formulation of $[Cu_2(\mu\text{-}OAc)_4\mathbf{L}]_n$ were obtained with **L** = **1**, **4**, **5**, **7**, **16**–**20**. However, in the case of ligand **1**, different reaction conditions and a longer reaction time also led to the formation of a double-stranded 1D-polymer, which was revealed to be the main product in experiments carried out under crystallization conditions, as confirmed by PXRD. On the other hand, the anticipated single-stranded 1D-polymer $[Cu_2(\mu\text{-}OAc)_4\mathbf{1}]_n$ containing paddle-wheel units was the main product of the preparative scale reaction. Although the polymers assembled from the other 4′-(4-*n*-alkyloxyphenyl)-3,2′:6′,3″-terpyridines (**4**, **5** and **7**) present the same topology as $[Cu_2(\mu\text{-}OAc)_4\mathbf{1}]_n$, they differ in the conformation adopted by the 3,2′:6′,3″-tpy unit. In fact, while it exhibits conformation **A** in ligand **1**, it assumes conformation **B** in **4**, **5** and **7**, indicating that the precise structure of the coordination polymer is responsive to changes in the length of the alkyloxy tails, and the dominant packing interactions in the crystal lattice change accordingly. The combination of five 4′-(4′-X-[1,1′-biphenyl-4-yl)-3,2′:6′,3″-terpyridines (**16**–**20**) with copper(II) acetate yielded five 1D-polymers containing paddle-wheel units linked by the ditopic ligands. The tpy unit was again shown to be sensitive to changes in the 4′-substituents incorporated in the ligands,

and this time the steric demands seemed to be the key factor in causing a switch in the conformation. In particular, conformation **A** was adopted in the polymers assembled from the ligands bearing X= H and X = F, whereas conformation **B** in the other three cases (X = Cl, Br or Me).

The second metal salt of choice was cobalt(II) thiocyanate, which allowed an extensive study of the effect of substituents incorporated in organic ligands on the assembly of 2D-coordination networks. In contrast to copper(II) acetate, the cobalt(II) center is a potential 4-connecting node, as it tends to adopt an octahedral geometry, with two sites occupied by thiocyanato ligands. Twenty-one 2D networks possessing *trans*-{$Co(NCS)_2N_4$} 4-connecting nodes and 3,2′:6′,3″-tpy linkers were prepared, structurally characterized, described and compared. Only one 1D structure formed, and this resulted from the reaction between cobalt(II) thiocyanate and ligand **1**. In this case, two molecules of methanol (one of the crystallization solvents) coordinated to the cobalt(II) center, thus reducing its nodal connectivity. In the same crystallization tube, two pseudopolymorphs possessing 2D nets also grew, but PXRD confirmed that the 1D-coordination polymer was the dominant product in the bulk sample. Systematic investigations on series of homologous ligands were carried out, in which only one parameter was varied at one time, to provide a better comprehension of the assembly algorithms. Once again, the chain length proved to be a crucial factor in causing a switch in the conformation of the 3,2′:6′,3″-tpy unit, and consequently in the packing interactions, as observed comparing the networks containing **2**, **3** and **4**, with those bearing ligands **5** and **6**. The first three polymers are similar and comprise two geometrically different rhombi, with nets that pack in an ABAB... manner and cone-like arrangements of *n*-alkyloxyphenyl groups; the 3,2′:6′,3″-tpy unit is in conformation **A**. In $[Co_2(\mathbf{5})_4(NCS)_4]_n$ and $[Co(\mathbf{6})_2(NCS)_2]_n$, the (4,4) nets comprise identical rhombi with a down/down/up/up arrangement of four 3,2′:6′,3″-tpy linkers around a rhombus, in contrast to the previously observed cone arrangement, with the tpy unit being in conformation **B**. Similar to this second group of structures are those assembled from the isomeric branched 4′-(4-butyloxyphenlyl)-3,2′:6′,3″-tpy ligands (*rac*-**11**, **12** and **13**) and ligand **15**, bearing an isopentyloxy chain. Despite the significant structural perturbation from linear (**4**) to branched substituents, changes in the spatial properties of the second group of ligands are accommodated with subtle conformational changes in the 3,2′:6′,3″-tpy domain. Similarities and differences between these nets are described in terms of internal angles in the rhombi, angles between the planes of pairs of bonded arene rings in the coordinated ligands and amount of solvent included in the crystal lattice. The reactions of $Co(NCS)_2$ with the five 4′-X-[1,1′-biphenyl]-4-yl-3,2′:6′,3″-tpy ligands were first carried out in a combination of chloroform and methanol. Five (4,4)-nets formed, which can be classified in three structure types. **20**, **16** and **17** (X = Me, H and F, respectively) formed highly symmetrical and porous nets, in which the 3,2′:6′,3″-tpy adopts conformation **A** and the 4′-substituted-[1,1′-biphenyl]-4-yl units are once again arranged in cones. $CHCl_3$ molecules occupy two types of cavities. TGA measurements showed that half of the solvent in $[Co(\mathbf{17})_2(NCS)_2]_n{\cdot}4n CHCl_3$ can be reversibly removed and replaced by $CDCl_3$ or CH_2Cl_2. $[Co(\mathbf{18})_2(NCS)_2]_n$ shows a second structure-type: the organic linkers lie over the rhombi

and the 3,2′:6′,3″-tpy exhibits conformation **B**; Cl…π interactions contribute to the packing. The network in [Co(**19**)$_2$(NCS)$_2$]$_n$·nCHCl$_3$ represents the third structure-type and in this case the (4,4) net defined by the Co atoms is non-planar. Two independent 3,2′:6′,3″-tpy ligands adopt conformations **A** and **B**, respectively. The same series of ligands was reacted with Co(NCS)$_2$ in a combination of toluene and methanol, but only the crystal structures of [Co(**16**)$_2$(NCS)$_2$]$_n$·3nC$_6$H$_5$CH$_3$, [Co(**17**)$_2$(NCS)$_2$]$_n$·4nC$_6$H$_5$CH$_3$ and [Co(**19**)$_2$(NCS)$_2$]$_n$·4.6nC$_6$H$_5$CH$_3$ were determined. These nets present similar asymmetric units, with the 3,2′:6′,3″-tpy domain in conformation **B**, identical rhombi (in each structure), and the 4′-X-[1,1′-biphenyl]-4-yl units directed up/up/down/down around each rhombus. However, the three coordination assemblies differ from one another in terms of interactions in the packing, amount of lattice solvent and void space (calculated in each non-solvated structure). Each of them presents either one or two molecules of toluene engaging in face-to-face π-stacking interactions with the central pyridine ring. The preliminary structure of the polymer assembled from **20** under the same conditions is consistent with the networks just described. Since the solvent plays a role in the assembly of the nets, ligand **21** (bearing a 4′-[4-(naphthalen-1-yl)phenyl] substituent) was reacted with cobalt(II) thiocyanate under crystal growth conditions using two different combinations of solvents. Single crystals of [Co(**21**)$_2$(NCS)$_2$]$_n$·2nCHCl$_3$ grew from acetonitrile and chloroform. In this first structure, the 3,2′:6′,3″-tpy unit adopts conformation **A** and the ligands are directed above and below the plane defined by cobalt(II) atoms, thus forming open channels perpendicular to the nets. Molecules of chloroform lie in the channels and can be reversibly taken out of the lattice and replaced with CDCl$_3$ or CH$_2$Cl$_2$, according to TGA-MS measurements. In contrast, [Co(**21**)$_2$(NCS)$_2$]$_n$·2nC$_6$H$_5$Me was isolated from a combination of methanol and toluene and the conformation **B** of the tpy unit is observed. The toluene molecules engage in π-stacking interactions and their removal was proven to be irreversible, demonstrating that they contribute to stabilize the structure. The presented study highlights the manner in which the 3,2′:6′,3″-tpy domain can adapt to ligand modifications through its conformational flexibility while retaining the same connectivity. Moreover, it demonstrates that there is scope to generate porous materials starting from conformationally flexible ditopic building blocks.

In the last part of the thesis, two new expanded ligands have been presented. These are bis(chelating) complexes of iron(II) possessing two divergent 3,2′:6′,3″- or 4,2′:6′,4″-tpy units capable of reacting with additional metal centers. They represent the expanded version of bis(3,2′:6′,3″-tpy) and bis(4,2′:6′,4″-tpy) ligands, respectively and are potential tetratopic building blocks for the assembly of coordination polymers. However, to date, no structures of this kind of metalloligand are present in the CSD, nor of their coordination polymers. In view of the great potential and versatility of ditopic 3,2′:6′,3″- and 4,2′:6′,4″-tpy and tetratopic bis(3,2′:6′,3″-tpy) and bis(4,2′:6′,4″-tpy) ligands, it could be interesting to develop this field and employ the metalloligands in further studies. Besides those described in Chapter 5, presenting a linear [1,1′-(biphenyl-4,4′-diyl] spacer, the new species might also include angular tetratopic metalloligands, containing [1,1′-(biphenyl-3,3′-diyl], benzene-1,3-diyl or benzene-1,2-diyl spacers.

Appendix

NMR spectra of the synthesized compounds

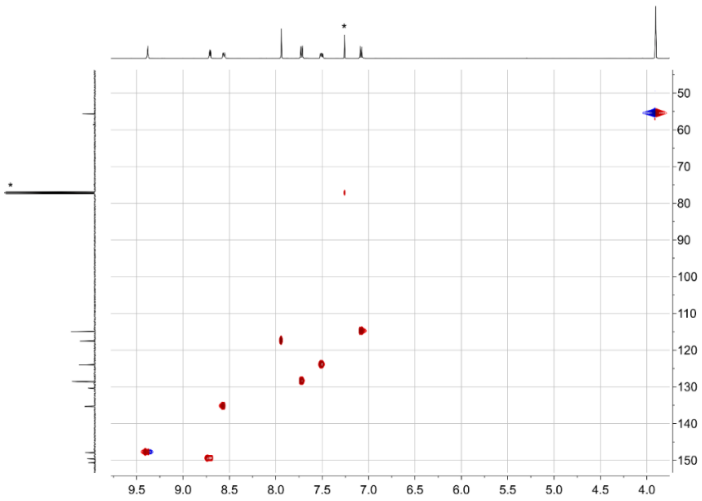

Figure S1. HMQC spectrum of **1** (500 MHz ^{1}H, 126 MHz ^{13}C{^{1}H}, $CDCl_3$, 298 K). * = $CDCl_3$ or residual $CHCl_3$.

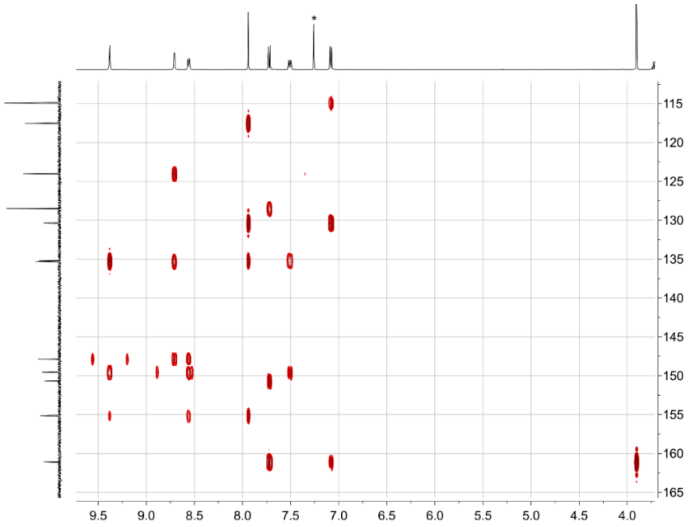

Figure S2. HMBC spectrum of **1** (500 MHz ^{1}H, 126 MHz ^{13}C{^{1}H}, $CDCl_3$, 298 K). * = residual $CHCl_3$.

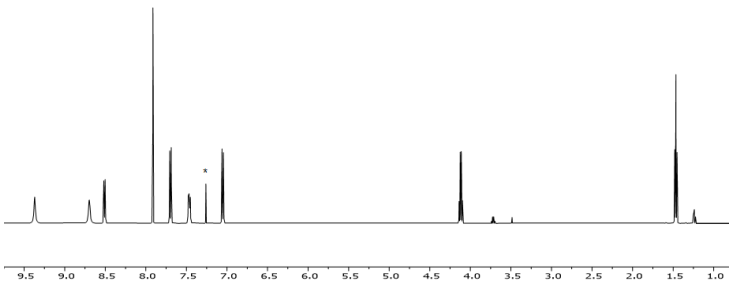

Figure S3. ^{1}H NMR spectrum of **2** (500 MHz, $CDCl_3$, 298 K). * = residual $CHCl_3$.

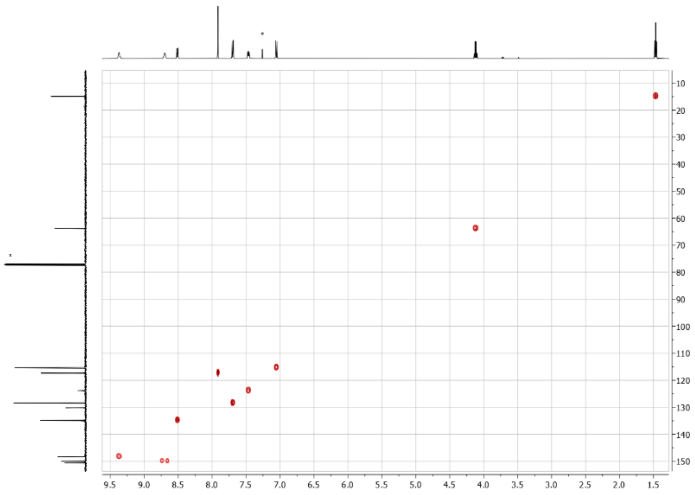

Figure S4. HMQC spectrum of **2** (500 MHz ^{1}H, 126 MHz $^{13}C\{^{1}H\}$, $CDCl_3$, 298 K). * = $CDCl_3$ or residual $CHCl_3$.

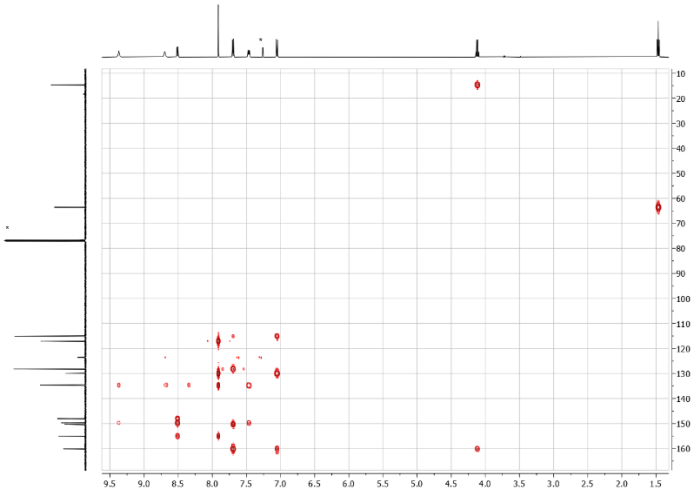

Figure S5. HMBC spectrum of **2** (500 MHz ^{1}H, 126 MHz $^{13}C\{^{1}H\}$, $CDCl_3$, 298 K). * = $CDCl_3$ or residual $CHCl_3$.

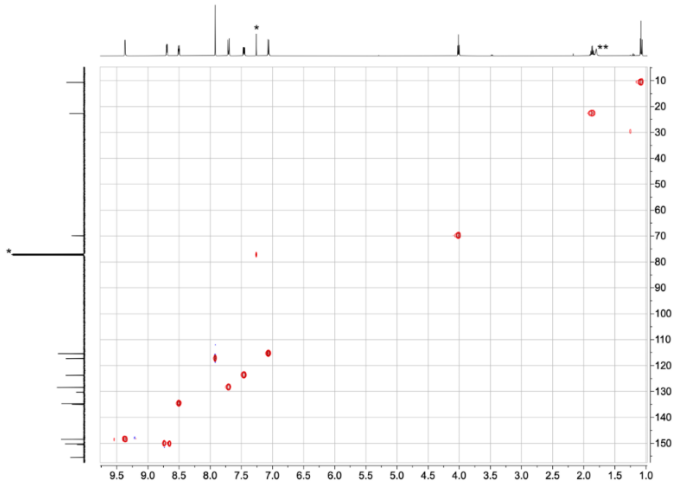

Figure S6. HMQC spectrum of **3** (500 MHz ^{1}H, 126 MHz $^{13}C\{^{1}H\}$, $CDCl_3$, 298 K). * = $CDCl_3$ or residual $CHCl_3$, ** = H_2O.

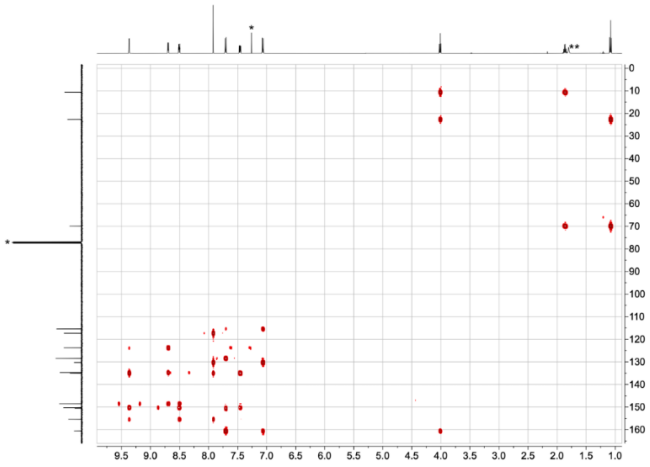

Figure S7. HMBC spectrum of **3** (500 MHz ^{1}H, 126 MHz $^{13}C\{^{1}H\}$, $CDCl_3$, 298 K). * = $CDCl_3$ or residual $CHCl_3$, ** = H_2O.

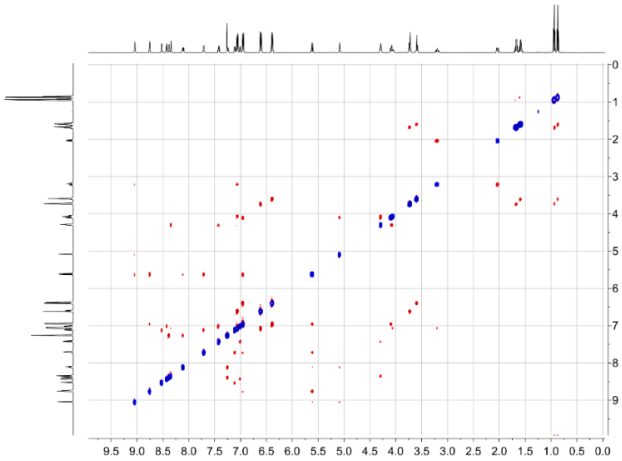

Figure S8. NOESY spectrum of **3a** (500 MHz, $CDCl_3$, 298 K).

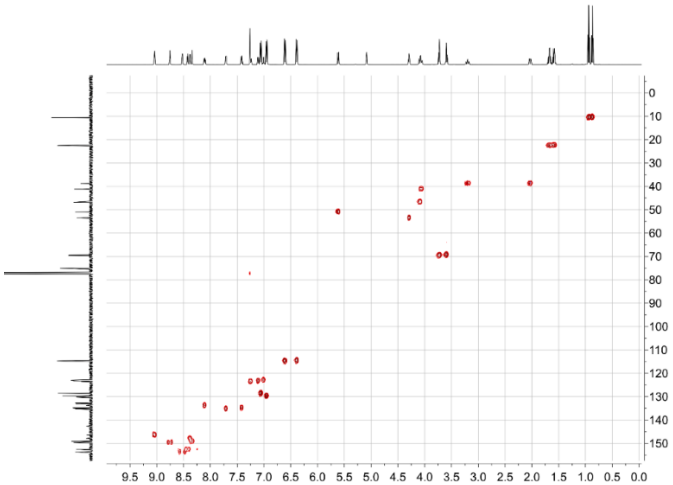

Figure S9. HMQC spectrum of **3a** (500 MHz ^{1}H, 126 MHz $^{13}C\{^{1}H\}$, $CDCl_3$, 298 K).

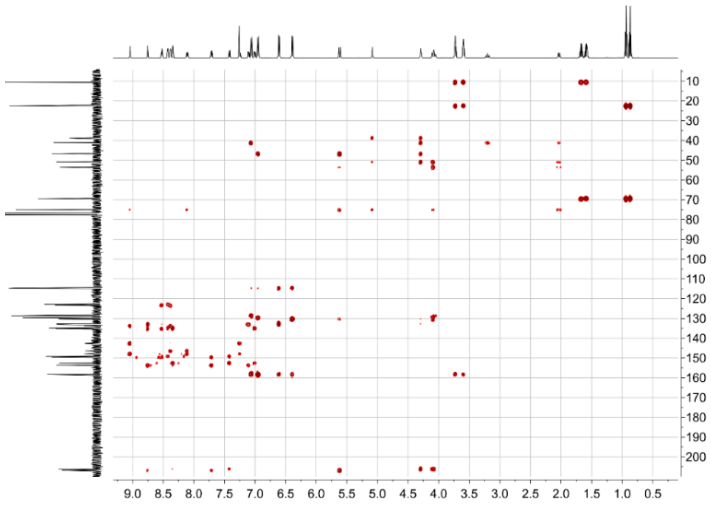

Figure S10. HMBC spectrum of **3a** (500 MHz ^{1}H, 126 MHz ^{13}C{^{1}H}, $CDCl_3$, 298 K).

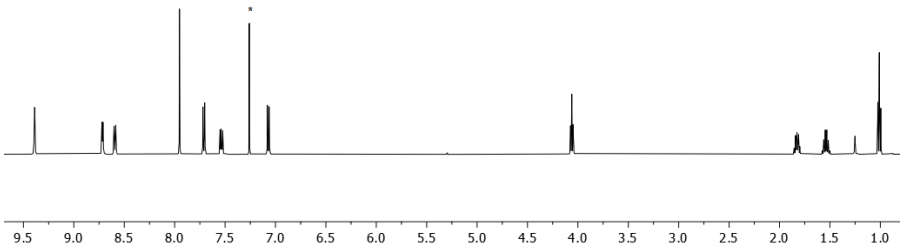

Figure S11. ^{1}H NMR spectrum of **4** (500 MHz, $CDCl_3$, 298 K). * = residual $CHCl_3$.

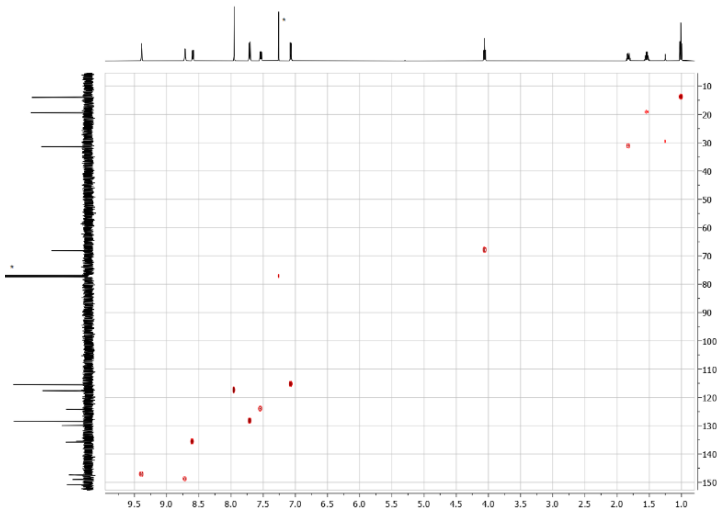

Figure S12. HMQC spectrum of **4** (500 MHz ^{1}H, 126 MHz ^{13}C{^{1}H}, $CDCl_3$, 298 K). * = $CDCl_3$ or residual $CHCl_3$.

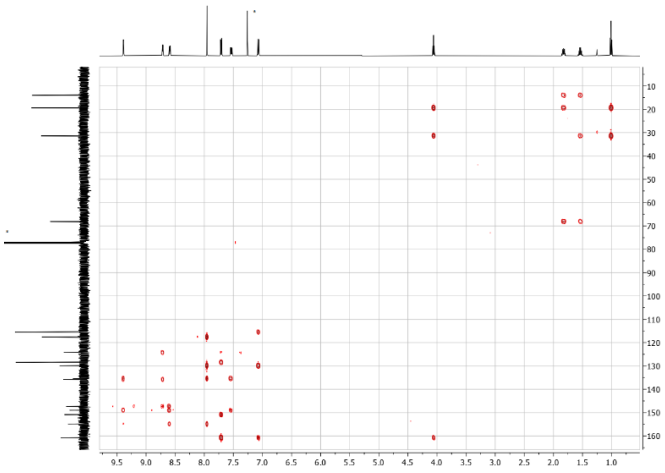

Figure S13. HMBC spectrum of **4** (500 MHz ^{1}H, 126 MHz ^{13}C{^{1}H}, $CDCl_3$, 298 K). * = $CDCl_3$ or residual $CHCl_3$.

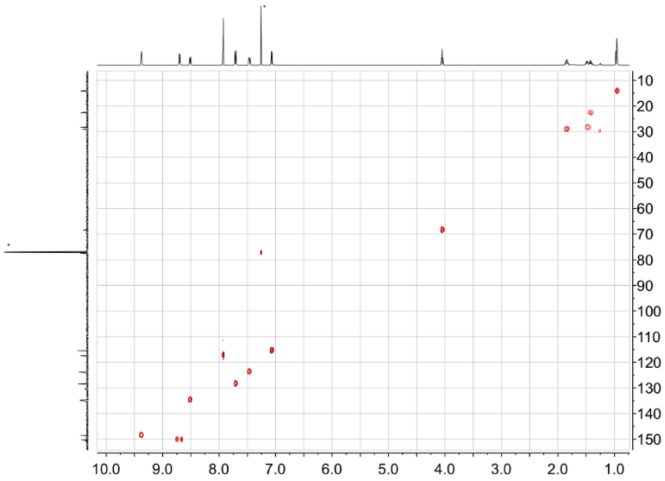

Figure S14. HMQC spectrum of **5** (500 MHz ^{1}H, 126 MHz ^{13}C{^{1}H}, $CDCl_3$, 298 K). * = $CDCl_3$ or residual $CHCl_3$.

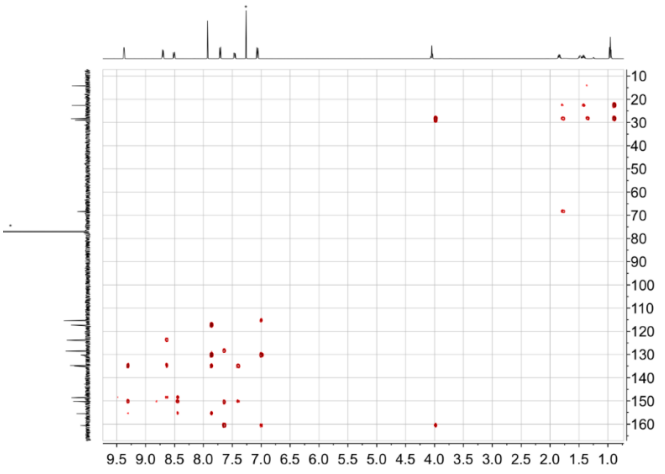

Figure S15. HMBC spectrum of **5** (500 MHz ^{1}H, 126 MHz ^{13}C{^{1}H}, $CDCl_3$, 298 K). * = $CDCl_3$ or residual $CHCl_3$.

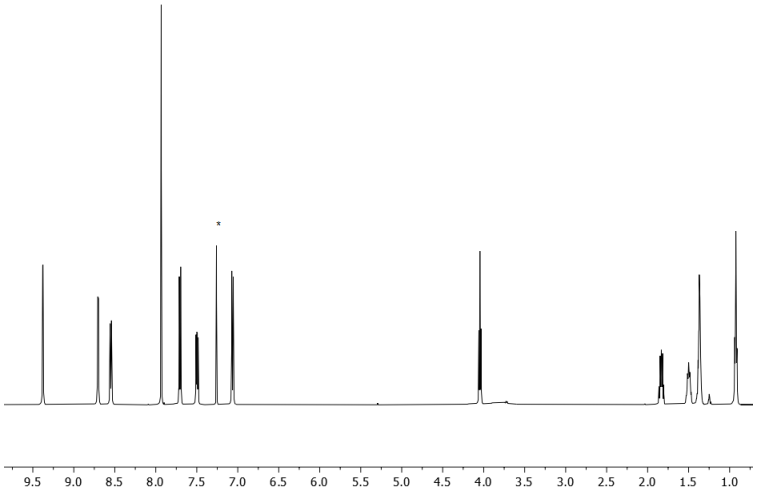

Figure S16. ^{1}H NMR spectrum of **6** (500 MHz, $CDCl_3$, 298 K). * residual $CHCl_3$.

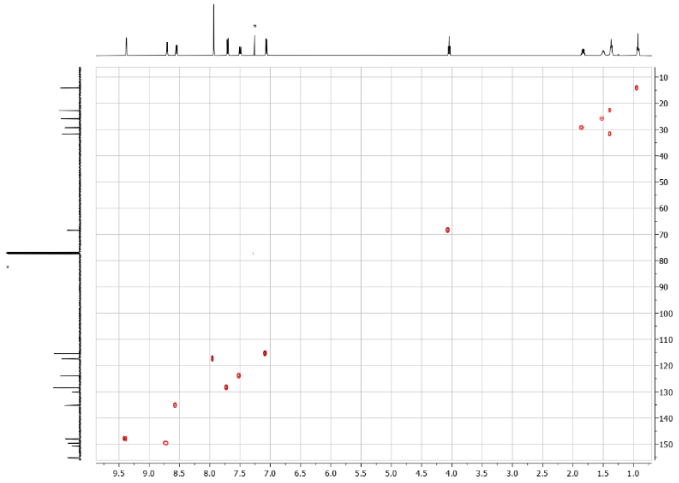

Figure S17. HMQC spectrum of **6** (500 MHz ^{1}H, 126 MHz $^{13}C\{^{1}H\}$, $CDCl_3$, 298 K). * = $CDCl_3$ or residual $CHCl_3$.

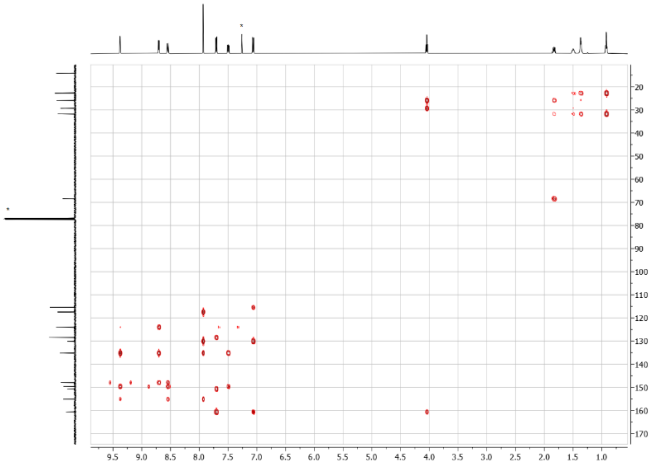

Figure S18. HMBC spectrum of **6** (500 MHz ^{1}H, 126 MHz $^{13}C\{^{1}H\}$, $CDCl_3$, 298 K). * = $CDCl_3$ or residual $CHCl_3$.

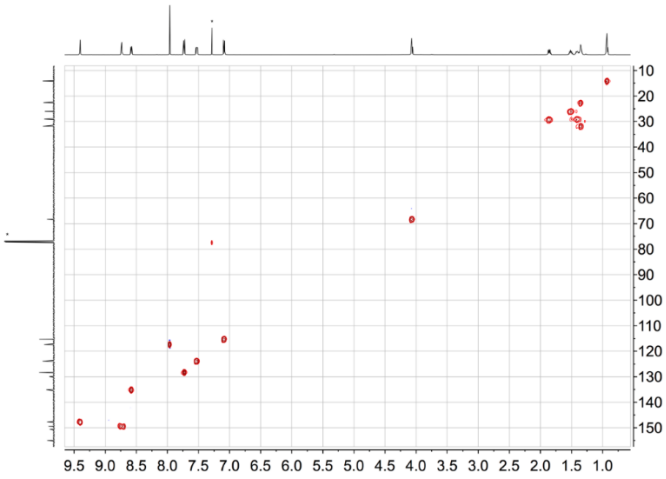

Figure S19. HMQC spectrum of **7** (500 MHz ^{1}H, 126 MHz $^{13}C\{^{1}H\}$, $CDCl_3$, 298 K). * = $CDCl_3$ or residual $CHCl_3$.

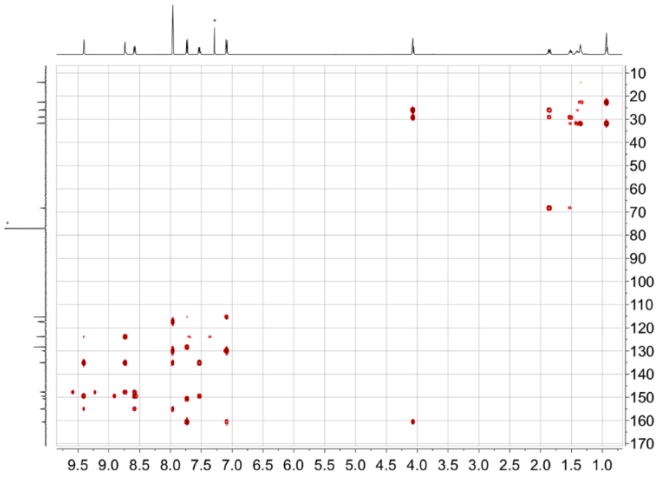

Figure S20. HMBC spectrum of **7** (500 MHz ^{1}H, 126 MHz $^{13}C\{^{1}H\}$, $CDCl_3$, 298 K). * = $CDCl_3$ or residual $CHCl_3$.

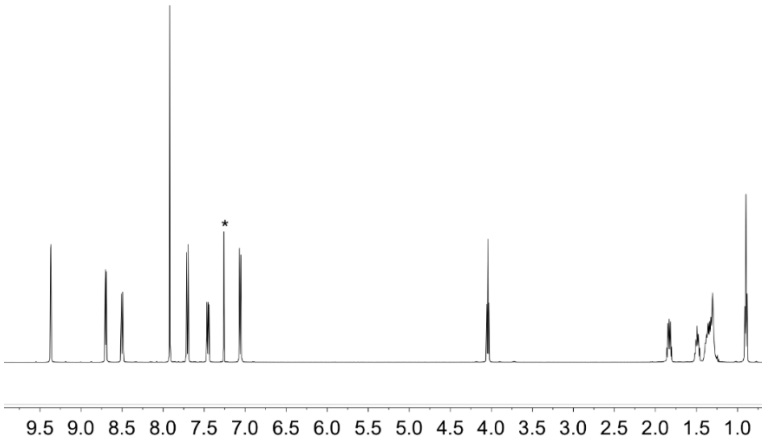

Figure S21. ^{1}H NMR spectrum of **8** (500 MHz, $CDCl_3$, 298 K). * = residual $CHCl_3$.

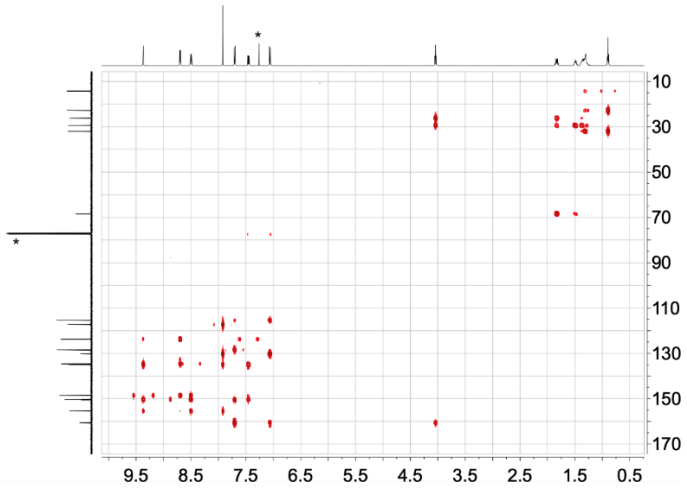

Figure S22. HMBC spectrum of **8** (500 MHz ^{1}H, 126 MHz ^{13}C{^{1}H}, $CDCl_3$, 298 K). * = $CDCl_3$ or residual $CHCl_3$.

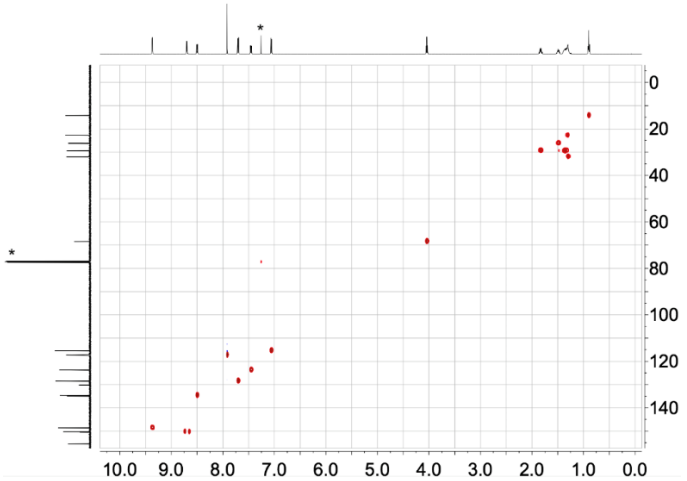

Figure S23. HMQC spectrum of **8** (500 MHz ^{1}H, 126 MHz ^{13}C{^{1}H}, $CDCl_3$, 298 K). * = $CDCl_3$ or residual $CHCl_3$.

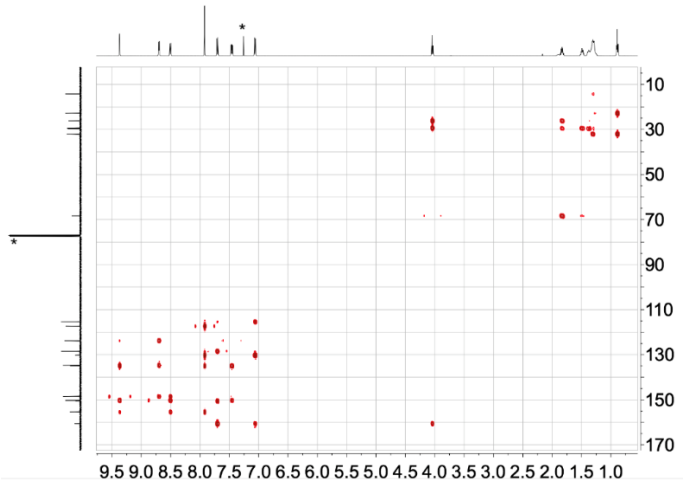

Figure S24. HMBC spectrum of **9** (500 MHz ^{1}H, 126 MHz ^{13}C{^{1}H}, $CDCl_3$, 298 K). * = $CDCl_3$ or residual $CHCl_3$.

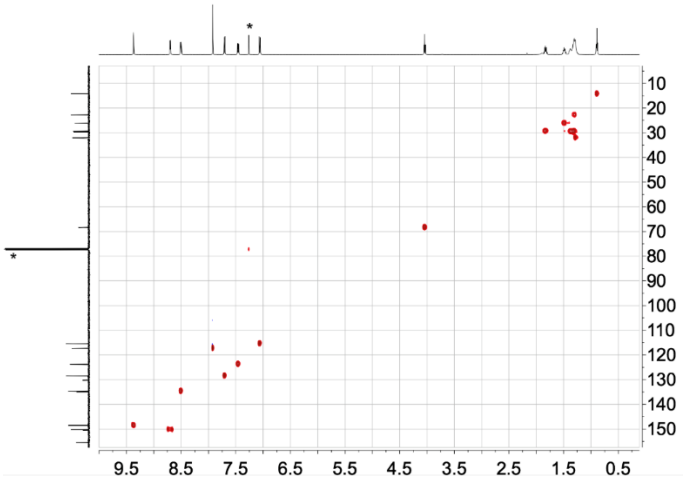

Figure S25. HMQC spectrum of **9** (500 MHz ^{1}H, 126 MHz ^{13}C{^{1}H}, $CDCl_3$, 298 K). * = $CDCl_3$ or residual $CHCl_3$.

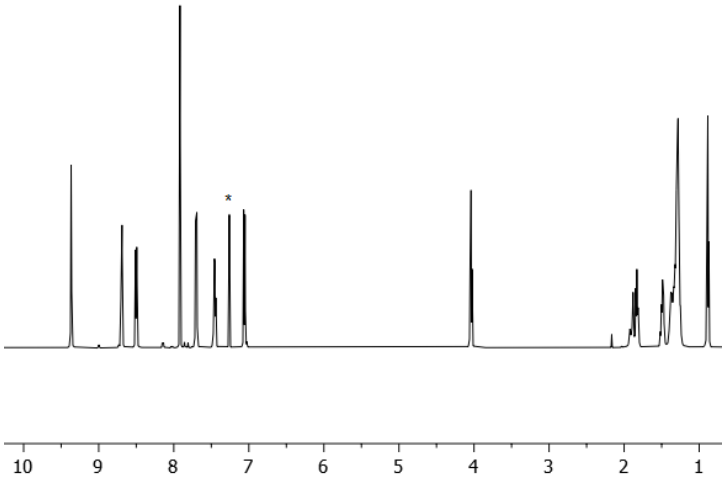

Figure S26. ^{1}H NMR spectrum of compound **10** (500 MHz, $CDCl_3$, 298 K). * = residual $CHCl_3$.

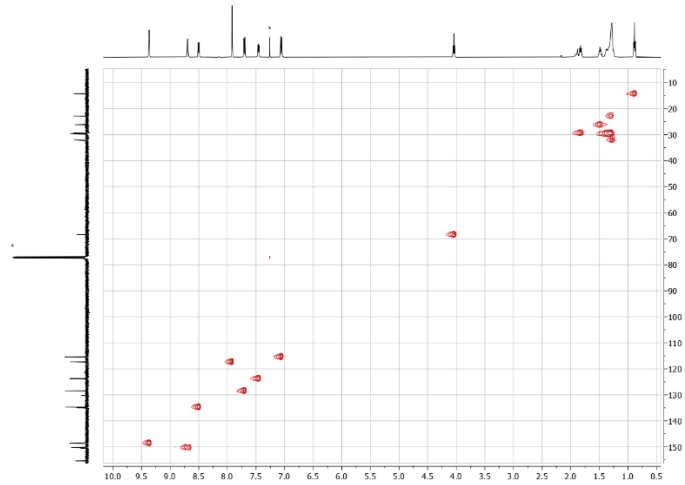

Figure S27. HMQC spectrum of **10** (500 MHz ^{1}H, 126 MHz ^{13}C{^{1}H}, $CDCl_3$, 298 K). * = $CDCl_3$ or residual $CHCl_3$.

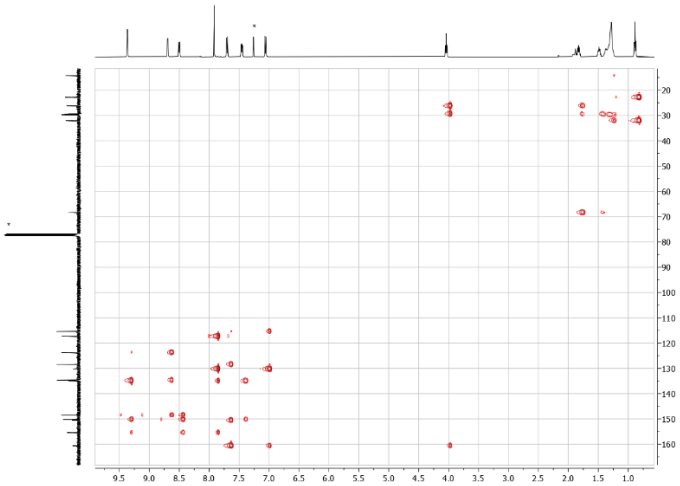

Figure S28. HMBC spectrum of **10** (500 MHz ^{1}H, 126 MHz ^{13}C{^{1}H}, $CDCl_3$, 298 K). * = $CDCl_3$ or residual $CHCl_3$.

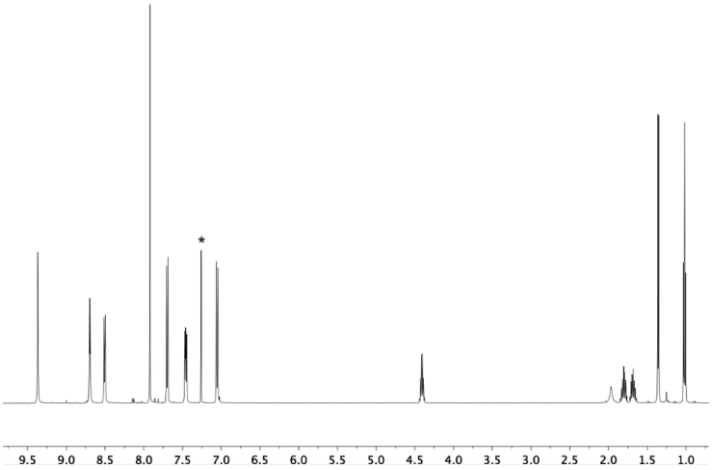

Figure S29. ^{1}H NMR spectrum of compound *rac*-**11** (500 MHz, $CDCl_3$, 298 K). * = residual $CHCl_3$.

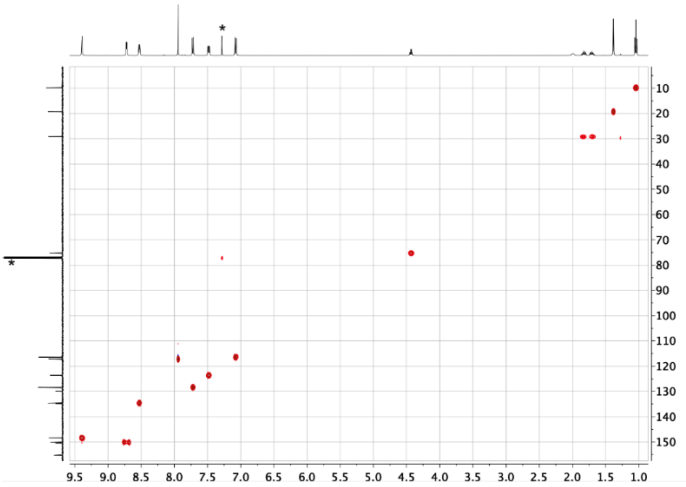

Figure S30. HMQC spectrum of *rac*-**11** (500 MHz ^{1}H, 126 MHz ^{13}C{^{1}H}, $CDCl_3$, 298 K). * = $CDCl_3$ or residual $CHCl_3$.

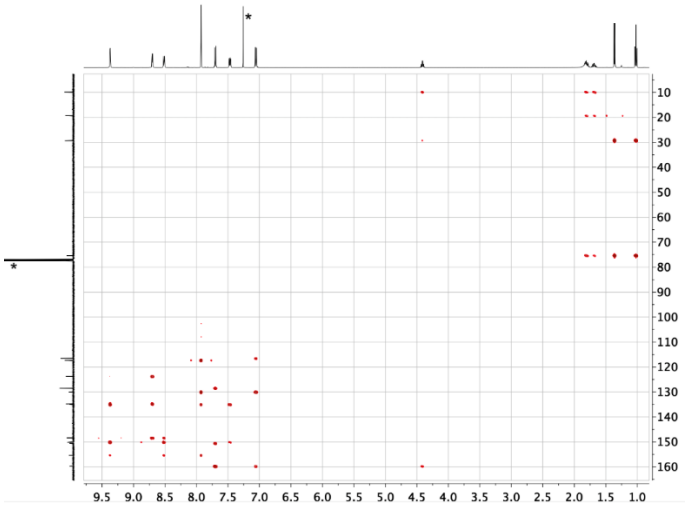

Figure S31. HMBC spectrum of *rac*-**11** (500 MHz ^{1}H, 126 MHz ^{13}C{^{1}H}, $CDCl_3$, 298 K). * = $CDCl_3$ or residual $CHCl_3$.

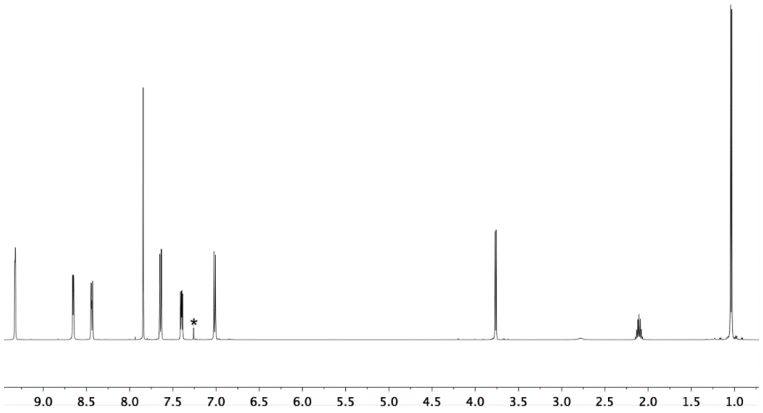

Figure S32. ^{1}H NMR spectrum of compound **12** (500 MHz, $CDCl_3$, 298 K). * = residual $CHCl_3$.

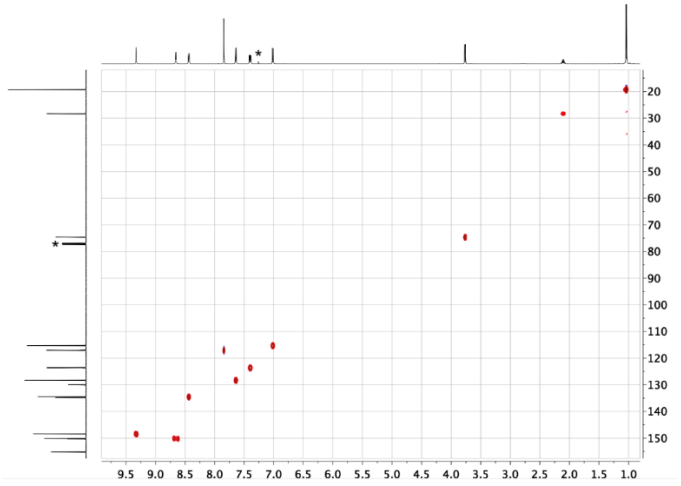

Figure S33. HMQC spectrum of **12** (500 MHz ^{1}H, 126 MHz ^{13}C{^{1}H}, $CDCl_3$, 298 K). * = residual $CHCl_3$ or $CDCl_3$.

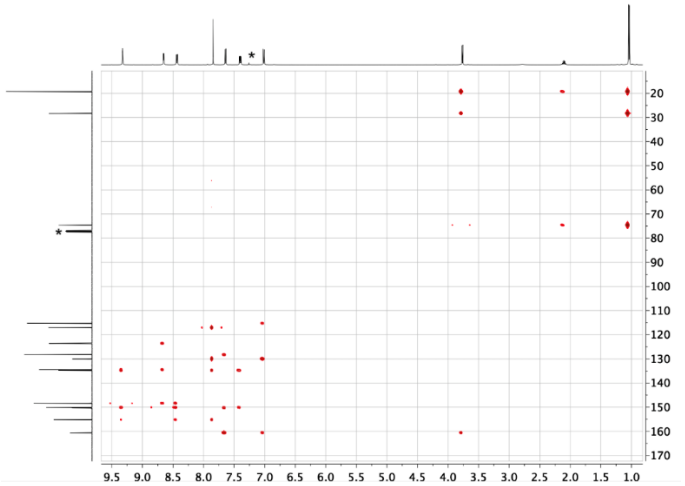

Figure S34. HMBC spectrum of **12** (500 MHz ^{1}H, 126 MHz $^{13}C\{^{1}H\}$, $CDCl_3$, 298 K). * = $CDCl_3$ or residual $CHCl_3$.

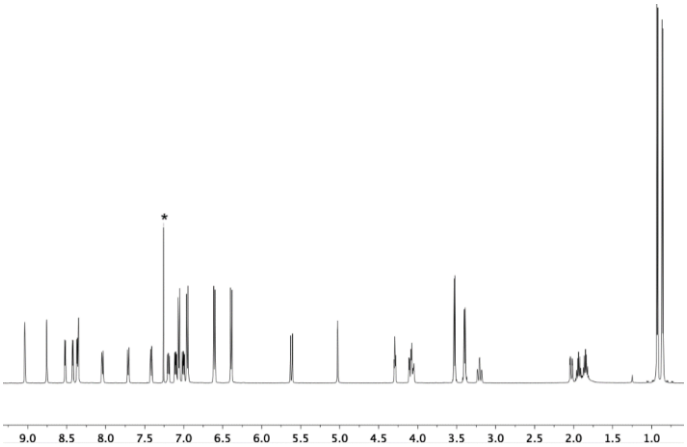

Figure S35. ^{1}H NMR spectrum of compound **12a** (500 MHz, $CDCl_3$, 298 K). * = residual $CHCl_3$.

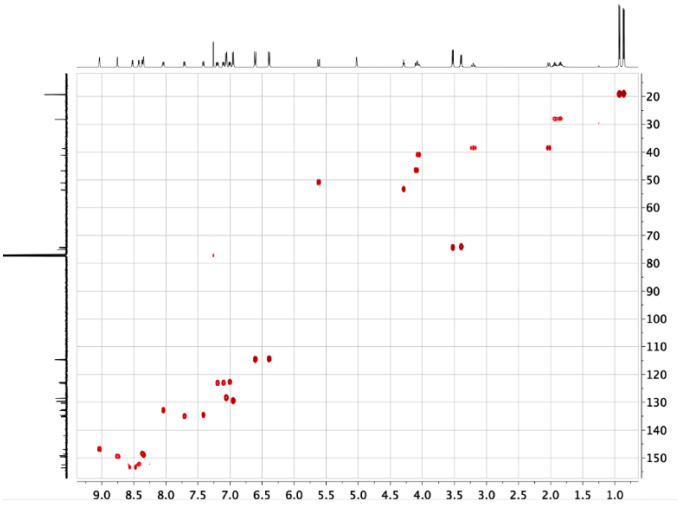

Figure S36. HMQC spectrum of **12a** (500 MHz ^{1}H, 126 MHz $^{13}C\{^{1}H\}$, $CDCl_3$, 298 K).

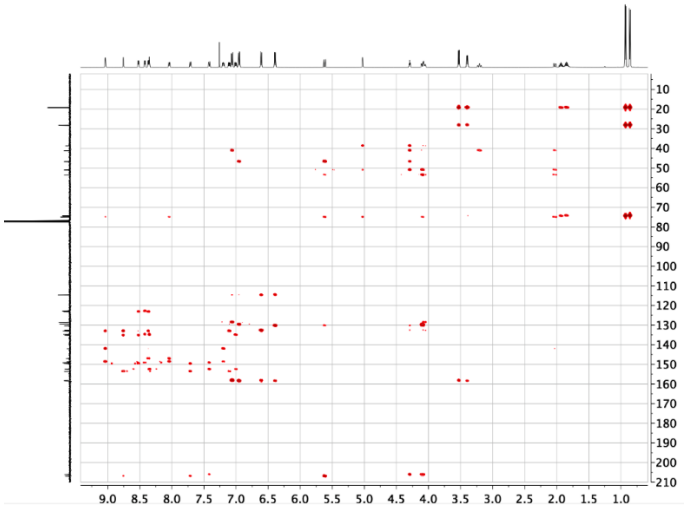

Figure S37. HMBC spectrum of **12a** (500 MHz ^{1}H, 126 MHz $^{13}C\{^{1}H\}$, $CDCl_3$, 298 K).

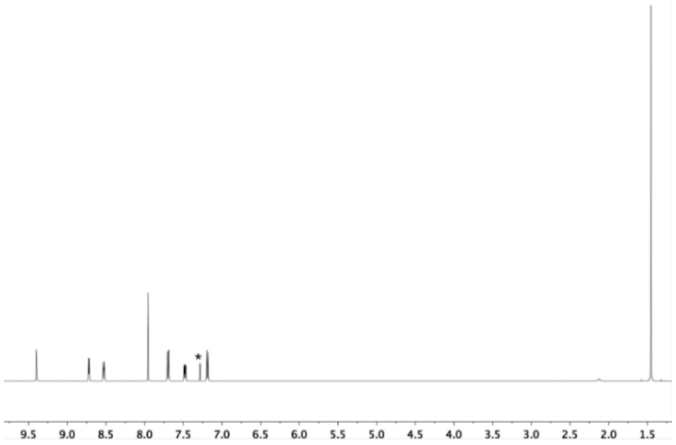

Figure S38. ^{1}H NMR spectrum of compound **13** (500 MHz, $CDCl_3$, 298 K). * = residual $CHCl_3$.

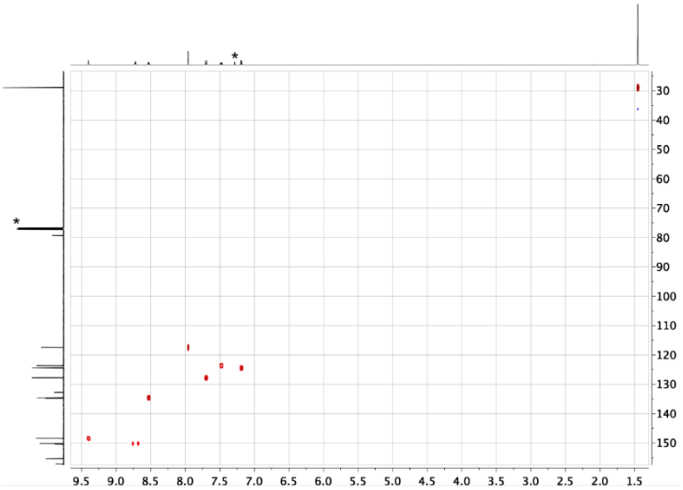

Figure S39. HMQC spectrum of **13** (500 MHz ^{1}H, 126 MHz $^{13}C\{^{1}H\}$, $CDCl_3$, 298 K). * = $CDCl_3$ or residual $CHCl_3$.

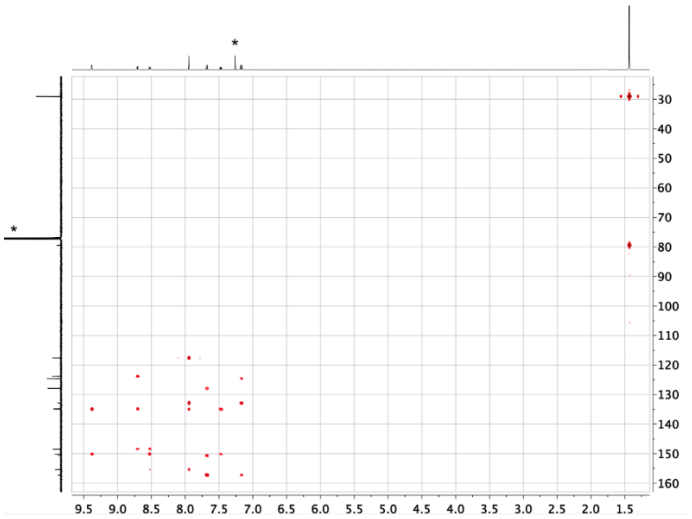

Figure S40. HMBC spectrum of **13** (500 MHz ^{1}H, 126 MHz ^{13}C{^{1}H}, $CDCl_3$, 298 K). * = $CDCl_3$ or residual $CHCl_3$.

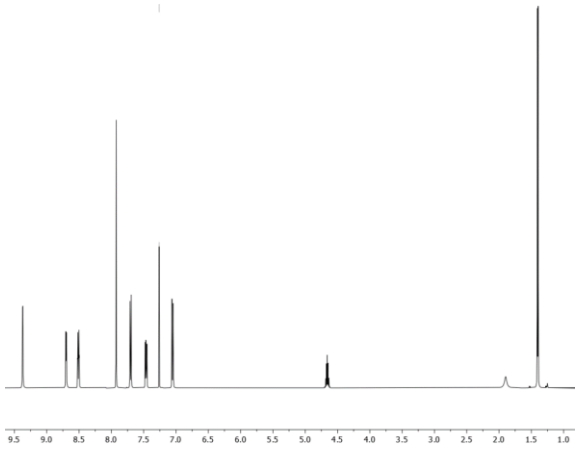

Figure S41. ^{1}H NMR spectrum of **14** (500 MHz, $CDCl_3$, 298 K).

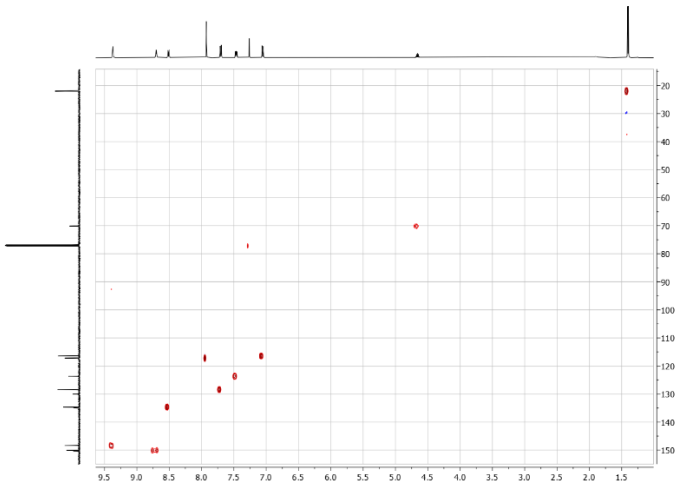

Figure S42. HMQC spectrum of **14** (500 MHz ^{1}H, 126 MHz ^{13}C{^{1}H}, $CDCl_3$, 298 K).

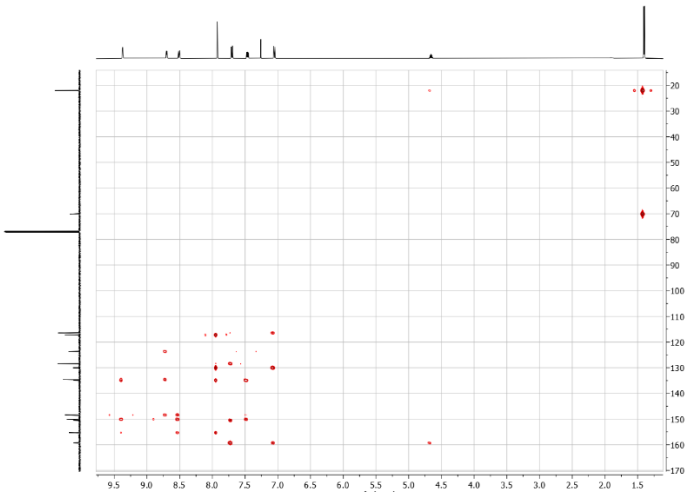

Figure S43. HMBC spectrum of **14** (500 MHz ^{1}H, 126 MHz ^{13}C{^{1}H}, $CDCl_3$, 298 K).

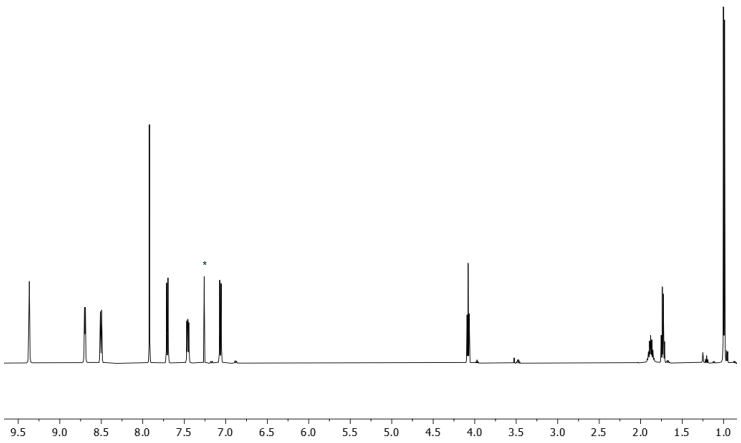

Figure S44. ^{1}H NMR spectrum of **15** (500 MHz, $CDCl_3$, 298 K). * = residual $CHCl_3$.

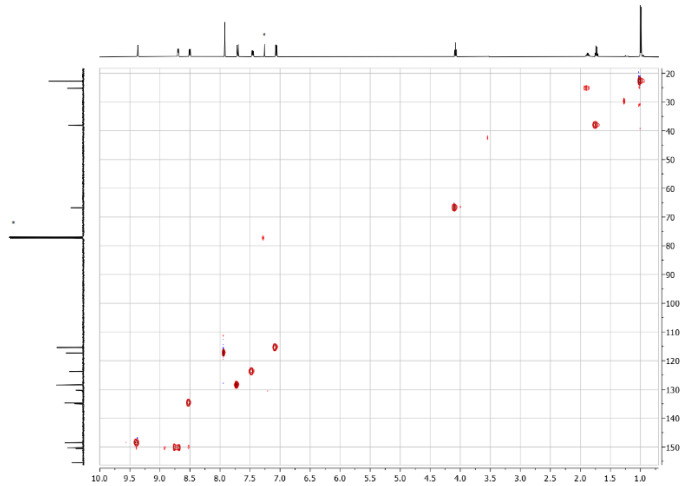

Figure S45. HMQC spectrum of **15** (500 MHz ^{1}H, 126 MHz ^{13}C{^{1}H}, $CDCl_3$, 298 K). * = $CDCl_3$ or residual $CHCl_3$.

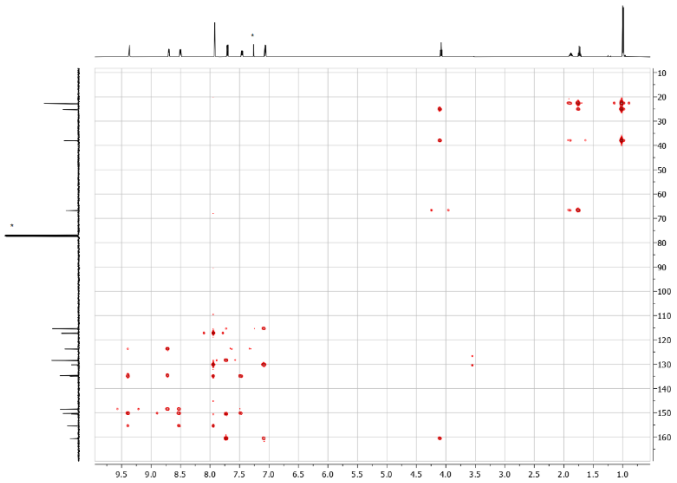

Figure S46. HMBC spectrum of **15** (500 MHz ^{1}H, 126 MHz ^{13}C{^{1}H}, $CDCl_3$, 298 K). * = $CDCl_3$ or residual $CHCl_3$.

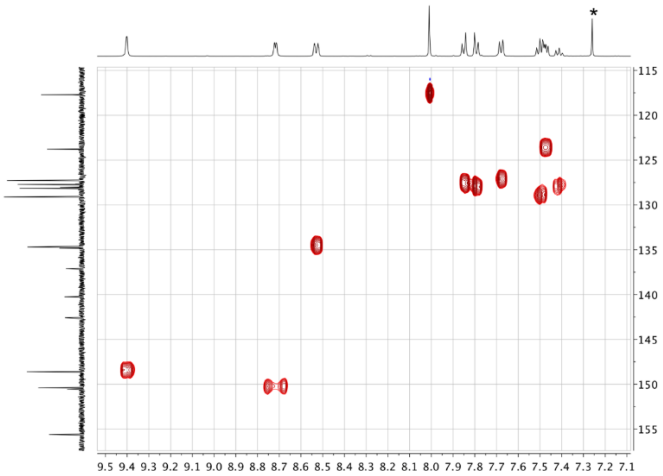

Figure S47. HMQC spectrum (aromatic region) of **16** (500 MHz ^{1}H, 126 MHz ^{13}C{^{1}H}, $CDCl_3$, 298 K). * = $CDCl_3$.

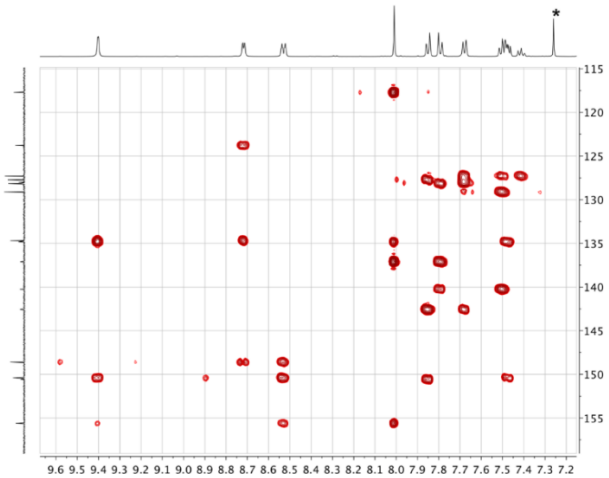

Figure S48. HMBC spectrum (aromatic region) of **16** (500 MHz ^{1}H, 126 MHz ^{13}C{^{1}H}, $CDCl_3$, 298 K). * = $CDCl_3$.

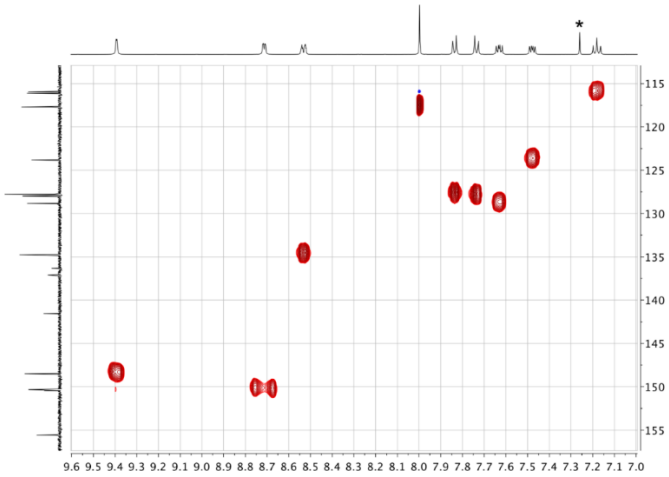

Figure S49. HMQC spectrum (aromatic region) of **17** (500 MHz ^{1}H, 126 MHz $^{13}C\{^{1}H\}$, $CDCl_3$, 298 K). * = $CDCl_3$.

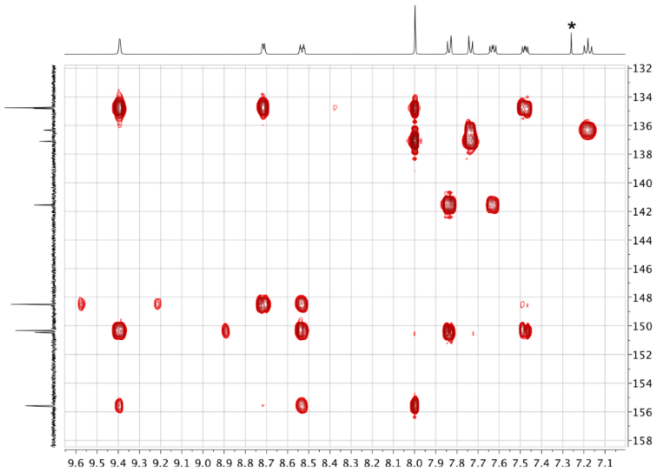

Figure S50. HMBC spectrum (aromatic region) of **17** (500 MHz ^{1}H, 126 MHz $^{13}C\{^{1}H\}$, $CDCl_3$, 298 K). * = $CDCl_3$.

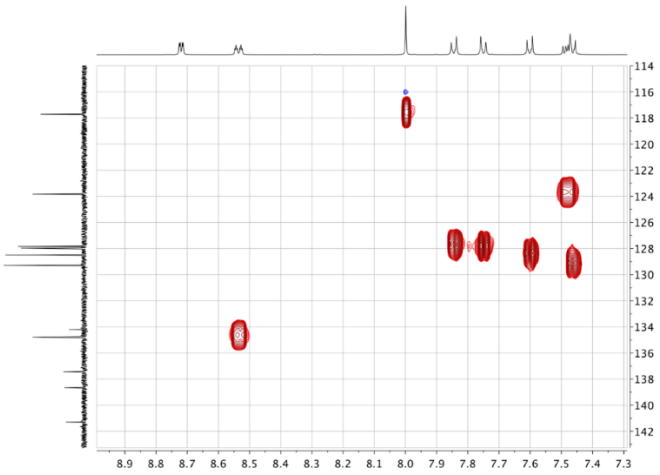

Figure S51. HMQC spectrum (aromatic region) of **18** (500 MHz ^{1}H, 126 MHz $^{13}C\{^{1}H\}$, $CDCl_3$, 298 K).

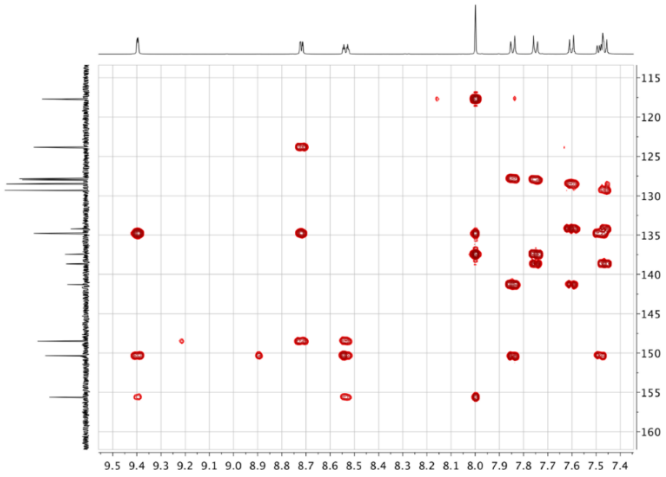

Figure S52. HMBC spectrum (aromatic region) of **18** (500 MHz ^{1}H, 126 MHz $^{13}C\{^{1}H\}$, $CDCl_3$, 298 K).

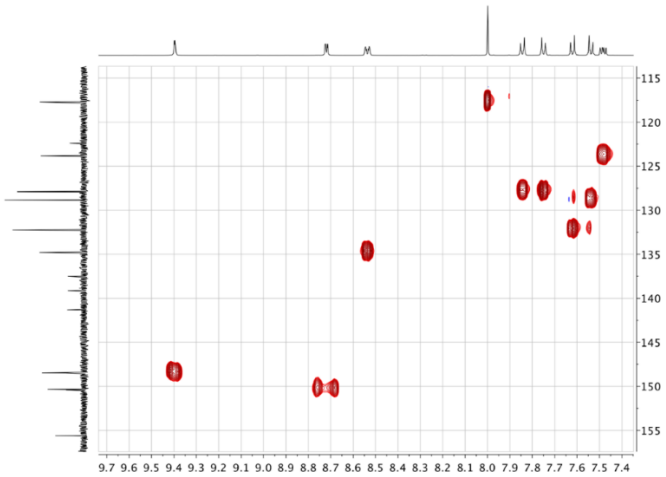

Figure S53. HMQC spectrum (aromatic region) of **19** (500 MHz ^{1}H, 126 MHz $^{13}C\{^{1}H\}$, $CDCl_3$, 298 K).

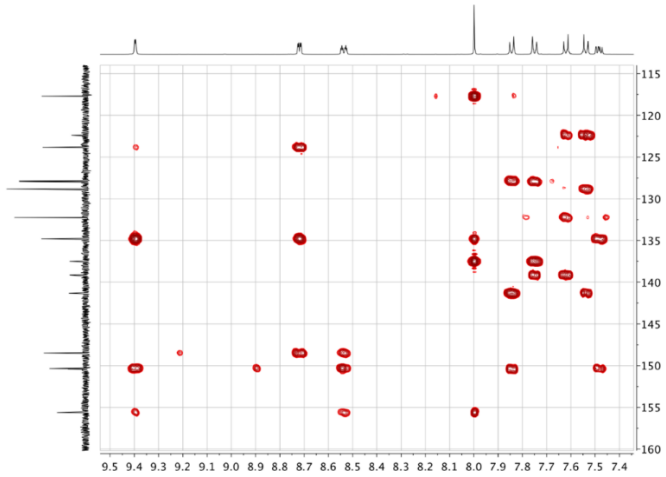

Figure S54. HMBC spectrum (aromatic region) of **19** (500 MHz ^{1}H, 126 MHz $^{13}C\{^{1}H\}$, $CDCl_3$, 298 K).

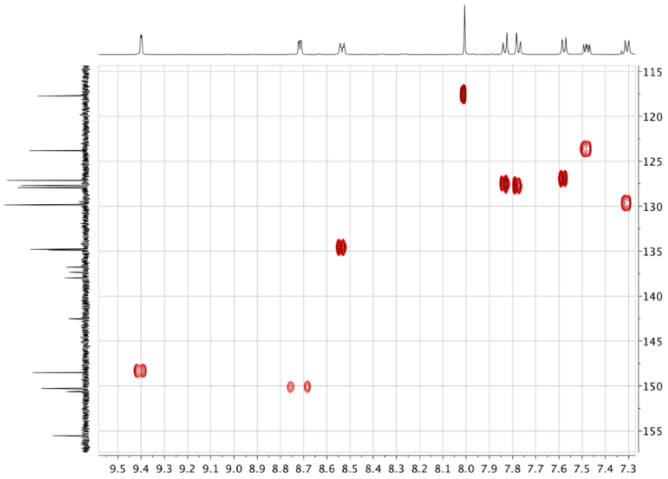

Figure S55. HMQC spectrum (aromatic region) of **20** (500 MHz ^{1}H, 126 MHz $^{13}C\{^{1}H\}$, $CDCl_3$, 298 K).

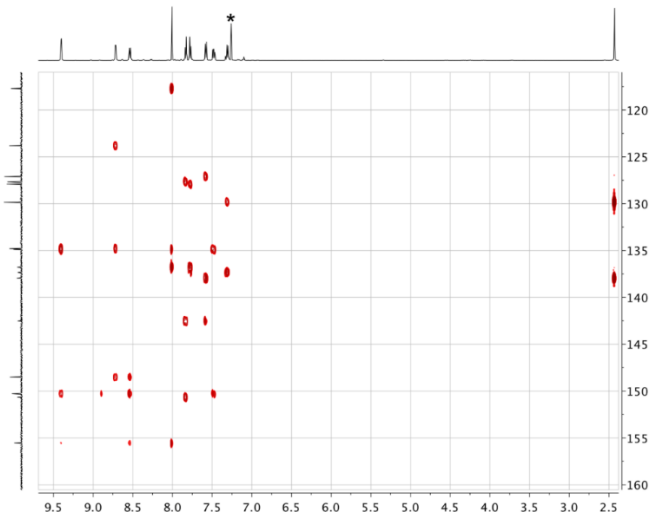

Figure S56. HMBC spectrum of **20** (500 MHz ^{1}H, 126 MHz $^{13}C\{^{1}H\}$, $CDCl_3$, 298 K). * = $CDCl_3$.

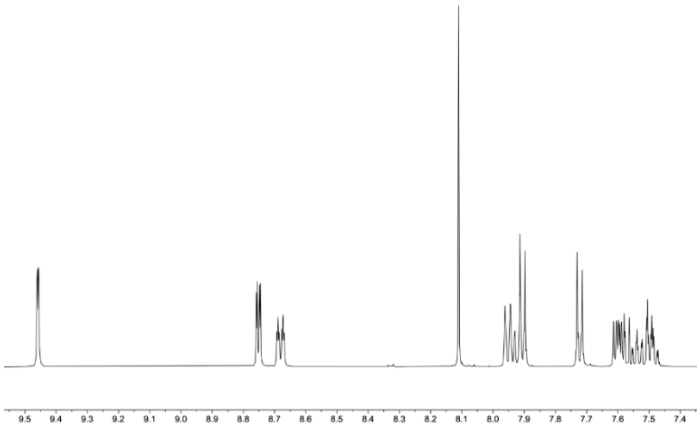

Figure S57. ^{1}H NMR spectrum of **21** (500 MHz, $CDCl_3$, 298 K).

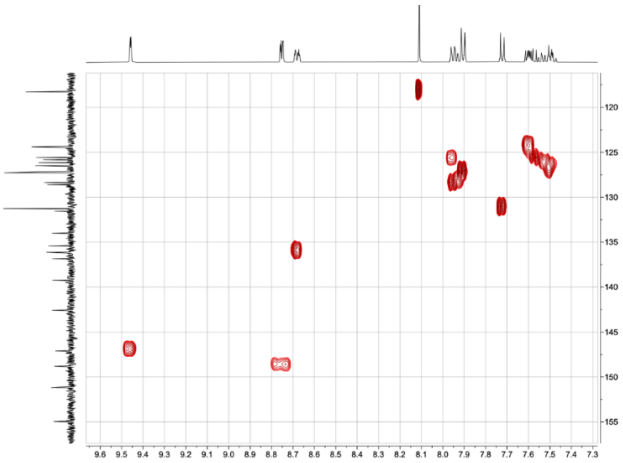

Figure S58. HMQC spectrum (aromatic region) of **21** (500 MHz ^{1}H, 126 MHz $^{13}C\{^{1}H\}$, $CDCl_3$, 298 K).

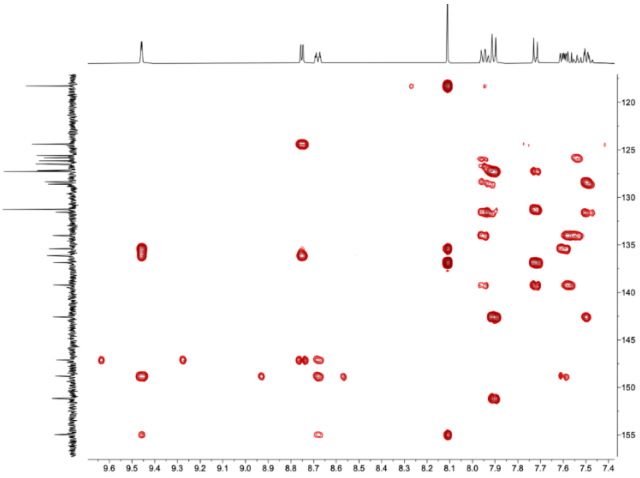

Figure S59. HMBC spectrum (aromatic region) of **21** (500 MHz ^{1}H, 126 MHz $^{13}C\{^{1}H\}$, $CDCl_3$, 298 K).

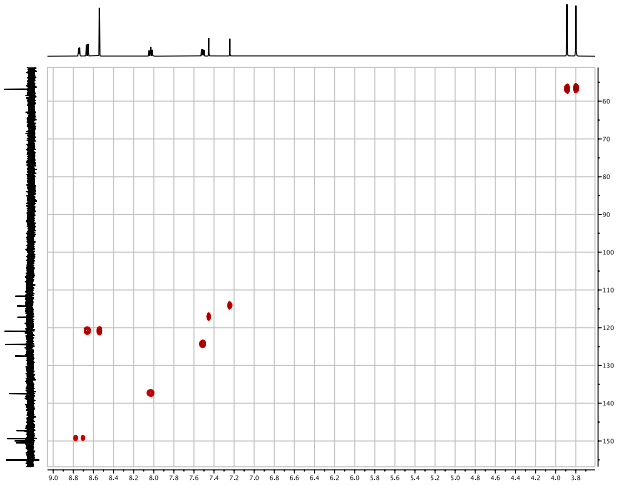

Figure S60. HMQC spectrum of **22** (500 MHz ^{1}H, 126 MHz $^{13}C\{^{1}H\}$, DMSO-d^6, 298 K).

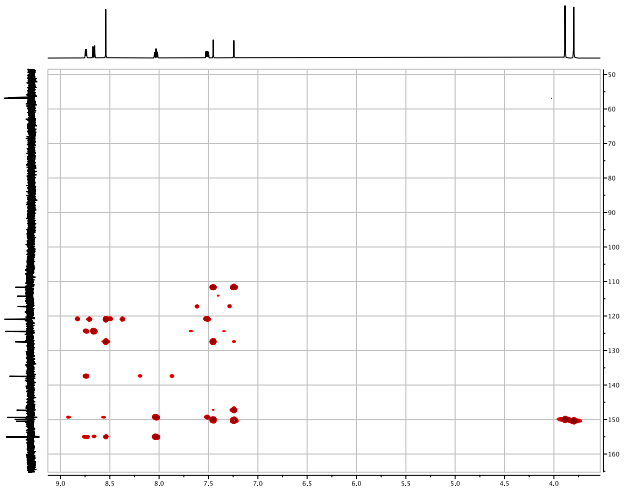

Figure S61. HMBC spectrum of **22** (500 MHz ^{1}H, 126 MHz ^{13}C{^{1}H}, DMSO-d^{6}, 298 K).

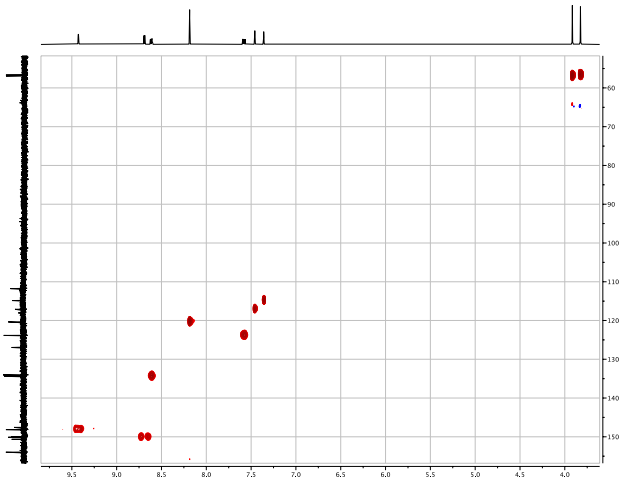

Figure S62. HMQC spectrum of **23** (500 MHz ^{1}H, 126 MHz ^{13}C{^{1}H}, DMSO-d^{6}, 298 K).

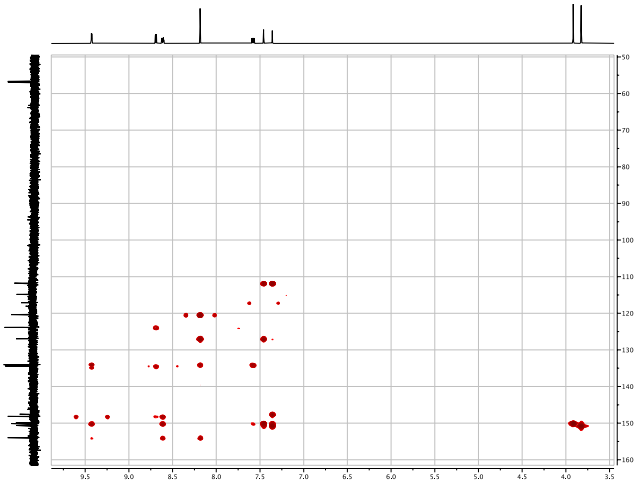

Figure S63. HMBC spectrum of **23** (500 MHz ^{1}H, 126 MHz ^{13}C{^{1}H}, DMSO-d^{6}, 298 K).

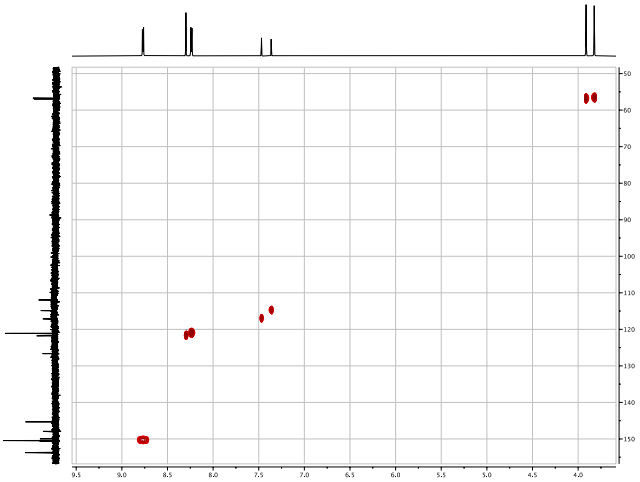

Figure S64. HMQC spectrum of **24** (500 MHz ^{1}H, 126 MHz ^{13}C{^{1}H}, DMSO-d^{6}, 298 K).

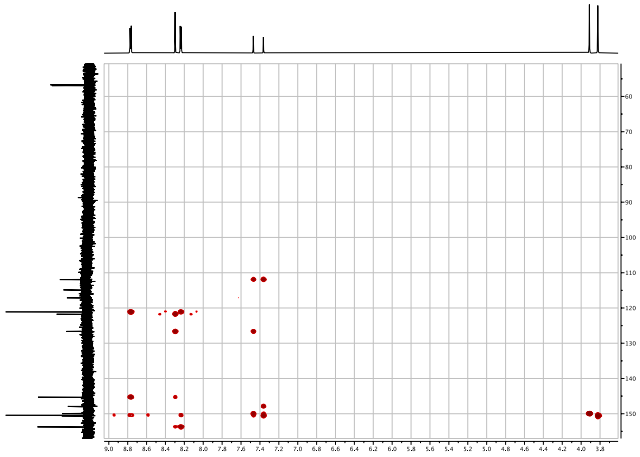

Figure S65. HMBC spectrum of **24** (500 MHz ^{1}H, 126 MHz ^{13}C{^{1}H}, DMSO-d^{6}, 298 K).

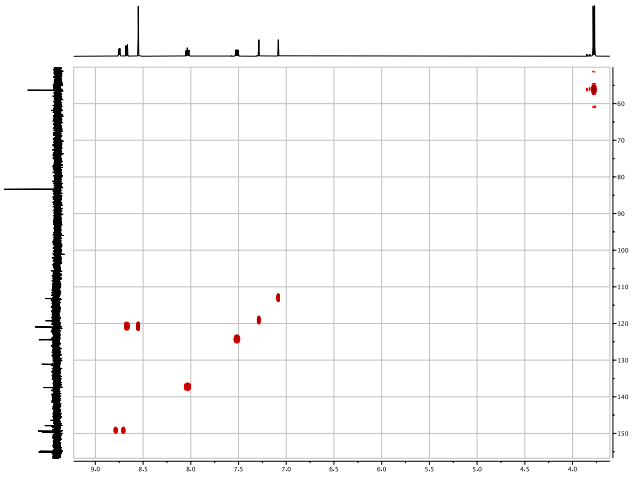

Figure S66. HMQC spectrum of **25** (500 MHz ^{1}H, 126 MHz ^{13}C{^{1}H}, DMSO-d^{6}, 298 K).

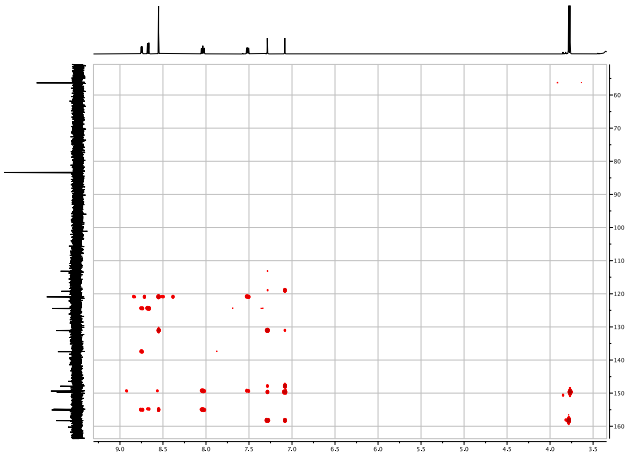

Figure S67. HMBC spectrum of **25** (500 MHz ^{1}H, 126 MHz $^{13}C\{^{1}H\}$, DMSO-d^{6}, 298 K).

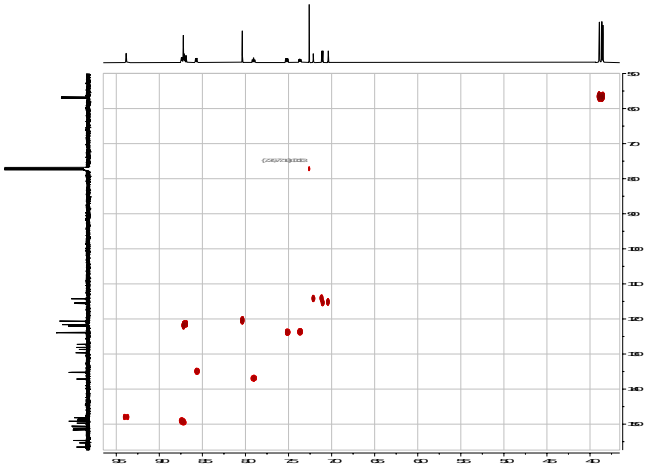

Figure S68. HMQC spectrum of **26** (500 MHz ^{1}H, 126 MHz $^{13}C\{^{1}H\}$, $CDCl_3$, 298 K).

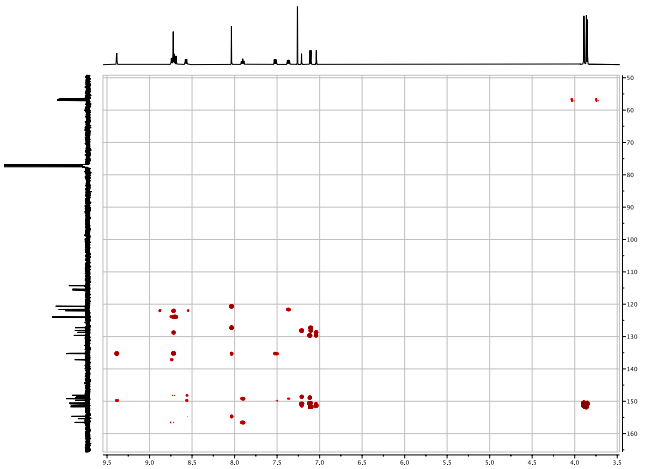

Figure S69. HMBC spectrum of **26** (500 MHz ^{1}H, 126 MHz $^{13}C\{^{1}H\}$, $CDCl_3$, 298 K).

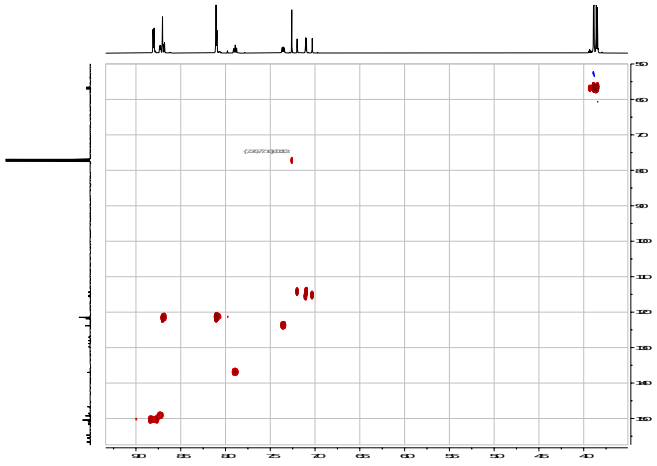

Figure S70. HMQC spectrum of **27** (500 MHz ^{1}H, 126 MHz ^{13}C{^{1}H}, $CDCl_3$, 298 K).

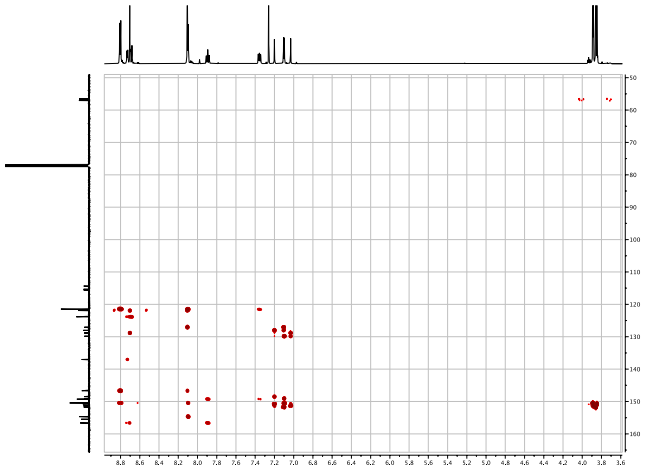

Figure S71. HMBC spectrum of **27** (500 MHz ^{1}H, 126 MHz ^{13}C{^{1}H}, $CDCl_3$, 298 K).

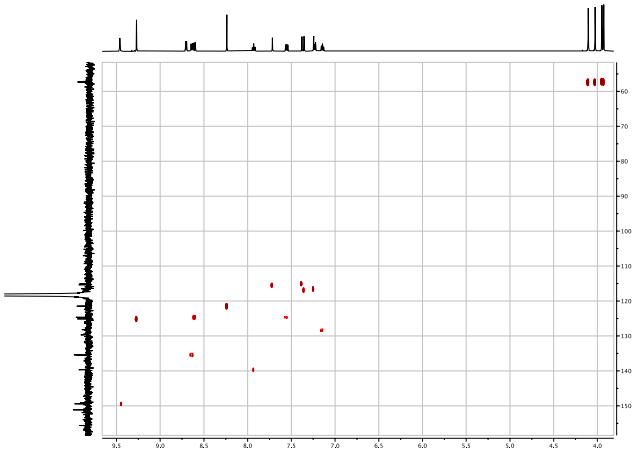

Figure S72. HMQC spectrum of [Fe(**26**)$_2$][NO_3]$_2$ (500 MHz ^{1}H, 126 MHz ^{13}C{^{1}H}, CD_3CN, 298 K). ^{13}C{^{1}H} signal at δ 118.26 ppm arises from CD_3CN.

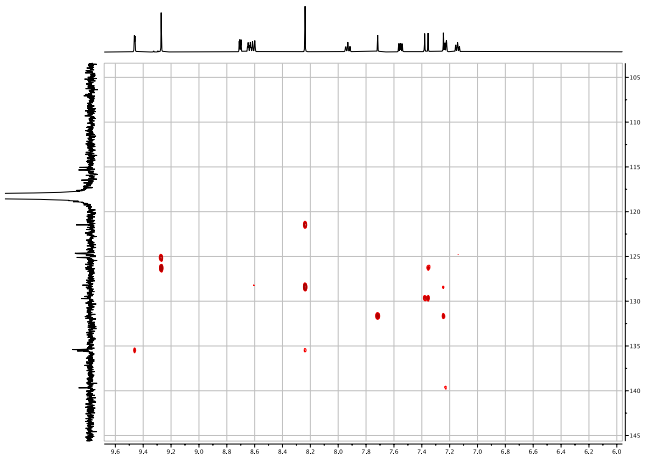

Figure S73. HMBC spectrum of [Fe(**26**)$_2$][NO_3]$_2$ (500 MHz ^{1}H, 126 MHz ^{13}C{^{1}H}, CD_3CN, 298 K). ^{13}C{^{1}H} signal at δ 118.26 ppm arises from CD_3CN.

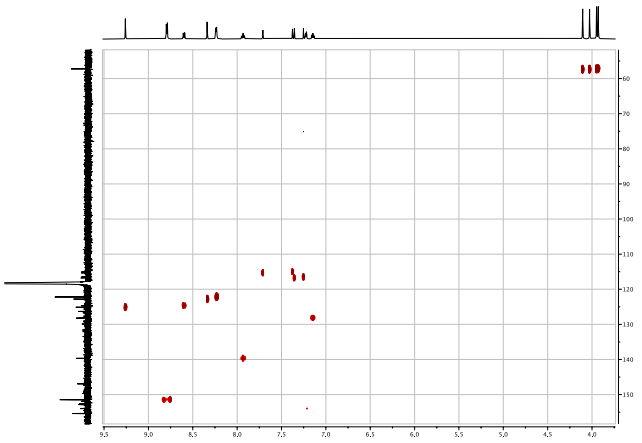

Figure S74. HMQC spectrum of [Fe(**27**)$_2$][BF_4]$_2$ (500 MHz ^{1}H, 126 MHz ^{13}C{^{1}H}, CD_3CN, 298 K).

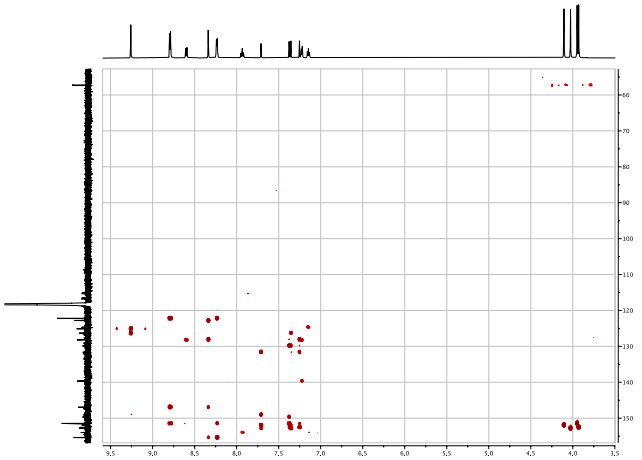

Figure S75. HMBC spectrum of [Fe(**27**)$_2$][BF_4]$_2$ (500 MHz ^{1}H, 126 MHz ^{13}C{^{1}H}, CD_3CN, 298 K).

Mass spectra and infrared spectra

For all published organic compounds, the mass spectra and infrared spectra are available in the corresponding Supporting Materials and the open access Zenodo.org links:

1. https://zenodo.org/record/6500007
2. https://zenodo.org/record/6510945
3. https://zenodo.org/record/6006205
4. https://zenodo.org/record/6510998
5. https://zenodo.org/record/6513479
6. https://zenodo.org/record/6513496
7. https://zenodo.org/record/6513425
8. https://zenodo.org/record/6500025
9. https://zenodo.org/record/6513459

TGA-MS spectra of some coordination polymers

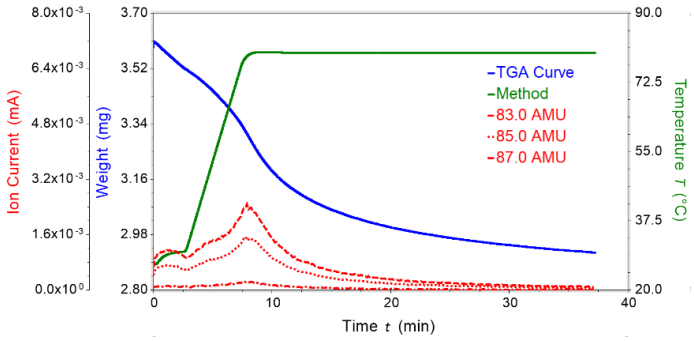

Figure S76. TGA and mass spectrometric traces for the analysis of $[Co(\mathbf{17})_2(NCS)_2]_n \cdot 4n CHCl_3$ (cycle 2: after 24 hour exposure to $CHCl_3$ vapor). Green: temperature vs. time; blue: weight of sample vs. time; red: mass detection for m/z 83.0 (most intense peak), 85.0 and 87.0. The initial mass of sample was 3.60 mg and a weight loss of 0.68 mg corresponds to ca. 19%.

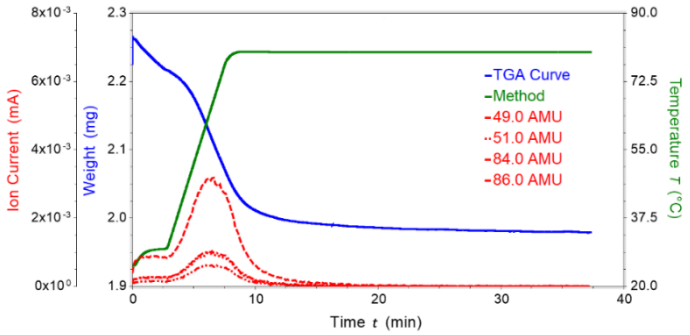

Figure S77. TGA and mass spectrometric traces for the analysis of $[Co(\mathbf{17})_2(NCS)_2]_n{\cdot}2n CHCl_3{\cdot}2n CH_2Cl_2$ (cycle 4: after 24 hours exposure to CH_2Cl_2 vapor). Green: temperature vs. time; blue: weight of sample vs. time; red: mass detection for *m*/*z* 49.0, 51.0, 84.0, 86.0. The initial mass of sample was 2.26 mg and a weight loss of 0.28 mg corresponds to ca. 12%.

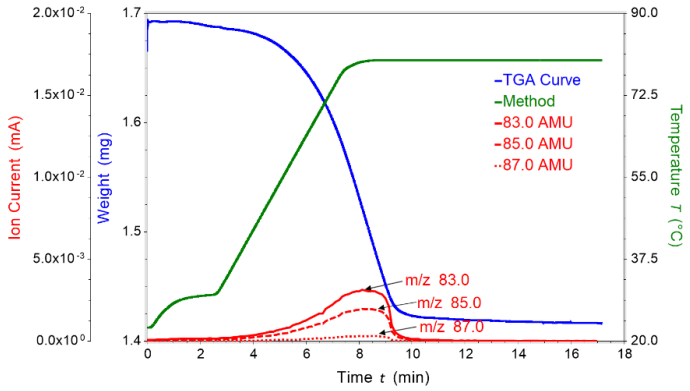

Figure S78. TGA and mass spectrometric traces for the analysis of $[Co(\mathbf{21})_2(NCS)_2]_n{\cdot}2n CHCl_3$ (cycle 2: after 48 hour exposure to $CHCl_3$ vapor). Green: temperature vs. time; blue: weight of sample vs. time; red: mass detection for *m*/*z* 83.0 (most intense peak), 85.0 and 87.0. The initial mass of sample was 1.69 mg and a weight loss of 0.28 mg corresponds to 16.6%.

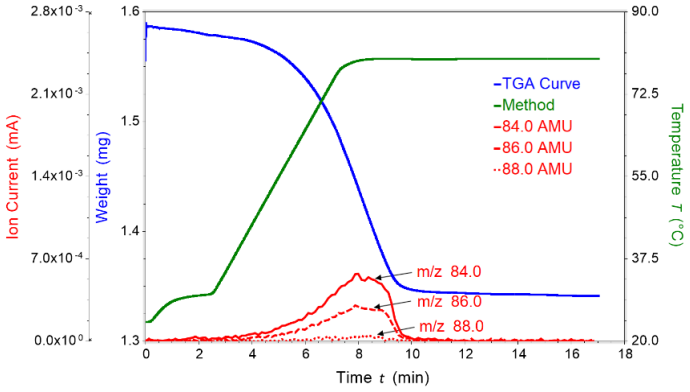

Figure S79. TGA and mass spectrometric traces for the analysis of $[Co(\mathbf{21})_2(NCS)_2]_n{\cdot}2n CDCl_3$ (cycle 3: after 24 hour exposure to $CDCl_3$ vapor). Green: temperature vs. time; blue: weight of sample vs. time; red: mass detection for *m*/*z* 84.0 (most intense peak), 86.0 and 88.0. The initial mass of sample was 1.59 mg and a weight loss of 0.25 mg corresponds to 15.7%.

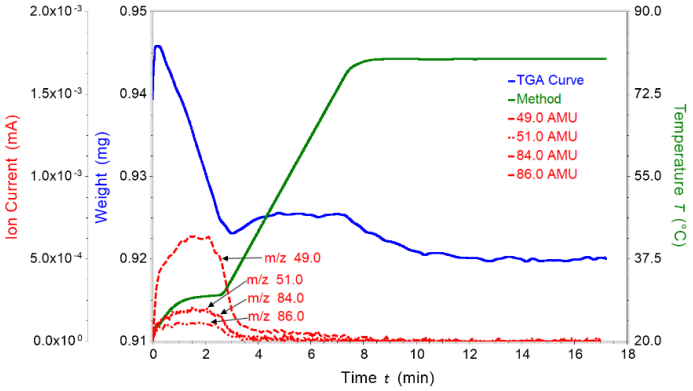

Figure S80. TGA and mass spectrometric traces for the analysis of $[Co(\mathbf{21})_2(NCS)_2]_n \cdot 2n CH_2Cl_2$ (cycle 4: after 72 hours exposure to CH_2Cl_2 vapor). Green: temperature vs. time; blue: weight of sample vs. time; red: mass detection for m/z 49.0, 51.0, 84.0, 86.0.